

Some pages of this thesis may have been removed for copyright restrictions.

If you have discovered material in AURA which is unlawful e.g. breaches copyright, (either yours or that of a third party) or any other law, including but not limited to those relating to patent, trademark, confidentiality, data protection, obscenity, defamation, libel, then please read our [Takedown Policy](#) and [contact the service](#) immediately

FIBRE GRATINGS IN NOVEL OPTICAL FIBRES FOR
APPLICATIONS IN SENSING

HELEN LINDSAY DOBB

Doctor of Philosophy

ASTON UNIVERSITY

April 2007

This copy of the thesis has been supplied on condition that anyone who consults it is understood to recognize that its copyright rests with its author and that no quotation from the thesis and no information derived from it may be published without proper acknowledgement.

ASTON UNIVERSITY

FIBRE GRATINGS IN NOVEL OPTICAL FIBRES FOR APPLICATIONS IN SENSING

HELEN LINDSAY DOBB

Doctor of Philosophy

April 2007

This thesis presents the fabrication of fibre gratings in novel optical fibres for sensing applications. Long period gratings have been inscribed into photonic crystal fibre using the electric-arc technique. The resulting sensing characteristics were found to depend on the air-hole geometry of the particular fibre. This provides the potential of designing a fibre to have enhanced sensitivity to a particular measurand whilst removing unwanted cross sensitivities. Fibre Bragg gratings have been fabricated in a variety of polymer optical fibres, including microstructured polymer optical fibre, using a continuous wave helium cadmium laser. The thermal response of the gratings have been characterised and found to have enhanced sensitivity compared to fibre Bragg gratings in silica optical fibre. The increased sensitivity has been harnessed to achieve a grating based device in single mode step index polymer optical fibre by fabricating an electrically tunable fibre Bragg grating. This was accomplished by coating the grating region in a thin layer of copper, which upon application of a direct current, causes a temperature induced Bragg wavelength shift.

Keywords

Polymer, Photonic Crystal Fibre

Acknowledgements

I would like to thank Aston Photonics Research Group and the Engineering and Physical Sciences Research Council (EPSRC) for funding this PhD. I particularly wish to thank my supervisors, Dr. David Webb and Dr. Kyriacos Kalli for their guidance, advice and endless enthusiasm for my research. My warmest thanks go to Dr. Tom Allsop for sharing his diverse experience, constantly challenging me and for his support and friendship over the last 4 years. Jovana Petrović and Dr. Vladimir Mezentsev must be thanked for their collaboration work on modelling the response of the long period gratings in photonic crystal fibre. Thanks also go to Bert Biggs for what must have seemed like endless requests for a wide variety of bits and pieces of equipment.

Thanks have to be made to both Dr. G.D. Peng and Dr. M.C.J. Large for providing step index and microstructured polymer optical fibre, respectively without which this thesis would not have been as successful.

To my parents who, despite a difficult few years, have been relentless in their support.

Finally, special thanks are given to Andrew Gillooly for his unending encouragement, patience and for restoring my determination to finish.

Table of Contents

1. THESIS OVERVIEW	12
2. FIBRE GRATING THEORY	15
2.1 MODES IN AN OPTICAL FIBRE	15
2.2 GRATINGS IN OPTICAL FIBRES	17
2.2.1 Fibre Bragg Gratings	17
2.2.2 Long Period Gratings	19
2.3 COUPLED MODE THEORY	22
2.3.1 Fibre Bragg Gratings	22
2.3.2 Long Period Gratings	25
2.4 SENSING CHARACTERISTICS.....	28
2.4.1 Fibre Bragg Gratings	28
2.4.1.1 Temperature Sensitivity	29
2.4.1.2 Axial Strain Sensitivity	29
2.4.2 Long Period Gratings	29
2.4.2.1 Temperature Sensitivity	30
2.4.2.2 Axial Strain Sensitivity	31
2.4.2.3 Refractive Index Sensitivity.....	31
2.4.2.4 Bend Sensitivity	33
2.5 GRATING INSCRIPTION TECHNIQUES.....	34
2.5.1 Fibre Bragg Grating Inscription Techniques	34
2.5.1.1 Amplitude-Division Interferometry	34
2.5.1.2 Wavefront-Division Interferometry	35
2.5.1.3 Phase Mask Inscription	36
2.5.1.4 Point-by-Point Inscription.....	43
2.5.2 Long Period Gratings Inscription Techniques	43
2.5.2.1 Permanent Modification.....	44
2.5.2.2 Physical Deformation of the Fibre	45
2.6 SUMMARY	45
3. ELECTRIC-ARC LONG PERIOD GRATINGS.....	46
3.1 INTRODUCTION	46
3.2 INSCRIPTION MECHANISM OF THE ELECTRIC-ARC TECHNIQUE.....	47
3.3 ULTRA-VIOLET PHOTOSENSITIVITY IN SILICA-BASED OPTICAL FIBRES	48
3.3.1 Hydrogen Loading	50
3.4 INSCRIPTION SET UP OF ELECTRIC-ARC LONG PERIOD GRATINGS	51
3.5 FABRICATED LPGs IN SMF USING THE ELECTRIC-ARC TECHNIQUE	52
3.6 THERMAL ANNEALING.....	56
3.7 SUMMARY	60
4. LONG PERIOD GRATINGS IN PHOTONIC CRYSTAL FIBRE	62
4.1 INTRODUCTION	62
4.2 BACKGROUND TO PCF	63

4.2.1 Different Classes of Photonic Crystal Fibres	63
4.2.1.1 High Index Guiding Photonic Crystal Fibre	64
4.2.1.2 Low Index Guiding Photonic Crystal Fibre	64
4.2.2 Fabrication of Photonic Crystal Fibres	65
4.2.3 Properties of Photonic Crystal Fibres	65
4.2.3.1 Endlessly Single Mode Operation	65
4.2.3.2 Dispersion Effects	67
4.3 GRATING FABRICATION TECHNIQUES IN PHOTONIC CRYSTAL FIBRE	68
4.4 INVESTIGATED PHOTONIC CRYSTAL FIBRES	69
4.5 LONG PERIOD GRATINGS IN PHOTONIC CRYSTAL FIBRE	71
4.5.1 Growth Characteristics	74
4.6 SENSING CHARACTERISTICS	75
4.6.1 Temperature	75
4.6.2 Bending	78
4.6.3 Refractive Index	83
4.6.4 Strain	86
4.7 MODELLED SENSING CHARACTERISTICS	89
4.7.1 Strain and Temperature Sensitivity	89
4.7.2 Refractive Index Sensitivity	91
4.8 SUMMARY OF THE EXPERIMENTAL SENSING CHARACTERISTICS	93
5. POLYMER OPTICAL FIBRE BACKGROUND	95
5.1 INTRODUCTION	95
5.2 CHEMISTRY OF POLYMER OPTICAL FIBRE	99
5.3 FREE RADICAL VINYL POLYMERISATION	102
5.4 INVESTIGATED POLYMER OPTICAL FIBRES	103
5.5 ATTENUATION	105
5.5.1 Absorption of Core Materials	106
5.5.2 Electronic Transition Absorption	108
5.5.3 Rayleigh Scattering	109
5.6 PHOTSENSITIVITY IN PMMA BASED OPTICAL FIBRES	110
5.6.1 UV irradiation at 325 nm	110
5.6.2 Effect of other UV wavelengths on PMMA	112
5.6.3 Femtosecond Laser Irradiation	115
5.7 CLEAVING	117
5.7.1 Razor Blade	117
5.7.2 Liquid Nitrogen and Razor Blade	119
5.7.3 Polishing	121
5.7.4 Microstructured POF	122
5.8 LIGHT TRANSMISSION THROUGH POLYMER OPTICAL FIBRE	123
5.8.1 Microstructured POF	126
5.9 SUMMARY	127
6. FIBRE BRAGG GRATING INSCRIPTION IN PLASTIC OPTICAL FIBRES	129
6.1 FBG FABRICATION	129
6.1.1 Amplitude-Division Interferometry	129
6.1.2 Phase Mask Inscription	131
6.1.2.1 Horizontal Alignment	131
6.1.2.2 Vertical Alignment	136
6.2 FIBRE BRAGG GRATINGS IN SILICA OPTICAL FIBRE USING 325 NM RADIATION	137

6.3 FIBRE BRAGG GRATINGS IN POLYMER OPTICAL FIBRE	139
6.3.1 <i>Step Index Polymer Optical Fibre</i>	140
6.3.1.1 Interferometric Devices in POF	144
6.3.2 <i>Microstructured Polymer Optical Fibre</i>	146
6.3.2.1 Transmission Profile of FBG in Microstructured Polymer Optical Fibre	152
6.4 DISCUSSION	154
6.5 SUMMARY	156
7. THERMAL TUNING OF FIBRE BRAGG GRATINGS IN PLASTIC OPTICAL FIBRES	158
7.1 INTRODUCTION	158
7.2 TEMPERATURE CHARACTERISTICS OF POF AND MPOF GRATINGS	159
7.2.1 <i>Thermal Response of FBGs in Single Mode Step Index POF (SMPengPOF)</i>	160
7.2.1.1 Discussion	163
7.2.2 <i>Thermal Response of FBGs in Single Mode Microstructured POF (SMmPOF)</i> ..	165
7.2.3 <i>Explanation of Thermal Hysteresis</i>	167
7.2.4 <i>Discussion</i>	168
7.3 TUNING COPPER COATED POLYMER OPTICAL FIBRE BRAGG GRATINGS	170
7.3.1 <i>Copper Coating Procedure</i>	170
7.3.2 <i>Wavelength Response of the Device</i>	171
7.3.3 <i>Tunable Filter Time Response</i>	173
7.3.4 <i>Summary</i>	178
8. THESIS CONCLUSIONS	179
9. PUBLICATIONS	183
9.1 PUBLICATIONS ON WORK REPORTED IN THIS THESIS	183
9.2 PUBLICATIONS ON WORK NOT REPORTED IN THIS THESIS	185
10. REFERENCES	187

Figure Captions

Figure 2-1:	Core and cladding modes supported by an optical fibre.....	16
Figure 2-2:	K-vector diagram for the diffraction from an FBG.....	17
Figure 2-3:	K-vector diagram for the diffraction from an LPG.....	17
Figure 2-4:	Fibre Bragg grating with cladding modes losses on the short wavelength side of the grating.....	19
Figure 2-5:	Transmission spectrum of an LPG with a period of 397 μm	20
Figure 2-6:	Phase matching curves for the first 9 cladding modes of a standard optical fibre with a cut-off wavelength of 675 nm [12].....	21
Figure 2-7:	Plots of the local intensity $I_z(r)$ of the four lowest order azimuthal first order cladding modes as a function of the radius of the optical fibre. All the modes are circularly symmetric and have been normalised to carry a power of 1 W [15].....	22
Figure 2-8:	FBG reflectivity with varying values of κL . $L = 25$ mm varying κ	24
Figure 2-9:	Changes in FBG bandwidth with changing values of N for $\kappa L = 2$	25
Figure 2-10:	Bar transmission through a uniform LPGs with $\kappa L = 3\pi/2$	27
Figure 2-11:	Cross transmission through uniform LPGs with $\kappa L = \pi/2$ (black line) and $\kappa L = 5\pi/2$ (grey line).....	27
Figure 2-12:	Spectral response of an LPG with a period of 400 μm inscribed into BGe co-doped fibre against various surrounding refractive indices.....	32
Figure 2-13:	Schematic diagram of a bent fibre showing the tensioned and compressed regions of the cladding.....	34
Figure 2-14:	Schematic diagrams of wavefront-division interferometric techniques. Left: prism interferometer, right: Lloyd's mirror interferometer.....	36
Figure 2-15:	Schematic of phase mask diffractions.....	37
Figure 2-16:	The intensity distribution along the x axis at $z = 0$ for different levels of zeroth-order: (a) = 0 %, (b) = 1 %, (c) = 3 % and (d) = 13 %.....	41
Figure 2-17:	Three-dimensional intensity distribution of the three beam interference for different levels of zeroth-order: (a) = 0 %, (b) = 1 %, (c) = 3 % and (d) = 13%... ..	42
Figure 3-1:	Ge(1) and Ge(2) electron trap centres associated with absorption bands at 281 nm and 213 nm respectively. Light grey circles represent oxygen atoms, black circles unpaired electrons.....	49
Figure 3-2:	GeO defect (wrong bond) absorbs a photon and creates a GeE' defect which contains an extra electron (black circle) which is free to move in the glass matrix until it is trapped by the original GeE' centre or another defect site. Grey circles represent oxygen atoms.....	49
Figure 3-3:	Schematic of the electric-arc inscription set up.....	51
Figure 3-4:	Various periods for LPG fabricated in single mode fibre.....	52
Figure 3-5:	Relationship between the melting region of a silica fibre and the electrode gap [58].....	53
Figure 3-6:	Formation of the attenuation bands of an electric-arc induced LPG with a period of 600 μm . Each trace taken after the fabrication of 5 grating planes... ..	54
Figure 3-7:	Wavelength (upper) and Transmission (lower) of an LPG attenuation band against time at room temperature [60].....	55

Figure 3-8:	Electrons excited by UV irradiation and trapped by a GeE' trap (left). Thermal depopulation of the traps (right).....	57
Figure 3-9:	Response of Electric-Arc and UV inscribed LPGs to temperature.....	59
Figure 3-10:	The shift in room temperature spectral location of the grating after each consecutive heating step. The x-axis depicts the temperature the grating was heated to before returning to room temperature.....	60
Figure 4-1:	Schematic of a microstructured optical fibre.....	64
Figure 4-2:	Typical cross section of ESM PCF.....	66
Figure 4-3:	Variation of V_{eff} against Λ/λ for various relative hole diameters d/Λ . Dashed line marks the standard fibre single mode step index cutoff V value, $V_{eff}=2.405$ [71].....	67
Figure 4-4:	Dispersion as a function of wavelength for PCFs with a hole separation of 2.3 μm and varying hole diameters [78].....	68
Figure 4-5:	Cross-section of the large-mode area PCF taken using a microscope with x 20 objective.....	70
Figure 4-6:	Cross-section of the endlessly single mode PCF taken using a microscope with x 20 objective.....	70
Figure 4-7:	Various periods of LPG fabricated using the fusion arc technique in LMA PCF.....	71
Figure 4-8:	Various periods of LPG fabricated using the fusion arc technique in ESM PCF.....	72
Figure 4-9:	Phase matching curves for all modes (i.e. not LP modes) of the ESM PCF where $\Lambda_B = \Lambda$ the period of the long period grating [84]. Some lines appear thicker due to overlapping.....	73
Figure 4-10:	Profile of resonance mode at 1402 nm for the 500 μm LPG in ESM PCF. Bright areas indicate areas of highest intensity [84].....	74
Figure 4-11:	Growth data of 500 μm period LPG in ESM PCF. Each trace taken after the fabrication of 5 grating planes.....	74
Figure 4-12:	Effect of temperature on the 1511 nm attenuation band in LMA PCF.....	76
Figure 4-13:	Effect of temperature on the 1402 nm attenuation band in ESM PCF.....	77
Figure 4-14:	Schematic of the bending rig.....	79
Figure 4-15:	Spectral response of the LMA LPG to bending. Black line, LPG with no curvature; dark grey line, curvature of -2.09 m^{-1} in the 180 degrees position and light grey line, curvature of $+2.09 \text{ m}^{-1}$ in the 0 degrees position.....	80
Figure 4-16:	Spectral sensitivity to bending of the attenuation band at 1668 nm in LMA PCF.....	81
Figure 4-17:	Spectral response of the LPG in ESM PCF to bending up to a curvature of 5.45 m^{-1} . Unbent curve in bold. Inset: Wavelength shift of band initially at 1402 nm as a result of induced curvature.....	82
Figure 4-18:	The effect of SRI on the attenuation bands in LMA PCF.....	84
Figure 4-19:	The wavelength shift of the four attenuation bands in LMA PCF as a function of the SRI (less than silica).....	84
Figure 4-20:	The wavelength shift of the attenuation bands in LMA PCF as a function of the SRI (greater than silica).....	85
Figure 4-21:	The wavelength shift of the attenuation bands in ESM PCF as a function of	86

	the SRI.....	
Figure 4-22:	Spectral response of LPG band at 1668 nm, in LMA PCF, to strain in the range 0–1.8 mε. Unstrained curve in bold. Inset: Wavelength shift as a result of the applied strain used to produce the spectral response shown.....	88
Figure 4-23:	Spectral response of LPG band at 1402 nm, in ESM PCF, to strain in the range 0–2.07 mε. Unstrained curve in bold. Inset: Wavelength shift as a result of applied strain.....	89
Figure 4-24:	Line plots along x-axis (solid lines) and y-axis (dashed) of the profiles of the core mode (black lines) and the 1402 nm resonant mode (blue lines) in air [84].....	92
Figure 4-25:	External refractive index sensitivity of resonant mode at 1402 nm in ESM PCF. Refractive indices: 1.0 (solid line), 1.2 (dashed), 1.3 (dotted), 1.35 (dash-dot), 1.4 (×), 1.42 (O) and 1.44 (∇) [84].....	92
Figure 5-1	aryl group for PFCB (TVE).....	101
Figure 5-2:	Chemical structures of free radical vinyl polymerisation initiators.....	102
Figure 5-3:	Thermal decomposition of AIBN; dots represent unpaired electrons (free radicals).....	102
Figure 5-4:	Initiation of PMMA; arrows indicate transfer of electrons. Left molecule: 2-cyano-2-propyl radical, Right molecule: methylmethacrylate monomer.....	103
Figure 5-5:	Monomer of MMA attaches to the initiator adding another free radical to the end of the chain enabling further molecules to attached to the chain.....	103
Figure 5-6:	Transmission loss for PMMA and PS core polymer optical fibre [126].....	106
Figure 5-7:	C-H harmonics in PMMA core optical fibre [126].....	107
Figure 5-8:	Attenuation of several different types of POF for different wavelengths, theoretical and experimental. The attenuation in silica is added for comparison [128].....	108
Figure 5-9:	(a) Attenuation due to Rayleigh scattering in PFCB (TVE), PMMA, Cytop, Teflon and Silica. (b) Attenuation due to Raleigh scattering linearised to $(1/\lambda^4)$ abscissa [130].....	110
Figure 5-10:	Reaction showing complete side chain scission by exposure to 248 nm radiation at 15 mJcm ⁻²	112
Figure 5-11:	Reaction showing further degradation of the free ester radical to continuous exposure to 248 nm at a fluence of 30 mJcm ⁻²	113
Figure 5-12:	Main polymer chain scission due to prolonged exposure of 248nm radiation.....	113
Figure 5-13:	Reaction showing partial side chain scission by exposure to 193 nm radiation.	113
Figure 5-14:	UV absorption spectrum of PMMA. Arrows correspond to the wavelengths of the emission lines from an excimer laser [134].....	114
Figure 5-15:	Cleaved SMPOF using a hot razor blade; images captured with ×20 objective: a) end face on, b) end side.....	118
Figure 5-16:	Cleaving FWPengPOF using a razor blade; images captured with ×20 objective: a) razor blade at room temperature, b) heated razor blade.....	118
Figure 5-17:	Cleaving SMPOF using liquid nitrogen and a razor blade at room temperature; images captured with ×20 objective: a) end face, b) end side on..	119
Figure 5-18:	Cleaving FMPengPOF using liquid nitrogen and a razor blade; image captured with ×20 objective.....	120

Figure 5-19:	Fraying observed with the FMPengPOF over time after cleaving; image taken with $\times 20$ objective.....	120
Figure 5-20:	Polished end of FWPengPOF mounted in a metal capillary, image taken with $\times 20$ objective.....	121
Figure 5-21:	Cleaved ends of microstructured POF by heating the fibre and razor blade to various temperatures; images taken using $\times 20$ objective.....	123
Figure 5-22:	HeNe light source through step-index POF; OSA resolution 1 nm.....	124
Figure 5-23:	Agilent BBS source through step index POF.....	125
Figure 5-24:	ASE light source through step index POF.....	125
Figure 5-25:	ASE light transmission through single mode mPOF.....	126
Figure 5.26:	Schematic representation of the pattern of HeNe laser light through mPOF; shaded region represents area of greatest intensity. (a): Light transmitting through the holey region, (b): Light in the fibre core.....	127
Figure 6-1:	Schematic of Mach-Zehnder Interferometer setup.....	130
Figure 6-2:	Initial fabrication set up for FBG inscription into POF.....	131
Figure 6-3:	Un-normalised absorption spectra of SM-800 after being exposed to 325 nm radiation.....	132
Figure 6-4:	Effect of 17 % zeroth-order on the fringes behind a $0.5742\ \mu\text{m}$ phase mask at a distance of zero behind the mask; $z = 0$	133
Figure 6-5:	Schematic of mounting the POF on to a microscope slide from the top view (left) and the side view (right).....	134
Figure 6-6:	Microscope image of damage fringes on the surface of MMPOF after 15 minutes of exposure taken using X63 objective.....	135
Figure 6-7:	Schematic of the vertical set up for FBG inscription [149].....	136
Figure 6-8:	Graph of the growth characteristic of an FBG fabricated in PS1200/1500 single mode silica fibre using the HeCd laser. Inset: grating profile.....	138
Figure 6-9:	Comparison of the growth of FBGs fabricated using 244 nm UV at 30 mW and 90 mW laser powers. Inset: 30 mW grating profile.....	139
Figure 6-10:	First FBG in POF fabricated in few-moded POF.....	141
Figure 6-11:	Temperature effect on FBG in POF. Black line: room temperature, grey line: arbitrary quantity of heat applied.....	141
Figure 6-12:	FBGs in few and single mode step index POF; OSA resolution 1 nm, grating length 10 mm.....	143
Figure 6-13:	Growth characteristics of an FGB in FMPengPOF.....	144
Figure 6-14:	Grating profile with a π phase shift [153].....	145
Figure 6-15:	Phase shifted FBG in single mode POF for different OSA bandwidths.....	146
Figure 6-16:	Backscattered diffraction patterns of the HeCd laser viewed by fluorescence; the pattern on the left was needed for successful inscription. Note that for clarity in the images, the fibre has been twisted slightly in order to shift the backscatter off the core region to the left of the main pattern; for correct alignment these would be superimposed. (photo: David Webb).....	148
Figure 6-17:	Grating profiles in the 3 different varieties of mPOF grating length 1 mm, OSA resolution 1 nm.....	149
Figure 6-18:	Reflection profile of FBG fabricated in few-moded mPOF.....	150
Figure 6-19:	Growth characteristics of the FBG in FMmPOF.....	150

Figure 6-20:	Reflection profile of FBG fabricated in SMmPOF.....	151
Figure 6-21:	Growth characteristics of the FBG in SMmPOF.....	152
Figure 6-22:	Transmission profile of FBG in mPOF [data provided by A. Argyros].....	153
Figure 7-1:	Setup of heating equipment for temperature calibration of POF FBG.....	159
Figure 7-2:	Spectral profile of the FBG in SMPengPOF.....	161
Figure 7-3:	Temperature sensitivity of the FBG in SMPengPOF.....	161
Figure 7-4:	The shift in room temperature spectral location of the grating after each consecutive heating step. The x-axis depicts the temperature the grating was heated to before returning to room temperature.....	163
Figure 7-5:	Wavelength dependence of the refractive indices of PMMA, PF polymer and silica. (A): 15 wt.% benzyl benzoate (BEN) added PMMA; (B) PMMA homopolymer; (C) 13.5 mol% GeO ₂ -doped SiO ₂ ; (D) pure SiO ₂ ; (E) 5.5 wt.% PF dopant added PF polymer; (F) PF homopolymer. Plots: experimental data. Solid line: approximated by Sellmeier equation [127].....	164
Figure 7-6:	Spectral profile of the FBG in SMmPOF at 26.6 °C and at 106.1 °C.....	165
Figure 7-7:	Temperature sensitivity of an FBG in SMmPOF. Black: Initial temperature cycling; Grey: second temperature cycle.....	166
Figure 7-8:	The shift in room temperature spectral location of the grating after each consecutive heating. The x-axis depicts the temperature the grating was heated to before returning to room temperature.....	167
Figure 7-9:	The effect of temperature on the young's modulus of PMMA. (graph obtained from [166]).....	167
Figure 7-10:	Transmission of ASE light source through SMmPOF before and after copper coating.....	171
Figure 7-11:	Wavelength Shift of the Bragg grating as a function of input power.....	172
Figure 7-12:	Rise time of thermally tuned fibre Bragg grating using a thin film copper coating as a resistive heater.....	173
Figure 7-13:	Temperature of the three input powers and the corresponding Bragg wavelength shift.....	177

1

Thesis Overview

Since the discovery of fibre Bragg gratings by Hill *et al* in 1978 [1], extensive research has been conducted into their spectral characteristics and potential applications. As a result these devices are currently deployed in applications as diverse as Wavelength Division Multiplexing (WDM) for telecommunication networks [2-3], optical fibre lasers [3-5] and sensing systems [3,6-9]. The work presented in this thesis focuses on using fibre gratings as sensing devices. Although extensive research has been conducted in this field of fibre optics, investigations have been primarily conducted with silica-based standard geometry fibres; i.e. circularly symmetric, one cladding, step index, single mode fibre. Recently however, interest has been developing in alternative optical fibre types, for example, photonic crystal fibres and polymer-based optical fibres. This thesis is concerned with investigating the sensing capabilities of fibre gratings inscribed in these fibres with the aim of discovering enhanced or differing sensitivities.

Photonic crystal fibres consist of a series of holes which run along the entire length of the optical fibre. These holes provide an effective refractive index for the cladding and the geometrical layout dictates the dispersion characteristics of the fibre. Consequently, since the spectral sensitivity of long period gratings depends on the dispersion properties of the fibre, fibres with different hole geometries could have significantly different sensing characteristics. The investigations presented in this thesis focus on determining the

sensing characteristics of long period gratings fabricated in two different geometries of photonic crystal fibre with the aim of verifying the dependence of the sensing characteristics on the geometrical layout of the fibre.

Polymer based optical fibres are becoming of increasing interest for biomedical applications such as in-vivo temperature profiling. As well as the obvious advantage that organic polymers are inherently biocompatible, their breaking strain is also higher than silica-based optical fibres. Fibre Bragg gratings fabricated in these fibres are expected to have enhanced thermal sensitivity over their silica counterparts initiating the work presented in this thesis.

The subsequent chapters are detailed as follows.

Chapter 2 introduces the theory of fibre Bragg gratings and long period gratings. The optical properties of both types of gratings are discussed with particular reference to their sensing characteristics. The chapter concludes with typical fabrication techniques of both varieties of fibre gratings.

Chapter 3 provides information on the differences between ultra-violet inscribed long period gratings and their electric-arc inscribed counterparts. The resulting difference in thermal stability is then discussed.

In chapter 4, the electric-arc inscription technique is used to inscribe long period gratings in two different types of non photosensitive photonic crystal fibre. The sensing characteristics of the resulting gratings are investigated. Different sensing characteristics are observed in the different fibres and are dependant on the geometry of the fibre. The results are then compared to modelled behaviour.

Although the majority of previously reported research has been concerned with silica-based optical fibres, polymer optical fibres are becoming of increasing interest. Chapter 5 provides an introduction to these fibres and their application in telecommunication systems as well as sensing systems, which is the primary focus of this thesis. The photosensitivity of these fibres is then detailed. Following this, fibre end preparation and light transmission through the fibre is discussed.

Chapter 6 is concerned with fibre Bragg grating inscription in a variety of different polymer optical fibres. Different attempts at inscription are detailed following knowledge gained from inscription in silica-based optical fibres. However, different considerations have to be implemented for successful inscription into these fibres. All the attempts are shown with explanations as to why some techniques were successful and others not. Implementation of the successful inscription technique revealed that fabrication in some polymer optical fibres was still unsuccessful which may be associated with the material composition of these particular fibres. Finally, the profiles of the successfully fabricated fibre Bragg gratings are shown.

Chapter 7 investigates the thermal characteristics of the fabricated polymer optical fibre Bragg gratings for potential implementation in biomedical sensing systems. The chapter concludes by measuring the response of a polymer optical fibre Bragg grating coated in a thin layer of copper and tuned using Joule heating.

Chapter 8 provides a summary of this thesis and suggestions for future research.

The thesis concludes with a summary of published works achieved during the progression of this PhD.

2

Fibre Grating Theory

This chapter aims to provide a background to the principles of optical fibre gratings. The phase matching and consequent power transfer between different modes in the optical fibre, in the presence of a fibre grating, is discussed. The difference between fibre Bragg gratings and long period gratings is detailed as well their associated sensing characteristics. Finally, fabrication techniques of both types of fibre gratings are discussed.

2.1 Modes in an Optical Fibre

Optical fibres consist of a core region of refractive index n_{co} which is surrounded by a cladding material with a lower refractive index, n_{cl} . The number of modes supported by the core in a step index fibre can be found by calculating the V-parameter [10]:

$$V = \frac{2\pi a}{\lambda_c} \sqrt{n_{co}^2 - n_{cl}^2} \quad (2.1)$$

where a is the radius of the core region and λ_c is the cut-off wavelength below which multiple modes propagate in the core region. For single mode operation the V-parameter must fulfil the requirement $V \leq 2.405$.

The propagation constant of the guided core mode, β_{co} , is given by:

$$\beta_{co} = \frac{2\pi}{\lambda} n_{co} \quad (2.2)$$

Glass optical fibres are surrounded by an acrylate coating, whose refractive index closely matches that of the cladding. As well as providing mechanical support, the coating effectively provides an infinite cladding, which minimises the possibility of guided cladding modes in the fibre due to the air/cladding interface. During grating inscription this coating is usually removed which results in a number of guided cladding modes being supported by the fibre which have a propagation constant in the range:

$$\frac{2\pi}{\lambda} n_3 < \beta_{cl} < \frac{2\pi}{\lambda} n_{cl}, \quad (2.3)$$

where n_3 is the refractive index of the surrounding material, usually $n_3 = n_{air} = 1$. Radiation modes, where the light is lost through the side of the fibre, also exist if the condition below is met.

$$0 < \beta_{rad} < \frac{2\pi}{\lambda} n_3. \quad (2.4)$$

A schematic diagram of the modes in an optical fibre is shown in Figure 2-1.

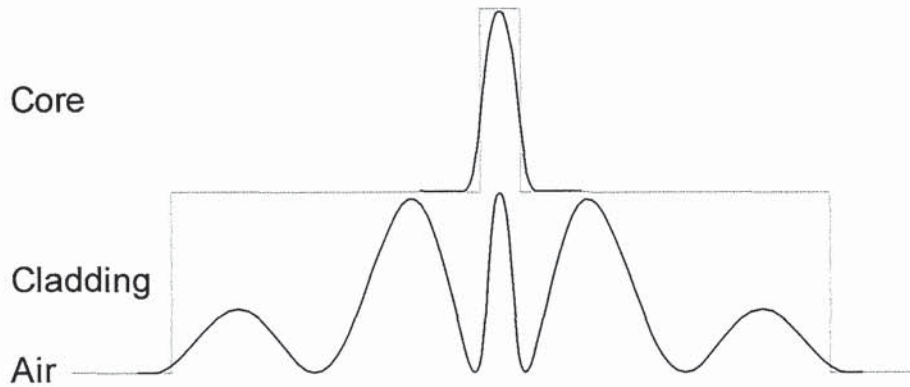


Figure 2-1: Core and cladding modes supported by an optical fibre.

When the electric fields of the modes overlap with each other there is a possibility of energy transfer between the modes. Phase matching of the modes can occur when the fields encounter a perturbation in the optical fibre and this is the principle mechanism of fibre gratings.

2.2 Gratings in Optical Fibres

The periodic perturbation in the core of an optical fibre is usually created by exposing the fibre to spatially periodic ultra-violet (UV) radiation, which locally changes the refractive index of the exposed regions. The resulting structure causes power transfer to occur between the different modes in the optical fibre. There are two different classifications of fibre gratings; fibre Bragg gratings (FBGs) and long period gratings (LPGs). Fibre Bragg gratings have short periodicities, typically less than $2\text{ }\mu\text{m}$ and couple light from the forward propagating core mode to a counter propagating core mode as demonstrated by the K-vector diagram in Figure 2-2.

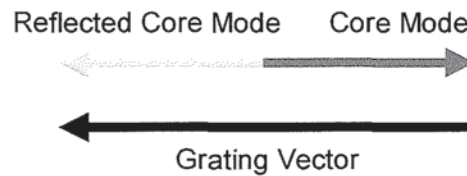


Figure 2-2: K-vector diagram for the diffraction from an FBG.

Long period gratings (LPGs) usually have periodicities ranging from $100\text{ }\mu\text{m}$ to 1 mm and couple light from the fundamental core mode to co-propagating cladding modes as shown by the K-vector diagram in Figure 2-3.

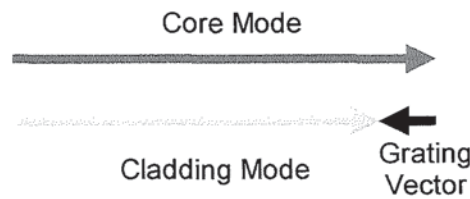


Figure 2-3: K-vector diagram for the diffraction from an LPG.

The following sections describe the different coupling mechanisms between the two types of fibre gratings.

2.2.1 Fibre Bragg Gratings

For an FBG the induced perturbation in the refractive index of the core along the length of the fibre (z axis) can be described by [11]:

$$\partial n_{eff}(z) = \overline{\partial n_{eff}}(z) \left[1 + \nu \cos\left(\frac{2\pi}{\Lambda} z + \phi(z)\right) \right], \quad (2.5)$$

where $\overline{\partial n_{eff}}$ is the ‘dc’ index change spatially averaged over a grating period, ν is the fringe visibility of the index change, Λ is the grating period and $\phi(z)$ is a term which describes the chirp of the grating. For a uniform grating with no chirp, $\phi(z)$ equals zero.

When white light is incident on an FBG, wavelengths of light which phase match with the period of the grating planes are coherently back reflected into counter propagating core modes. At the phase matching condition, the propagation constant of the diffracted wave, β_2 , is related to the propagation constant of the incident wave, β_1 , by:

$$\beta_2 = \beta_1 + m \frac{2\pi}{\Lambda}, \quad (2.6)$$

where m is the diffraction order of the grating, which for a fibre Bragg grating is predominately the first order resulting in $m = -1$. The propagation constants of the co and counter propagating core modes are equal in value, but due to the vector relationship, opposite in sign. Consequently, substituting equation 2.2 into 2.6 and rearranging provides the resonant wavelength, λ_B , for the counter propagating core mode:

$$\lambda_B = 2n_{co}^{eff} \Lambda. \quad (2.7)$$

where n_{co}^{eff} is the effective refractive index of the core region.

As well as coupling to the counter propagating core mode, a small amount of the transmitted light is coupled to counter propagating cladding modes. For this condition equation 2.7 becomes:

$$\lambda_{res} = (n_{co}^{eff} + n_{cl,m}^{eff}) \Lambda, \quad (2.8)$$

where $n_{cl,m}^{eff}$ is the effective refractive index of the m^{th} cladding mode. Although this coupling is significantly less than that of the counter propagating core mode, the effect is to observe a series of transmission dips in the spectrum on the short wavelength side of the Bragg resonance; see Figure 2-4.

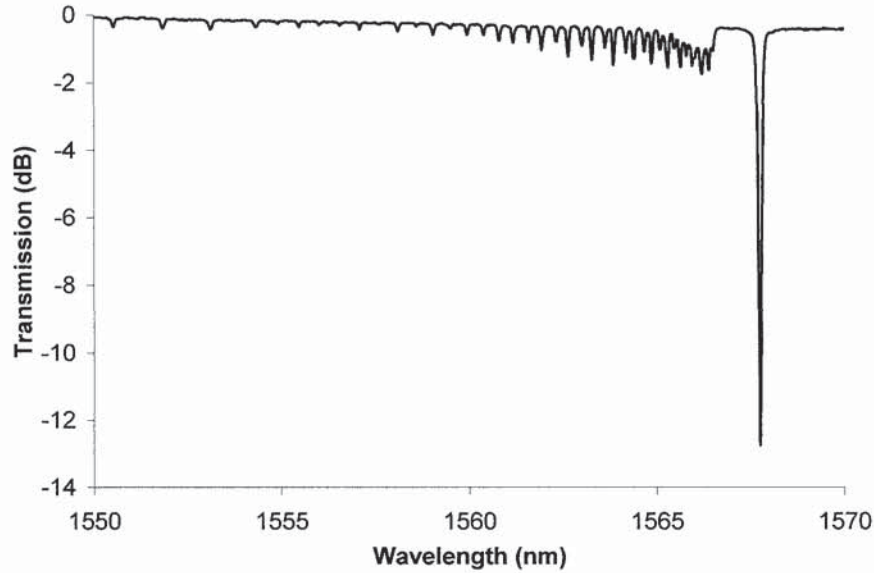


Figure 2-4: Fibre Bragg grating with cladding modes losses on the short wavelength side of the grating.

2.2.2 Long Period Gratings

LPGs couple light from the fundamental co-propagating core mode, LP_{01} to phase matched circularly symmetric co-propagating cladding modes, $HE_{l,v}$ [15]. These cladding modes are attenuated as they propagate along the fibre due to losses at the cladding coating interface and fibre bends. This leads to a series of attenuation bands in the transmission spectrum of the fibre; as shown in Figure 2-5.

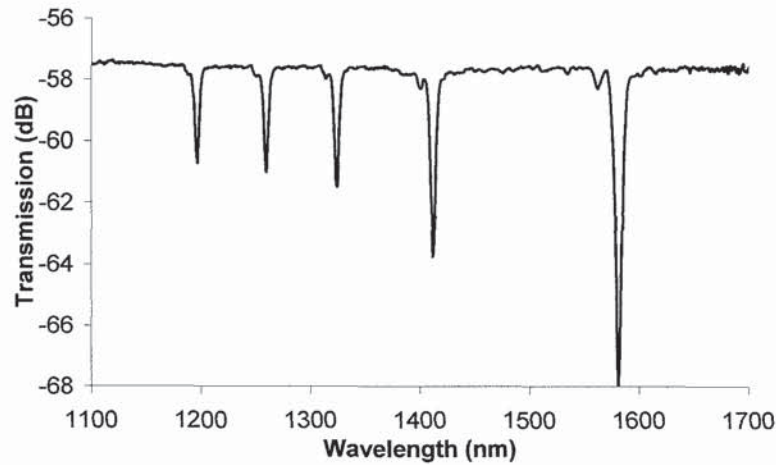


Figure 2-5: Transmission spectrum of an LPG with a period of 397 μm .

The difference between the propagation constants of the co propagating core and cladding modes, $\Delta\beta$, is small. Since the periodicity of a grating is related to $\Delta\beta$ by:

$$\Lambda = \frac{2\pi}{\Delta\beta}, \quad (2.9)$$

LPGs have large periodicities compared to FBGs. The phase matching equation for LPGs is given by:

$$\lambda_{res} = (n_{co}^{eff} - n_{cl,m}^{eff}) \Lambda. \quad (2.10)$$

For standard optical fibre geometries, the only non-zero coupling constants occur between the fundamental mode and the first order circularly symmetric azimuthal cladding modes i.e. $l = 1$. The effective refractive indices of the core and cladding material depend on the material and waveguide dispersion of the optical fibre which, from equation 2.10, affects the wavelength at which particular cladding modes couple to the fundamental core mode. By calculating the effect of dispersion on the propagation constants of the core mode and different cladding modes, phase matching/dispersion curves can be drawn. These depict the theoretical resonance wavelengths which occur for a given grating period; see Figure 2-6. The calculation of these curves is well documented [12-14].

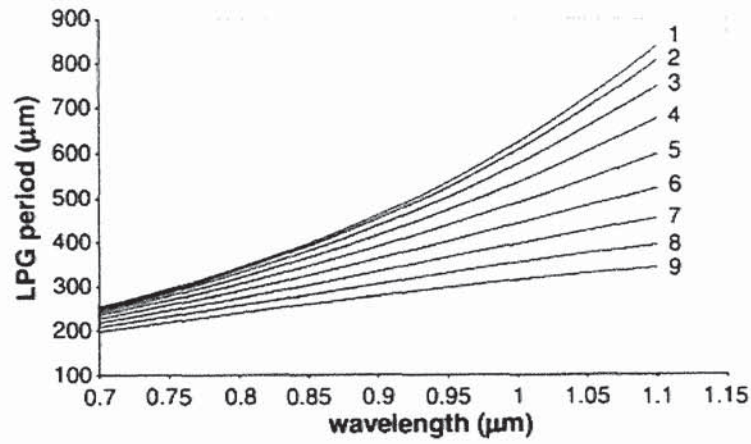


Figure 2-6: Phase matching curves for the first 9 cladding modes of a standard optical fibre with a cut-off wavelength of 675 nm [12].

Coupling however, can only occur between the fundamental mode and cladding modes which have an overlap integral with the core mode. Erdogan [15] used the strongly guiding condition to calculate the intensity of the 4 lowest order azimuthal first order cladding modes as a function of the optical fibre radius using the equation:

$$I_z(r) = \frac{1}{2} \text{Re}(E \times H^*) \cdot \hat{z} = \frac{1}{2} \text{Re}(E_r^{cl} H_\phi^{cl*} - H_r^{cl*} E_\phi^{cl}), \quad (2.11)$$

where E_r^{cl} is the radial component of the electric field of the cladding mode, E_ϕ^{cl} is the azimuthal component of the electric field, H_r^{cl} and H_ϕ^{cl} are the radial and azimuthal components of the magnetic field of the cladding mode, respectively. The resulting intensities are shown in Figure 2-7 and demonstrate that even numbered modes have very little intensity in the core region of the fibre whereas the odd modes have a significant proportion of their intensity in the core region. This suggests that the coupling to the even modes is extremely small.

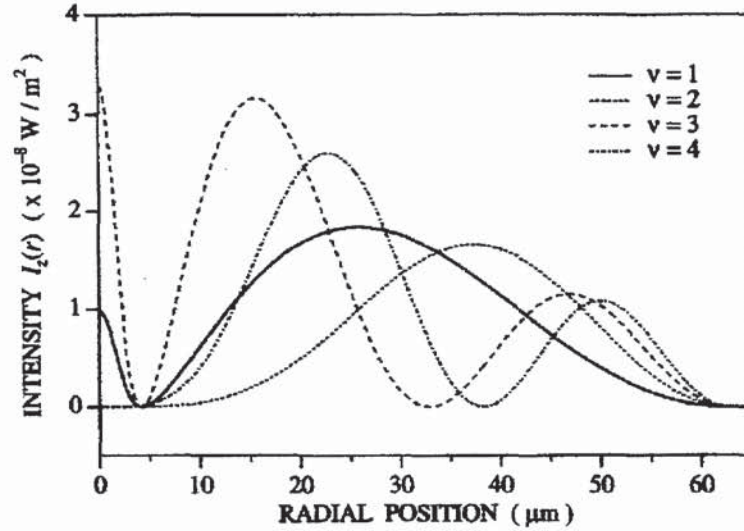


Figure 2-7: Plots of the local intensity $I_z(r)$ of the four lowest order azimuthal first order cladding modes as a function of the radius of the optical fibre. All the modes are circularly symmetric and have been normalised to carry a power of 1 W [15].

2.3 Coupled Mode Theory

Coupled mode theory is a mathematical model used to theoretically describe the power transfer between phase matched modes and deduce the resulting spectra of optical fibre gratings. The derivation of the equations is not reported here since it is covered in detail by Yariv [16].

2.3.1 Fibre Bragg Gratings

The amplitudes of the co propagating and counter propagating core modes can be represented by $A(z)$ and $B(z)$ respectively. Energy transfer between these modes can only occur in the presence of a perturbation. Along the length of the grating the amplitude of the two modes alters as coupling between the modes occurs. The amplitudes of the individual two modes is given by R and S for the co and counter propagating modes respectively [11]:

$$R(z) = A(z)e^{i\Delta\beta z - \frac{\phi}{2}}, \quad (2.12)$$

and

$$S(z) = B(z)e^{-i\Delta\beta z - \frac{\phi}{2}}, \quad (2.13)$$

where $\Delta\beta = \beta - m\pi/\Lambda$ is the detuning wave vector (a measure of the amount by which the Bragg condition is violated),

Assuming that all the power is transferred from one mode to another:

$$\frac{dR}{dz} = i(\Delta\beta R(z) + \kappa S(z)), \quad (2.14)$$

and

$$\frac{dS}{dz} = -i(\Delta\beta S(z) + \kappa^* R(z)), \quad (2.15)$$

where κ is the coupling coefficient and equals $\kappa = \kappa^* = \frac{\pi}{\lambda} \overline{\delta n_{eff}}$.

For a uniform grating, $\overline{\delta n_{eff}}$ and κ are constant and ϕ is zero. Assuming that no backward propagation occurs for $z \geq L/2$, where L is the length of the grating and that the incident wave originates from $z = -\infty$, the amplitude reflectivity, ρ , of the grating is given by:

$$\rho = \frac{S(-L/2)}{R(-L/2)}, \quad (2.16)$$

which results in:

$$\rho = \frac{-\kappa \sinh(QL)}{\Delta\beta \sinh(QL) + i\sqrt{S} \cosh(QL)}, \quad (2.17)$$

where $Q = \sqrt{\kappa^2 - \Delta\beta^2}$. The reflection coefficient is given by $R = |\rho|^2$:

$$R = \frac{\sinh^2(QL)}{-\frac{\Delta\beta^2}{\kappa^2} + \cosh^2(QL)} . \quad (2.18)$$

A graph of the reflection characteristics are shown in Figure 2-8 for a grating of length $L = 25$ mm, with varying coupling constant κ and detuning $\Delta\beta$. As κL increases, the peak reflectivity increases to unity with a broadening of the spectrum and increased sidelobe level.

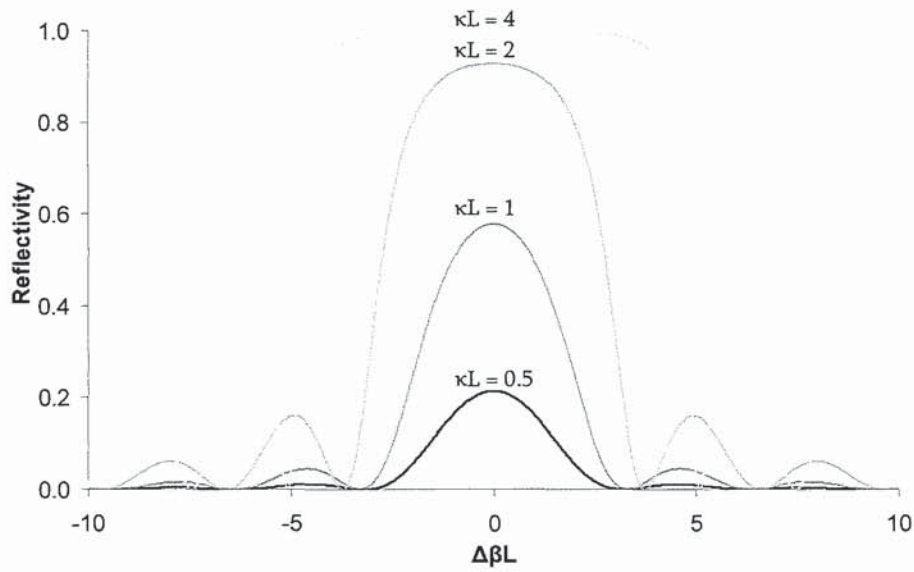


Figure 2-8: FBG reflectivity with varying values of κL . $L = 25$ mm varying κ .

The maximum grating reflectivity occurs when the detuning wave vector $\Delta\beta = 0$ i.e. at the point of exact phase matching. At this condition the reflectivity is given by:

$$R_{\max} = \tanh^2(\kappa L) . \quad (2.19)$$

Using equation 2.19, R_{\max} equals 21.4% for $\kappa L = 0.5$, 58% for $\kappa L = 1$, 92.9% for $\kappa L = 2$, and 99.8% for $\kappa L = 4$.

With an increasing number of grating planes, $N = L/\Lambda$, the bandwidth of a grating for a particular κL decreases as shown in Figure 2-9.

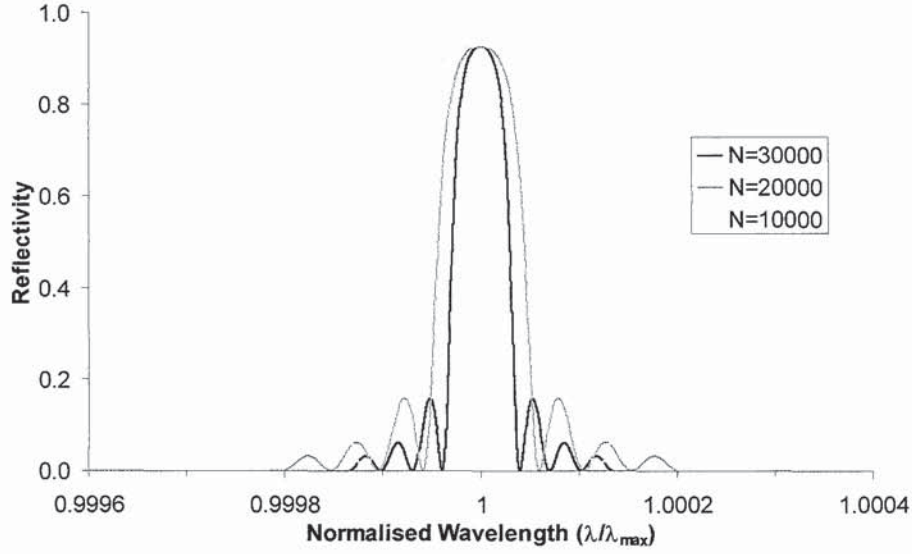


Figure 2-9: Changes in FBG bandwidth with changing values of N for $\kappa L=2$.

Figure 2-9 shows the reflectivity of an FBG against normalised wavelength λ / λ_{\max} where:

$$\frac{\lambda}{\lambda_{\max}} = \frac{1}{1 + \frac{\Delta\beta L}{\pi N}}. \quad (2.20)$$

The full-width half-maximum (FWHM) bandwidth can be approximated by [17]:

$$\Delta\lambda_{FWHM} \approx \lambda_B s \sqrt{\left(\frac{\partial n}{2n_{core}}\right)^2 + \left(\frac{1}{N}\right)^2}, \quad (2.21)$$

where $s \approx 1$ for strong gratings with near 100% reflectivity and $s \approx 0.5$ for weak gratings.

2.3.2 Long Period Gratings

The amplitudes of the co propagating core and cladding modes for an LPG can be represented by A_1 and A_2 respectively. Equations (2.14) and (2.15) still apply but $\kappa = \kappa_{21} = \kappa_{12}^*$, which are the “ac” cross-coupling coefficients and the new amplitudes are given by:

$$R(z) = A_1 e^{\left[-i(\sigma_{11} + \sigma_{22})\frac{z}{2}\right]} e^{\left(i\Delta\beta z - \frac{\phi}{2}\right)}, \quad (2.22)$$

and

$$S(z) = A_2 e^{\left[-i(\sigma_{11} + \sigma_{22}) \frac{z}{2} \right]} e^{\left(-i\Delta\beta z - \frac{\phi}{2} \right)}, \quad (2.23)$$

where σ_{11} and σ_{22} are the “dc” coupling coefficients.

The resulting transmission spectra can be found by assuming that one mode originates from negative infinite ($z = -\infty$) giving the initial conditions $R(0) = 1$ and $S(0) = 0$. Consequently, the power *bar* and *cross* transmissions, $t_{\pm} = |R(z)|^2 / |R(0)|^2$ and $t_x = |S(z)|^2 / |R(0)|^2$ are given by equations [16]:

$$t_{\pm} = \cos^2 \sqrt{\kappa^2 + \Delta\beta^2} z + \frac{1}{1 + \frac{\kappa^2}{\Delta\beta^2}} \sin^2 \sqrt{\kappa^2 + \Delta\beta^2} z, \quad (2.24)$$

and

$$t_x = \frac{1}{1 + \frac{\Delta\beta^2}{\kappa^2}} \sin^2 \sqrt{\kappa^2 + \Delta\beta^2} z. \quad (2.25)$$

The *bar* transmission is a measure of the transmission response of the core mode which has induced loss through coupling to a cladding mode; see Figure 2-10 for a grating with coupling constant $\kappa L = 3\pi/2$.

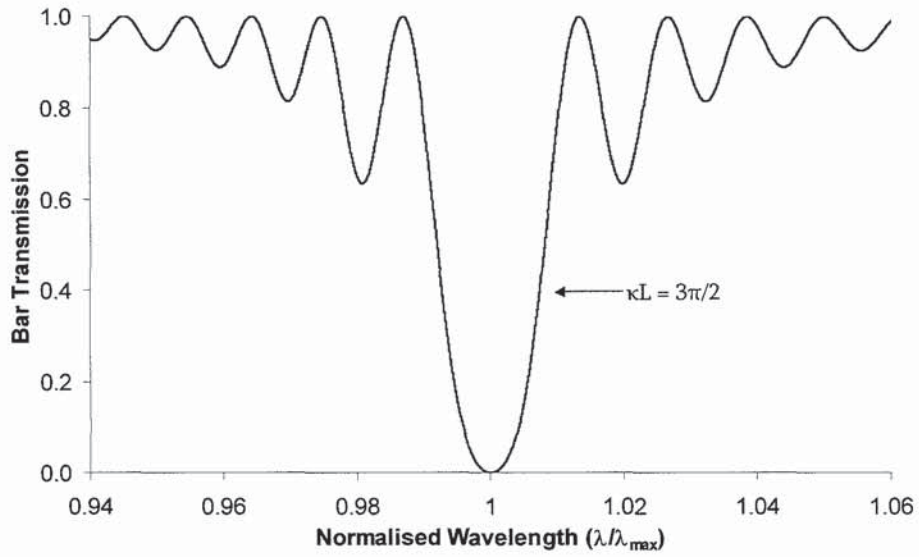


Figure 2-10: Bar transmission through a uniform LPGs with $\kappa L = 3\pi/2$.

The *cross* transmission is a measure of the ratio of power coupled into the cladding mode from the fundamental core mode. Examples can be seen in Figure 2-11 for gratings with $\kappa L = \pi/2$ and $\kappa L = 5\pi/2$.

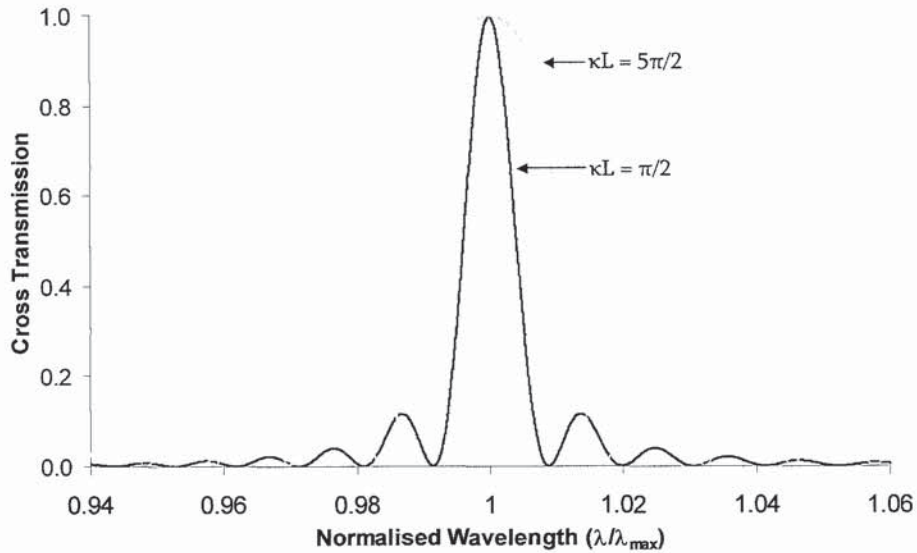


Figure 2-11: Cross transmission through uniform LPGs with $\kappa L = \pi/2$ (black line) and $\kappa L = 5\pi/2$ (grey line).

As with FBGs, the maximum coupling occurs when the detuning parameter $\Delta\beta = 0$. At this condition the equations become:

$$t_{\text{max}} = \cos^2(\kappa L), \quad (2.26)$$

and

$$t_{x,\max} = \sin^2(\kappa L). \quad (2.27)$$

Comparison of Figure 2-9 and 2-10, clearly demonstrates that there is a significant difference in bandwidth of LPGs and FBGs with FBGs having narrower features. The bandwidth of an LPG is typically measured as being the separation between the first zero points on either side of the main spectral peak and is given by [11]:

$$\frac{\Delta\lambda_0}{\lambda} = \frac{2\lambda}{\Delta n_{\text{eff}} L} \sqrt{1 - \left(\frac{\kappa L}{\pi}\right)^2}, \quad (2.28)$$

for a grating which at the most has one complete exchange of power between two modes ($\kappa L \leq \pi$). For extremely weak gratings the normalised bandwidth is $\Delta\lambda_0 / \lambda = 2 / N$.

2.4 Sensing Characteristics

The main emphasis of the remaining chapters of this thesis is concerned with using fibre gratings as sensing devices. As shown by section 2.2, the resonant wavelength depends on the grating period as well as the effective refractive index of the optical fibre's constituent materials. Both of these parameters can be affected by external measurands such as temperature and strain. Consequently, the resultant shift in resonant wavelength can be directly related to the magnitude of the external measurands.

2.4.1 Fibre Bragg Gratings

FBGs are only capable of sensing measurands which affect the effective refractive index of the core and/or the periodic spacing of the grating planes. Examples of such measurands are temperature and strain.

2.4.1.1 Temperature Sensitivity

The temperature induced Bragg wavelength shift, $\Delta\lambda_{BT}$, for a temperature change, ΔT , is given by [18]:

$$\Delta\lambda_{BT} = \lambda_B (\alpha_\Lambda + \alpha_n) \Delta T, \quad (2.29)$$

where α_Λ is the thermal expansion coefficient for the fibre given by $(1/\Lambda)(\partial\Lambda/\partial T)$, which is approximately 0.55×10^{-6} for silica and α_n is the thermo-optic coefficient given by $(1/n_{eff})(\partial n_{eff}/\partial T)$ which is approximately 8.6×10^{-6} for a germanium doped silica core fibre. The typical temperature sensitivity of silica fibre FBGs at 1550 nm is +10 pm/°C [19].

2.4.1.2 Axial Strain Sensitivity

The axial strain induced Bragg wavelength shift, $\Delta\lambda_{BS}$, for applied longitudinal strain, $\Delta\epsilon_z$, is given by [18]:

$$\Delta\lambda_{BS} = \lambda_B (1 - \rho_\alpha) \Delta\epsilon_z, \quad (2.30)$$

where ρ_α is the photoelastic coefficient of the fibre defined as:

$$\rho_\alpha = \frac{n^2}{2} [\rho_{12} - \nu(\rho_{11} - \rho_{12})], \quad (2.31)$$

ρ_{11} and ρ_{12} are the components of the fibre-optic strain tensor and ν is Poisson's ratio. In silica-based optical fibres the strain sensitivity of 1550 nm FBGs has been measured to be 1.15 pm/ $\mu\epsilon$ [19].

2.4.2 Long Period Gratings

LPGs are capable of sensing any external parameter that modifies the core and cladding guiding properties. The magnitude of the response is primarily due to a differential change

in the propagation constants of the core and cladding modes, which alters the resonant coupling wavelengths. As with FBGs, the external measurands can also affect the periodicity of the grating planes. Therefore the sensitivity of the long period grating to external measurands depends on the material and waveguide dispersion of the core and cladding materials. This results in optical fibres with different dispersion characteristics having significantly different sensing capabilities.

The range of sensing parameters of LPGs is greater than for FBGs. As well as temperature and strain, LPGs can also detect changes in the external refractive index. They also have increased sensitivity over FBGs to bends in the optical fibre located at the grating region.

2.4.2.1 Temperature Sensitivity

The temperature sensitivity of an LPG can be found by differentiating equation 2.10 to give [20]:

$$\frac{d\lambda}{dT} = \frac{d\lambda}{d(\delta n_{eff})} \left(\frac{dn_{co}^{eff}}{dT} - \frac{dn_{cl}^{eff}}{dT} \right) + \Lambda \frac{d\lambda}{d\Lambda} \frac{1}{L} \frac{dL}{dT}, \quad (2.32)$$

where λ is the central wavelength of the attenuation band being investigated, T is the temperature, $\delta n_{eff} = n_{co}^{eff} - n_{cl}^{eff}$, L is the length of the LPG and Λ the period. This equation demonstrates the dependence of the sensitivity on the material and waveguide dispersion; the material dispersion, calculated from the first term on the right hand side of equation (2.32) and the waveguide dispersion (the change of grating period with temperature) described by the second term on the right-hand side of equation (2.32). Both terms can be either negative or positive; the waveguide dispersion however, is strongly dependant on the slope of the phase matching curve of the particular cladding mode. Since these curves have differing responses for different cladding modes and the effective refractive indices vary between cladding modes, the temperature response of each individual attenuation band varies.

2.4.2.2 Axial Strain Sensitivity

The axial strain sensitivity is of similar structure to the temperature sensitivity. The longitudinal strain sensitivity is therefore provided by the equation [20]:

$$\frac{d\lambda}{d\varepsilon} = \frac{d\lambda}{d(\delta n_{eff})} \left(\frac{dn_{co}^{eff}}{d\varepsilon} - \frac{dn_{cl}^{eff}}{d\varepsilon} \right) + \Lambda \frac{d\lambda}{d\Lambda}. \quad (2.33)$$

The material effects for this measurand arise from the changes in the fibre dimensions from the applied strain as well the strain optic effect. The waveguide dispersion component comes from the slope of the dispersion term $d\lambda/d\Lambda$.

2.4.2.3 Refractive Index Sensitivity

LPGs can only detect external refractive index changes if part of the relevant cladding mode comes into contact with the surrounding material. Subsequent changes in the refractive index of the surrounding medium change the effective refractive index of the cladding mode and consequently the phase matching condition.

The equation for the refractive index sensitivity of long period gratings is shown below [12]:

$$\frac{d\lambda}{dn_3} = \frac{d\lambda}{dn_{cl}} \frac{dn_{cl}}{dn_3}, \quad (2.34)$$

where n_3 is the refractive index of the surrounding material. For bulk immersion, this effect is dependant on the surrounding refractive index being less than the refractive index of the cladding material. The sensitivity response of the attenuation bands increases exponentially with increasing values of surrounding refractive index. This continues until the surrounding refractive index matches the effective refractive index of the particular cladding mode being investigated. At this point the cladding appears to be infinite and since the cladding mode is no longer supported, it is lost from the fibre by radiation.

For surrounding refractive indices greater than that of the cladding material, guided cladding modes cannot exist because total internal reflection cannot occur at the cladding-surrounding material interface. However, attenuation bands are still present because Fresnel reflections occur at the cladding-surrounding material interface resulting in leaky cladding modes. The magnitude of the Fresnel reflections increases with increasing external refractive index leading to deeper attenuation bands. However, the external index no longer affects the propagation constant of the cladding mode. Consequently the phase matching condition is not affected and no significant wavelength shift of the bands occurs with further increases in external refractive index. The change in wavelength shift and attenuation band strength for different values of external refractive index is shown in Figure 2-12.

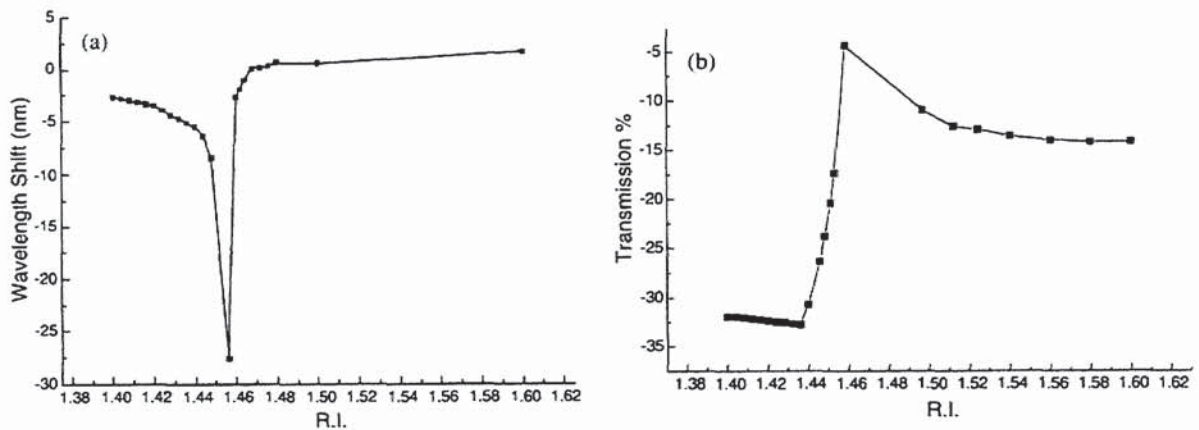


Figure 2-12: Spectral response of an LPG with a period of 400 μm inscribed into BGe co-doped fibre against various surrounding refractive indices (R.I.): (a) wavelength shift (b) minimum transmission value [12].

As well as the bulk immersion spectral response of the LPG to refractive index changes, investigations have been conducted by depositing thin films of material onto the optical fibre whose refractive index is dependent on the environmental conditions. This has resulted in a species-specific chemical sensor [21] and a tunable loss filter [22]. Research into the effect the thickness of the overlap material has on the response of LPGs was investigated by using the Langmuir-Blodgett technique to deposit one molecular layer at a time [23]. For thin films with refractive indices higher than that of the cladding material, the spectral response of the LPG was found to have a high sensitivity when thicknesses

around a few hundred nanometres had been deposited. In contrast, materials of lower refractive index than the cladding showed reduced sensitivity to the thickness of the deposition.

2.4.2.4 Bend Sensitivity

When inducing curvature into a fibre containing an LPG there are two possible responses of the transmission spectrum. As with the sensitivity to the other external measurands, a shift in the central wavelength of the attenuation bands can occur, which unlike the aforementioned sensitivities, is accompanied by spectral broadening of the band as well as a reduction in the power, whilst the other potentially observed effect is resonance splitting, where each band splits into two components.

The wavelength shift occurs through stress induced changes in the effective refractive index altering the phase matching condition. Whilst this effect is possible in fibre Bragg gratings, LPGs exhibit increased sensitivity due to the differential between the core and cladding effective refractive indices. The reduction in the magnitude of the attenuation band is attributed to the field profile of the cladding mode changing with increasing bend so that there is less overlap with the core mode and hence a smaller coupling constant.

The splitting of an attenuation band during bending is attributed to the symmetry of the fibre being disrupted which results in two degenerate spatial cladding modes becoming non-degenerate. One of these modes propagates in the tensioned region of the cladding resulting in a red wavelength shift and the other propagates in the compressed region resulting in a blue wavelength shift [24]. Consequently, with increasing curvature these modes move further away from each other spectrally.

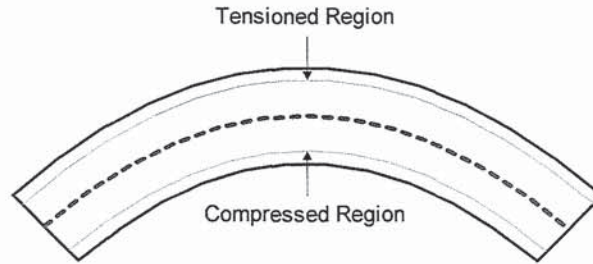


Figure 2-13: Schematic diagram of a bent fibre showing the tensioned and compressed regions of the cladding.

2.5 Grating Inscription Techniques

Described in this section are the different fabrication techniques for inscribing fibre Bragg gratings and long period gratings into optical fibres.

2.5.1 Fibre Bragg Grating Inscription Techniques

In order to inscribe FBGs, a periodic UV interference pattern is usually required, although recently pulsed laser systems have been used to inscribe each fringe of the grating individually. Consequently, there are currently, four different techniques for inscribing FBGs into optical fibres:

1. Amplitude-Division Interferometry
2. Wavefront-Division Interferometry
3. Phase Mask Inscription
4. Point-by-Point Inscription

2.5.1.1 Amplitude-Division Interferometry

This technique is performed by splitting monochromatic light into two components which are then recombined with an angular separation. The result is a sinusoidal variation in intensity at the intersection of the two beams. The period of the resulting intensity fringes, Λ , depends on the wavelength of the monochromatic light, λ_{UV} , as well as the angle of intersection, θ , by the equation:

$$\Lambda = \frac{\lambda_{UV}}{2 \sin(\theta/2)}. \quad (2.35)$$

This method was first proposed by Meltz *et al* in 1989 [25], where a beam splitter was used to divide a UV laser beam into two paths. These two beams were then directed to converge at a point using two mirrors. This system has the advantage that by changing the intersection angle, the Bragg wavelength of the grating can be changed to any desired value, provided the diffraction limit of the inscription wavelength ($\lambda/2$) is not exceeded.

However, the major drawback of this technique is its susceptibility to vibrations in the environmental conditions as well as in the mechanical mounts of the optics. These vibrations cause submicron displacements of the recombining beams causing the fringe pattern to drift, reducing the fringe visibility and consequently the strength of the grating. It is also important to ensure that the optical path length difference is significantly less than the coherent length of the laser source otherwise coherent interference of the beams does not occur and grating inscription via the interferometric technique is made impossible.

2.5.1.2 Wavefront-Division Interferometry

This technique involves directing a parallel laser beam at a reflective surface so that half of the beam is reflected across the path of the unreflected section of the beam. Interference occurs where the reflected and unreflected beams overlap. Examples of this technique are the prism interferometer [3,26] and the Lloyd's mirror interferometer [3,26]; see Figure 2-14.

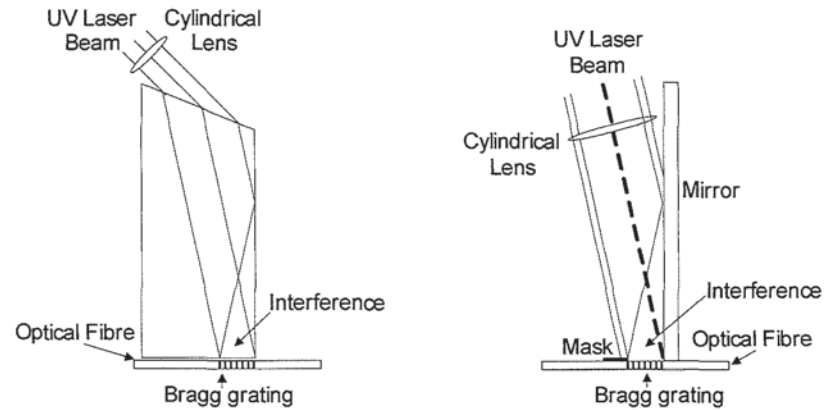


Figure 2-14: Schematic diagrams of wavefront-division interferometric techniques. Left: prism interferometer, right: Lloyd's mirror interferometer.

The main advantage of the wavefront-division interferometer over the amplitude-division interferometer is that only one optical component is needed which reduces the susceptibility to mechanical vibrations. In the Lloyd's mirror interferometer the distance over which the components of the UV beam are separated is shorter than in the amplitude-division interferometer reducing the effects of air currents. However, the length of the resulting FBG is restricted to half the beam width of the incident laser beam.

2.5.1.3 Phase Mask Inscription

Phase mask inscription has been shown to be a reliable method for fabricating FBGs into photosensitive fibre [27-28] since it was first demonstrated in 1993. A phase mask is a diffracting optical element which is used to generate an interference pattern similar to that achieved by the interferometric technique. It is constructed of a surface relief grating which has been etched onto the surface of fused silica and is designed to spatially modulate a UV inscription beam. Consequently, when UV radiation is incident normally to the mask it is diffracted into the different orders of the mask; see Figure 2-15. For phase masks designed to produce FBGs in the 1550 nm telecommunications window, the plus and minus first order diffractions are maximised to be greater than 35 %. The mask is also designed to ensure the zero-order diffraction contains less than 3 % of the transmitted power.

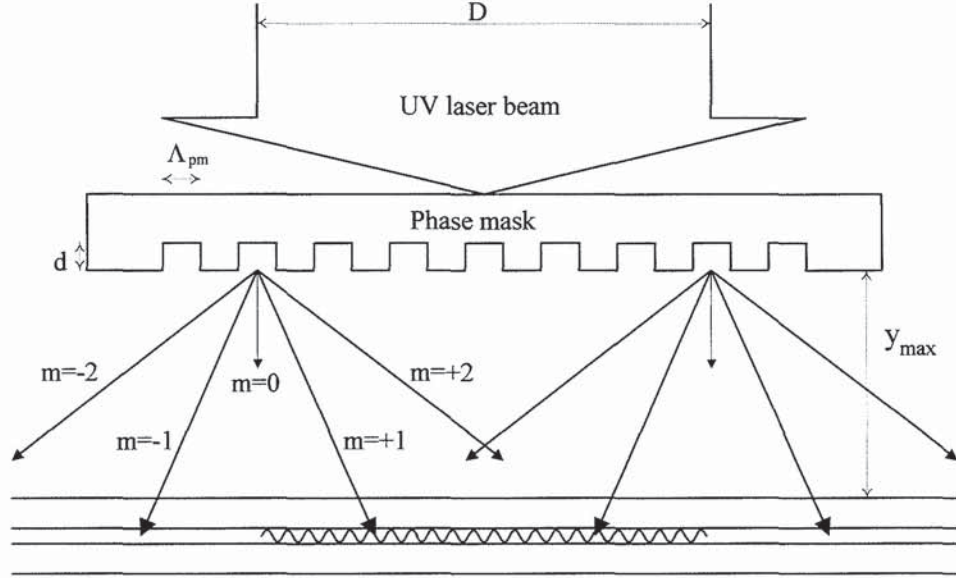


Figure 2-15: Schematic of phase mask diffractions.

The first order diffractions interfere with each other creating the near-field fringe pattern. Therefore for successful grating inscription the zero-order diffraction must be eliminated or reduced as much as possible to achieve the maximum fringe visibility and reduce the effect of three-beam interference. To achieve this minimisation, the etch depth of the surface relief grating of the phase mask is controlled to equal one half of the UV inscription wavelength, λ_{UV} , and is given by the equation [26]:

$$d = \frac{\lambda_{UV}}{2(n-1)}, \quad (2.36)$$

where n is the refractive index of the phase mask material. For absolute elimination of the zeroth-order, the phase modulation amplitude is exactly π resulting in totally destructive interference. Consequently, for maximum efficiency different phase masks are required for different laser sources.

When using a phase mask to inscribe FBGs, the period of the resulting fibre grating, Λ_g , is half that of the phase mask period, Λ_{pm} :

$$\Lambda_g = \frac{\Lambda_{pm}}{2}. \quad (2.37)$$

The angle subtended between the $\pm N^{\text{th}}$ orders of the mask is being given by:

$$\theta_N = \sin^{-1} \left(\frac{N\lambda_{UV}}{\Lambda_{pm}} \right). \quad (2.38)$$

Consequently, the maximum depth of the interference patterns behind the phase mask, y_{\max} , is dependant on the diameter on the inscription beam, D and the angle between the 1st orders, as given by the equation:

$$y_{\max} = \frac{D}{2 \tan \theta}. \quad (2.39)$$

Although phase masks are designed to minimise the zeroth-order, a component always remains. Consequently, the intensity pattern behind the phase mask is not just defined by the interference of the $\pm 1^{\text{st}}$ orders but also by the interaction of these beams with the zeroth-order. This three-beam interference results in more complex interference patterns, which affect the quality of the induced FBGs and is detailed in the following section.

Mathematical Description of Three-Beam Interference

This section considers the effect that the zeroth-order has on the interference pattern of the $\pm 1^{\text{st}}$ orders and how this affects FBG inscription; the higher order contributions have been ignored since these can be minimised by placing the fibre a sufficient distance from the mask.

Whilst the effect of the zeroth-order on the interference behind the phase mask has been analysed by Dyer *et al* [29], the mathematical description presented here follows that provided by Xiong *et al* [30]. Whilst this method does not provide detailed information on the amplitude and phase of the diffracted orders from the phase mask it does give the characteristics of the field distribution.

The phase change of the electric field behind the phase mask at a position (x, z) is provided by the expression:

$$\phi_N = x \sin(\theta_N) + z \cos(\theta_N), \quad (2.40)$$

where ϕ_N is defined by equation (2.38), the x axis is the length of the grating (i.e. parallel to the mask) and the z axis corresponds to the direction of the incident laser beam (i.e. normal to the phase mask). The resulting electric field distribution from the interfering N^{th} diffraction orders is given by:

$$E = \sum_{k=-N}^N C_k \exp[i2\pi\phi_k / \lambda_{UV}], \quad (2.41)$$

where C_k is the amplitude of the electric field of the k^{th} -order diffraction. The symmetrical diffraction situation $C_k = C_{-k}$ is only considered in this analysis and the zeroth-order amplitude is replaced with $2C_0$. The intensity distribution EE^* is then provided by:

$$I = 4 \left\{ \sum_{k=0}^N \left[C_k^2 \cos^2 \left(\frac{2\pi kx}{\Lambda_{pm}} \right) + \sum_{j \neq k} C_k C_j \cos \left(\frac{2\pi kx}{\Lambda_{pm}} \right) \cos \left(\frac{2\pi jx}{\Lambda_{pm}} \right) \right] \times \cos \left(\frac{2\pi z (\cos \theta_k - \cos \theta_j)}{\lambda_{UV}} \right) \right\}. \quad (2.42)$$

Finally, when just the interference between the $\pm 1^{\text{st}}$ orders and the zeroth-order are taken into consideration, the intensity distribution given by Xiong *et al* [30] is:

$$I_{o,\pm 1} = 4 \left[C_1^2 \cos^2 \left(\frac{2\pi x}{\Lambda_{pm}} \right) + C_0^2 + 2C_0 C_1 \cos \left(\frac{2\pi x}{\Lambda_{pm}} \right) \times \cos \left(\frac{2\pi z \left(1 - \sqrt{1 - (\lambda_{UV} / \Lambda_{pm})^2} \right)}{\lambda_{UV}} \right) \right] \quad (2.43)$$

The effect of the zeroth-order diffraction from the phase mask

When there is no power in the zeroth-order the intensity distribution arises solely from the first term in equation (2.43) and therefore is oscillatory in the x -direction with a spatial period of half the phase mask period and with no variation along the z axis.

The second term, C_0^2 , in equation (2.43) is a constant associated with the zeroth-order which reduces the contrast in the fringe pattern of the first term. The third term demonstrates that the interaction between the zeroth-order and the 1st order beams not only creates oscillation in the x axis but also in the z direction with a period, Λ_z , defined by:

$$\Lambda_z = \frac{\lambda_{UV}}{1 - \sqrt{1 - (\lambda_{UV} / \Lambda_{pm})^2}}. \quad (2.44)$$

Therefore, for an inscription wavelength of 325 nm and a phase mask period, $\Lambda_{pm} = 1.06085 \mu\text{m}$ the period of the oscillation in the z direction is $6.9 \mu\text{m}$.

In order to demonstrate the effect of the zeroth-order on the interference fringes of the grating, intensity distributions for different levels of the zeroth-order were calculated and are shown in Figure 2-16.

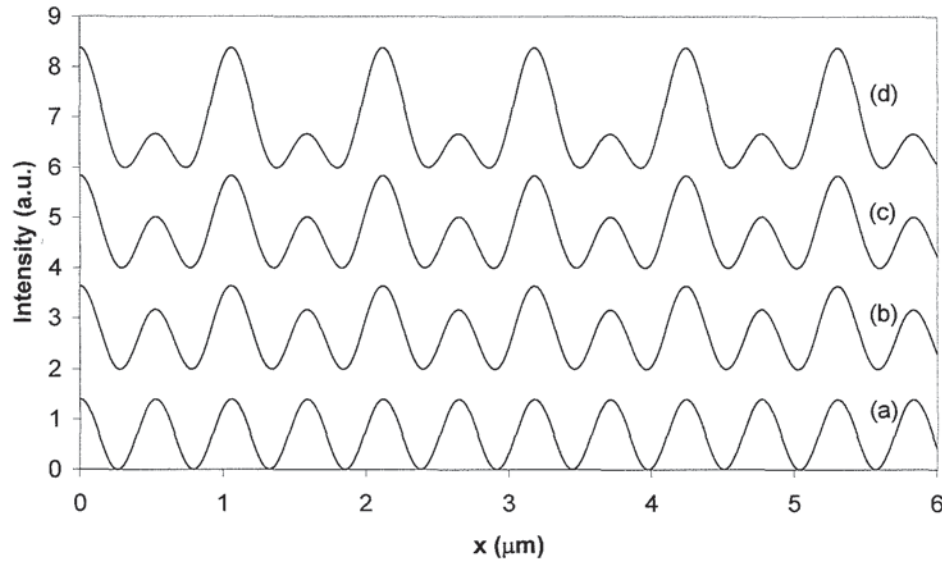


Figure 2-16: The intensity distribution along the x axis at $z = 0$ for different levels of zeroth-order: (a) = 0 %, (b) = 1 %, (c) = 3 % and (d) = 13 %.

The $\pm 1^{\text{st}}$ order contribution was taken as being $C_1^2 = 35$ %. Figure 2-16 shows that as the level of the zeroth-order increases, the resulting interference pattern changes. For large levels of zeroth-order (trace (d) in Figure 2-16), fringes with periodicities equal to the phase mask periodicity become dominant, whereas with no zeroth-order (trace (a) in Figure 2-16) a sinusoidal distribution is observed with the fringe spacing equal to half that of the phase mask.

Figure 2-17, shows the three-dimensional diffraction distribution behind the phase mask for the same zeroth-order contributions shown in Figure 2-16 and clearly shows the oscillation in the z axis which destroys the visibility of the fringes culminating in reduced grating quality.

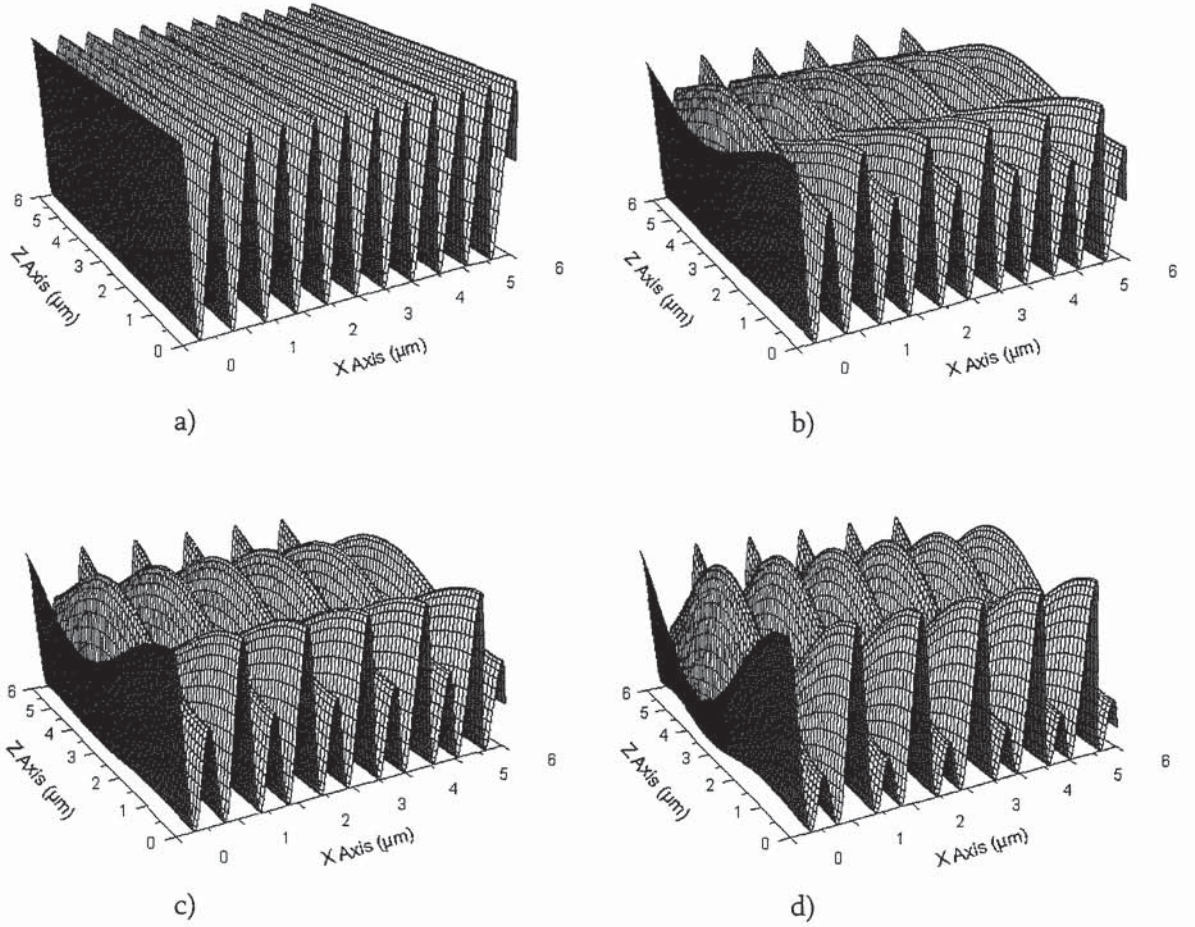


Figure 2-17: Three-dimensional intensity distribution of the three beam interference for different levels of zeroth-order: (a) = 0 %, (b) = 1 %, (c) = 3 % and (d) = 13 %.

Advantages and Disadvantages of the Phase Mask Technique

The huge advantage of the phase mask technique is the stability of the system compared to the interferometry-based techniques, due to the beam not being split until the exit face of the phase mask. The distance from the mask to the fibre is typically in the order of 100 μm reducing the effect of the environmental instabilities.

However, the main disadvantage of the phase mask technique is that the FBG is totally dependent on the period of the phase mask. Consequently, although the phase mask technique is capable of producing high quality gratings with repeatable results for mass production, the producible wavelengths are limited by the period of the expensive phase

mask. Although pre-straining the fibre and then inscribing an FBG can change the Bragg wavelength of the released fibre [31], typically by the order of a few nanometres for silica-based optical fibres, the amount of applied strain is restricted by elastic limit of the optical fibre's constituent materials. Therefore in order to fabricate a range of operational wavelengths several phase masks are required. Also, since the separation of the mask to fibre is small ($\sim 100 \mu\text{m}$) any residue remaining on the fibre once it has been stripped can be ablated by the laser on to the phase mask damaging the fragile pattern, rendering it useless.

2.5.1.4 Point-by-Point Inscription

This technique for FBG inscription utilises pulsed laser systems to individually inscribe each fringe of the grating one step at a time [32]. Initial reports used a KrF (krypton fluoride, $\lambda = 248 \text{ nm}$) excimer laser which was passed through a slit with a lens to image the slit onto the core of the optical fibre. A single pulse was used to create a change in the refractive index of the core at the irradiated point. The fibre was then translated by a distance, Λ , equal to the desired period of the grating and the procedure repeated. Recently, this has also been achieved using a femtosecond laser [33]. Since the point-by-point technique involves individual fringe inscription, no phase masks are required and the only restriction on the range of Bragg gratings that can be inscribed is the resolution of the translation stage which defines the period of the grating and the size of the focused inscription radiation.

2.5.2 Long Period Gratings Inscription Techniques

LPG fabrication can be achieved by either one of two ways [12]:

- 1) Permanent modification of the refractive index of the core
- 2) Temporary physical deformation of the fibre

2.5.2.1 Permanent Modification

Some of the permanent modification inscription techniques of LPGs are briefly described in this section with further details provided throughout the thesis in relevant sections.

Ultra Violet Radiation

As with FBGs, LPGs can also be fabricated by exposure to UV radiation. However, due to the significantly larger period of LPGs the inscription techniques are slightly different. Firstly, each fringe of the grating can be inscribed separately by a point-by-point inscription technique [34], which is an extremely flexible methodology, secondly amplitude masks can also be used [13].

Ion Implantation

Fujimaki *et al* [35] demonstrated that LPGs can be fabricated by periodically implanting helium ions into the core of an optical fibre to create the refractive index change. This was achieved by exposing SMF 28 to He^{2+} ions at room temperature and a pressure of $1.3 \times 10^{-4} \text{ N/m}^2$. The ions were accelerated towards the fibre through a metallic mask, constructed of nickel and cobalt, which had 29 periods with a pitch of $170 \mu\text{m}$ and a spacing of $60 \mu\text{m}$. The ions only had a penetration depth of $24 \mu\text{m}$ so in order to implant the ions in the core region, the optical fibre had to be etched away using hydrofluoric acid.

Femtosecond Lasers

Femtosecond lasers have been shown to be capable of inscribing LPGs into optical fibres. Kondo *et al* [36] first demonstrated that a femtosecond laser emitting at 800 nm , with a repetition rate of 200 kHz and pulse width of 120 fs could be used to inscribe LPGs in standard telecommunications optical fibre. Further work has since been conducted using femtosecond lasers with different emission wavelengths and improving the resulting strength of the attenuation bands [37-38].

Carbon Dioxide Lasers

Davis *et al* [39] were the first to demonstrate that carbon dioxide lasers which emit at 10.6 μm could also be used to inscribe long period gratings. Later these gratings were found to have high temperature stability [40].

Electrical Discharge

This inscription technique uses electrical discharge, typically from the electrodes of a fusion splicer, to periodically alter the refractive indices of the core and cladding materials [41-43]. This technique will be discussed in further detail in chapter 3.

2.5.2.2 Physical Deformation of the Fibre

Mechanical Bending

LPGs can be temporarily induced by a process called microbending. This technique involves applying pressure to a, typically metallic, corrugated block which is placed on top of an optical fibre. Periodic refractive index changes are created through localised induced stress in the fibre. Once the pressure is removed no grating is observed [44].

All of these inscription techniques show the diversity and flexibility of fabricating LPGs into optical fibres, the large periodicities of these gratings enabling relative ease of manufacture.

2.6 Summary

Phase matching between different modes in optical fibres has been discussed. The different mechanisms involved between fibre Bragg gratings and long period gratings are detailed. The sensing characteristics of both types of gratings have been demonstrated along with the different fabrication techniques associated with the different gratings.

3

Electric-Arc Long Period Gratings

This chapter details research on long period gratings fabricated in standard single mode silica-based optical fibres using the electric-arc technique. Firstly, the inscription mechanism of the electric-arc technique is compared to that of ultra-violet inscription. This is followed by a comparison of the growth characteristics of fabricated gratings using the two different techniques. The thermal annealing of the two different inscription techniques and the implication for long term stability and high temperature measurement is also discussed.

3.1 Introduction

The majority of grating inscription techniques rely on expensive and complex laser systems. The electric-arc technique however, provides a comparatively low cost and easily implemented process. The technique is limited to long period grating (LPG) inscription due to the size of the electrical discharge but does have the additional advantage of providing different annealing properties when compared to standard ultra-violet (UV) inscribed gratings. One major topic of interest, in the field of photonics, is Photonic Crystal Fibre (PCF). The majority of these fibres have pure silica cores and so are not inherently photosensitive. This is increasing the interest in the electric-arc technique for LPG inscription since it does not require the fibre to be photosensitive. Before inscription

attempts could be conducted in PCF, a full understanding of the electric-arc technique in standard fibres had to be attained and is the focus of this chapter.

3.2 Inscription Mechanism of the Electric-Arc Technique

Several investigations into the inscription mechanism of the electric-arc technique in standard telecommunication fibres have been conducted. Rego *et al* [42] proposed three potential mechanisms:

- 1) Fibre diameter perturbation
- 2) Dopant diffusion
- 3) Glass property change by the fast local heating-cooling process

They concluded that fibre perturbation and dopant diffusion were minor contributions to the refractive index changes with the majority of the cladding mode coupling occurring through localised changes of the glass properties. Rego *et al* [42] proposed these changes to be due to the fast heating and cooling of the fibre, resulting from the electrical discharge, which changes the fictive temperature of the glass. This results in a change of the glass density, viscosity, refractive index and Rayleigh scattering of the exposed sections of fibre.

Recently, Rego *et al* [45] have estimated the peak temperature reached by the fibre during the process to be 1400 ± 50 °C which is above the glass transition temperature of silica; 1127 °C [46]. They achieved this thermal estimation by exposing a section of optical fibre to an electric-arc discharge for 1 second. The low intensity radiation emitted by the fibre during the exposure was guided through the same fibre towards a Cronin spectrometer. At the spectrometer the radiation is separated by a holographic grating and then directed towards an array of detectors. Each wavelength range is allocated simultaneously to a particular detector. Consequently, there is no wavelength sweep, as provided by an optical spectrum analyser, ensuring detection occurs at the same time for all wavelengths. This

data was then fitted to the blackbody expression to achieve an estimation of the temperature. Further information can be found in reference [45].

Malki *et al* [47] in 2003 used Raman and luminescence spectroscopy to investigate the mechanisms involved with this technique. Comparing the Raman spectrum of an unexposed and a periodically exposed fibre showed a significant decrease in the Raman intensity of the exposed sample over the Raman shift range of 200-700 cm^{-1} . A decrease in this spectral range has been shown to correspond to an increase in density or in fictive temperature of the exposed regions. However, measurements showed the fictive temperature to remain unchanged. The spectral luminescence measurements showed a large increase in red luminescence intensity which can be due to specific structural changes in the glass. They consequently concluded, that the mechanism is mainly caused by a local rearrangement of the fibre structure (densification).

3.3 Ultra-Violet Photosensitivity in Silica-Based Optical Fibres

Although several mechanisms for the photosensitivity of silica-based optical fibres have been proposed, the current consensus is that it is initiated through the formation of colour centres [48] that give way to densification of the UV exposed glass [3, 49-50].

There are several absorption bands associated with germanium doped silica optical fibres, principally located at 180, 213, 240, 281, 325 and 517 nm [51-52]. The bands at 213 nm (5.8 eV) and 281 nm (4.4 eV) have been assigned to Ge(2) and Ge(1) centres, respectively [52]; see Figure 3-1 for schematic representations of the two centres.

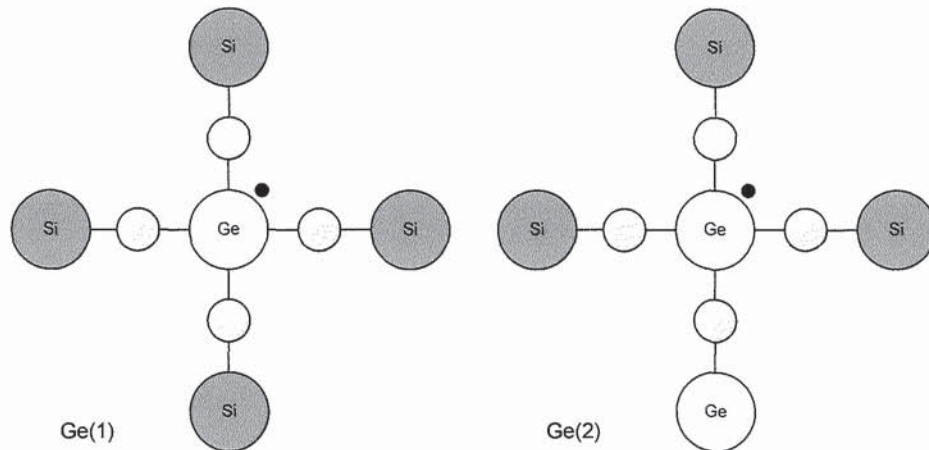


Figure 3-1: Ge(1) and Ge(2) electron trap centres associated with absorption bands at 281 nm and 213 nm respectively. Light grey circles represent oxygen atoms, black circles unpaired electrons.

The absorption band located at 517 nm has been assigned to an oxygen hole centre by Friebele *et al* [52]. The predominant effect in germanium-doped silica is however associated with the band at 240 nm. This strong band at 240 nm and the weak band at 325 nm have been assigned to the 'wrong bond' defect [52-53]. These defects occur during fibre manufacture when the GeO_2 molecules dissociate to the GeO molecule since it has higher stability at these elevated temperatures. Consequently, when incorporated in the glass structure, oxygen vacancy Ge-Si or Ge-Ge 'wrong bonds' are formed. The centres are known as germanium oxygen-deficient centres (GODC). Upon exposure to 240 nm or 325 nm radiation this bond breaks and an electron is released in to the glass matrix.

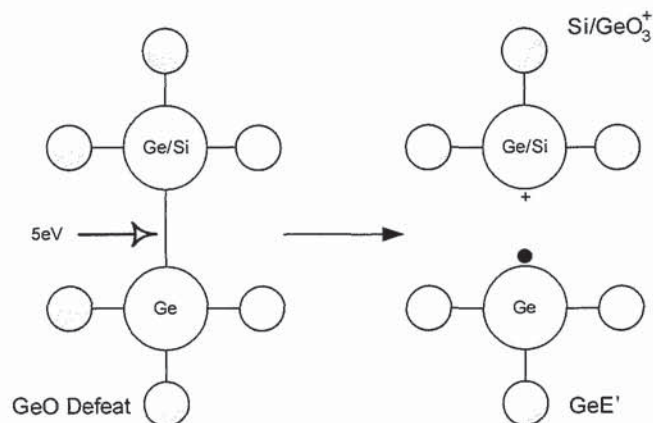


Figure 3-2: GeO defect (wrong bond) absorbs a photon and creates a GeE' defect which contains an extra electron (black circle) which is free to move in the glass matrix until it is trapped by the original GeE' centre or another defect site. Grey circles represent oxygen atoms.

The UV light excites the carriers into the conduction band, from where they fall into traps and remain; the 240 nm band is attributed to singlet-to-singlet transition (S_0 to S_1) and the 325 nm band to the partially forbidden singlet-to-triplet transition (S_0 to T_1). The weakly allowed S_0 to T_1 transition, which involves a change in spin state, is a slow transition compared to the S_0 to S_1 where no change in spin state occurs. Consequently, grating formation takes longer with 325 nm radiation than with 240 nm.

This ‘colour-centre model’ results in the photoinduced refractive index changes through the Kramers-Kronig relationship [48, 54]:

$$\Delta n_{eff}(\lambda) = \frac{1}{2\pi^2} P \int_0^\infty \frac{\Delta \alpha_{eff}(\lambda')}{1 - (\lambda/\lambda')^2} d\lambda', \quad (3.1)$$

where P is the principle part of the integral, λ is the wavelength, λ' the wavelength at which the refractive index is calculated and $\Delta \alpha_{eff}(\lambda)$ is the effective change in the absorption coefficient of the defect given by:

$$\Delta \alpha_{eff}(\lambda) = \left(\frac{1}{L} \right) \int_0^L \Delta \alpha(\lambda, z) dz, \quad (3.2)$$

where L is the thickness of the sample.

3.3.1 Hydrogen Loading

The photosensitivity of germanium doped optical fibres can be enhanced by hydrogen loading which diffuses molecular hydrogen into the fibre core through the cladding [55-56]. The concentration and rate at which the molecules diffuse into the core is dependant on the pressure and temperature of the gas. The saturated hydrogen concentration, κ_{sat} , is given by [57]:

$$\kappa_{sat} = 3.3481 p \exp\left(\frac{8.67 kJ/mol}{RT}\right), \quad (3.3)$$

where p is the pressure (atmospheres), T is the temperature (Kelvin) and R is the gas constant which for hydrogen is 8.311 J/[K-mol] . Consequently, the hydrogen saturation level increases with increasing pressure but decreases with increasing temperature. The diffusion coefficient of hydrogen, D , is given by [57]:

$$D = 2.83 \times 10^{-4} p \exp\left(\frac{-40.19 \text{ kJ/mol}}{RT}\right), \quad (3.4)$$

and so increasing the pressure and temperature increases the diffusion rate. Therefore at higher temperatures the saturation level is reached faster but the ultimate concentration is lower than if left at the same pressure at a lower temperature.

The hydrogen in the core of the fibre reacts with Ge-SiO₂, upon UV exposure, to form GeH therefore creating more GeE' centres. As well as the refractive index increases associated with GeE' centres, GeH changes the band structure in the UV region further increasing the refractive index change according to the Kramers-Kronig relationship (3.1). The hydrogen molecules also disassociate forming Si-OH and Ge-OH bonds which also enhance the resulting refractive index change [26].

3.4 Inscription Set Up of Electric-Arc Long Period Gratings

The inscription set up used to inscribe LPGs using the electric-arc technique is shown in Figure 3-3.

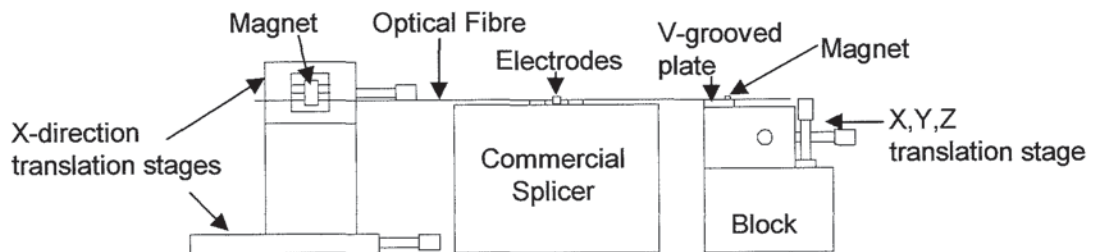


Figure 3-3: Schematic of the electric-arc inscription set up.

The electrical discharge was provided by a commercial splicer (Fitel S175 v2000) which had an electrode separation of $\sim 1 \text{ mm}$. A stripped section of optical fibre was positioned

between the electrodes of the splicer with one end of the fibre clamped onto a x-direction translation stage using a strong magnet and the other end of the fibre mounted on a v-groove attached to a x,y,z translation stage. The fibre was held on to the v-grooved plate by a small weak magnet, which ensured the fibre remained located in the v-groove but could still slide through the groove. The same negligible tension was applied to the fibre each time by moving the x,y,z translation stage away from the splicer, by altering the micrometer screw, until the fibre slid in the v-groove. The x,y,z translation stage also enabled the position of the fibre to be altered relative to the electrodes ensuring that the fibre was completely perpendicular to the electrical discharge and parallel to the optical table ensuring a uniform distribution of the discharge over the fibre. After each discharge, the x-direction translation stage was displaced by a distance corresponding to the desired period of the LPG.

3.5 Fabricated LPGs in SMF using the Electric-Arc Technique

Several different periods of LPGs were fabricated validating the operation of the inscription technique. Using the commercially defined electric-arc power of 87 (arbitrary units) and arc duration of 750 ms, periods of 400 μm , 500 μm , 600 μm and 800 μm were successfully fabricated in the single mode fibre; see Figure 3-4.

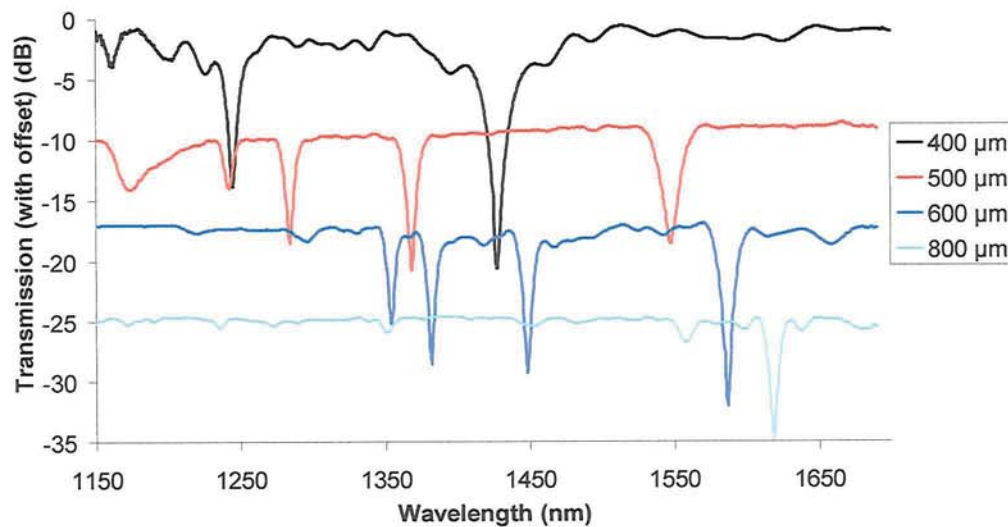


Figure 3-4: Various periods of LPG fabricated in single mode fibre.

The LPGs were fabricated in 10-15 minutes each, including set up time. Provided the same technique was used each time to put the tension on the fibre, gratings made on the same day with the same period were repeatable to an attenuation band location of less than 0.5 nm. However, this technique is susceptible to degradation of the electrodes, which affects the reproducibility of the attenuation band location.

Periods equal to and less than 350 μm were not successfully fabricated using this technique. Kato *et al* [58] have investigated the optimum splice conditions for single mode fibres. They demonstrated that as the electrode separation increases the dimensions of the electric discharge also increases; see Figure 3-5.

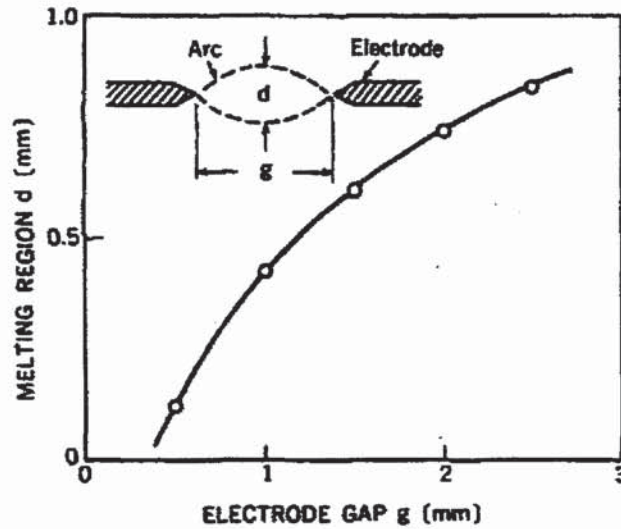


Figure 3-5: Relationship between the melting region of a silica fibre and the electrode gap [58].

Since the electrode separation of the electrodes in the Fitel splicer used in the fabrication of the LPGs shown in Figure 3-4 had a separation of ~ 1 mm the affected area of the fibre was approximately 400 μm . When this is coupled with the shape of the electric discharge being Gaussian, periods less than 400 μm will not have significant fringe contrast in the refractive index fringes for coupling to occur.

The growth of the attenuation bands of an LPG with increasing numbers of grating planes is shown in Figure 3-6.

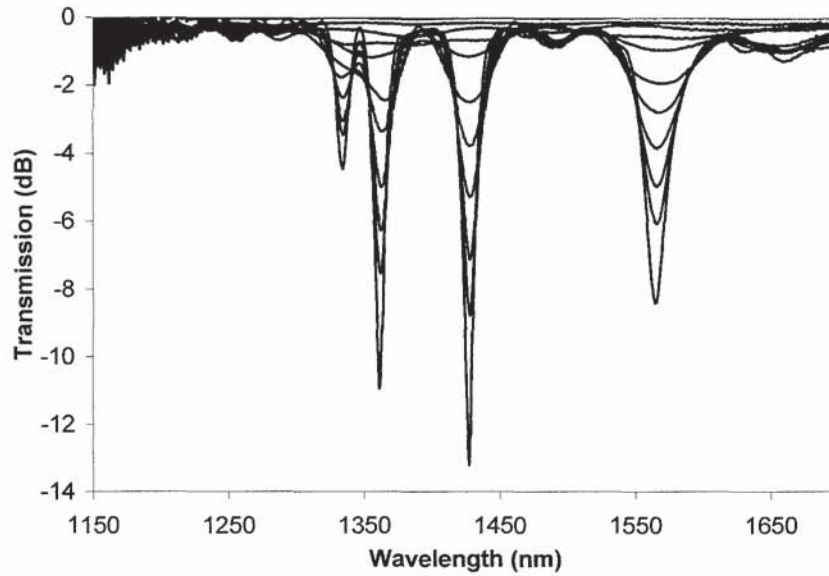


Figure 3-6: Formation of the attenuation bands of an electric-arc induced LPG with a period of 600 μm . Each trace taken after the fabrication of 5 grating planes.

During and after fabrication of the LPG, no shift in the spectral location of the attenuation bands was observed. This is significantly different to UV inscribed LPGs which experience spectral shifts in the location of the attenuation bands. This shift is associated with the out diffusion of hydrogen from the fibre which changes the effective refractive indices of the core and cladding. Jang *et al* [59] and Fujita *et al* [60] have studied the effect that the diffusing hydrogen molecules have on the phase matching condition of LPGs. A typical trajectory of the attenuation bands during the diffusion is shown in Figure 3-7.

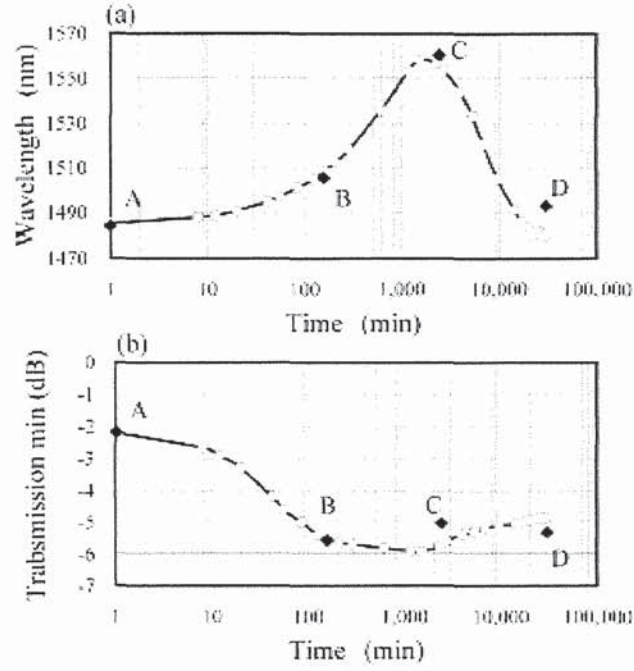


Figure 3-7: Wavelength (upper) and Transmission (lower) of an LPG attenuation band against time at room temperature [60].

During hydrogen loading of the optical fibre, equal quantities of hydrogen are diffused into the core and cladding material, upon saturation, raising the overall refractive index of the fibre but retaining the same refractive index profile. Exposure to UV radiation increases the refractive index of the core causing the attenuation bands to shift to longer wavelengths (Points A to B) according to the phase matching condition:

$$\lambda_{res} = (n_{co}^{eff} - n_{cl,m}^{eff})\Lambda, \quad (3.5)$$

The rate of change of the core refractive index slows as the concentration of hydrogen in the core is reduced by the photoinscription mechanism. When no hydrogen remains in the core a state called quenching is reached (Point B). At this point the hydrogen still present in the cladding of the fibre migrates into the core raising the refractive index of the core back to the level before quenching took place (Points B to C). Once the core has been refilled with hydrogen, (Point C) the hydrogen molecules in the core and cladding start to diffuse out of the fibre until the fibre is free from hydrogen molecules (Points C to D). The time shown for all the hydrogen to diffuse out of the fibre at room temperature is 9 weeks. Annealing the fibre in an oven at 80 °C reduces this time to 2-3 days according to

equation (3.4). Only once annealing has taken place can the final location of the attenuation bands be accurately known.

For UV inscribed LPGs the resulting spectral location of the attenuation bands depends not only on the grating period but also on the coupling strength or the amplitude of the index modulation. This is because the increment of the average core refractive index by the UV radiation induces a change in the beat length of the two coupled modes. As demonstrated by Figure 3-6, the resonance wavelength of the electric-arc induced gratings is independent of the coupling strength and so is only defined by the period of the grating. Consequently, the grating parameters such as the central wavelength, bandwidth, transmission strength and the filter profile can be easily controlled. An explanation for this different behaviour is provided by Nam *et al* [61]. The resonance wavelength phase matching equation can be expressed as [61]:

$$\lambda_{res} = \left[n_{co}^{eff}(\lambda_{res}) - (n_{cl,m}^{eff}(\lambda_{res})) + \overline{\partial n(z)} (\partial n_{co}^{eff} - \partial n_{vj}^{eff}) \right] \Lambda. \quad (3.6)$$

where $\overline{\partial n(z)}$ is the induced refractive index change. The relative effective index perturbation between the core and cladding modes, $\partial n_{co}^{eff} - \partial n_{vj}^{eff}$, differs depending on the inscription technique of the LPG. In UV inscribed LPGs the induced refractive index change is primarily in the core of the optical fibre making $\partial n_{co}^{eff} \gg \partial n_{vj}^{eff}$. The electric-arc inscription technique on the other hand modifies the core and cladding materials by approximately the same amount resulting in $\partial n_{co}^{eff} \approx \partial n_{vj}^{eff}$. Since both materials are being affected by the same amount, the ratio of the core to cladding effective indices remains the same resulting in no spectral shift of the attenuation bands during fabrication.

3.6 Thermal Annealing

A continued area of study is the reliability of fibre gratings over time [62]. UV inscribed fibre gratings experience temperature and time dependant annealing (photobleaching) which reduces the strength of the grating until erasure occurs. Erdogan *et al* [63]

demonstrated that the decay was due to the electrons, which were trapped in the GeE' centres, receiving enough energy to escape back into the conduction band; the energy typically provided by heat. The trapped electrons distribute themselves with a Gaussian function across the energy range; see Figure 3-8.

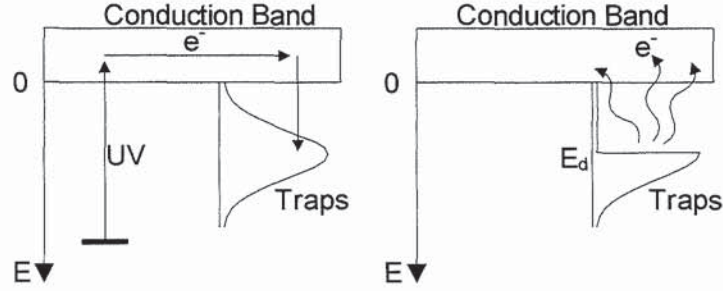


Figure 3-8: Electrons excited by UV irradiation and trapped by a GeE' trap (left). Thermal depopulation of the traps (right).

The position of the electrons is referenced to a demarcation energy, E_d , which depends on time and temperature by the equation:

$$E_d = k_B T \ln(vt), \quad (3.7)$$

where k_B is the Boltzmann constant and v is acquired from experimental data. If the energy state of the electrons $E < E_d$, thermal equilibrium between the conduction band and the electrons is reached and the electrons are able to escape the trap at any time returning to the conduction band; see right hand side of Figure 3-8. Electrons with higher energy states than the demarcation energy are too deep to be thermally excited and so remain in the trap until acquiring sufficient energy to leave. This process is described as the power law of fibre Bragg grating decay and the normalised refractive index change of Ge doped silica fibres is given by [63]:

$$\eta = \frac{1}{1 + \exp\left[\frac{(E_d - \Delta E)}{k_B T_0}\right]}, \quad (3.8)$$

where T_0 is an experimentally determined temperature related constant measured in Kelvin. However, fibre gratings inscribed in hydrogenated fibre do not follow the power

law. This is thought to be due to the trapped electrons having a wider energy distribution which allows more states to be close to the conduction band, with these electrons requiring less energy to escape the trap. This leads to a more rapid decay in hydrogenated fibres. Baker *et al* [64] demonstrated that for hydrogenated fibres a 'log time' model best describes the behaviour observed in these fibres.

$$\begin{aligned} \eta &= 1 - K \log\left(\frac{t}{\tau}\right), & \text{for } t > \tau \\ \eta &= 1 & \text{for } t \leq \tau \end{aligned} \quad (3.9)$$

where K is a constant, τ is temperature dependant and t is time. Values for K and τ are found by fitting curves to experimentally obtained data of the annealing.

Although less research has been conducted on the thermal annealing of LPGs fabricated using the electric-arc technique, some studies have been conducted by Rego *et al* [42] and Allsop *et al* [65]. Electric-arc gratings are fabricated primarily by the structural rearrangement of the glass at high temperature. Consequently, annealing is not observed until high temperatures are reached where structural rearrangement can once again prevail. Two distinct temperature regions have been observed. Up to about 800 °C linear shifts in resonance wavelength occur, whereas increasing the temperature further to ~1200 °C demonstrates a nonlinear dependence on temperature. The nonlinear section initiates at the strain point in the fibre where structural rearrangement can occur. This point is defined by the viscosity of the fibre [66] and so depends on the glass composition of the fibre. Consequently, different fibres have different strain points. Investigations by Rego *et al* [42] demonstrated that for standard optical fibres, no hysteresis occurred in the spectral location of the LPGs at 500 °C, after they have been previously heated to 600 °C for 13 hours, 700 °C for 1 hour and 800 °C for 10 minutes. However, when the gratings were heated to 800 °C for 15 minutes or to 700 °C for 75 minutes the whole spectrum shifted to lower wavelengths by typically 3.5 nm; the magnitude of the shift depended on the

particular cladding mode investigated. They also discovered that at 1190 °C it took an hour to almost fully erase a grating in standard fibre.

Work done in collaboration with Dr. T. Allsop from Aston University's Photonic Research Group has verified the findings by Rego *et al* [42]. A UV and electric-arc inscribed LPG with periods of 350 μm and 400 μm , respectively, were placed into an oven and the temperature cycled between room temperature and increasing temperature settings in the range 100-850 °C. The same cladding mode attenuation band in both gratings was investigated for its susceptibility to thermal affects. The resulting effect on the central wavelength of the attenuation band can be seen in Figure 3-9.

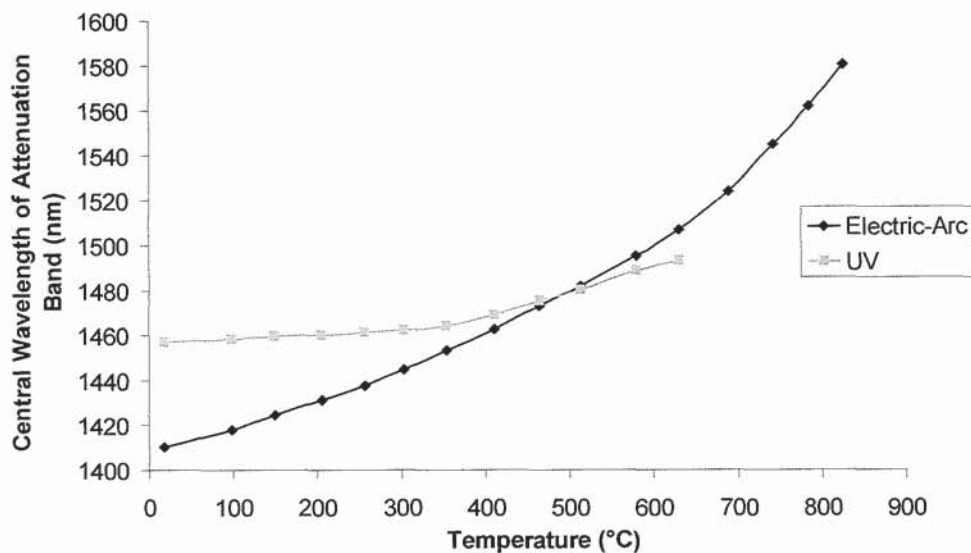


Figure 3-9: Response of Electric-Arc and UV inscribed LPGs to temperature.

The strength of the UV LPG had significantly decayed with temperatures over 650 °C with the result that measurements could not be taken on the performance of the grating for these temperatures.

The hysteresis of the spectral location at room temperature following each temperature setting is shown in Figure 3-10.

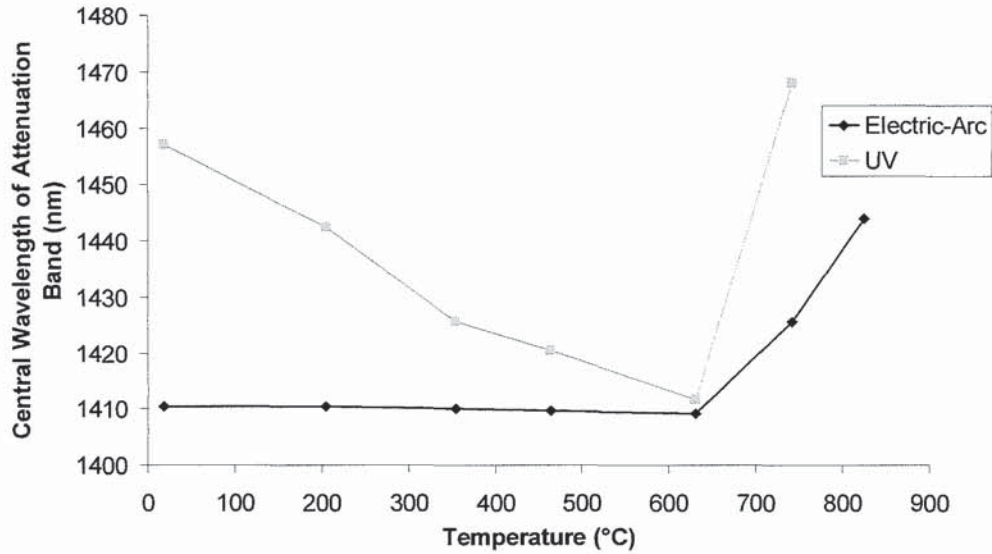


Figure 3-10: The shift in room temperature spectral location of the grating after each consecutive heating step. The x-axis depicts the temperature the grating was heated to before returning to room temperature.

Figures 3-9 and 3-10 demonstrate that the thermal annealing occurs in the UV LPG at a significantly lower temperature than for the electric-arc LPG where it occurs at around 500-600 °C. Figure 3-10 demonstrates that up to 600 °C both LPGs experience blue wavelength shifts with the electric-arc LPG having a coefficient of $-2 \text{ pm}/^\circ\text{C}$ and the UV LPG having a coefficient of $-76 \text{ pm}/^\circ\text{C}$. After 600 °C both LPGs experienced red wavelength shifts; $+500 \text{ pm}/^\circ\text{C}$ for the UV inscribed LPG and $+180 \text{ pm}/^\circ\text{C}$ for the electric-arc inscribed LPG. The significant blue shift observed by the UV LPG is attributed to the photobleaching described earlier. The escape of the electrons from the traps reduces the effective refractive index of the core affecting the phase matching condition. The red wavelength shift observed in both gratings is related to the rearrangement of the glass structure described earlier.

3.7 Summary

The inscription mechanism outlined in section 3.2 for electric-arc induced LPGs is unreliable on the optical fibre being inherently photosensitive or hydrogen loaded to increase the photosensitivity. This results in the ability to inscribe gratings in fibres such as silica core fibres. These fibres are of significant importance for implementation in areas that

could be exposed to nuclear radiation. Gratings in hydrogen loaded germano-silica fibres can experienced a wavelength shift of several tens of picometers when exposed to a Megagray (MGy) dose of radiation [67]. Ionizing radiation also significantly increases the transmission loss of these fibres compared with fibres with pure silica cores. Rego *et al* [68] have shown LPGs fabricated in silica core optical fibres using the electric-arc technique to be almost unaffected by doses of radiation in excess of 0.5 MGy without the temperature and strain sensing characteristics of the grating being unaffected.

The electric-arc technique is a significantly cheaper fabrication method since it eliminates the need for expensive laser systems and pre-hydrogenation of the optical fibre. When this is coupled with enhanced thermal stability of the resulting gratings and the ease of manufacture, it is clearly an advantageous technique and worth using on, not only standard geometry fibres but specialised optical fibres such as photonic crystal fibre.

4

Long Period Gratings in Photonic Crystal Fibre

Contained within this chapter is a brief introduction to Photonic Crystal Fibres followed by a description of long period gratings inscribed into two different varieties using the electric-arc technique. Initial modelling results of the gratings are described followed by the experimental spectral sensitivity to external measurands of the fabricated long period gratings.

4.1 Introduction

One of the major drawbacks against industrial implementation of long period gratings in sensing systems is the device's cross-sensitivity to a multitude of different measurands. The cross sensitivity makes it difficult to distinguish wavelength shifts produced due to the desired measurand from those produced by other external variables. This culminates in the need to deploy discriminatory schemes to separate the effects, which further increases the cost and complexity of the system. Such schemes may, for example, involve interrogating either, an LPG using the reflection of two fibre Bragg gratings (FBGs) [69] or the first and second order diffraction attenuation bands associated with a particular LPG cladding mode [70], or two different cladding modes of an LPG [71]. However, the spectral sensitivity of long period gratings depends on the material and waveguide dispersion [13] and consequently gratings inscribed into some optical fibres have been shown to have reduced sensitivity to some measurands whilst maintaining good

sensitivity to others. For example, long period gratings inscribed into multi-clad optical fibres such as progressive three layered (PTL), air-clad and depressed-cladding fibre [72-74] have been shown to possess reduced sensitivity to external refractive index changes. Elimination of strain sensitivity has been achieved by inscribing gratings into fibre whose waveguide and material dispersion are equal in magnitude but opposite in sign [75]. Since the sensing characteristics depend on the dispersion properties of the optical fibre it should be possible to design a fibre to have optimum sensitivity to desired measurand(s) whilst minimising, or removing completely, undesirable cross-sensitivities.

Photonic Crystal Fibre (PCF) has good potential for such optimisation due to its dispersion properties being strongly dependent on the air-hole geometry [76]. The flexibility of this fibre's drawing technique [77] enables a wide variety of geometries to be produced which potentially have dramatically differing sensing characteristics. Consequently, the fabrication of long period gratings in PCF and their resulting sensing characteristics are the focus of this chapter.

4.2 Background to PCF

Photonic Crystal Fibres (PCF) were first introduced in 1996 by Knight *et al* [77]. They differ from standard telecommunications fibre by consisting of a periodic series of holes which run through the structure of an otherwise homogeneous fibre; see Figure 4-1.

4.2.1 Different Classes of Photonic Crystal Fibres

There are currently, two classifications of PCF defined by the different light guiding mechanisms of the fibres:

1. High Index Guiding (shown in Figure 4-1)
2. Low Index Guiding (Photonic Band Gap optical fibre,)

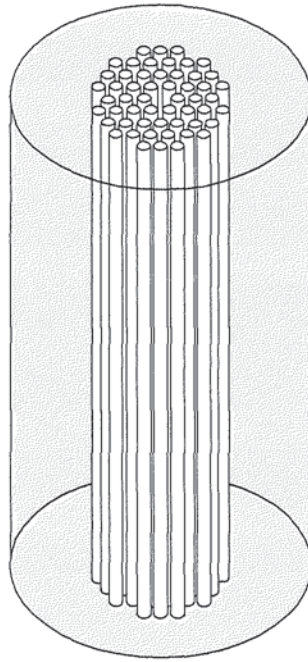


Figure 4-1: Schematic of a microstructured optical fibre.

4.2.1.1 High Index Guiding Photonic Crystal Fibre

These fibres guide light in a solid core region by a very similar mechanism to standard fibre; Modified Total Internal Reflection (M-TIR). The microstructured region of fibre creates an effective cladding with a refractive index less than that of the core enabling the condition for total internal reflection to occur. Whilst this is analogous to standard fibre geometries, the microstructured cladding exhibits completely different wavelength dependence. As a result, microstructured optical fibres can be designed to have a completely different set of novel advantageous properties such as endlessly single mode operation, extreme nonlinearity and anomalous dispersion in visible wavelengths [78].

4.2.1.2 Low Index Guiding Photonic Crystal Fibre

These fibres have a defect in the photonic band gap structure (analogous to the effect in electronics), typically an extra hole, at the centre of the fibre where the light can propagate. These fibres consequently have narrow transmission bandwidths that can propagate in this region, the wavelength of which depends on the photonic band-gap structure; an operating wavelength of 1550 nm only has a bandwidth of around 200 nm. The hollow core of these fibres provides several advantages like high power delivery

without damaging the fibre and potential as gas sensors. Interestingly, these fibres have been shown to be extremely insensitive to bending and have extreme dispersion properties with values of thousands of ps/nm/km obtainable [78].

4.2.2 Fabrication of Photonic Crystal Fibres

Fabrication of PCF is similar to step index geometry fibres with a preform being placed into a high temperature oven and drawn down. However, the preform consists of silica tubes and rods stacked together to form the desired crystal structure [77]. This process offers extreme flexibility of fibre design since replacing a tube for a rod changes the fibre's hole geometry dramatically affecting the resulting fibre properties.

4.2.3 Properties of Photonic Crystal Fibres

This section describes some of the different properties PCFs have in comparison to conventional optical fibre geometries.

4.2.3.1 Endlessly Single Mode Operation

One of the most important properties of PCF is its ability to be designed to achieve endlessly single mode operation, i.e. single mode operation is achieved regardless of the transmitted wavelength. This is clearly an important advantage over standard fibre which becomes multimode below a certain cut off wavelength, λ_c , defined by equation (2.1) and the V-parameter ≤ 2.405 .

In 1996, J.C. Knight *et al* [77] confirmed the unusual endlessly single mode (ESM) operation of certain PCFs by examining the near-field patterns emanating from the fibres. It was found that at shorter wavelengths the light becomes more confined to the silica core region. Since there is less light intensity distributed in the holey region of the fibre, the effective refractive index of the cladding increases becoming close to that of pure silica. This dispersion counteracts the dependence of the V-parameter on the wavelength, extending the single mode range to at least 400-1700 nm.

Knight *et al* defined the V-parameter for photonic crystal fibre as being [76]:

$$V_{eff} = k\Lambda F^{\frac{1}{2}}(n_{co}^2 - n_a^2)^{\frac{1}{2}}, \quad (4.1)$$

where n_a is the refractive index of the material in the holes (usually air=1), n_{co} the refractive index of the core material (usually undoped silica), k is the wave vector which equals $2\pi/\lambda$, Λ the hole separation (centre-to-centre spacing, see Figure 4-2) and F is the air filling fraction given by d/Λ , where d is the diameter of the holes; see Figure 4-2.

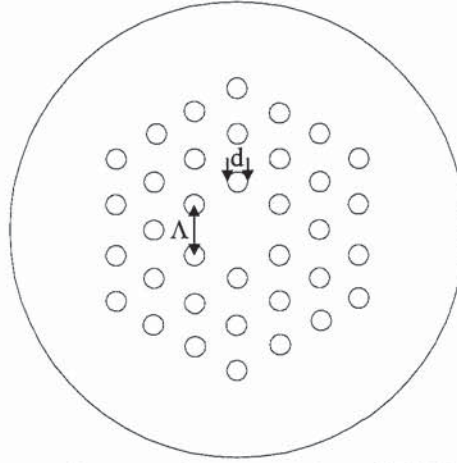


Figure 4-2: Typical cross section of ESM PCF.

Curves of V_{eff} against Λ/λ for a fibre with a core refractive index of 1.45 and a hole refractive index of 1, for fibres with differing filling factors, d/Λ , are shown in Figure 4-3.

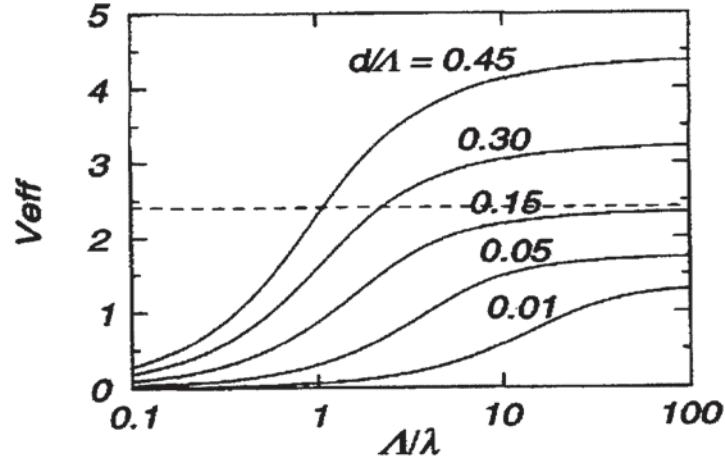


Figure 4-3: Variation of V_{eff} against Λ/λ for various relative hole diameters d/Λ . Dashed line marks the standard fibre single mode step index cutoff V value, $V_{eff} = 2.405$ [76].

Figure 4-3 shows that fibres with relative hole diameters ≤ 0.15 were all below the standard optical fibre single mode cutoff V-parameter of 2.405. Single mode operation in PCF is not defined by this particular parameter but has been experimentally approximated to 2.5 [79]. Consequently, designing a fibre to always have a V_{eff} value of less than 2.5 across the desired wavelength range ensures endlessly single mode operation.

4.2.3.2 Dispersion Effects

Dispersion effects within fibres are extremely important for telecommunication applications as well as for sensing systems containing long period gratings. Figure 4-4 shows the dispersion for 5 different geometries of PCF. For small air fill fractions, the material dispersion is the dominant contribution. Its value is very close to that of pure silica since the light hardly penetrates into the holes. This results in the overall dispersion being very similar to that of standard fibre with a zero dispersion point at around 1300 nm; see $d/\Lambda = 0.10$. As the hole size is increased, the waveguide dispersion becomes increasingly dominant reducing the dispersion; see $d/\Lambda = 0.40$ and 0.50 .

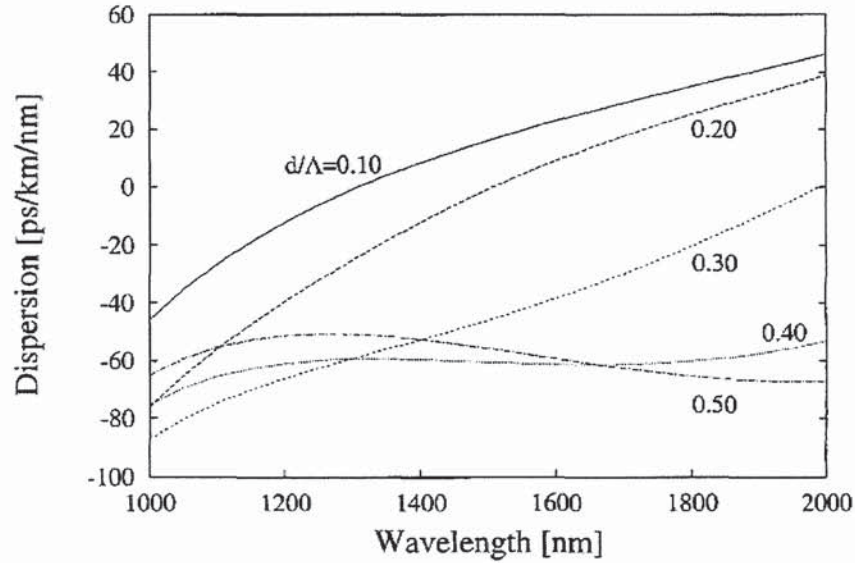


Figure 4-4: Dispersion as a function of wavelength for PCFs with a hole separation of $2.3 \mu\text{m}$ and varying hole diameters [78].

This evidence demonstrates that PCFs with different air-hole geometries have different dispersion properties.

4.3 Grating Fabrication Techniques in Photonic Crystal Fibre

The first reported fabrication of both fibre Bragg gratings (FBG) and long period gratings (LPG) in PCF was by Eggleton *et al* [80]. The fibre used in their investigations had a hexagonal crystal lattice with hole diameters of $2 \mu\text{m}$ and a spacing of $\sim 10 \mu\text{m}$. The core region was $\sim 2 \mu\text{m}$ in diameter and germanium doped, resulting in a photosensitive fibre. Therefore inscription attempts were conducted with an excimer-pumped frequency-doubled dye laser ($\lambda = 242 \text{ nm}$) with a fluence of 240 mJ/cm^2 and the fibre was deuterium loaded to increase the photosensitivity. Successful FBG inscription was achieved using the standard phase mask technique. Following this work, an LPG with a period of $155 \mu\text{m}$ was fabricated with a resulting resonance at $\sim 1600 \text{ nm}$.

The majority of PCFs, however, do not have a doped core region since the holes provide the effective cladding. Fabrication of long period gratings in non-photosensitive PCF has been achieved by a number of different techniques: periodically collapsing the holes by

heat treatment with a carbon dioxide (CO₂) laser [39], by using an electric-arc to modify the fibre structure [81] and by microbending [82].

These techniques remove the need for pre-hydrogenation of the fibre and consequent post-thermal annealing to stabilise the gratings. CO₂ laser fabrication systems are, however, more expensive than the electric-arc and microbending techniques. For commercial applications the cost is of importance as well as having a permanent change in the fibre. Therefore, the electric-arc technique was investigated for its stability for long period inscription in PCF.

4.4 Investigated Photonic Crystal Fibres

Two different geometries of PCF were investigated for their potential as sensing devices: a large mode area (LMA) fibre and an endlessly single mode (ESM) fibre, both supplied by Crystal Fiber A/S [83].

The first fibre investigated was the Large-Mode Area (LMA) PCF (Crystal Fiber, LMA 10). This fibre was designed to be endlessly single mode with a large effective mode field area of approximately 40 μm^2 . It had an outside diameter of 125 μm and a core diameter of 11 μm , which was surrounded by 89 air holes with a separation distance of 7.1 μm ; see Figure 4-5. Using the microscope image, the hole radii were measured to be $2.0 \pm 0.2 \mu\text{m}$. The symmetry of the photonic crystal was disrupted by a hole missing in the outer ring and two holes of radii 4.3 μm and 0.9 μm . Consultation with Crystal Fibre, revealed the asymmetric crystal to be due to errors in the fabrication process which has since been improved.

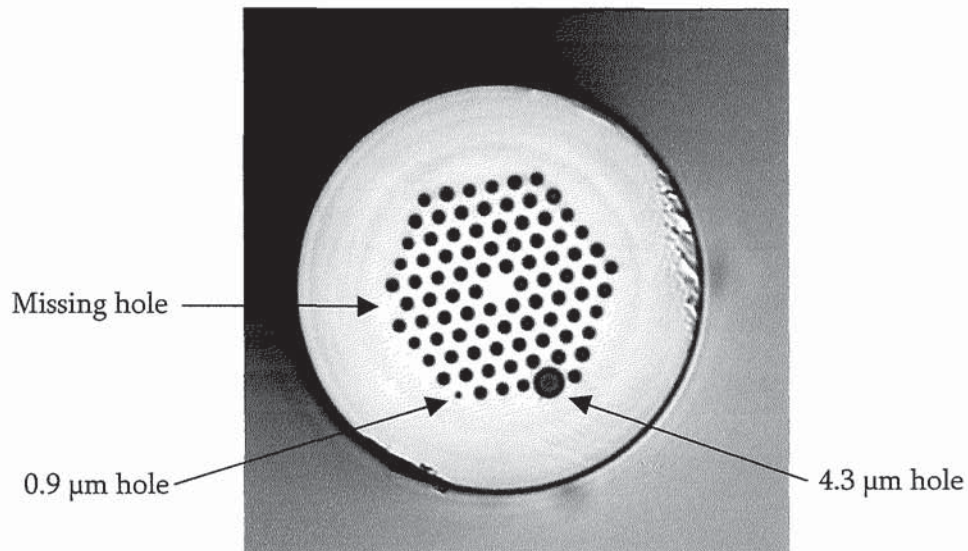


Figure 4-5: Cross-section of the large-mode area PCF taken using a microscope with x 20 objective.

The endlessly single mode (ESM) PCF used for this work (Crystal Fibre, ESM-1550-01) had an outer diameter of 125 μm , a core diameter of 12 μm surrounded by 54 air holes with diameters of 3.7 μm . The space between adjacent holes was 8 μm giving a filling factor of $d/\Lambda = 0.46$; see Figure 4-6.

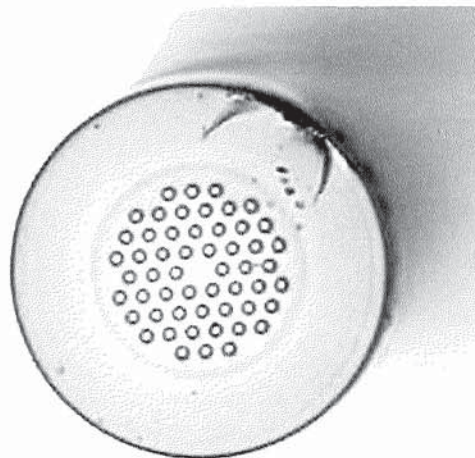


Figure 4-6: Cross-section of the endlessly single mode PCF taken using a microscope with x 20 objective.

Both fibres have attenuation at 1550 nm of less than 1 dB/km which is higher than the attenuation of standard telecommunications fibre (Corning SMF 28) which has a value of less than 0.2 dB/km. Although this level of attenuation would restrict the quantity of PCF

used for long distance telecommunication networks, sensing systems require significantly less fibre resulting in this loss having negligible effect.

4.5 Long Period Gratings in Photonic Crystal Fibre

The fabrication process used was exactly the same as defined in chapter 3 i.e. the same arc current, arc duration and fibre tension. Due to a limited quantity of fibre, the PCF was connectorised to single mode fibre patch cords using bare fibre adapters, giving an insertion loss of 1 dB. However, it is possible to splice the PCF to standard fibre using a modified program on a commercial splicer giving a loss of around 1 dB per splice.

The resulting gratings in the LMA PCF can be seen in Figures 4-7.

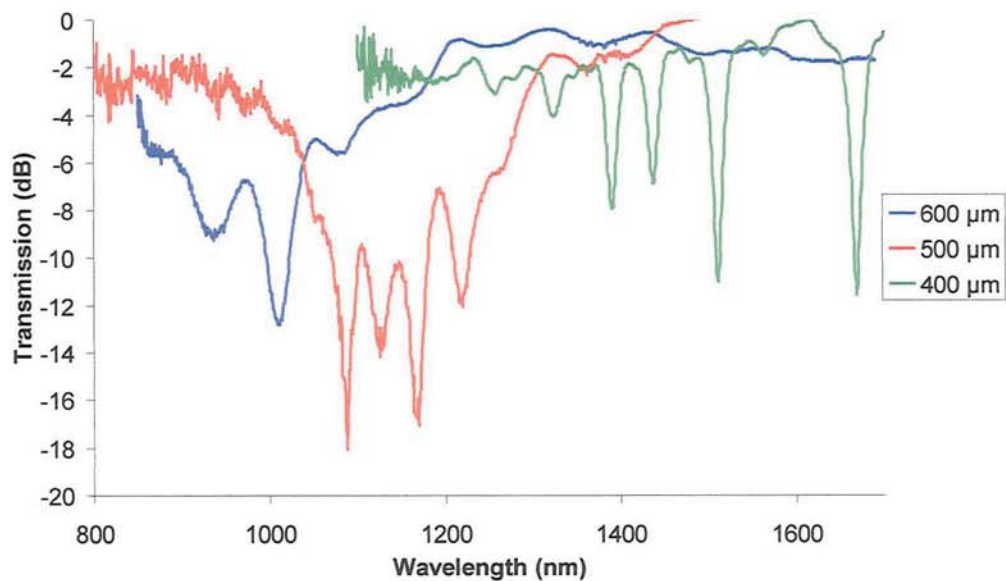


Figure 4-7: Various periods of LPG fabricated using the fusion arc technique in LMA PCF.

The grating with period 400 μm had a length of 37.6 mm, 500 μm had a length of 25 mm and the 600 μm period grating had a length of 18 mm.

The LPGs in the ESM PCF are shown in Figure 4-8.

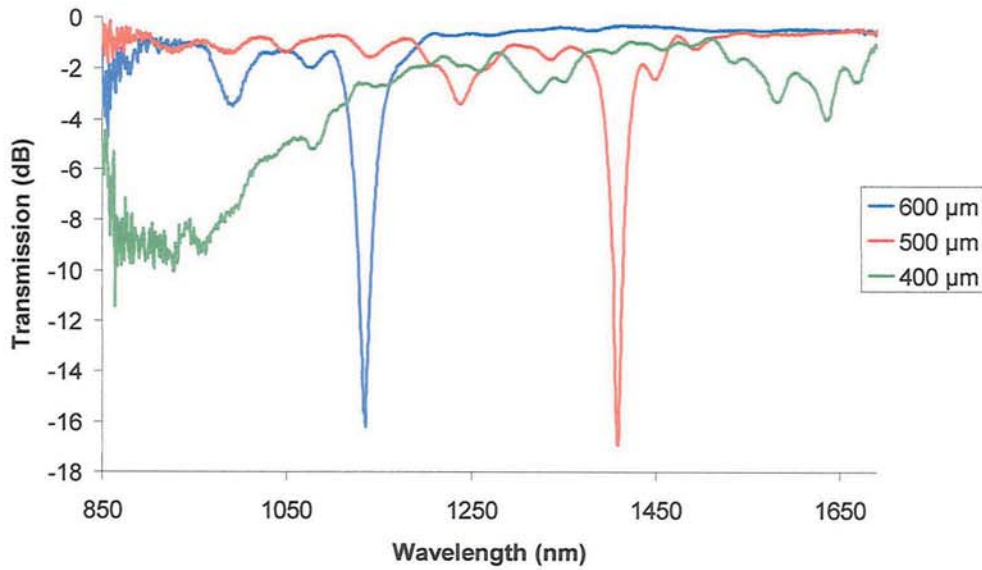


Figure 4-8: Various periods of LPG fabricated using the fusion arc technique in ESM PCF.

The grating with period 400 μm had a length of 34 mm, 500 μm had a length of 19 mm and the 600 μm period grating had a length of 18 mm.

As can be seen from Figures 4-7 and 4-8, as the grating periodicity increases the location of the attenuation bands decrease in wavelength. This is contrary to long period gratings in standard single mode fibre where the location of the attenuation bands increases with increasing period [13].

The fill factor of the ESM PCF is $d/\Lambda = 0.46$. Referring to Figure 4-4, this indicates that this particular optical fibre has negative dispersion. It is therefore predicted that the phase matching curves for the experimentally investigated fibres, LMA PCF and ESM PCF, will have negative slopes, which is supported by the reduction in resonance location with increasing period shown in Figure 4-7 and 4-8.

Jovana Petrović of Aston University's Photonics Research Group has commenced work theoretically characterising these fibres and long period gratings fabricated in them [84]. The phase matching curves for the ESM PCF have consequently been calculated using the coupled mode equations for a 1st order long period grating and the commercial full-

vectorial finite element Maxwell solver, Comsol (www.comsol.com) to determine the effective refractive indices. The resulting curves can be seen in Figure 4-9. As confirmed by the experimental data, the dispersion curves for this particular PCF have negative slopes. This is mainly attributed to the waveguide dispersion. With increasing wavelength the light propagates further into the holes reducing the effective refractive index of the cladding and increasing the differential between the core and cladding effective indices. If the increase in differential index is non-linearly faster than the linear increase in wavelength, the beat length decreases and the slope of the curves becomes negative.

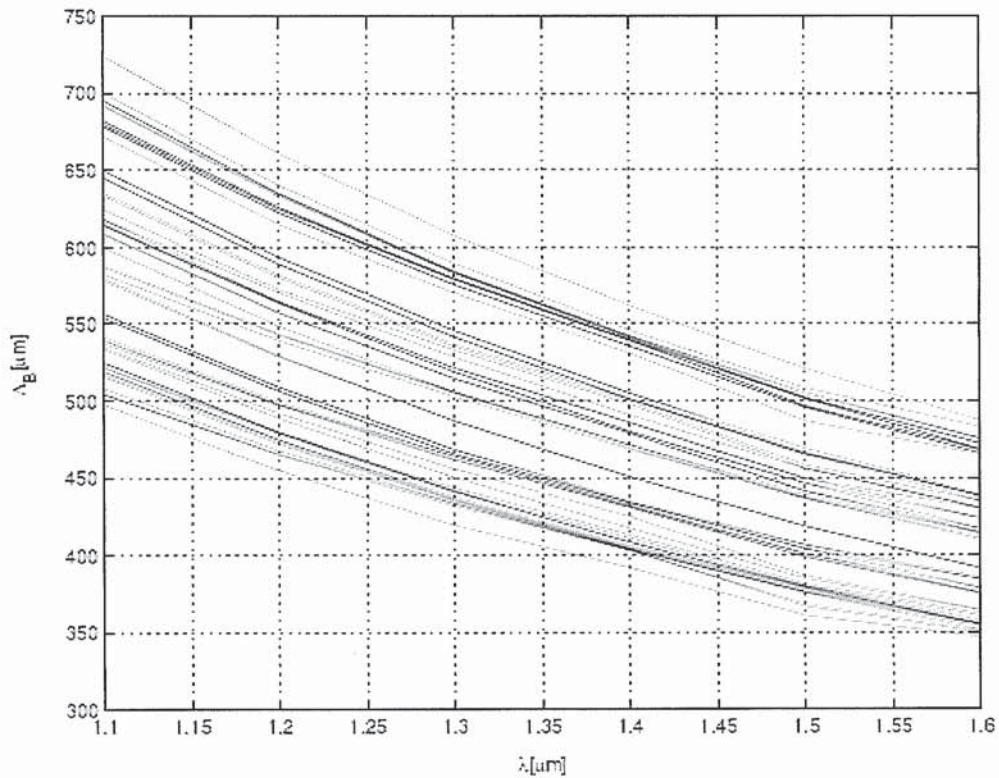


Figure 4-9: Phase matching curves for all modes (i.e. not LP modes) of the ESM PCF where $\Lambda_B = \Lambda$ the period of the long period grating [84]. Some lines appear thicker due to overlapping.

For a period of 500 μm and a wavelength of 1402 nm (see Figure 4-8), Figure 4-9 predicts the possibility of coupling occurring to three cladding modes. However, calculation of the overlap integrals revealed only one mode to have a significant overlap and this was therefore determined as the coupled mode. The profile of the resonance mode at 1402 nm is shown in Figure 4-10.

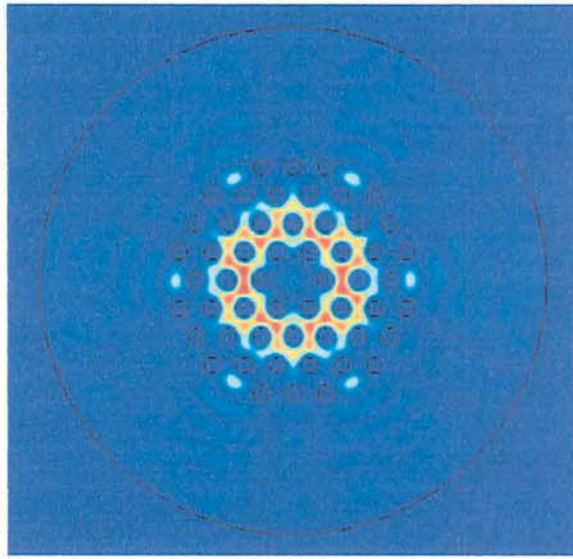


Figure 4-10: Profile of resonance mode at 1402 nm for the 500 μm LPG in ESM PCF. Bright areas indicate areas of highest intensity [84].

4.5.1 Growth Characteristics

The growth characteristics of the gratings in PCF are exactly the same as the electric-arc induced LPGs in standard single mode optical fibre with no shift in the location of the attenuation bands occurring with increasing length; see Figure 4-11.

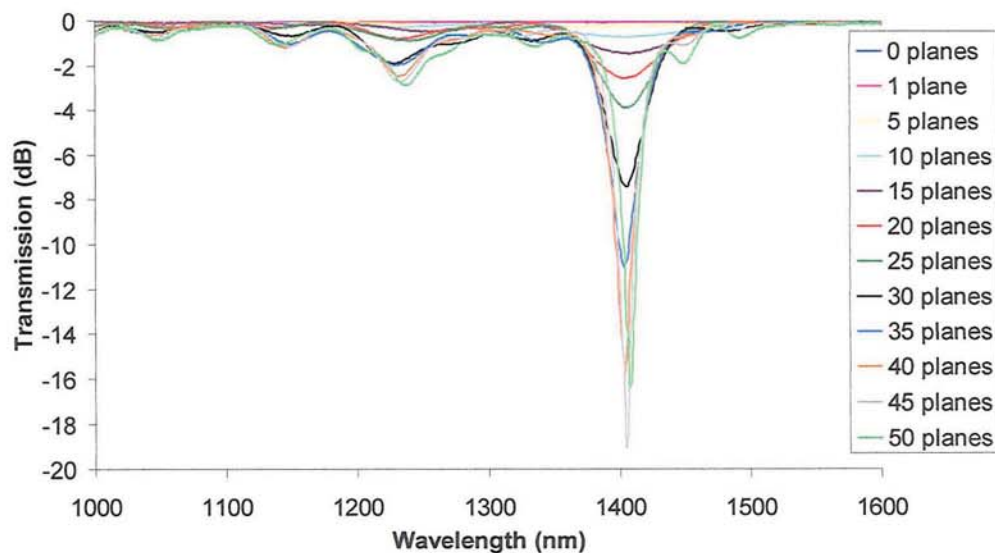


Figure 4-11: Growth data of 500 μm period LPG in ESM PCF. Each trace taken after the fabrication of 5 grating planes.

This is again associated with the fibre not needing to be hydrogen loaded and both the cladding and core material being affected by the electric-arc; see section 3.5.

4.6 Sensing Characteristics

Investigations into the spectral sensing characteristics of the two fibres were carried out on the 400 μm period LPG in the LMA PCF and the 500 μm period LPG in the ESM PCF. Both gratings were chosen due to their attenuation bands being located in the higher wavelength range giving ease of interrogation. The LMA PCF 400 μm grating had a length of 37.6 mm and a transmission spectrum containing four strong attenuation bands located at 1668 nm, 1511 nm, 1434 nm and 1389 nm. The ESM PCF 500 μm grating had a length of 19 mm and two attenuation bands located at 1245 nm and 1402 nm.

4.6.1 Temperature

The temperature sensitivity was investigated by placing the LPGs on an insulated Peltier heater. The Peltier was fixed inside a plastic box with two slits at either end for the optical fibre to enter and exit. The insulation was provided by polystyrene surrounding the heater and a polystyrene lid, which was placed on top of the fibre once it was in position. The Peltier had a built-in thermocouple to feed back the actual temperature attained by the device. Investigations using this experimental set up with UV inscribed LPGs in standard single mode fibre revealed expected thermal sensitivities.

The temperature of the Peltier was varied in temperature from 20 °C to 90 °C. Each individual attenuation band was investigated separately enabling the lowest resolution of the OSA, 0.1 nm, to be used, maximising the accuracy of the measurements. No change in the central wavelength of any of the attenuation bands was observed on the OSA. To evaluate the temperature response, the resonance wavelength at each temperature was determined by noting the maximum attenuation value, extrapolating from the data to find

the two wavelength values corresponding to a transmission 3 dB above this level and finally averaging the values obtained. Linear regression was then carried out on the data.

LMA PCF

The resulting sensitivity of the 400 μm LPG in LMA PCF was found to be $3.9 \pm 0.5 \text{ pm}/^\circ\text{C}$, $5.9 \pm 0.7 \text{ pm}/^\circ\text{C}$, $2.1 \pm 0.5 \text{ pm}/^\circ\text{C}$ and $3.4 \pm 0.2 \text{ pm}/^\circ\text{C}$ for the attenuation bands located at 1389 nm, 1434 nm, 1511 nm and 1668 nm, respectively. The spectrum at 20.0 $^\circ\text{C}$ and 90.2 $^\circ\text{C}$ for the attenuation band at 1511 nm can be seen in Figure 4-12, which clearly demonstrates the minimal temperature sensitivity.

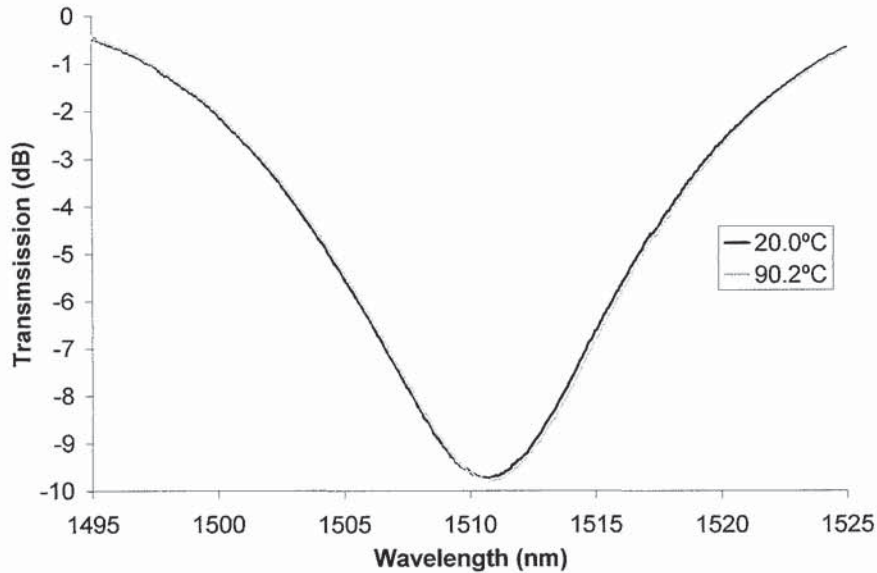


Figure 4-12: Effect of temperature on the 1511 nm attenuation band in LMA PCF.

ESM PCF

The temperature sensitivity of the LPG in the ESM PCF was found to be $3.7 \pm 1.0 \text{ pm}/^\circ\text{C}$ and $2.2 \pm 1.3 \text{ pm}/^\circ\text{C}$, for the bands at 1245 nm and 1402 nm, respectively. The spectral effect of 20.0 $^\circ\text{C}$ and 90.4 $^\circ\text{C}$ on the 1402 nm attenuation band can be seen in Figure 4-13.

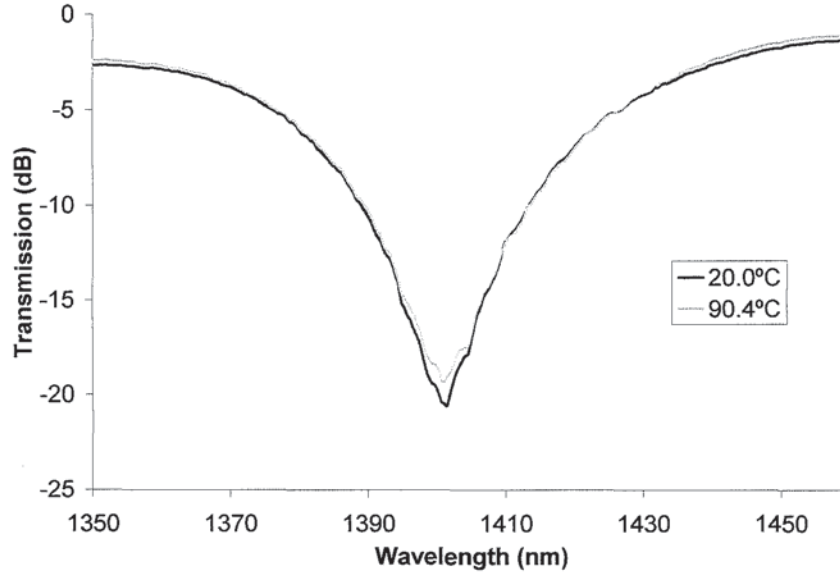


Figure 4-13: Effect of temperature on the 1402 nm attenuation band in ESM PCF.

The size of the uncertainties for both fibres shows that the sensitivity is often at the limit of the measurement resolution in this experiment. These data may be compared with the results of Humbert *et al* [81] who quote a temperature sensitivity of 9 pm/°C in the range of 25-160 °C for a pure silica endlessly single mode PCF. By way of further comparison, a typical temperature sensitivity for an electric-arc induced LPG in standard single mode fibre is 70 pm/°C [85].

The low temperature sensitivity observed in photonic crystal fibre can be explained by examining the temperature sensitivity equation defined in chapter 2:

$$\frac{d\lambda}{dT} = \frac{d\lambda}{d(\partial n_{eff})} \left(\frac{dn_{co}^{eff}}{dT} - \frac{dn_{cl}^{eff}}{dT} \right) + \Lambda \frac{d\lambda}{d\Lambda} \frac{1}{L} \frac{dL}{dT}. \quad (4.2)$$

In conventional fibres, the significant temperature sensitivity arises due to the core being doped which causes the effective core index to be more temperature sensitive than that of the cladding. In PCF, the core and cladding effective indices have very similar temperature dependences (close to that of pure silica), which significantly reduces the

contribution provided by the first term in equation 4.2. The second term, which describes the thermal expansion of the grating period, may be estimated to be around $1 \text{ pm}/^{\circ}\text{C}$, consistent with the measured values.

4.6.2 Bending

As discussed in chapter 2, LPGs are spectrally sensitive to fibre curvature. This coupled with the small size of optical fibres allowing them to be embedded within materials, has resulted in several potential applications including respiratory monitoring [86] and structural health monitoring [6-7]. Structural deformation can occur in any direction so it is imperative to have sensors capable of not only detecting curvature but the direction of the perturbation. However, vectorial curvature sensors cannot be simply realised using LPGs inscribed into standard symmetrical optical fibre. LPGs inscribed into asymmetrical fibre geometries such as D-shaped fibre [87,88] and eccentric core optical fibres [89] have been shown to have reasonable vectorial curvature sensing with red and blue wavelength shifts of the attenuation bands occurring depending on the induced bend direction. When asymmetric fibre geometries are bent, different strain areas are created within the fibre. The magnitude and location of the strain depends upon the fibre orientation. Since strain affects the phase matching condition, differing spectral responses are observed for different fibre orientations. Asymmetric fibre geometries are however difficult to connect to standard fibres for interrogation purposes. Recently, an UV inscribed LPG in standard symmetrical telecommunications optical fibre was made to have directional sensitivity by using a femtosecond laser to induce an asymmetric change in the refractive index of the cladding of the fibre [90]. However, the sensitivities achieved were less than those achieved by asymmetric structures.

Consequently, since PCF has the same outer diameter as standard fibre and a concentric core region, the LPGs in both PCFs were investigated for their spectral bend sensitivity. The measurements were made by clamping the fibre into two rotational stages. Two labels were attached to the fibre prior to mounting to ensure that no twist occurred when

clamping the fibre. The rotational stages were fixed onto two blocks, one of which was mounted on a translation stage that was moved inwards, inducing a bend in the fibre; see Figure 4-14. The rotational stages allowed the direction of the bend to be controlled, permitting the investigation of directional bend sensitivity.

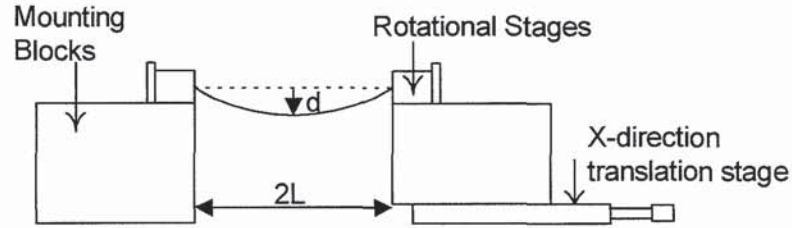


Figure 4-14: Schematic of the bending rig.

When the LPG is midway between the two blocks, the resulting curvature, R , of the sensor is given by [91]:

$$R = \frac{2d}{d^2 + L^2}, \quad (4.3)$$

where d is the bending displacement and L is half the distance between the fibre clamping points.

LMA PCF

Investigating the bend sensitivity of the LPG in the LMA PCF showed the attenuation bands to be sensitive to the direction of bending. This manifested itself as red and blue shifts in the central wavelength of the attenuation bands for different orientations of the rotational stages. The maximum sensitivities were found to occur at positions which were 180 degrees apart. These positions were arbitrarily designated 0 degrees and 180 degrees. The dependence on curvature was investigated at these two positions; the resulting wavelength shifts can be seen in Figure 4-15.

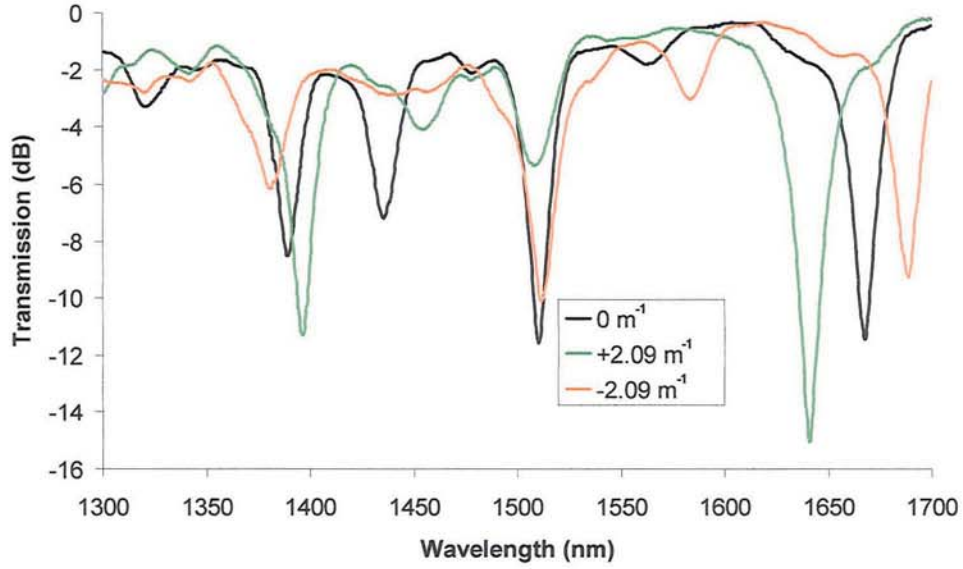


Figure 4-15: Spectral response of the LMA LPG to bending. Black line, LPG with no curvature; dark grey line, curvature of -2.09 m^{-1} in the 180 degrees position and light grey line, curvature of $+2.09 \text{ m}^{-1}$ in the 0 degrees position.

With the rotational stages set at 0 degrees, the attenuation bands at 1668 nm and 1511 nm experienced a blue wavelength shift while the bands at 1434 nm and 1389 nm experienced a red shift. With the rotational stages set at 180 degrees all shifts were in the opposite direction. This is an effect previously unreported in LPGs fabricated in PCF. The details of the theoretical explanation for the blue and red shifts are currently under investigation. It is most likely accredited to the asymmetric air hole geometry of this particular PCF leading to the presence of asymmetric cladding modes.

The spectral sensitivities of all the attenuation bands were investigated and the band centred at 1668 nm was found to have the maximum sensitivity to bending with a value of $d\lambda/dR = 9.6 \pm 1.0 \text{ nm.m}$ with the fibre in the 180 deg rotational state and a sensitivity of $d\lambda/dR = -12.4 \pm 1.2 \text{ nm.m}$ when in the 0 deg position; as shown by the trend lines in Figure 4-16.

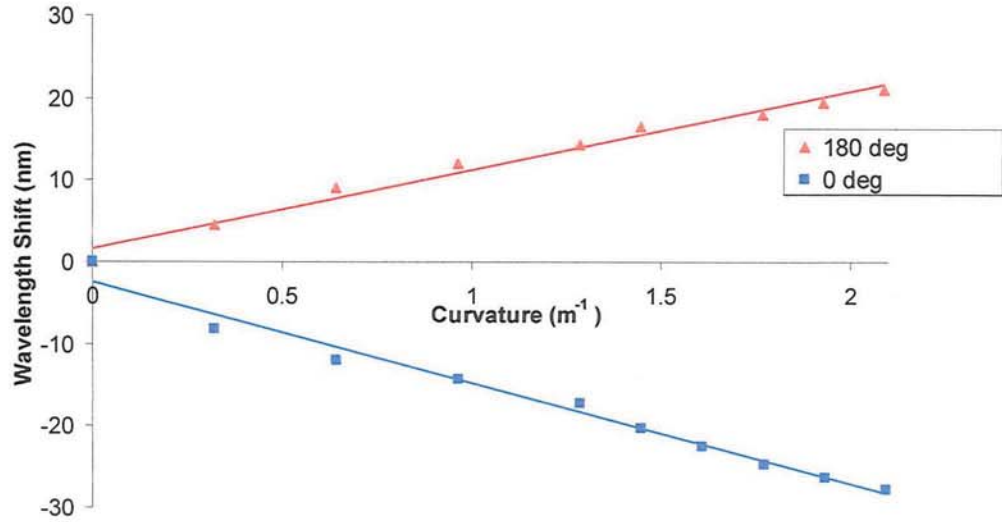


Figure 4-16: Spectral sensitivity to bending of the attenuation band at 1668 nm in LMA PCF.

This maximum sensitivity compares favourably against other directional bend sensors such as the SMF altered by a femtosecond laser [90], which had maximum directional sensitivities of -1.6 nm.m and $+3.8 \text{ nm.m}$, the D-shaped fibre [88] which had sensitivities of -3.56 nm.m and 6.51 nm.m and the eccentric core fibre [89] which had maximum sensitivities of -9.6 nm.m and 10.4 nm.m . The results for all the attenuation bands can be seen in Table 4.1. The negative signs indicate blue wavelength shifts.

Table 4.1: Table showing the spectral responses of all the attenuation bands in LMA PCF to the induced curvature.

	Attenuation Bands			
	1668 nm	1511 nm	1434 nm	1389 nm
0 degree rotation	$-12.4 \pm 1.2 \text{ nm.m}$	$-1.1 \pm 0.1 \text{ nm.m}$	$6.5 \pm 0.3 \text{ nm.m}$	$4.5 \pm 0.4 \text{ nm.m}$
180 degree rotation	$9.6 \pm 1.0 \text{ nm.m}$	$0.7 \pm 0.1 \text{ nm.m}$	$-4.0 \pm 0.5 \text{ nm.m}$	$-4.3 \pm 0.5 \text{ nm.m}$

The spectral investigation of the band at 1668 nm was carried out up to a curvature of 2.09 m^{-1} , whereas the attenuation bands at 1511 nm, 1434 nm and 1389 nm were only taken up to 1.45 m^{-1} . This was because at larger curvatures it became increasingly difficult to determine the location of the bands at 1434 nm and 1511 nm due to their reduction in size and broadening bandwidth.

ESM PCF

Investigations into the bend sensitivity of the LPG in ESM PCF showed no directional bend sensitivity. On bending, the attenuation band at 1245 nm disappeared after a curvature of 2.56 m^{-1} and the band at 1402 nm experienced a red wavelength shift as well as a reduction in power. Another attenuation band also appeared induced by the bending, which increased in strength with increasing curvature as well as experiencing a red wavelength shift. This band had a central wavelength of 1354 nm at the finishing curvature of 5.45 m^{-1} . The results can be seen Figure 4-17.

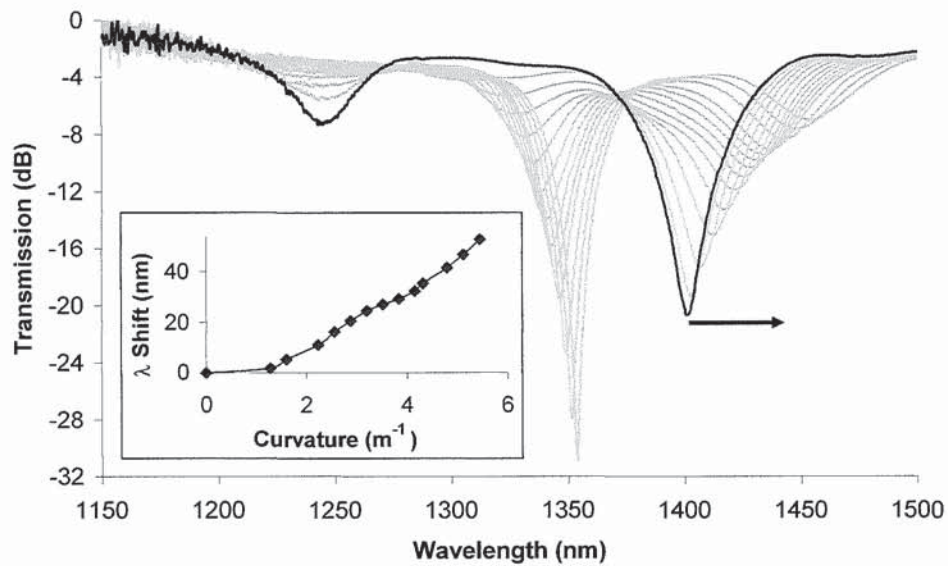


Figure 4-17: Spectral response of the LPG in ESM PCF to bending up to a curvature of 5.45 m^{-1} . Unbent curve in bold. Inset: Wavelength shift of band initially at 1402 nm as a result of induced curvature.

The wavelength shift of the 1402 nm attenuation band at a curvature of 5.45 m^{-1} was $53.0 \pm 1.4 \text{ nm}$ and the induced band had a wavelength shift of $29.8 \pm 1.4 \text{ nm}$ in the curvature range 1.60 m^{-1} to 5.45 m^{-1} . The purely symmetrical crystal structure resulting in symmetric cladding modes and no directional bend sensitivity.

4.6.3 Refractive Index

The spectral sensitivity to surrounding refractive index (SRI) was investigated by placing the LPG in a v-groove and immersing the grating in certified refractive index (CRI) liquids (supplied by Cargille laboratories Inc). The refractive index values of the oils are quoted at a wavelength of 580 nm with an accuracy of ± 0.0002 . Before immersion in each of the CRI liquids, the LPG and v-groove were cleaned using methanol, then deionised water and finally dried, to prevent cross contamination. All measurements were made at a constant room temperature of 25 °C to eliminate any thermally induced refractive index variations in the oils.

The v-groove was created in an aluminium plate and was clamped to the optical table to ensure no movement occurred. The fibre was attached to two small metallic blocks either side of the v-groove. These ensured that the fibre was suspended in the middle of the v-groove and was not touching the metal, giving total bulk immersion. After each cleaning and subsequent repositioning of the fibre, it was ensured that the fibre was under the same tension each time by comparing the spectrum on the OSA with a saved trace of the original spectrum. Several different CRI liquids were compared in the range $n = 1.325$ to $n = 1.514$. Since the refractive index of silica is 1.444 (at a wavelength of 1550 nm and temperature of 25 °C) this range enabled a study of the response of the grating to refractive indices lesser and greater than that of the fibre.

LMA PCF

The effect of SRI changes on the transmission spectrum of the grating in LMA PCF for CRI liquids of index less than that of silica is shown in Figure 4-18. As can be seen, all attenuation bands experience a red wavelength shift with increasing index.

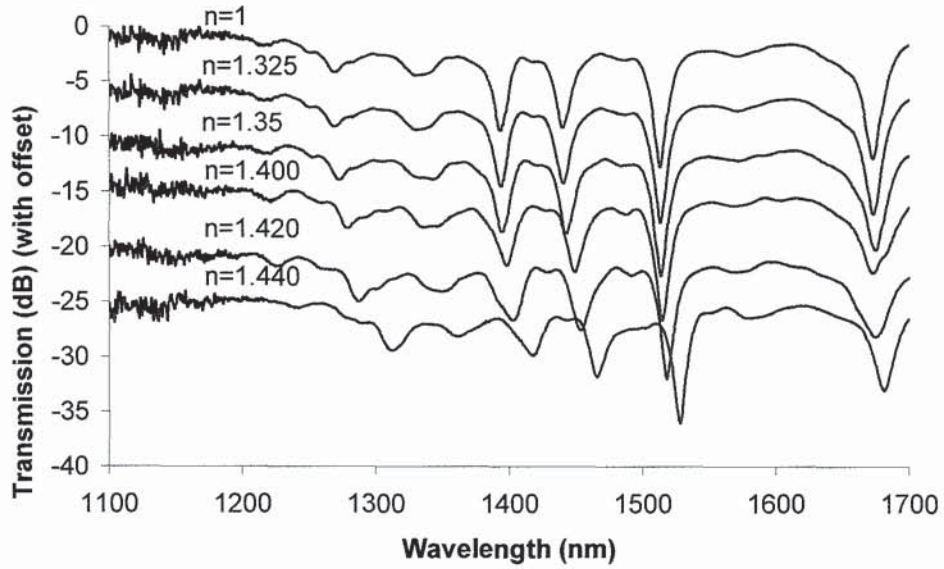


Figure 4-18: The effect of SRI on the attenuation bands in LMA PCF.

The wavelength shift as a function of the SRI for each attenuation band is shown in Figure 4-19. This figure shows that the peak initially centred at 1434 nm has the greatest wavelength shift followed by the peak at 1389 nm then 1511 nm and finally 1668 nm.

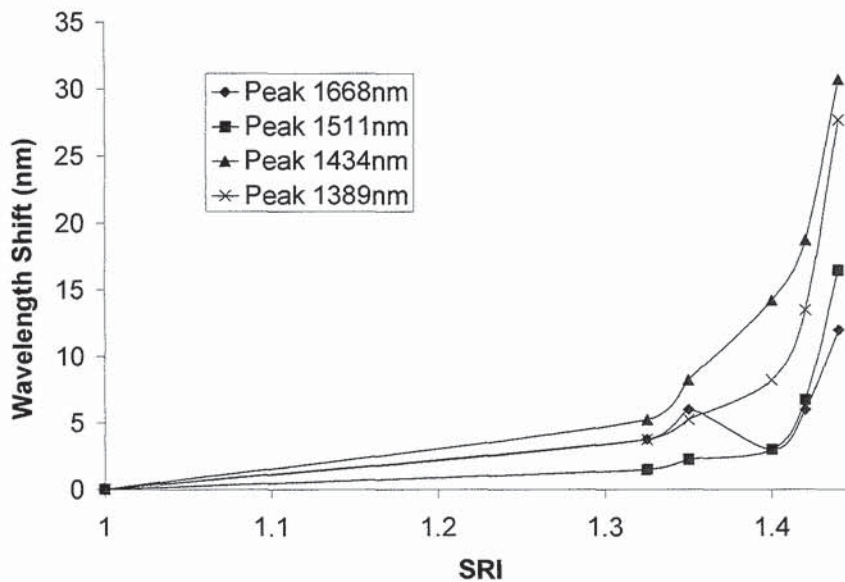


Figure 4-19: The wavelength shift of the four attenuation bands in LMA PCF as a function of the SRI (less than silica).

The sensitivity increases markedly as the SRI approaches that of the cladding with a maximum shift of 30.8 ± 0.2 nm by the attenuation band at 1434 nm and a minimum shift of 12.0 ± 0.2 nm by the 1668 nm attenuation band. When the SRI and cladding indices are

matched, the cladding appears to be infinite and thus no co-propagating cladding modes are supported. This spectral response is similar to the behaviour of LPGs fabricated in standard single mode fibre, except that standard fibre typically shows a blue wavelength shift instead of the red shift observed in the PCF [13,69].

For refractive indices greater than that of silica, the spectrum of the LPG changes with only three attenuation bands present, see Figure 4-20. This plot also shows that as the SRI is increased the amplitude of the attenuation bands grow without any significant spectral shifting and the fourth attenuation band starts to reappear.

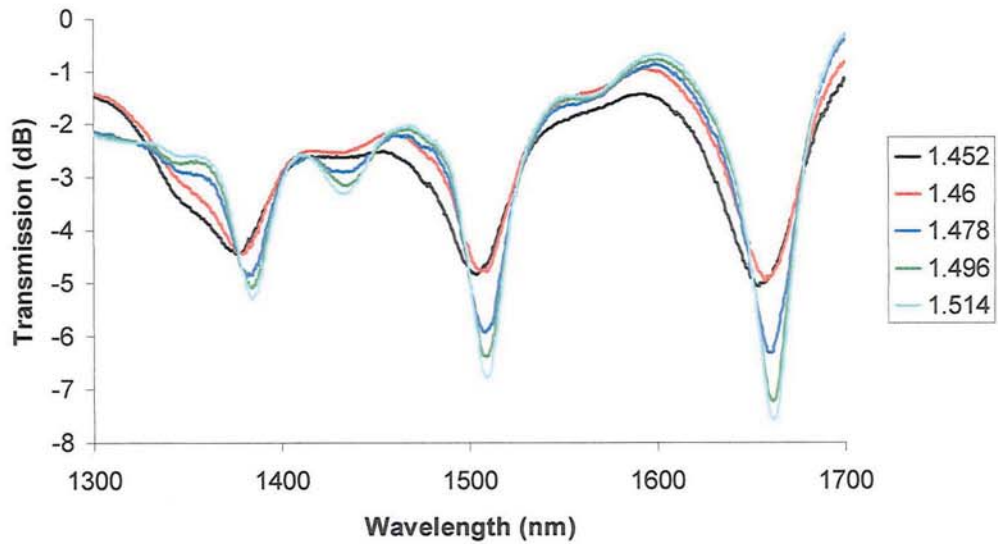


Figure 4-20: The wavelength shift of the attenuation bands in LMA PCF as a function of the SRI (greater than silica).

ESM PCF

The ESM PCF grating also experienced red wavelength shifts with increasing SRI values less than silica. No shift was observed for values higher than silica; the results are shown in Figure 4-21.

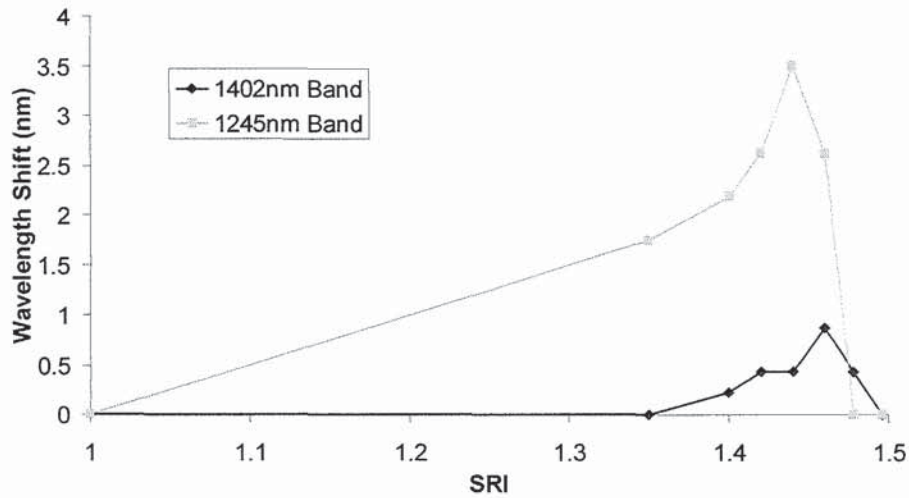


Figure 4-21: The wavelength shift of the attenuation bands in ESM PCF as a function of the SRI.

The maximum wavelength shift was observed in the 1245 nm attenuation band which had a shift of 3.5 ± 0.1 nm. The maximum wavelength shift for the 1402 nm attenuation band was 0.8 ± 0.1 nm. For values of SRI 1.5 and above, all the attenuation bands were present and no wavelength shift was observed. The difference in sensitivity between the modes is attributed to the mode at 1239 nm have more interaction with the surrounding material than the mode at 1402 nm.

The SRI sensitivity for the ESM PCF is significantly less than for the LMA PCF demonstrating that there is a dependence on the air-hole geometry of the fibre. Jovana Petrović has found the air-hole geometry to dictate how much of the cladding mode propagates in the bulk cladding and consequently is able to interact with the surrounding material [84].

4.6.4 Strain

The axial strain sensitivity was investigated by fixing one end of the stripped section of fibre to a metallic block using Norland Optical Adhesive No. 81 (NOA 81). The other end

of the stripped fibre was fixed to an x-direction translation stage, which was the same height as the block, using NOA 81. The distance between the block and translation stage was measured using a pair of Vernier Callipers. Axial strain was applied to the LPG by moving the translation stage away from the block in steps of 100 μm . The spectral response after each 100 μm increment was recorded using an OSA. The resulting strain was calculated using:

$$\varepsilon = \frac{\Delta L}{L} \quad (4.4)$$

where L is the distance between the translation stage and the block with no strain applied to the LPG and ΔL is the change in length induced by altering the translation stage.

LMA PCF

A linear blue wavelength shift of the central wavelength of all the attenuation bands was observed, see Figure 4-22 for details of the band at 1668 nm. The attenuation band centred at 1668 nm had a strain sensitivity of $d\lambda/d\sigma = -2.50 \pm 0.04 \text{ pm}/\mu\text{e}$. The other attenuation bands demonstrated similar strain sensitivities, except for the band centred at 1389 nm which had a sensitivity of $d\lambda/d\sigma = -1.8 \pm 0.2 \text{ pm}/\mu\text{e}$.

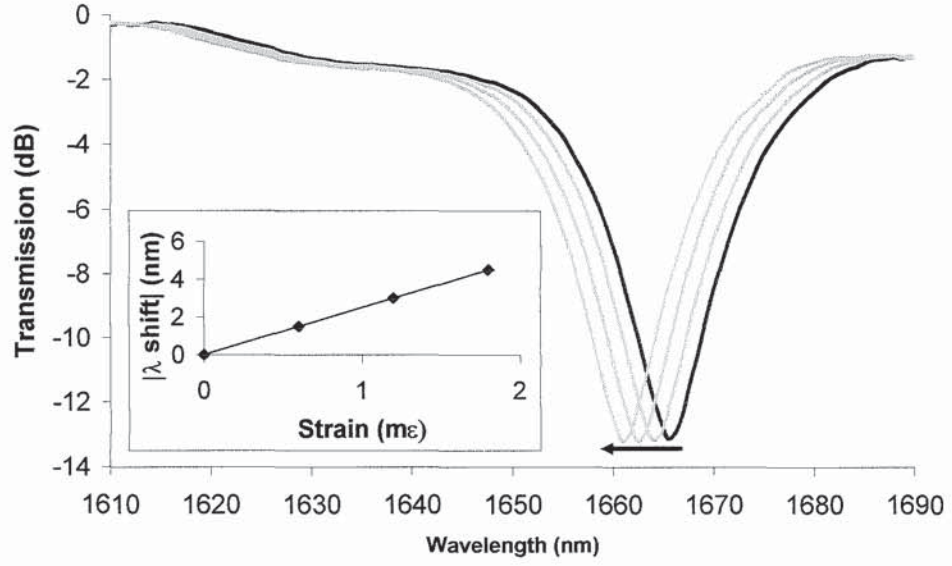


Figure 4-22: Spectral response of LPG band at 1668 nm, in LMA PCF, to strain in the range 0–1.8 mε. Unstrained curve in bold. Inset: Wavelength shift as a result of the applied strain used to produce the spectral response shown.

ESM PCF

A blue wavelength shift was again observed with increasing strain giving a strain sensitivity of $d\lambda/d\sigma = -2.08 \pm 0.05 \text{ pm}/\mu\epsilon$. The result can be seen in Figure 4-23.

Chapter 2 showed the strain sensitivity of an LPG to be defined by:

$$\frac{d\lambda}{d\epsilon} = \frac{d\lambda}{d(\partial n_{eff})} \left(\frac{dn_{co}^{eff}}{d\epsilon} - \frac{dn_{cl}^{eff}}{d\epsilon} \right) + \Lambda \frac{d\lambda}{d\Lambda}, \quad (4.5)$$

In the case of the studied PCF, the strain-optic coefficients applicable to the core and cladding modes are very similar (close to that of pure silica) and as a result, the strain sensitivity is largely determined by the second term on the right hand side of equation 4.5, i.e. the grating period extension with applied strain. Increasing the periodicity of the grating causes the resonance wavelength to decrease resulting in a blue wavelength shift with increasing strain.

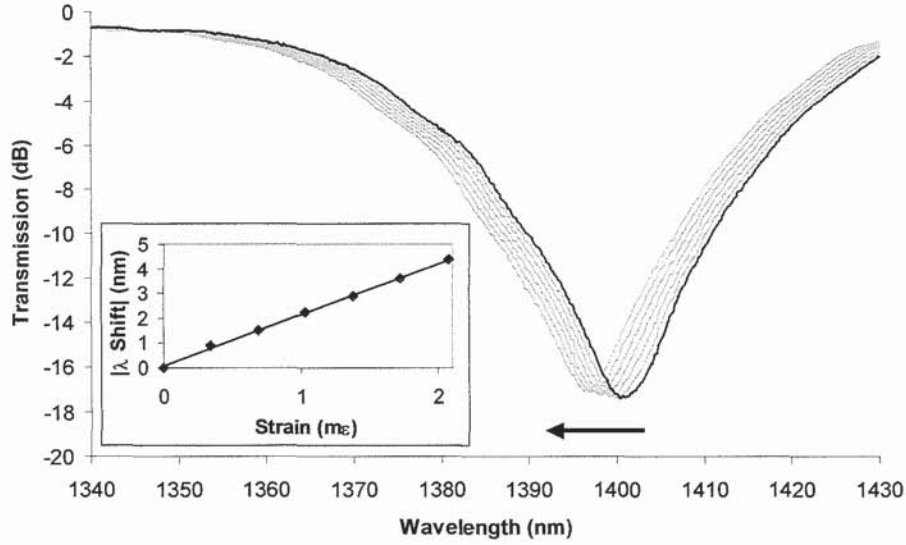


Figure 4-23: Spectral response of LPG band at 1402 nm, in ESM PCF, to strain in the range 0–2.07 mε. Unstrained curve in bold. Inset: Wavelength shift as a result of applied strain.

The two PCF types have similar strain sensitivities which can be attributed to the fact that the LPGs were fabricated under the same conditions. It has been shown by Rego *et al* [92] that the sensing characteristics of LPGs fabricated in SMF 28 using the electric-arc technique can be altered by varying the current of the electric discharge and the tension on the fibre under fabrication and hence great care was taken to keep these parameters constant.

4.7 Modelled Sensing Characteristics

Jovana Petrović has conducted theoretical modelling on the spectral response of the LPG attenuation band located at 1402 nm in ESM PCF to the various measurands investigated experimentally [84].

4.7.1 Strain and Temperature Sensitivity

The strain calculations were conducted using the equation:

$$\frac{d\lambda}{d\varepsilon} = \gamma\lambda \left(1 + \frac{\partial \delta n_{eff}}{\partial n} \frac{\eta_\varepsilon}{\delta n_{eff}} \right), \quad (4.5)$$

where

$$\eta_\varepsilon = -0.5n^3(p_{12} - \mu(p_{12} + p_{11})) = -0.3, \quad (4.6)$$

taking the elements of the strain-optic tensor as $p_{11} = 0.121$, $p_{12} = 0.27$ and the Poisson's coefficient for fused silica as $\mu = 0.17$ [93]. The derivative $\partial\delta n/\partial n = -1.17 \times 10^{-3}$ was found by linearisation with the fixed wavelength and the refractive index range of $\pm 5 \times 10^{-4}$. The change in refractive index at the maximum experimentally applied strain of $2 \text{ m}\varepsilon$ was found to be -6×10^{-4} . The grating period was increased for, $\Delta\Lambda = \varepsilon\Lambda$ and the new resonant wavelength was found by interpolation at the point $\Lambda' = \Lambda(1 + \varepsilon)$. Although both the change in index profile and the change in grating period contribute to the strain sensitivity, the change in period was found to dominate. The resulting strain sensitivity was found to be $-1.85 \text{ pm}/\mu\varepsilon$.

The temperature sensitivity was found from the equation:

$$\frac{d\lambda}{dT} = \gamma\lambda \left(\alpha + \frac{\partial\delta n_{\text{eff}}}{\partial n} \frac{\eta_T}{\delta n_{\text{eff}}} \right), \quad (4.7)$$

where the thermal expansion coefficient of silica is $\alpha = 4.1 \times 10^{-7}/^\circ\text{C}$ and the thermo-optic coefficient of silica is $\eta_T = 7.8 \times 10^{-6}/^\circ\text{C}$ [93]. For the temperature range of 70.4°C the maximum change of refractive index is 5×10^{-4} . Assuming that the grating response is linear the already calculated derivatives used to calculate the strain were applied. The resulting temperature sensitivity was calculated as being $3.9 \text{ pm}/^\circ\text{C}$.

The theoretically modelled strain and temperature sensitivities closely match those achieved experimentally; see comparison in Table 4.2.

Table 4.2: Comparison of modelled results of the spectral sensitivity of the LPG in ESM PCF with the experimentally recorded data.

	Theoretical Result	Experimental Result
Temperature Sensitivity	3.9 pm/°C	< 4 pm/°C
Strain Sensitivity	-1.85 pm/μ ϵ	-2.08 \pm 0.05 pm/μ ϵ

4.7.2 Refractive Index Sensitivity

Refractive index sensitivity is only achievable if a part of the resonance mode comes into contact with the surrounding material. This can only happen in PCF if the resonant mode propagates through the bulk silica cladding. Modelling of the profile of the resonant mode at 1402 nm has shown the mode to protrude outside of the fibre, see Figure 4-24. External refractive index sensing does not cause the grating period to alter. Consequently, any wavelength shift is attributed to the change in effective refractive index of the cladding mode, which affects the phase matching condition. Figure 4-25 shows the dependence the phase matching curve has on the external refractive index and clearly shows the red wavelength shift with increasing index.

All these results show that the modelling and consequent understanding of these fibres and LPGs is progressing well with the potential in the future of designing a PCF for specific sensing applications minimising all unwanted cross sensitivities.

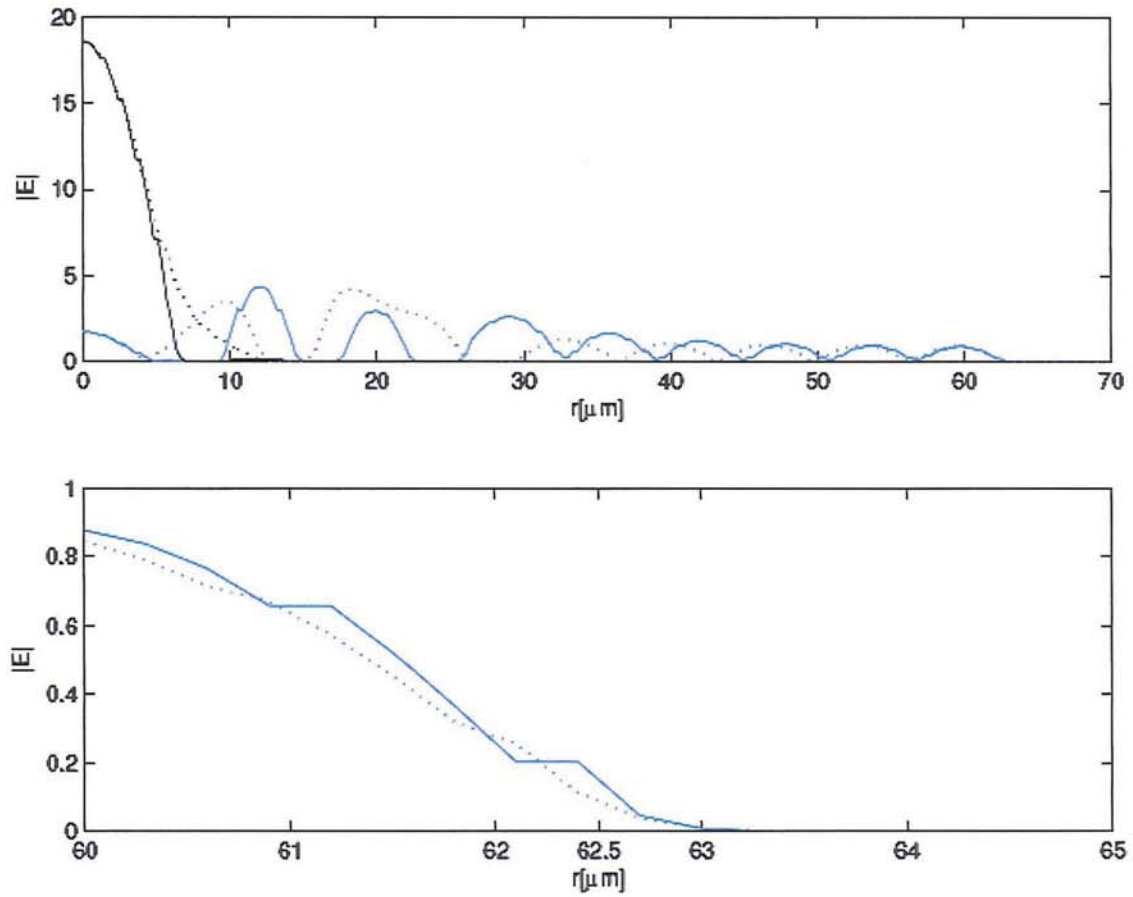


Figure 4-24: Line plots along x-axis (solid lines) and y-axis (dashed) of the profiles of the core mode (black lines) and the 1402 nm resonant mode (blue lines) in air [84].

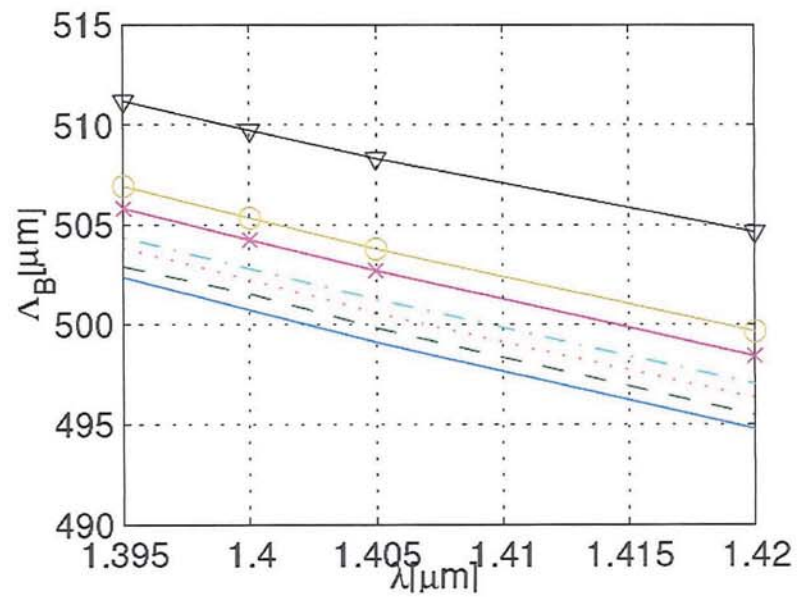


Figure 4-25: External refractive index sensitivity of resonant mode at 1402 nm in ESM PCF. Refractive indices: 1.0 (solid line), 1.2 (dashed), 1.3 (dotted), 1.35 (dash-dot), 1.4 (\times), 1.42 (O) and 1.44 (∇) [84].

4.8 Summary of the Experimental Sensing Characteristics

Table 4.3 shows a summary of the dimensions of the two investigated PCFs and their associated sensing characteristics.

Table 4.3: Summary of sensing characteristics of the two investigated PCFs and an LPG in standard telecommunications fibre (period 300 μm , $L = 5\text{ cm}$, sensitivities @ 1550nm [94]) for comparison.

		LMA PCF	ESM PCF	SMF
Dimensions	Core Size	11 μm	12 μm	8 μm
	Hole Size	Mostly 2.0 μm	3.7 μm	
	Separation	7.1 μm	8 μm	
	No. Holes	89	54	
Temperature		< 6 $\text{pm}/^\circ\text{C}$	< 4 $\text{pm}/^\circ\text{C}$	-410 $\text{pm}/^\circ\text{C}$
Curvature		-12.4 \pm 1.2 nm.m 9.64 \pm 1.0 nm.m	At $R = 4.54\text{ m}^{-1}$ shift 53.0 \pm 1.4 nm	+9.5 nm.m
SRI	max	30.8 \pm 0.2 nm	3.5 \pm 0.1 nm	-465 nm
	min	12.0 \pm 0.2 nm	0.8 \pm 0.1 nm	
Strain		-2.50 \pm 0.04 $\text{pm}/\mu\epsilon$	-2.08 \pm 0.05 $\text{pm}/\mu\epsilon$	+0.9 $\text{pm}/\mu\epsilon$

The investigations revealed a temperature sensitivity in the order of a few $\text{pm}/^\circ\text{C}$ which for many applications is considered negligible. This is important for applications where cross sensitivity is undesirable, eliminating the need for discriminatory schemes and reducing the overall cost of the system. Another important result from these experiments is the directional bend sensitivity observed in the LMA PCF. The sensitivity compares well against other reported sensors and is attributed to the disrupted symmetry of the photonic crystal fibre. The ESM PCF, which has a completely symmetric photonic crystal structure, did not show directional bend sensitivity. The fibres also show significantly differing sensitivities to surrounding refractive index demonstrating that they could be either used for refractive index sensing or embedded into composite material without significantly changing the spectral response of the device. Similar strain sensitivities were observed which is mostly attributed to the gratings being fabricated under the same inscription conditions and both fibres being constructed of pure silica.

All these results demonstrate that different PCFs can have different sensing characteristics with the ability to have reduced or no sensitivity to some measurands whilst having good sensitivity to others, which is mainly attributed to the air-hole geometry of the fibre.

5

Polymer Optical Fibre Background

This chapter aims to provide an introduction to polymer optical fibres. To start with, the uses and potential applications of polymer optical fibre are discussed followed by details of typical polymers used for fabricating fibres. The effect that the different polymers have on the resulting fibre attenuation is then detailed. The photoinscription mechanisms involved in fibre Bragg grating fabrication in polymer optical fibre is provided. Practical techniques for fibre end preparation are demonstrated with different processes required for different fibre types. Finally, light transmission through the available polymer optical fibres is studied with an emphasis placed on compatibility with specific light sources.

5.1 Introduction

Polymer optical fibre (POF) has advanced significantly in the last few years with the ever increasing potential that it will become an integral part of future transmission networks. Although the majority of today's transmission network consists of high bandwidth glass optical fibre, the last sections, local area networks (LANs) and 'in house' transmission, still consist of copper cabling. With the rapid expansion of the internet and increased demands on bandwidth, copper cabling will soon be obsolete due to its limited bandwidth. Consequently, the remaining section of non-optical network will potentially need replacing resulting in a completely optical system. However, the large quantity of wiring

to be replaced demands an economically sound, efficient and easily installed solution. Due to the numerous connections and junctions contained within LANs, silica-based optical fibres are a costly solution since they require precise connection, dedicated installation and handling. Polymer-based optical fibres may provide a solution to this increasingly pertinent issue. Multimode polymer optical fibres typically have an outer fibre diameter of approximately 1 mm. Unlike their glass counterparts, polymer optical fibres (POF) with these dimensions still retain their mechanical flexibility allowing easy installation and inexpensive connectivity of the fibres due to their large multimode core. However, large core step index polymer optical fibres (SI POF) have limited bandwidth, a problem which can be improved by using graded index polymer optical fibres (GI POF) [95].

The majority of polymer optical fibres are based around polymethylmethacrylate (PMMA) more commonly known as Perspex® or Plexiglas®. Recently however, prefluorinated (PF) graded index polymer optical fibre (PF GI POF) has been shown to have a higher data transmission over not only PMMA-based step index POF but PMMA-based graded index POF as well [96]. Consequently, PF GI POF is likely to be a potential replacement medium for the existing copper cabling. A table comparing the data transmission rates of copper cabling, glass and polymer optical fibre is shown in Table 5.1, which clearly shows that PF GI POF is a suitable replacement for copper cabling. Not only does it provide a greater bandwidth than copper but also provides the advantages of optical cabling such as insensitivity to electromagnetic radiation and tapping immunity. Consequently, in 2000 a 1 Gbit/s campus LAN constructed of PF GI POF was implemented at Keio University and has subsequently led on to networks in housing complexes, hospitals and medical conference halls in Tokyo [97,98].

In order to increase the bandwidth of a POF data network, optically based techniques such as wavelength division multiplexing (WDM), already developed for glass optical fibre based systems, can also be employed. WDM works by using a number of different wavelengths as separate data channels increasing the total bandwidth attainable.

Table 5.1: Comparison of the transmission performance of copper cables and optical fibre [95-101]. PNA (Phone Network Association) existing copper cables; PLC (PowerLine Communications) electrical power supply.

Transmission Medium	Transmission Rate
<i>Copper Cables</i>	
PNA	Some Mbit/s
Coaxial	Some 100 Mbit/s
Data Cables	1 Gbit/s < 100m
PLC	Some Mbit/s
<i>Optical Fibres</i>	
Glass SM-Fibre	160 Gbit/s
Glass MM-Fibre	2.5 Gbit/s
MM PMMA POF	Some 100 Mbit/s < 100m
PMMA GI POF	3.0 Gbit/s < 100 m
PF GI POF	1 Gbit/s < 1000 m
	11 Gbit/s < 100 m

A fundamentally important component used in this technique is the fibre Bragg grating (FBG) which filters and separates the different wavelengths. Whilst this is a mature technology for glass-based systems, it is a relatively new area for polymer-based systems. Z. Xiong *et al* at the University of New South Wales in Australia were the first to report on FBGs inscribed in POF [102].

As well as components of telecommunications devices, fibre Bragg gratings are also used in sensing applications, where shifts in the central wavelength location occur as a result of external measurands such as temperature or strain perturbing the optical fibre. Standard uniform FBGs in silica-based optical fibres have limited spectral sensitivity to external measurands with typical strain responses of ~ 1 pm/ $\mu\epsilon$ and temperature responses of ~ 10 pm/ $^{\circ}\text{C}$, for gratings at 1550 nm [19]. The sensitivity of these devices can be increased by inscribing complex grating structures such as Moiré gratings [103] or Fabry Perot cavities [104]. Such structures are however difficult and time consuming to manufacture. These limitations could potentially be overcome by using FBGs fabricated in polymer optical fibres. Since polymers have different mechanical properties to silica, FBGs fabricated in polymer have different spectral sensitivities to external measurands. Liu *et al* [105] from

the University of New South Wales in Australia, characterised their uniform fibre Bragg gratings in POF and demonstrated that they possess increased sensitivity to strain with a recoverable strain of 13%. Temperature sensitivity was also found to be 130x greater than uniform FBGs in silica-based optical fibre. For medical sensing applications, a resolution of 0.1 °C is required over a temperature range of ~35-50 °C [3], which is significantly below the glass transition temperature of ~100°C for POF. Although current medical applications such as in-vivo temperature profiling [106] and remote temperature sensing in NMR (nuclear magnetic resonance) machines [107] use multiplexed FBGs in silica optical fibre, the enhanced temperature sensitivity of POF FBGs (130x) as well as the inherent biocompatibility of organic polymers, is clear motivation for increased research in this field.

Microstructured optical fibres are becoming of increasing interest due to their unique properties over standard optical fibre; see chapter 4. In silica-based optical fibres, the holes are fabricated by drawing a preform constructed of stacked silica rods and tubes. The manufacturing process in polymer is more versatile with a number of different techniques available including drilling, extrusion, casting, polymerisation inside a mould and injection moulding [108]. Whilst the viscosity of silica and polymer at their respective drawing temperatures are very similar [109-110] the surface tension of the polymer is of several orders of magnitude less than silica [111-112], minimising hole collapse and enabling fine structures to be created. This results in almost any hole arrangement being fabricated and consequently single mode fibres and graded index fibres can be manufactured relatively easily by controlling the size and position of the holes in the fibre preform.

Microstructured POF has also been recently shown to have applications in imaging [113]. Since the light can either be guided in the multiple polymer cores between the air holes, or by the air holes themselves, this allows multiple signals to be transmitted by the same fibre. This results in the potential for a miniaturised endoscope consisting of one fibre,

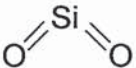
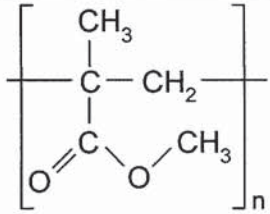
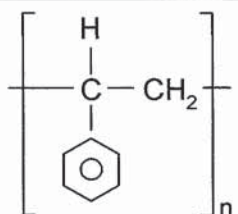
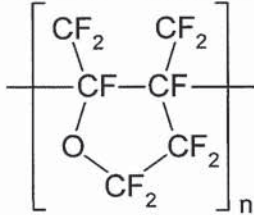
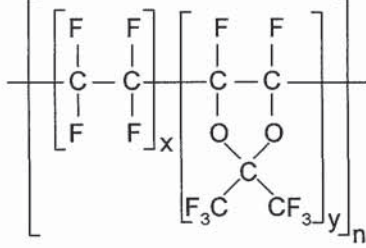
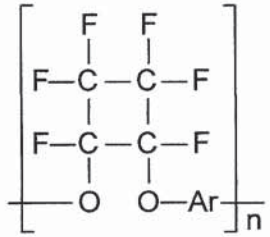
instead of the numerous glass fibres currently employed. This makes the fibre ideal for small areas where current endoscopes do not fit, such as for cochlear implant surgery [114].

The work reported in this thesis is concerned with inscribing FBGs in step-index and microstructured POF with the main emphasis towards their potential as sensing devices. This chapter provides background information on the polymer optical fibres investigated, effects of attenuation in typical fibres as well as photosensitivity and fibre preparation.

5.2 Chemistry of Polymer Optical Fibre

In order to understand the optical and mechanical properties of polymer optical fibre, as well as the mechanisms for grating inscription in these fibres, the chemical construction and properties of the most commonly used polymers needs to be considered and compared with silica. Polymers are constructed of vinyl monomers; small molecules containing carbon-carbon double bonds. During vinyl polymerisation, this double bond splits allowing the monomers to attach together to form a long chain molecule; see section 5.3. Table 5.2 contains the chemical formulae, glass transition temperature (the temperature below which molecules have little relative mobility) and refractive index of the most commonly utilised polymers, as well as silica for the sake of comparison. The square brackets in Table 5.2 show the repeating units (monomers) of the polymer chains. There are numerous different varieties of the polymer PFCB which vary in structure from each other by differing aryl groups (Ar): molecules containing 6 carbon atoms in a ring (benzene) schematically depicted as hexagons. A commonly investigated PFCB is PFCB (TVE) for which the aryl group is trifluorovinylether; shown in Figure 5-1 [115].

Table 5.2: Table of the different polymers used to construct POF. Silica is added for comparison [46,116].

Material	Formula	Refractive Index	Glass Transition Temperature	Structure
Silica	SiO ₂	1.46	1127 °C	
Polymethyl methacrylate (PMMA)	C ₅ H ₈ O ₂	1.49	105 °C	
Polystyrene (PS)	C ₈ H ₈	1.59	100 °C	
CYTOP® (Asahi Glass)	C ₆ F ₇ O	1.34	108 °C	
Teflon-AF® (Dupont)	(C ₂ F ₂) _x (C ₅ F ₈ O ₂) _y	1.29	160 °C	
Perfluoro-cyclobutane (PFCB)	C ₄ F ₆ O ₂ Ar	1.5	350 °C	

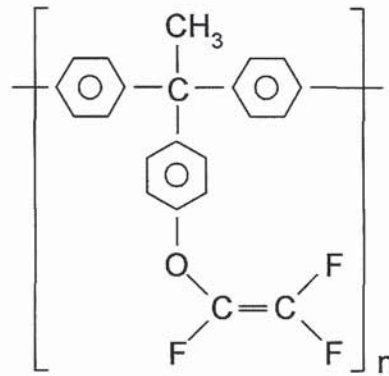


Figure 5-1: aryl group for PFCB (TVE).

Perfluorinated polymers such as CYTOP[®], Teflon-AF[®] and PFCB are becoming of increasing importance because their lower attenuation makes them feasible for short haul telecommunication links. Despite this obvious advantage, the lower refractive index of these polymers makes the choice of cladding material limited in order to maintain a sufficient numerical aperture for coupling light into the fibre. In the future, microstructured polymer optical fibre (mPOF) may provide a solution to this limitation since the air holes create an effective refractive index for the cladding, which is less than that of the core material.

However, Asahi Glass Co. Ltd in partnership with Keio University have designed a successful fibre which is available commercially under the trade name CYTOP[®]. Liu *et al* [117] have investigated inscribing FBGs into slabs of CYTOP[®]; since it proved difficult to inscribe into the core of a multimode fibre constructed of CYTOP[®]. The gratings were inscribed using a frequency tripled Nd:YAG laser emitting at 355 nm. Temperature testing of these gratings revealed minimal thermal decay in reflectivity over 200 minutes with the gratings held at either 45 °C or 60 °C. Similar investigations into PMMA FBGs showed a reduction in the normalised reflectivity from 1 to 0.8 and from 1 to 0.7 when held at 50 °C and 65 °C, respectively, for a duration of 140 minutes [117]. However, the thermal sensitivity of the gratings in CYTOP[®] was reduced to a 9 nm wavelength shift over a temperature range of 60 °C, compared to 18 nm for a grating in PMMA over the same temperature range.

5.3 Free Radical Vinyl Polymerisation

Free radical polymerisation is a standard chemical procedure which creates long molecules (polymer chains) from small molecules (monomers). In order for polymerisation to occur, the monomer has to be exposed to another molecule called an initiator. Typically used initiators are either 2,2'-azo-bis-isobutyronitrile (AIBN) or benzoyl peroxide; see Figure 5-2.

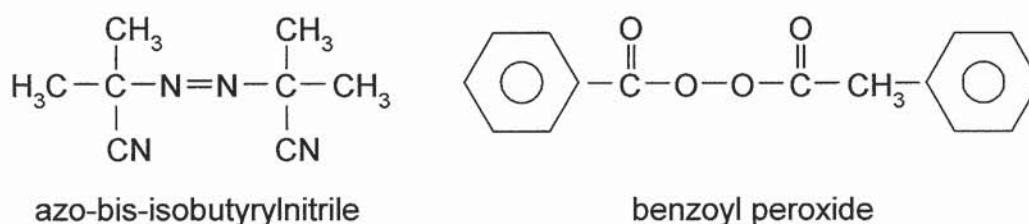


Figure 5-2: Chemical structures of free radical vinyl polymerisation initiators.

Azo-compounds and peroxides are extremely unstable molecules which break up into free radicals (chemical molecules which have a single unpaired electron) with moderate heat. The thermal decomposition of AIBN is shown below in Figure 5-3.

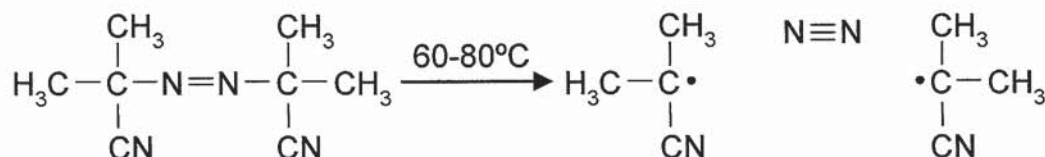


Figure 5-3: Thermal decomposition of AIBN; dots represent unpaired electrons (free radicals).

This reaction is irreversible due to the formation and subsequent escape of nitrogen molecules; which are extremely stable due to the triple covalent bond. The C-N bonds in AIBN thermally cleave resulting in a pair of 2-cyano-2-propyl radicals and nitrogen. The resulting free radicals are unstable due to the unpaired electron so consequently will bond easily with other molecules in order to gain stability. The carbon-carbon double bonds in vinyl monomers are prime examples of easily attained electrons which initiate the polymerisation process, as shown in Figure 5-4.

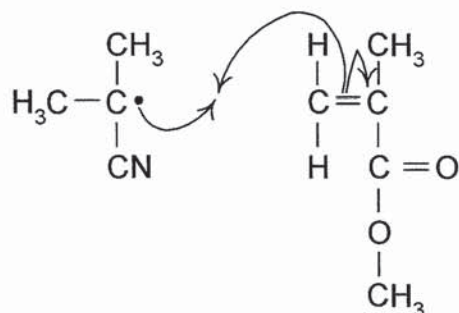


Figure 5-4: Initiation of PMMA; arrows indicate transfer of electrons. Left molecule: 2-cyano-2-propyl radical, Right molecule: methylmethacrylate monomer.

One of the electrons in the carbon-carbon double bond in the monomer joins with the free radical on the 2-cyano-2-propyl molecule. The remaining free radical in the methylmethacrylate molecule moves to the last carbon atom in the chain enabling more monomer to attach to the chain by the same process; see Figure 5-5.

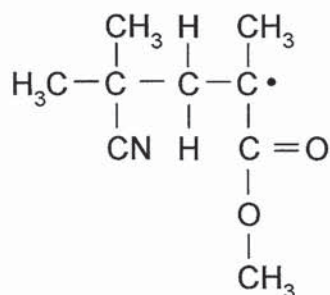


Figure 5-5: Monomer of MMA attaches to the initiator adding another free radical to the end of the chain enabling further molecules to attached to the chain.

Termination of the process occurs if the ends of two growing chains meet, 'coupling', or by a process called disproportionation; instead of bonding with the free radical from another chain, bonding occurs with a hydrogen bond on another growing chain, terminating one chain with a hydrogen atom and the other with a carbon double bond.

5.4 Investigated Polymer Optical Fibres

In this thesis, several different varieties of POF have been investigated for their suitability for FBG inscription. Initially, step index single mode and multimode POF were obtained from the commercial company, Paradigm Optics Incorporated [118]. In addition to this fibre, some POF was acquired through collaborations with other institutions. Single mode

and few mode standard step index fibre was supplied by G.D. Peng from the University of New South Wales in Australia. Microstructured polymer optical fibre (mPOF) was made available by M.C.J. Large of the Optical Fibre Technology Centre (OFTC), also in Australia. A summary of the POFs used in this work, their dimensions and material composition, are shown in Table 5.3.

Table 5.3: Table of the different varieties of POF investigated for FBG inscription. MMA = methylmethacrylate, EMA = ethylmethacrylate, BzMA = benzylmethacrylate.

POF Type	Supplier	Mode Operation	Identity Acronym	Core/Cladding Dimensions, (μm)	Core/Cladding Material
SIPOF	Paradigm Optics Ltd	single mode multimode	SMPOF MMPOF	8/125 60/120	PMMA-PS /PMMA
SIPOF	G. D. Peng, University of New South Wales, Australia	single mode few mode	SMPengPOF FMPengPOF	12/240 18/220	MMA-EMA- BzMA/PMMA
mPOF	M.J. Large, OFTC, University of Sydney, Australia	single mode few mode multimode	SMmPOF FMmPOF MMmPOF	13/150 13/160 50/160	PMMA

As can be seen from Table 5.3, the primary constituent material of the above polymer optical fibres is PMMA. PMMA has been shown to be a photoreactive material from the very first studies conducted in the 1970s [119-121]. Consequently, PMMA based optical fibres were investigated for their suitability for FBG inscription.

The few mode and single mode mPOF incorporated 60 air holes arranged in four hexagonal rings; see Figures 5-20a and 5-20d respectively. The single mode mPOF had hole diameters of $2.7 \mu\text{m}$ with a separation of $8.8 \mu\text{m}$ resulting in the ratio of hole diameter to spacing, d/Λ , being 0.31. This placed the fibre in the endlessly single mode regime; see chapter 4. By contrast, the few mode mPOF had air holes with diameters of $5.5 \mu\text{m}$ with a separation of $10 \mu\text{m}$, giving $d/\Lambda = 0.55$. The multimode mPOF however, had

72 holes of diameter 5 μm and separation of 10 μm arranged in three hexagonal rings; see Figure 5-20b,c.

Detailed descriptions of the fabrication methods of polymer optical fibres are outside the scope of this thesis but if the reader requires information they are directed towards the references [122-125].

5.5 Attenuation

The attenuation in polymer optical fibres is significantly higher than in silica-based optical fibres, resulting in them being impractical for long or medium haul telecommunication links. The various loss mechanisms in polymer and silica based optical fibres are essentially the same, however, the relative contributions of the mechanisms varies between the two. A summary of the loss mechanisms in POF are shown in Table 5.4 [126].

Table 5.4: Loss contributions in polymer optical fibre.

Intrinsic		Extrinsic	
<i>Absorption</i>	<i>Scattering</i>	<i>Absorption</i>	<i>Scattering</i>
Higher Harmonics of CH Absorption	Rayleigh Scattering	Transition Metals	Dust and Microvoids
Electronic Transition		Organic Contaminants	Fluctuation of Core Diameter
			Orientational Birefringence
			Core-Cladding Boundary Imperfections

The intrinsic losses are associated with the polymer optical fibre constituent materials and so comprise the absorption and scattering losses of these materials. The extrinsic losses are artefacts of the manufacturing process of the fibre itself and so can be minimised by careful, optimum design and control of the fabrication conditions. This therefore results in

the major loss contribution in polymer optical fibre coming from the intrinsic losses of the fibre. The intrinsic losses are consequently described in further detail in the following sections.

5.5.1 Absorption of Core Materials

Organic materials such as polymers have numerous high strong absorption bands due to the different chemical bonds within the material. The most influential absorption in the infrared region is associated with the vibrational absorption of the carbon-hydrogen (CH) bonds. This results in polymers such as PMMA and PS having extremely high attenuation at 1550 nm resulting in recoverable data only being capable of transmission through extremely short lengths of fibre. The lowest absorption loss for these polymers is in the visible region of the optical spectrum as shown in Figure 5-6.

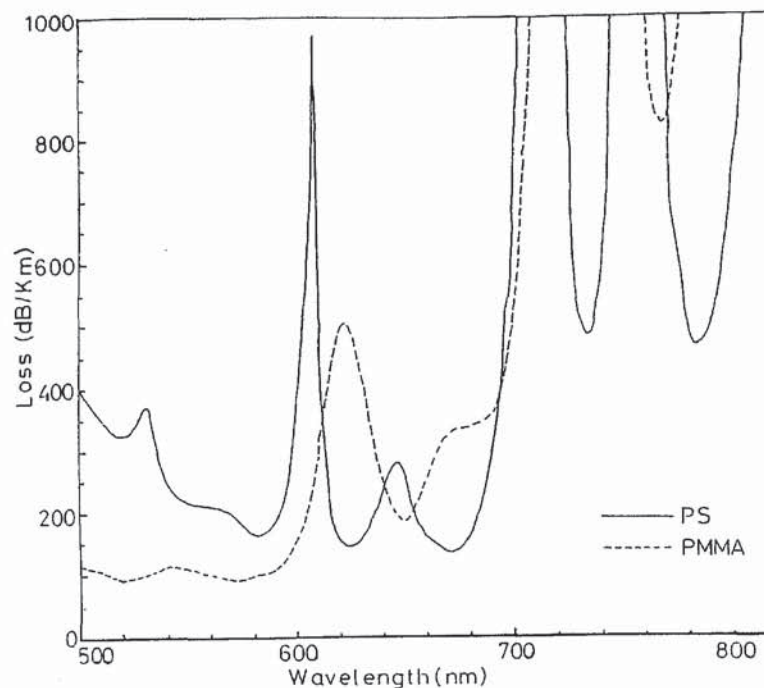


Figure 5-6: Transmission loss for PMMA and PS core polymer optical fibre [126].

In PMMA core optical fibre, the visible spectrum absorption is dominated by the stretching vibrations of the C-H bonds at 544, 622 and 740 nm. The lowest transmission loss of 89 dB/km occurs at 522 and 570 nm. The PS core optical fibre has a higher transmission loss with the lowest value of 114 dB/km at 670 nm.

The high C-H harmonics in PMMA core polymer optical fibres are shown in Figure 5-7. This graph clearly demonstrates the adverse dependence the transmission loss has on increasing wavelength; the loss at 1550 nm approximately equalling 10^6 dB/km.

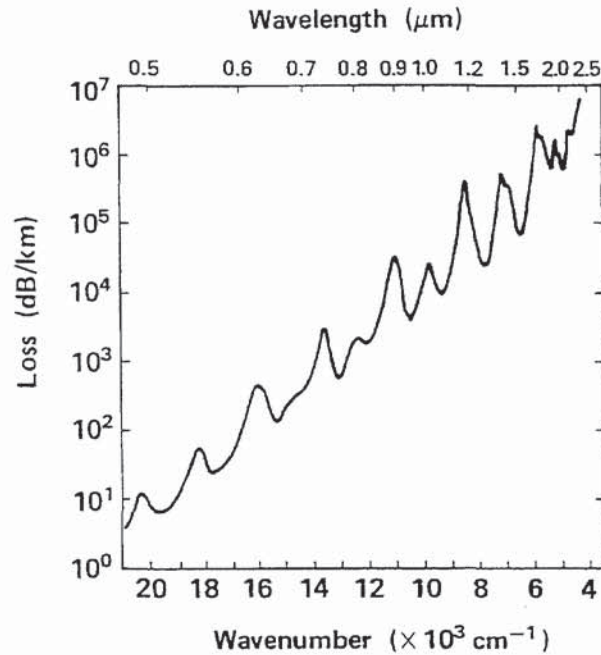


Figure 5-7: C-H harmonics in PMMA core optical fibre [126].

The high attenuation of PMMA based polymer optical fibres in the 1500 nm telecommunications window means that it could never replace medium or long haul communications networks currently consisting of glass optical fibre. Indeed the enormous disadvantage of this high attenuation prompted investigations into polymers not containing hydrogen atoms. Substitution of fluorine atoms for hydrogen atoms have been shown to lower the attenuation in polymer optical fibres [127].

In Figure 5-8, van den Boom *et al* [128] demonstrate that perfluorinated (PF) polymer-based graded index polymer optical fibre has dramatically lower attenuation than PMMA based fibres. This is primarily due to fluorine compounds preventing the penetration of

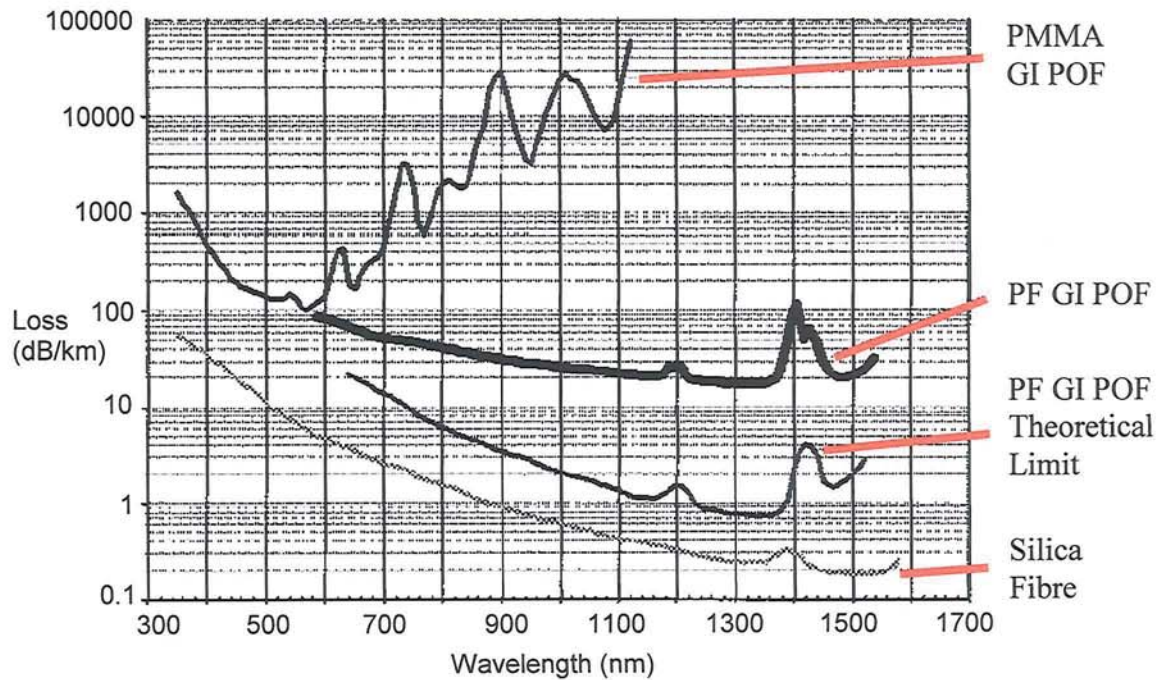


Figure 5-8: Attenuation of several different types of POF for different wavelengths, theoretical and experimental. The attenuation in silica is added for comparison [128].

moisture into the polymer compared with polymers containing hydrogen or deuterium that prolifically absorb moisture [129]. Fluorine also causes the fundamental absorptions to occur at longer wavelengths, ultimately resulting in the intrinsic attenuation loss being primarily due to the Rayleigh scattering.

These factors have served as the impetus behind introducing perfluorinated GI POF into the final stages of the telecommunications network.

5.5.2 Electronic Transition Absorption

Polymers absorb light in the ultraviolet region of the spectrum. The absorption mechanism depends on transitions between electronic energy levels of the bonds within the materials. Although the transitions occur in the UV, the absorption tail extends into the low infra-red.

PMMA core POFs have transitions associated with an $n - \pi^*$ due to an ester group in the MMA molecules, $n - \sigma^*$ of the chain transfer agent and $\pi - \pi^*$ of an azo-group when azo-

components like AIBN are used as polymerisation initiators. The most significant is attributed to the $n - \pi^*$ transition in the double bond of the monomer. In polystyrene core POF the $\pi - \pi^*$ transition within the delocalised bonds of the benzene ring produce extremely high absorption. This results in PS core POF having a higher attenuation contribution from the electronic transition than the PMMA-core POF [126].

5.5.3 Rayleigh Scattering

This particular intrinsic loss is caused by structural irregularities within the core of an optical fibre. It is predominantly caused by fluctuations in the material density and composition. Consequently, Rayleigh scattering in fully polymerised material is attributed mainly to material density whilst scattering in partially polymerised materials is from the material composition. When the density fluctuations are small in comparison with the incident wavelength, Rayleigh scattering dominates the attenuation of the fibre. The attenuation of the fibre attributed to Rayleigh scattering is conventionally given by [46]:

$$\gamma_R = \frac{8\pi^3}{3\lambda^4} n^8 \rho^2 \beta (kT_f), \quad (5.1)$$

where n is the refractive index, ρ is the photoelastic constant, β is the isothermal compressibility, k is the Boltzmann constant and T_f is the fictive temperature of the material (the temperature at which the material reaches thermal equilibrium on cooling down). Although equation (5.1) is only valid for single component systems (e.g SiO₂), it can be applied to macromolecules and inorganic multicomponent glasses if the local dielectric fluctuations remain small when compared to the wavelength.

Ballato *et al* [130] calculated the Rayleigh scattering for various polymers and found them all to have lower Rayleigh scattering than silica; see Figure 5-9. From equation (5.1) and Table 5.2 it can be seen that this is primarily due to the lower glass transition temperatures of the polymers which are typically an order of magnitude less than silica.

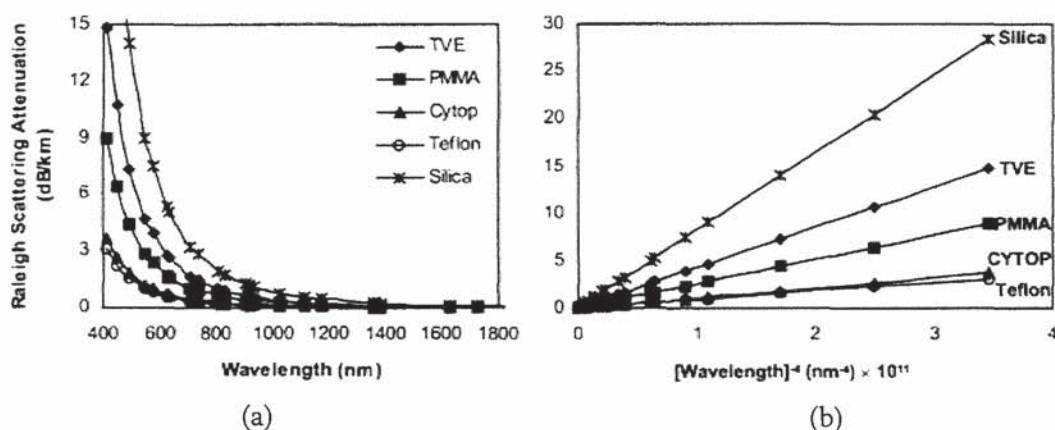


Figure 5-9: (a) Attenuation due to Rayleigh scattering in PFCB (TVE), PMMA, Cytop, Teflon and Silica. (b) Attenuation due to Rayleigh scattering linearised to $(1/\lambda^4)$ abscissa [130].

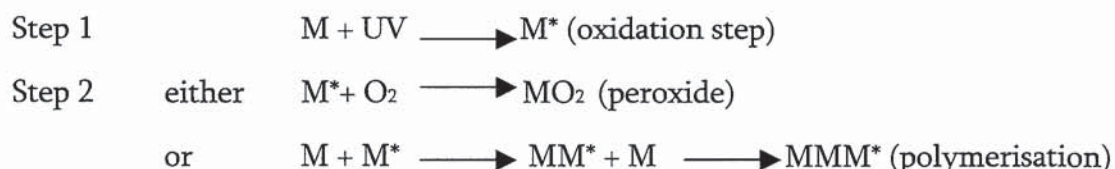
5.6 Photosensitivity in PMMA based Optical Fibres

Considerable research has been conducted investigating the photosensitivity of PMMA. This section aims to provide an overview to some of the different inscription wavelengths investigated and their effect on the material.

5.6.1 UV irradiation at 325 nm

The first studies of photosensitivity or photoreactivity in PMMA based polymers were conducted over 30 years ago by Tomlinson [119], Moran [120] and Bowden [121]. These investigations were directed to inscribing gratings or waveguides into polymer slabs. Tomlinson *et al* [119] were the first to report that when prepared PMMA is exposed to UV radiation of 325 nm, supplied from an helium cadmium (HeCd) laser, a significant increase in refractive index of the exposed region can be achieved. However to create the change in refractive index through UV exposure, essential pre-processing of the PMMA samples had to take place. This involved peroxidation of the monomer methylmethacrylate, (MMA) prior to the polymerisation step. This pre-processing was done by stirring the MMA in an oxygen atmosphere for 48 hours whilst irradiating the sample with UV light from a 5W low pressure mercury (Hg) lamp. PMMA which has not undergone this oxidation step before polymerisation shows no increase in refractive index when exposed to UV radiation indicating that it is the presence of oxidation products

which is the essential requirement for the photoreactive effects to take place. Monomer prepared without the presence of oxygen completely polymerises, demonstrating that the oxygen is acting as an inhibitor to the polymerisation by the formation of unreactive peroxides [131]. The reactions are shown below.



where M is the unreactive monomer and M* the free radical monomer.

It has been demonstrated [119] that, after the pre-processing step of the monomer and consequently polymerisation using the initiator azo-bis-isobutyronitrile (50-200mg/litre) at 40 °C, refractive index changes of 3×10^{-3} could be induced by exposure to UV light.

There are two ways in which the refractive index of a material can be changed; either the density of the material can be altered or the molecular polarisability can be changed (or a combination of both). Tomlinson *et al* [119] found the origin of the refractive index change to be attributed to an increase in the density of the material, with densities of 0.8% greater than unirradiated samples of PMMA. This has also been verified by Bowden *et al* [121], who confirmed the density changes by using a bath of calcium nitrate, $\text{Ca}(\text{NO}_3)_2$. The concentration of the bath was adjusted to ensure that an unirradiated sample would just float at the surface. Irradiated samples placed in the calibrated bath sank to the bottom demonstrating clearly a change in density. Unirradiated samples which have been heated to 100 °C also showed the same increase in density, thus heating also causes the active component to create the density change. However, samples which had not been prepared from the preoxidised monomer, which demonstrates no sensitivity to irradiation by a HeCd laser, also showed an increase in density after annealing. This demonstrates that the mechanism for the density increase by irradiation is not necessarily the same as attained by heating the samples. Recently, Hiscocks *et al* [132] have

demonstrated that permanent long period gratings can be fabricated in microstructured POF by thermal imprinting. Consequently, although refractive index changes are observed through irradiation by 325 nm light the exact mechanism behind the change is not confirmed.

5.6.2 Effect of other UV wavelengths on PMMA

Modifications to the optical properties of PMMA have also been investigated using a pulsed UV excimer laser at output wavelengths of 193 nm and 248 nm [133]. The different wavelengths resulted in different photochemical effects. Irradiation by 248 nm at a relatively low fluence (15 mJcm^{-2}) resulted in a free methyl formate radical being formed demonstrating that complete side chain scission from the main polymer chain is occurring; see Figure 5-10.

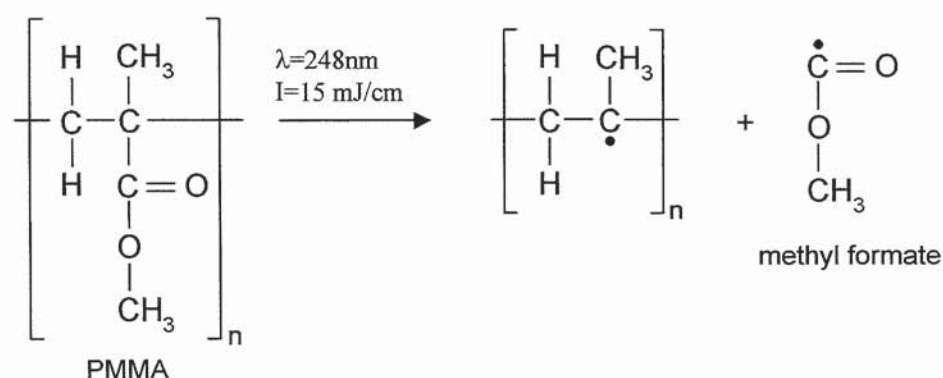


Figure 5-10: Reaction showing complete side chain scission by exposure to 248 nm radiation at 15 mJcm^{-2} .

Continuous irradiation at a high fluence, 30 mJcm^{-2} or greater, degrades the free ester radical either into methane and carbon dioxide or methanol and carbon monoxide; see Figure 5-11.

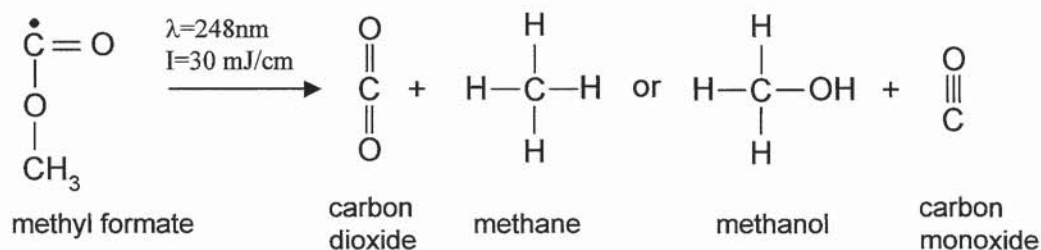


Figure 5-11: Reaction showing further degradation of the free ester radical to continuous exposure to 248 nm at a fluence of 30 mJcm⁻².

The formation of the free radical in the main polymer chain destabilises the chain, which during prolonged exposures, results in scission of the main polymer chain; see Figure 5-12.

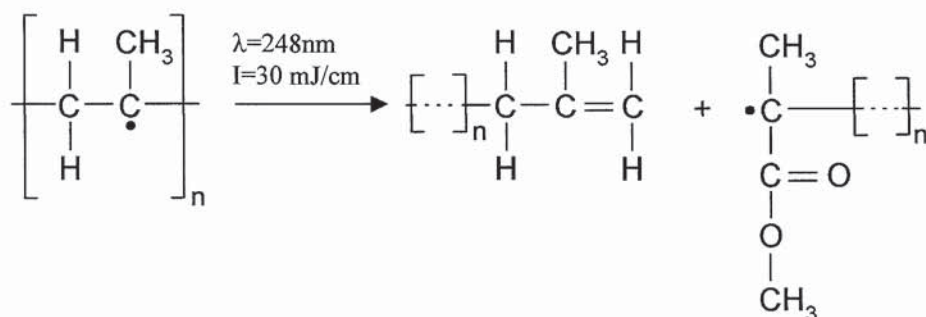


Figure 5-12: Main polymer chain scission due to prolonged exposure of 248nm radiation.

In comparison, irradiation by 193 nm UV radiation only causes partial side chain scission resulting in free methanol radicals; see Figure 5-13.

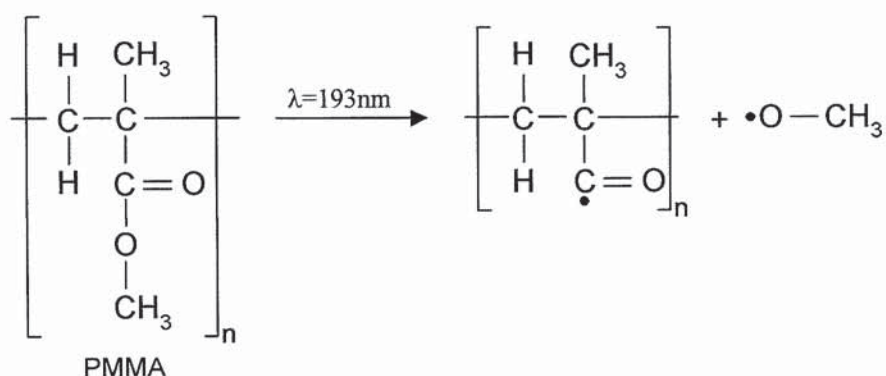


Figure 5-13: Reaction showing partial side chain scission by exposure to 193 nm radiation.

Both 193 nm and 248 nm, exposed samples experienced an increase in the refractive index as a result of the partial or total side chain scission. This change occurs through an

increase in mechanical density via volume contraction by Van der Waals interactions [42]. The maximum refractive index change of 0.01 occurred as a result of exposure to 248 nm at a fluence of 17 mJcm^{-2} . The refractive index changes through exposure to 193 nm were less than those achieved with 248 nm since the partial side chain scission results in weaker volume contraction.

Despite the ability to create refractive index changes using 248 nm and 193 nm the penetration depth in PMMA at both wavelengths is less than $10 \mu\text{m}$. For standard optical fibre geometries the distance to the core of the optical fibre is $62.5 \mu\text{m}$ making these wavelengths impractical for grating inscription in the core. Srinivasan *et al* [134] investigated the UV absorption of PMMA and the results are shown in Figure 5-14. It clearly demonstrates that 193 nm and 248 nm are impractical for inscription into PMMA-based optical fibres whereas the absorption for 325 nm is, comparatively, very low.

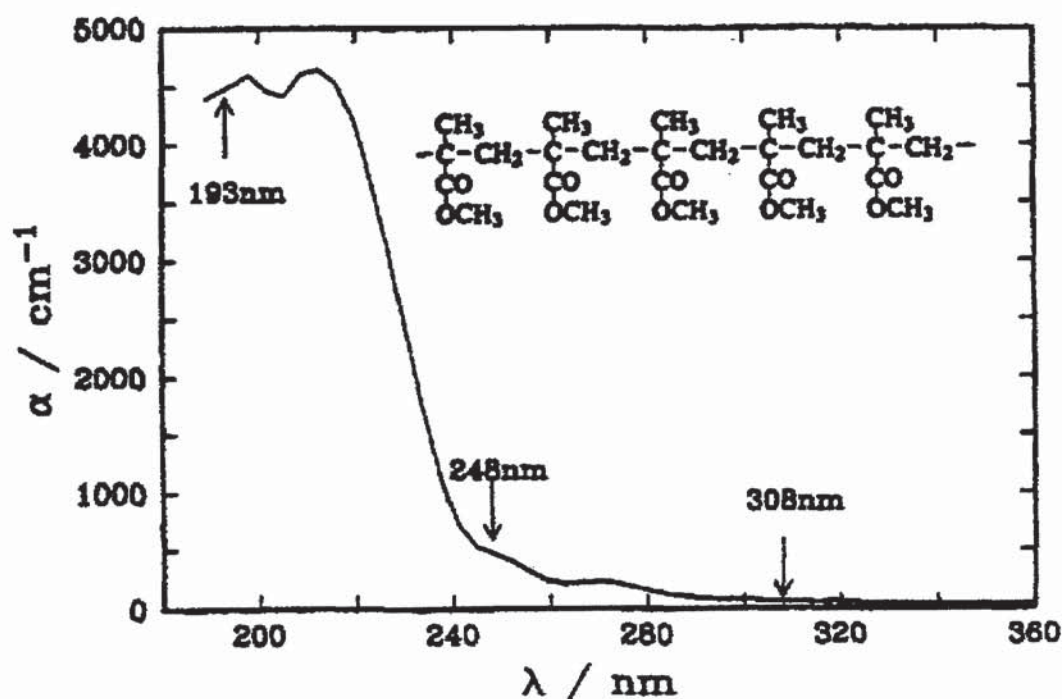


Figure 5-14: UV absorption spectrum of PMMA. Arrows correspond to the wavelengths of the emission lines from an excimer laser [134].

5.6.3 Femtosecond Laser Irradiation

Femtosecond lasers have been used to process polymeric materials by focusing the laser beam inside a substrate. Since the beam comprises of very short laser pulses, when the beam is focused the intensity at the focal point becomes extremely high. This in turn induces nonlinear effects like multi-photon absorption, which modify the polymeric material creating a change in the refractive index. Femtosecond lasers typically emit radiation in the near infrared, where the absorption in polymer is negligible compared with UV sources and operate at photon energies far below the bandgap energy of the processing material. These facts allow processing within a polymeric material without ablation occurring at the surface of the material due to absorption of the incident radiation. This enables devices such as waveguides, three-dimensional structures and grating structures to be fabricated within the polymer.

Waveguides

Zoubir *et al* [135] have demonstrated that tubular waveguides of 25 μm diameter cross section and a guiding region of 5 μm can be fabricated inside a 25 mm slab of PMMA using a Ti:sapphire laser with a repetition rate of 25 MHz, that produces 20 nJ pulses of 30 fs duration. Refractive-index profiles of this type have been shown to be used for optically trapping and manipulating micrometer-sized particles [136].

Three-Dimensional Structures

With increasing speed and miniaturisation of modern day computer components and devices, the requirement for high data storage in a small area is becoming of increasing importance. Three-dimensional (3D) optical data storage has the ability to increase the data stored capacity of a particular area. Recently, this has been demonstrated in transparent materials by using femtosecond lasers to create refractive index changes, photoreduction and void creation [137-139].

The ability to produce this effect in PMMA based polymers has been demonstrated by Jiu *et al* [140]. They used $\text{Sm}(\text{DBM})_3$ phen-doped PMMA and a 800 nm Ti:sapphire laser which emitted 200 fs pulses at a 1 kHz repetition rate with an average power of 800 mW. Using the laser, voids were created in the material each from a single laser pulse of energy 14.5 nJ. The laser pulse causes microexplosions to occur within the material at the focal point of a 0.65 NA microscope objective. The ability to create voids at different locations within the material allows a 3D storage pattern to be fabricated. The data can be retrieved by illuminating the altered regions with radiation from a 514.5 nm laser. This causes the regions to fluoresce, the result of which can be interrogated using a laser-scanning fluorescence microscope.

Grating Structures

Femtosecond lasers have also been used to create gratings inside bulk polymeric materials [141-144]. Si *et al* [141] were the first to demonstrate gratings fabrication inside bulk azodye doped PMMA using a holographic set up and a femtosecond laser. However, as well as the volume grating inside the bulk material, two surface relief gratings were also fabricated, one on the top surface of the material with the other on the bottom surface. Li *et al* [142] found that ablation occurred at the surface of a block of un-doped PMMA if the energy in a single beam was higher than 180 μJ . Consequently, they were able to successfully fabricate gratings inside the block of PMMA with no by-product surface relief gratings, provided the two laser interference beams contained between 60-100 μJ each.

Recently, studies have been conducted by Wochnowski *et al* into the effect of femtosecond laser radiation on other inexpensive and industrially wide spread polymers and compared with the more familiar PMMA [144]. They fabricated surface gratings and volume gratings in PMMA, fluorinated PMMA, PMMI (poly-N-methacrylimide), PC (Polycarbonate), PI (Polyimide) and Polysiloxane. They discovered that the volume gratings fabricated inside PMMA had extremely low diffraction efficiencies and were the worst of the investigated polymers. Volume gratings in PMMI had the best performance

over both fluorinated PMMA and PMMA. The highest overall diffraction efficiency was attained by volume gratings in polysiloxane with the remaining aromatic polymers having lower efficiencies than PMMI but higher than the fluorinated PMMA volume gratings.

5.7 Cleaving

In order to observe grating structures inscribed into POF, sufficient quantities of light need to be coupled into the fibre. Consequently, the fibre end has to be perfectly flat to minimise scattering from the end face. To achieve this in silica-based optical fibres commercially available cleavers are used. These operate by scratching the fibre with a diamond blade. Strain is then applied on the fibre which propagates a fracture perpendicular to the longitudinal axis of the fibre, originating from the scratch. Polymers however, are constructed of long chains of molecules, which vary in length and can be randomly aligned. Consequently, commercial cleavers are ineffective on polymer optical fibres. Due to the high attenuation in these fibres, it is important to couple as much light as possible into the fibre. Therefore, techniques for successfully cleaving POF had to be investigated.

5.7.1 Razor Blade

The first method investigated used a razor blade (Wilkinson Sword classic twin edge) to slice through the POF. The razor blade was heated to between 60-70 °C to aid propagation of the blade through the fibre. The polymer optical fibre was laid flat under no tension on an optical table. The cleaving result on SMPOF was inspected using a microscope (Zeiss Axioskop 2 mot plus) and can be seen in Figures 5-15.

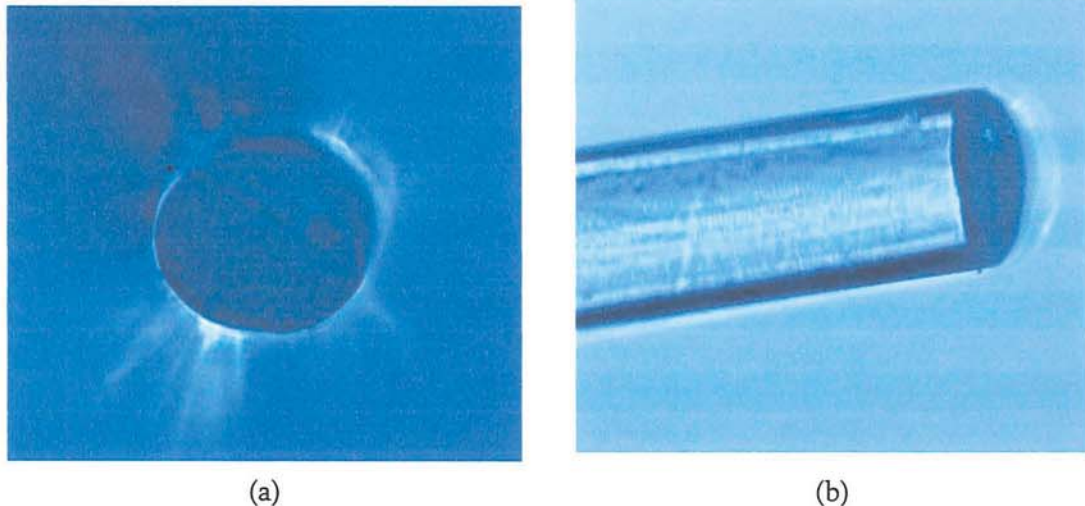


Figure 5-15: Cleaved SMPOF using a hot razor blade; images captured with $\times 20$ objective: a) end face on, b) end side.

These pictures demonstrate that a sufficiently flat and smooth end face is unachievable on this fibre using this technique. The process was repeated, firstly with a razor blade at room temperature and then with a heated razor blade, on the FWPengPOF; the result can be seen in Figure 5-16.

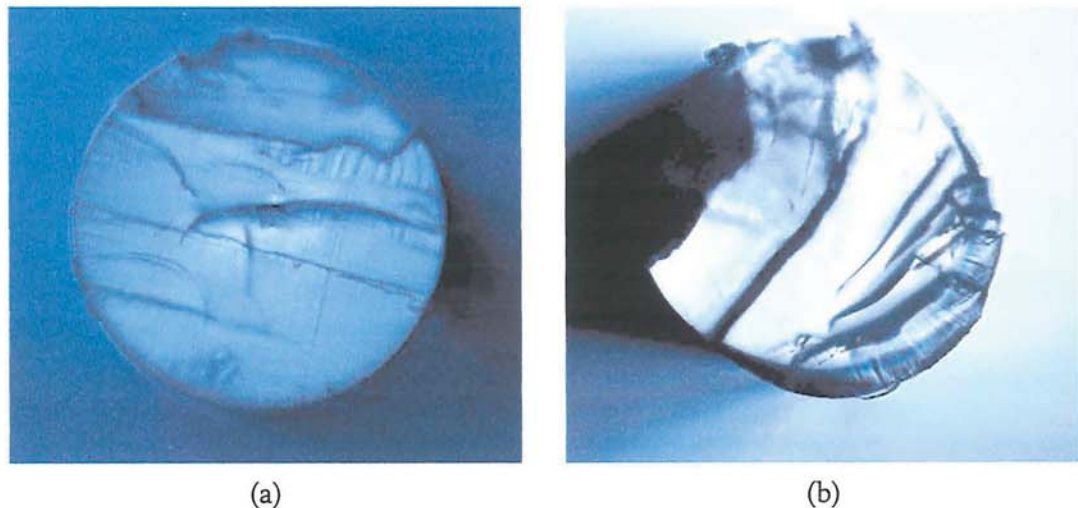


Figure 5-16: Cleaving FWPengPOF using a razor blade; images captured with $\times 20$ objective: a) razor blade at room temperature, b) heated razor blade.

Figure 5-15 shows that both the conditions cause layers of polymer to be pushed over each other and more importantly the core region. It also illustrates that the heated razor blade actually melted the fibre. Both attempts show ridges in the end face of the fibre.

The unsatisfactory results of using purely the razor blade to cleave the polymer optical fibres meant that another technique to prepare the ends of the fibres was needed.

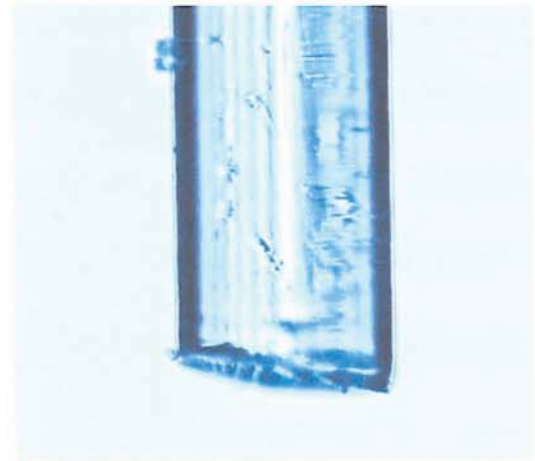
5.7.2 Liquid Nitrogen and Razor Blade

The next investigations were conducted using liquid nitrogen, which has a temperature of -40°C . It was hoped that this would be of a sufficiently low temperature for the polymer to become more brittle and cleave in a similar way to silica.

The liquid nitrogen was carefully dispensed into a thermos flask and poured over the POF. The POF was then cleaved using a razor blade at room temperature. The results can be seen in Figures 5-17 and 5-18, for the two different step index POFs.



(a)



(b)

Figure 5-17: Cleaving SMPOF using liquid nitrogen and a razor blade at room temperature; images captured with $\times 20$ objective: a) end face, b) end side on.



Figure 5-18: Cleaving FMPengPOF using liquid nitrogen and a razor blade; image captured with $\times 20$ objective.

There was no significant improvement in the end faces of the POF using this technique.

A further complication was encountered with the preparation of end face of the fibre supplied by G.D. Peng. After cleaving, the fibre started to loose its integrity and fray apart; see Figure 5-19.



Figure 5-19: Fraying observed with the FMPengPOF over time after cleaving; image taken with $\times 20$ objective.

This particular effect is prevalent in unannealed plastic optical fibres and is symptomatic of fibres with a high degree of chain alignment [124], which can occur if a fibre has been drawn under too high tension. Whilst annealing the fibre reduces this effect, it also reduces the Young's modulus and tensile strength of the fibre; ductility is however, increased.

A technique had to be found which not only produced a flat end face but also reduced or eliminated the post processing loss of fibre cohesion. Consequently, polishing the end face of the fibre was investigated.

5.7.3 Polishing

In order to polish the fibre end faces whilst maintaining the fibre integrity, the ends of the fibre were embedded into metal capillaries. The metal capillaries were purchased from Cooper's Needle Works Ltd, with a length of 1 cm, an inner diameter of 254 μm and outer diameter of 1590 μm . The POF was fixed in place using Norland Optical Adhesive (NOA) No 81, which is designed to precisely bond optical components including polymers. Once the epoxy was fully cured using UV radiation, the end of the POF was polished using aluminium oxide lapping film of various different abrasives sizes. Films 5 μm , 1 μm , 0.1 μm and 0.05 μm were used in this order. The polishing had to be done extremely slowly and lightly to minimise any heat build up which could adversely affect the polishing result. The polishing was also implemented using a figure of eight pattern on the films to ensure an even polish over the whole surface and reduce directionality of any surface marks. The result can be seen in Figure 5-20, where a very flat smooth end face results from this method.

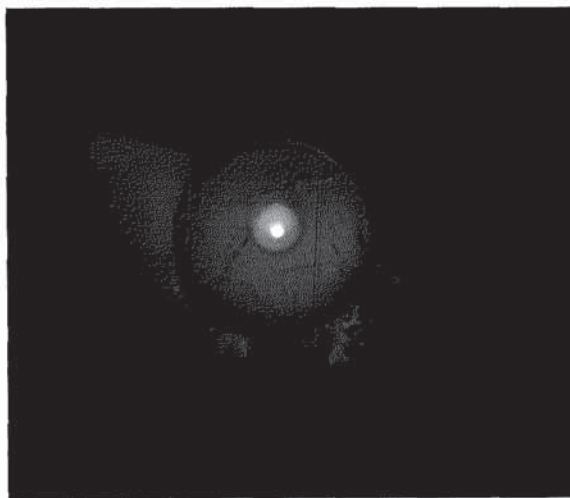


Figure 5-20: Polished end of FWPengPOF mounted in a metal capillary, image taken with $\times 20$ objective.

The figure demonstrates that the result is good enough for the short length of fibre to transmit light from the microscope; the bright spot indicating the core of the fibre. Figure 5-20, also demonstrates the core to be non concentric. Since the POF was embedded in epoxy, which in turn was inside a metal capillary, the fibre did not fray apart.

This preparation method was tested on the microstructured POF. However, the technique was unsuccessful. The polishing process pushes residue from the technique up into the holes. Since the holes are then filled with a material of a very similar refractive index to the polymer, the condition for light guiding is dramatically reduced and insufficient light can be transmitted through the fibre.

5.7.4 Microstructured POF

A different technique needed to be found to prepare the end of microstructured polymer optical fibre. Therefore the razor blade approach was attempted with this fibre and proved to be more effective than with the step index POF. Whilst working with this fibre, Aston's collaboration partners at the OFTC in Sydney in conjunction with the University of Auckland, found an even more successful method of cleaving this particular fibre type. They found that the fibre and razor blade needed to be heated to between 65-85 °C for the best cleave to occur [145]. This is due to a brittle-to-ductile transition which can occur around 50 °C; a temperature well below the glass transition temperature of 105 °C [146]. Kusy [147] also showed that the brittleness of bulk PMMA is strongly dependant on its viscosity molecular mass, M_v , with brittle behaviour occurring for $M_v < 10^4$ and ductile behaviour occurring for $M_v > 10^5$. As the temperature of a material increases the viscosity molecular mass increases, changing it from the brittle material to the ductile regime. This behaviour has been reported as evidence of a phase transition.

Reproduction of the results by Law *et al* [145] using a hot plate set to a variety of temperatures also verified this technique to be the most efficient for end preparation for microstructured polymer optical fibre; see Figure 5-21.

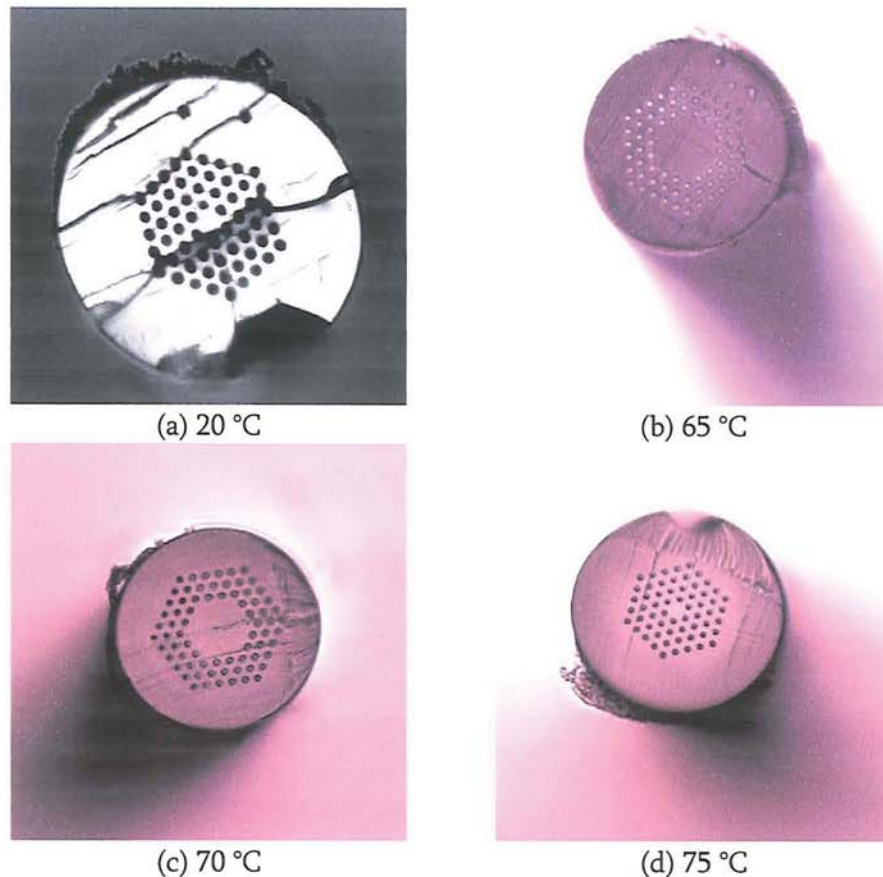


Figure 5-21: Cleaved ends of microstructured POF by heating the fibre and razor blade to various temperatures; images taken using $\times 20$ objective.

These fibres did not fray apart after cleaving indicating that they had been drawn under a lower tension than the fibre supplied by G.D. Peng.

5.8 Light Transmission Through Polymer Optical Fibre

Due to the large attenuation of the investigated POFs, different light sources had to be investigated for their suitability and successful transmission through sections of POF.

An AFC/PC pigtail was butted up against the launch end of the polymer optical fibre with a small amount of index matching gel to reduce the Fresnel reflections from the end and aid coupling into the POF. Initially, a helium neon (HeNe) laser with an output of 15 mW at a wavelength of 633 nm was used to couple light in the fibre. This was used to enable visual verification that the light was in the core of the fibre. The attenuation of the polymer at this wavelength is also low, maximising throughput. An SMF patchcord, butt-

coupled to the other end of the POF, was used to monitor the transmission through the POF on an optical spectrum analyser (OSA). The resulting HeNe transmission for the step index POFs can be seen in Figure 5-22.

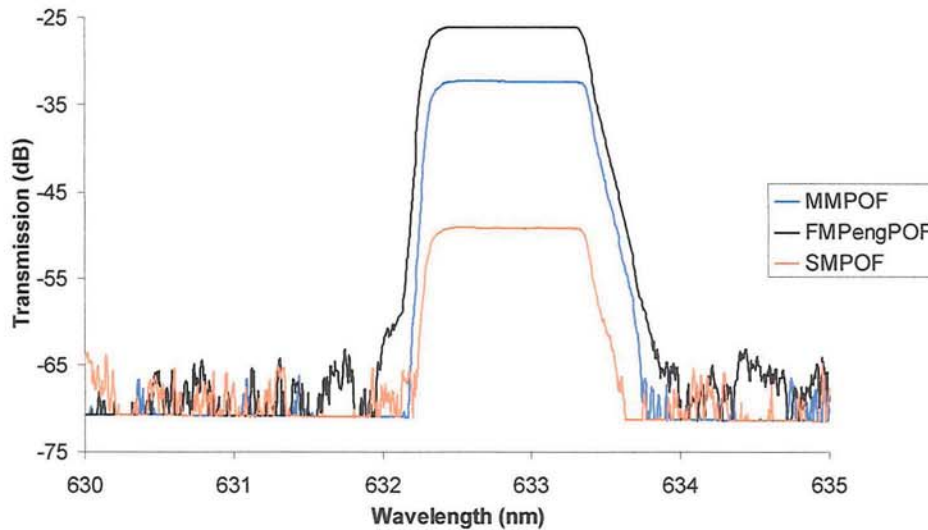


Figure 5-22: HeNe light source through step-index POF; OSA resolution 1 nm.

In order to measure an FBG fabricated in the 1550 nm telecommunications window, a suitable light source had to be used that would have sufficient light transmission through the POF in this higher attenuation region. The first source investigated was an Agilent broadband source (BBS) 83437A which covers the wavelength range of 1150 nm to 1700 nm and consists of four edge-emitting light emitting diodes (1200 nm/-17 dBm, 1310 nm/-13 dBm, 1550 nm/-13 dBm, 1650 nm/-17 dBm). The resulting light transmission of this source through the POFs is shown in Figure 5-23. Although there is some transmission around the 1550 nm wavelength, it is of insufficient quantity and range to observe any FBGs fabricated in this region.

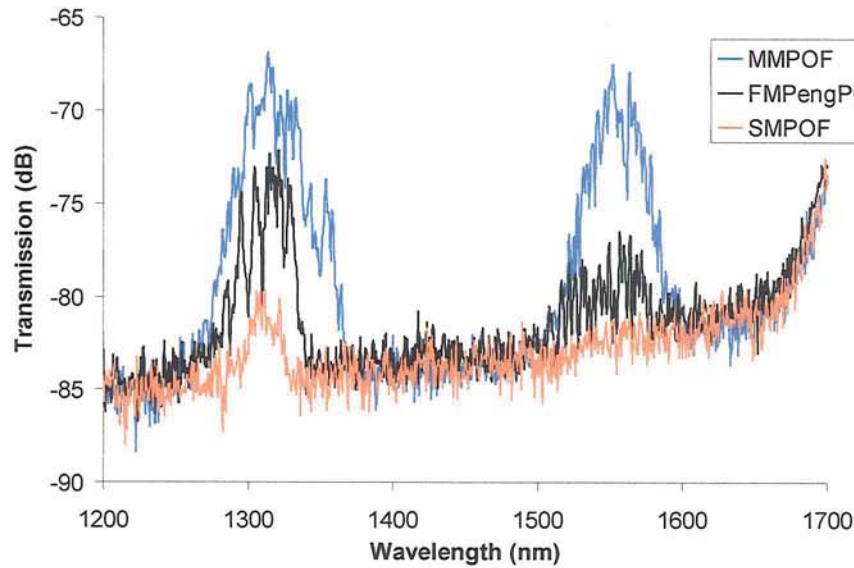


Figure 5-23: Agilent BBS source through step index POF.

The next source investigated was an ASE light source (Thorlabs ASE-FL7002-C4, 5 mW output power) with an operating wavelength range of 1530-1610 nm. The results from this source can be observed in Figure 5-24. Reasonable transmission is seen with this source and was deemed acceptable for grating inscription at these wavelengths.

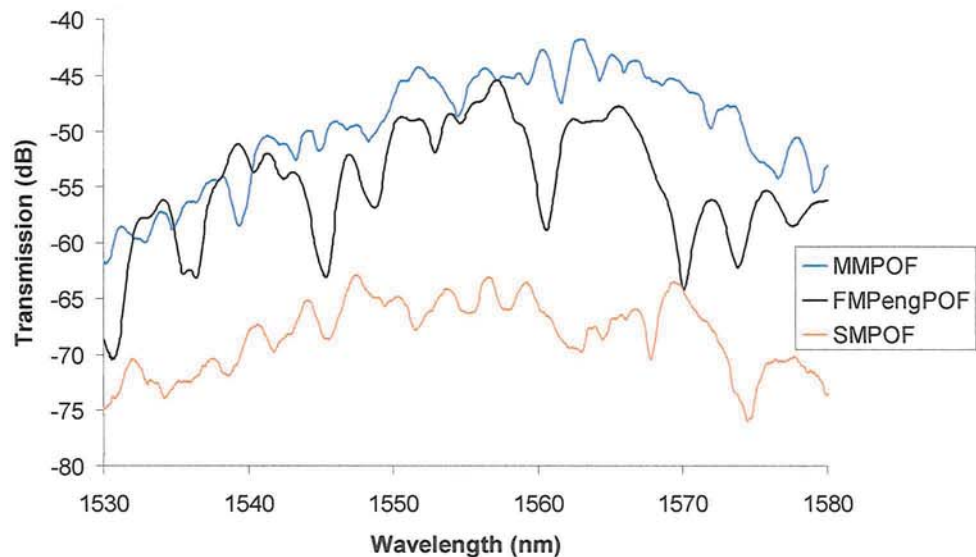


Figure 5-24: ASE light source through step index POF.

The structure observed in the all the spectrum in Figure 5-24, is most likely due to cladding modes, excited during the initial launch conditions, which have not been lost from the fibre due to the short lengths of fibre, 11.4 cm.

5.8.1 Microstructured POF

All the microstructured POF investigated in this thesis also showed good transmission of the Thorlabs ASE light source, enabling FBG fabrication attempts in this fibre; see Figure 5-25 for the transmission through the single mode mPOF.

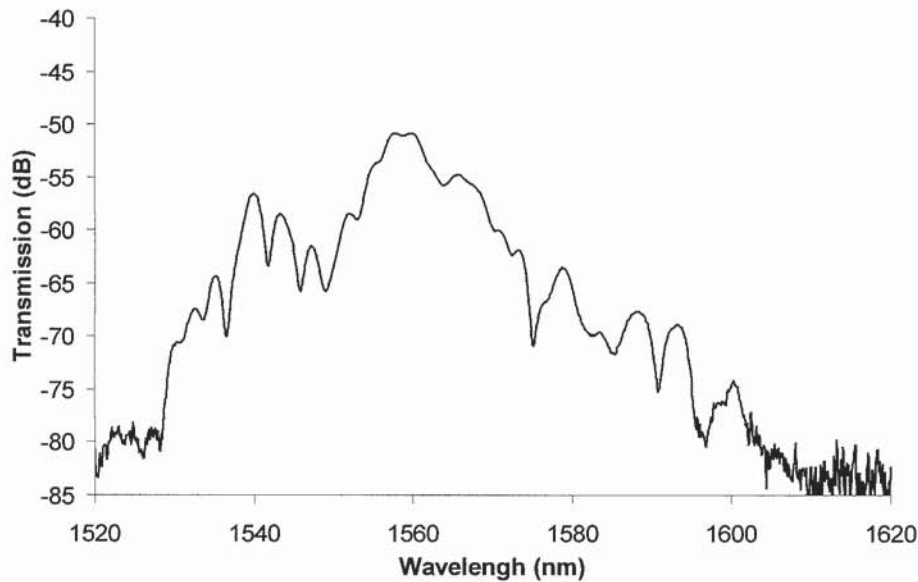


Figure 5-25: ASE light transmission through single mode mPOF.

The graph clearly shows that there is more light transmission through the single mode mPOF with a maximum of 35 dB signal above the noise floor than there was through the single mode step index paradigm POF shown in Figure 5-24, which had a maximum of 20 dB above the noise floor. However, the launching conditions were slightly different for this variety of POF. With the AFC/PC connector a millimetre from the end of the POF, changes in coupling HeNe light into the mPOF, caused changes in the far field pattern emitting from the other POF fibre end. Certain launching positions enabled the light to travel through the holey region of the fibre [113] stimulating the cladding modes instead of the core mode. This demonstrated itself by a 'doughnut' shape in the output pattern of light from the fibre. The centre was dark indicating that no light was in the core region. When the light was in the core a small bright spot is seen; see Figure 5-26 for a schematic representation.

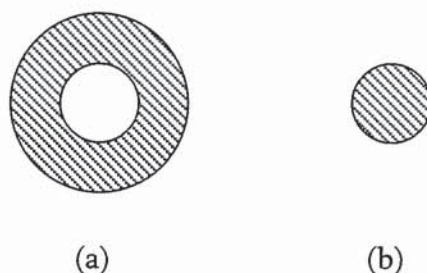


Figure 5-26: Schematic representation of the pattern of HeNe laser light through mPOF; shaded region represents area of greatest intensity. (a): Light transmitting through the holey region, (b): Light in the fibre core.

In order to see an FBG in the core of the mPOF, pattern (b) in Figure 5-26 is required. However, once the index matching gel on the end of the AFC/PC connector touched the fibre end, the ‘doughnut’ pattern could no longer be observed. This removed the ability to know if the light was in the core or the holey (cladding) region. Consequently, it was essential to align the fibre to achieve pattern (b) just before the gel touched the fibre, to ensure coupling in the core region of the fibre. It was important not to use too much index matching gel since it was found to enter the holes via capillary action removing the light guiding conditions of the fibre.

5.9 Summary

An introduction to polymer optical fibre has been presented. Typical polymers for optical fibre manufacture have been discussed along with the loss mechanisms within the fibre which limit its use at higher wavelength ranges. The mechanisms for photopolymerisation by different wavelengths of ultra-violet radiation have been described with the aim of understanding the process of fibre Bragg grating inscription. This demonstrated that, for successful fibre Bragg grating inscription in polymer optical fibre, a laser with an output wavelength of 325 nm was required. Importantly, practical techniques for cleaving and fibre end preparation for successful light transmission have been shown. It was found that step index polymer optical fibre requires the ends of the fibre to be mounted into metal capillaries and then polished to produce an acceptable end face. This technique was unsuccessful with microstructured polymer optical fibre due to the residue from the polishing process being pushed up into the holes. Instead, the microstructured polymer

optical fibre was found to require heating to between 65-80 °C and the end cut using a razor blade heated to the same temperature as the fibre. Finally, techniques for light transmission through polymer optical fibres and suitable light sources were discussed.

6

Fibre Bragg Grating Inscription in Plastic Optical Fibres

Described in this chapter are various attempted fabrication set ups for fibre Bragg grating inscription in polymer optical fibres. Fibre Bragg gratings are inscribed in step index polymer optical fibre and, for the first time, in microstructured polymer optical fibre.

6.1 FBG Fabrication

This section describes various attempted fabrication set ups for FBG inscription in POF. The most suitable ultraviolet (UV) wavelength to achieve fabrication is 325 nm (see section 5.6). Consequently, a Kimmon IK series (IK3301R-G) helium cadmium (HeCd) laser which emits at 325 nm was used. This laser had a continuous wave output, a rated output power of 30 mW, a beam diameter ($1/e^2$) of 1.2 mm and its transverse mode was TEM₀₀ providing the laser with a Gaussian beam profile.

6.1.1 Amplitude-Division Interferometry

Amplitude-Division Interferometry is an extremely versatile technique which enables any Bragg wavelength to be inscribed, provided the diffraction limit of the inscription wavelength ($\lambda/2$) is not exceeded, by changing the convergence angle of the intersecting laser beams; see section 2.5.1.1. This allows inscription of Bragg gratings at lower

wavelengths where the attenuation of POF is significantly lower; see section 5.5.1. However, one major system limitation of this technique is its susceptibility to vibrations and drift. A Mach-Zehnder Interferometer was set up to investigate the presence of any system vibrations that could limit the effectiveness of this technique. The set up is shown in Figure 6-1.

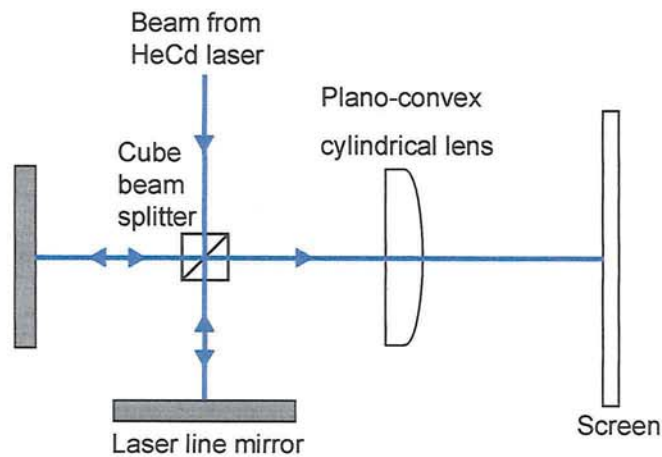


Figure 6-1: Schematic of Mach-Zehnder Interferometer setup.

To reduce as many mechanical vibrations as possible, the optical table was floated. The temporal coherence length of the laser was measured to be greater than 10 cm. Therefore, the maximum likely beam path imbalance of 2 mm could be ignored.

The resulting interference pattern displayed on the white card screen was continuously moving randomly more than a fringe width, demonstrating significant system instabilities. These were likely to originate from a number of different sources. The laser resided on the optical table so vibrations from the laser could be transmitted to the table and mechanical mounts. Secondly, the laser was air-cooled by a fan located on top of the laser which pumps the hot air into the surrounding atmosphere. Since the grating fabrication area was not enclosed by a laser safety cage, the resulting convection currents could cause instabilities in the system. Finally, there could be mechanical instability in the mirror mounts and posts.

The substantial instability indicated that the Amplitude-Division Interferometer inscription technique would be of insufficient stability for grating inscription given the likely exposure times required.

6.1.2 Phase Mask Inscription

Phase mask inscription is less susceptible to system vibrations since the path length of the interference beams is limited to the distance between the phase mask and the optical fibre; typically around 100 μm and the beam path distances are common to the two beams. Despite the restriction in the resulting fibre Bragg grating wavelength decreed by the periodicity of the phase mask, this technique was investigated for its suitability for inscription into POF.

6.1.2.1 Horizontal Alignment

Initially, a standard FBG fabrication set up was implemented, whereby the laser beam is maintained along the axis it emerges from the laser i.e. the horizontal axis; see Figure 6-2.

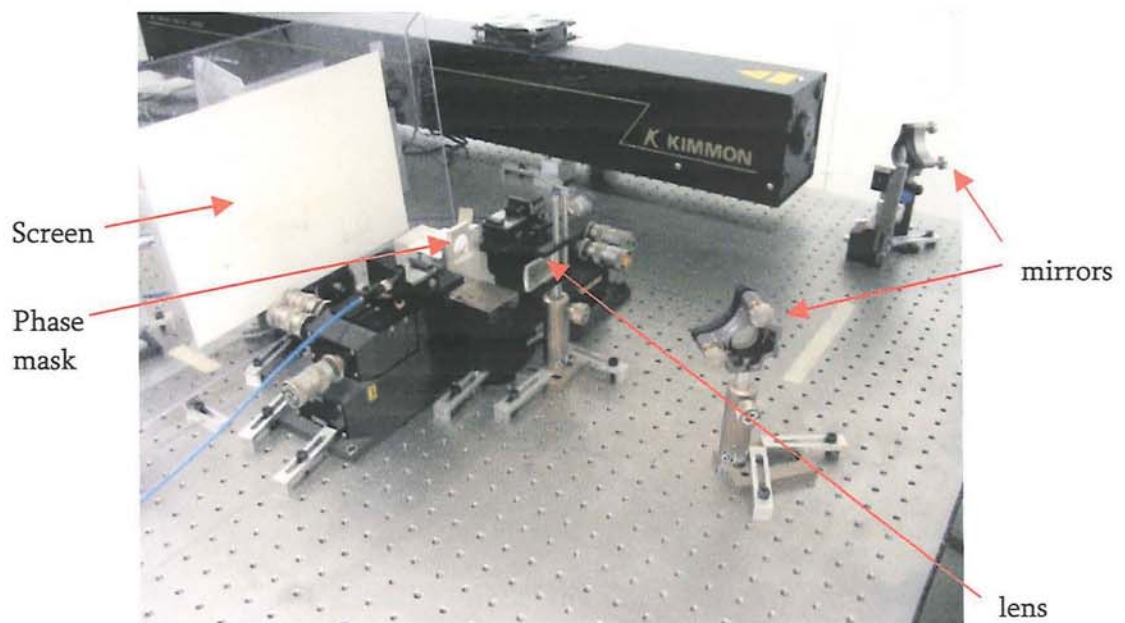


Figure 6-2: Initial fabrication set up for FBG inscription into POF.

Each end of the POF was fixed to a v-groove mounted on a three dimensional translation stage. Due to the high attenuation of POF at higher wavelengths, a phase mask with a

period of $0.5742\ \mu\text{m}$, designed to produce FBGs in silica at around $836\ \text{nm}$ with an inscription wavelength of $248\ \text{nm}$, was used. A superluminescent diode (Superlum, SLD-37-MP) with a central wavelength of $835\ \text{nm}$ and a wavelength range of $50\ \text{nm}$ was coupled into the POFs to measure the grating growth. After exposing a sample for 30 minutes, no fibre Bragg grating was observed. Inspection of the exposed region of fibre using a microscope (Zeiss Axioskop 2 mot plus) did not reveal any refractive index fringes. The absence of fringes was either due to minuscule changes in the fibre position during inscription or beam movement of the interferometer arms from vibrations on the phase mask.

Consequently, a piece of hydrogenated SM-800 silica-based optical fibre (Oxford Electronics Limited), which is designed to have a single mode cut off wavelength of $770\ \text{nm}$, was placed into the fabrication setup to establish if fibre or beam movements were preventing grating inscription. No grating was formed within the $50\ \text{nm}$ bandwidth of the $825\ \text{nm}$ diode. Inspection of the transmission spectrum through the fibre using a white light source revealed the molecular hydrogen associated absorption band at $1245\ \text{nm}$ [55] and the silica-hydroxyl band absorption band at $1390\ \text{nm}$ [55,148] as well as a grating at $1656\ \text{nm}$; see Figure 6-3.

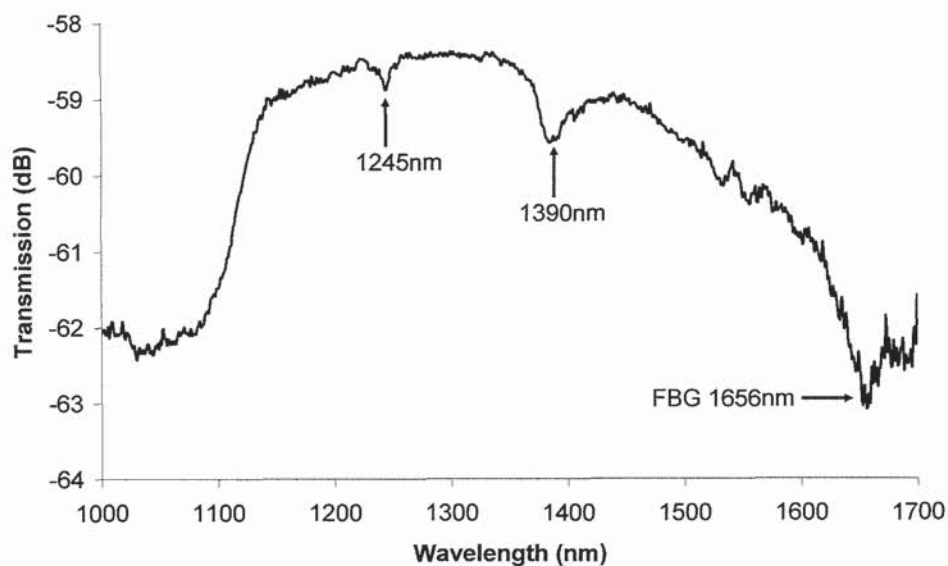


Figure 6-3: Un-normalised absorption spectra of SM-800 after being exposed to $325\ \text{nm}$ radiation.

The grating was located 820 nm away from the design wavelength of 836 nm. The shift in Bragg wavelength was attributed to the diffraction efficiency of the phase mask which for 325 nm radiation contained 33.2 % and 35.6 % respectively in the plus and minus first orders and 17.4 % transmitted power in the zeroth-order. The resulting intensity pattern produced behind the mask is shown in Figure 6-4 and has been calculated from the equations shown in section 2.5.1.2.

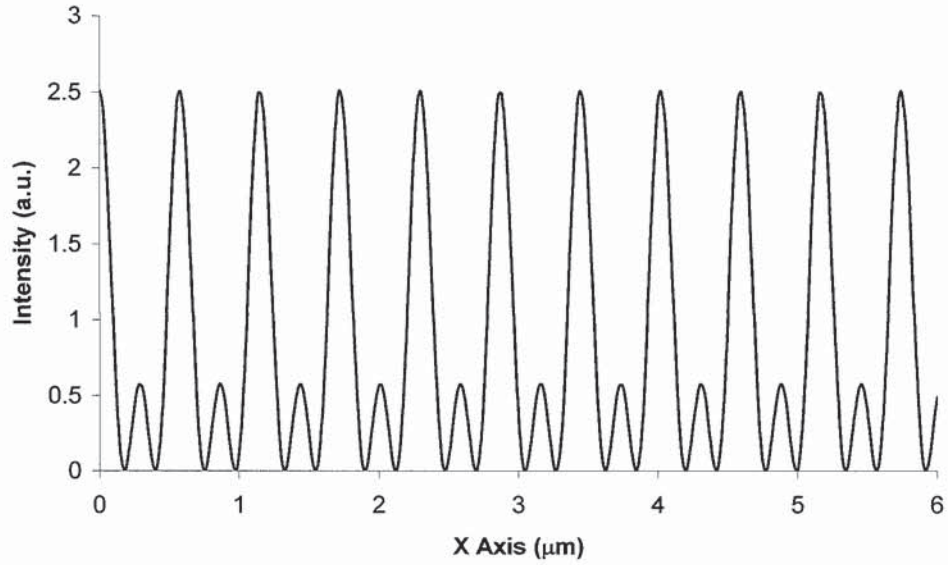


Figure 6-4: Effect of 17 % zeroth-order on the fringes behind a 0.5742 μm phase mask at a distance of zero behind the mask; $z = 0$.

This is equivalent to the summation of two sine waves having periodicities of 0.5742 μm and 0.2871 μm and demonstrates that for 325 nm radiation, the period of the diffraction pattern behind this mask predominately equals that of the phase mask instead of half that of the phase mask. Therefore the phase matching condition becomes:

$$N\lambda_B = 2n_{eff}^{co}\Lambda_{PM} . \quad (6.1)$$

Verification of this result was obtained by calculating the Bragg wavelength to be 1657 nm ($n_{eff}^{co}=1.443$ at 1650 nm and 25 °C, $\Lambda_{PM} = 0.5742 \mu\text{m}$), which is 1 nm away from the experimentally observed grating.

Whilst there should still be a grating located at 836 nm associated with half the period of the phase mask, the visibility of these fringes are extremely low. The strength of the grating at 1656 nm of -1 dB, where the fringes are of higher visibility, suggests that the grating at 836 nm would not be seen due to a weak coupling coefficient. The small strength of the grating at 1656 nm could be due to insufficient quantities of hydrogen in the fibre. This is evidenced by the size of the absorption bands, which are intrinsically linked to the amount of UV exposure and hydrogen content of the fibre, and which are also comparatively small. The inscription wavelength of 325 nm also affects the strength of the grating due to the lower UV absorption and partially forbidden singlet-to-triplet transition; see chapter 3.

Although the grating was weak, fringes in the core of the silica optical fibre were observed with the microscope indicating that fringes were not formed in the polymer optical fibre using this technique due to fibre movement. To prevent movement of the fibre during inscription, the POF was fixed on to a microscope slide (25.4 mm x 76.2 mm x 1 mm) by sandwiching it between the slide and two cover glass slides. The cover slides (20 mm x 20 mm x 0.2 mm) were attached with super glue at the four corners and two polymer optical fibres were mounted to keep the cover glass slides and microscope slide parallel to one another; as shown in Figure 6-5.

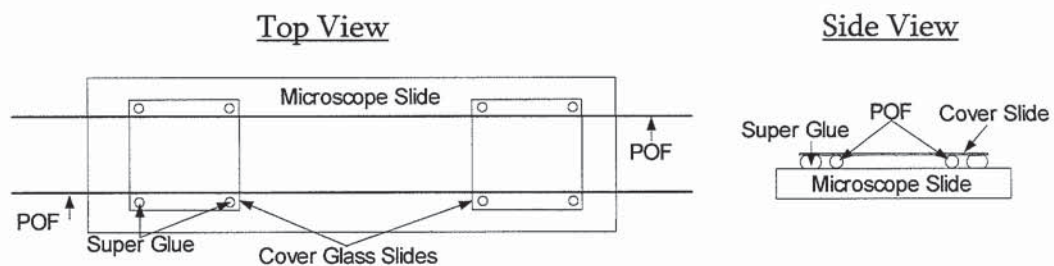


Figure 6-5: Schematic of mounting the POF on to a microscope slide from the top view (left) and the side view (right).

The 0.2 mm thick cover glass slides attenuated the 30 mW laser beam to 23 mW which was still deemed sufficient for grating inscription to occur. Due to this mounting

arrangement, light could not be coupled into the fibre during the exposure so the fibre was inspected afterwards using the microscope for evidence of inscription.

All the phase masks owned by Aston University's Photonics Research Group were designed to operate with an inscription wavelength of 244 - 248 nm and so were tested to find the highest diffraction efficiency for 325 nm radiation. The most efficient mask was found to contain 13.8 % in the zeroth-order whilst the plus and minus first orders contained 34.4 % and 32.5 % respectively. The mask supplied from QPS Technology Inc had a period of 1060.85 nm designed to produce FBGs in silica at 1535.9 nm, where the attenuation of POF is extremely high. This particular mask was used for the rest of the experiments involving FBG inscription in polymer optical fibre.

Exposures of duration, 1 minute, 2 minutes, 5 minutes, 15 minutes, 20 minutes and 35 minutes, were used with the Paradigm MMPOF mounted on the microscope slide. Fringes were observed in the material from 5 minute exposures onwards. The effect of 15 minutes of exposure can be seen in Figure 6-6.

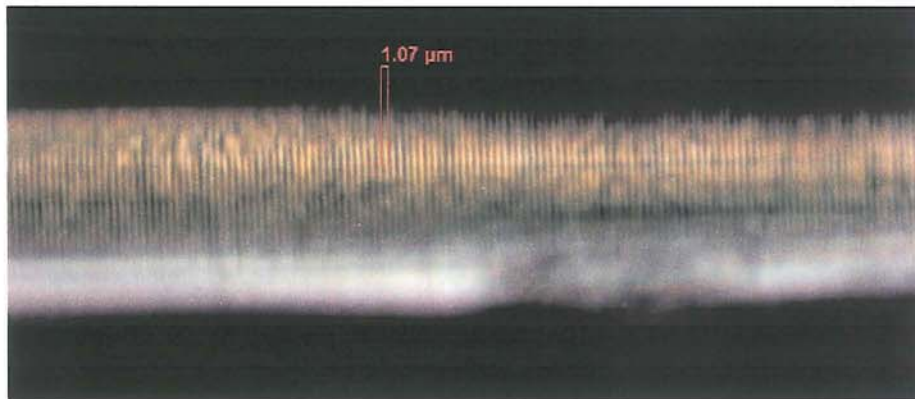


Figure 6-6: Microscope image of damage fringes on the surface of MMPOF after 15 minutes of exposure taken using X63 objective.

The uniform fringes are clearly visible and have a measured spacing of 1.07 μm ; the period of the phase mask. Exposures longer than 15 minutes, whilst still creating stable fringes in the material, the power density of $\sim 1200 \text{ mW/mm}^2$ on the fibre, also resulted in surface charring as the laser beam heated the optical fibre.

This proved FBGs could be inscribed into POF if the fibre was held rigid to eliminate fibre movement. However, light still needed to be coupled into the fibre to determine if a grating was fabricated in the core region. The current set up could not cater for this requirement and so had to be changed.

6.1.2.2 Vertical Alignment

To enable the grating to be monitored during inscription and the fibre to be supported along its entire length during fabrication, the inscription set up was changed and can be seen in Figure 6-7. To prevent miniscule positional changes of the polymer optical fibre occurring during inscription, the fibre was placed in three consecutive v-grooves and anchored in position using polyimide tape. This arrangement enabled light to be coupled into the fibre by butt coupling the end of the POF to an AFC/PC connector; see section 5.8. However, for FBG inscription to be achieved with the fibre mounted in this way required the laser beam to be directed down on to the fibre from above. To achieve this, two periscopes were employed with the second one positioned above the three v-grooves.

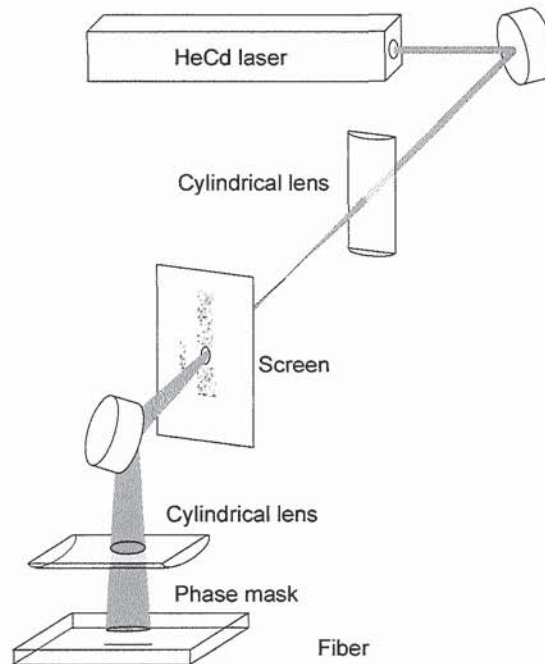


Figure 6-7: Schematic of the vertical set up for FBG inscription [149].

In order to align the laser beam perpendicular to the fibre, a card with an aperture was placed in the beam between the two periscopes. On this card the fluorescence of the UV back reflections from the lens, the edge of the fibre and the fibre core are observed. Alignment is correct when all of these back reflections overlap each other and propagate along the same optical path as the incident beam; examples of typical back reflections can be seen in Figure 6-16. Since the optical fibre was placed in metal v-grooves, a gap of 5 mm was created between two of the v-grooves and the laser beam directed to enter this region. This was done to ensure that the back reflections observed on the card for alignment of the fibre was purely due to the fibre and lens and not from any spurious reflections from the metallic v-grooves. During fabrication of fibre Bragg gratings the alignment card was removed to prevent clipping the laser beam.

Typically, a distance of 100 μm is required between the phase mask and the fibre during the inscription process. In this set up, the phase mask was placed on top of the v-grooves and the separation distance attained by attaching layers of polyimide tape to the unpatterned section of the mask. Since the tape had a thickness of 20 μm , four layers of tape were added to achieve a separation of around 80 μm .

6.2 Fibre Bragg Gratings in Silica Optical Fibre Using 325 nm Radiation

To validate the inscription stability of the vertical alignment setup, FBGs were fabricated in highly photosensitive boron germanium co-doped silica optical fibre (Fibercore, PS1200/1500). Although this fibre is intrinsically photosensitive, not requiring hydrogenation, the low inscription efficiency of 325 nm radiation compared with that of 244 nm radiation required the fibre to be highly hydrogenated at a pressure of 200 bar for 94 hours at 80 °C. The same phase mask intended for use with the polymer optical fibre (QPS, period 1060.85 nm) was used for the inscription, as well as the maximum output power of the laser, 30 mW. The growth data of the resulting FBG is shown in Figure 6-8.

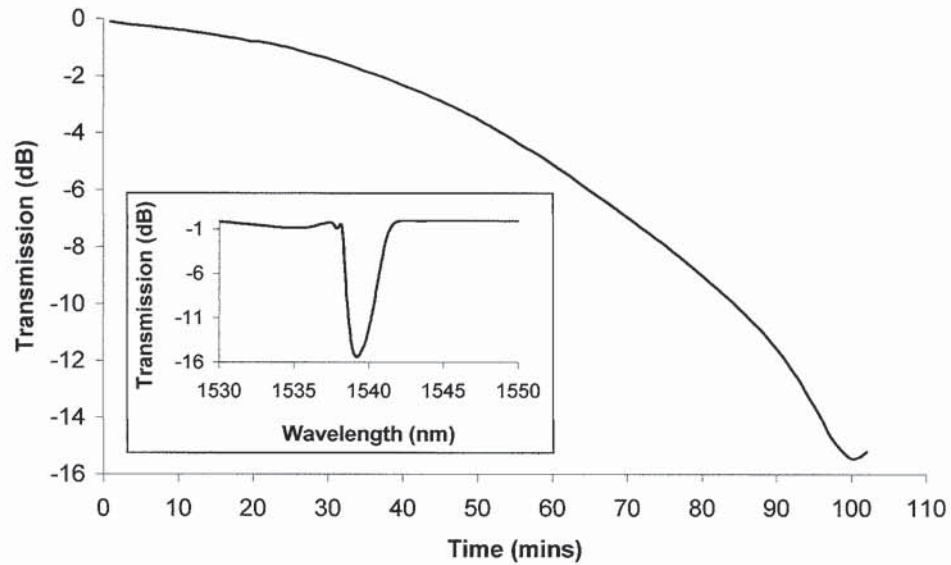


Figure 6-8: Graph of the growth characteristic of an FBG fabricated in PS1200/1500 single mode silica fibre using the HeCd laser. Inset: grating profile.

After an exposure time of 100 minutes, an FBG with a transmission depth of -15.5 dB at a wavelength of 1539.3 nm with a FWHM of 1.4 nm was obtained. The growth data demonstrates that after 100 minutes of exposure the grating was saturated. The length of time needed to produce the saturated grating demonstrates that the inscription setup was sufficiently stable to produce gratings and therefore likely to be successful at inscribing FBGs in polymer optical fibre.

The long exposure time required for saturation to occur is attributed to the inscription wavelength of the laser; 325 nm. For comparison, inscription was conducted in the same fibre using a continuous wave frequency doubled argon ion laser emitting at 244 nm. Static beam exposure was conducted and the resulting growth data can be seen in Figure 6-9 for laser output powers of 90 mW and 30 mW. The 90 mW exposure required a total time of 10 seconds to achieve a transmission notch depth of -27.9 dB at a wavelength of 1539.1 nm with a FWHM of 1.2 nm. The FBG fabricated at 30 mW had a transmission notch depth of -24.2 dB at a wavelength of 1539.2 nm with a FWHM of 1.3 nm.

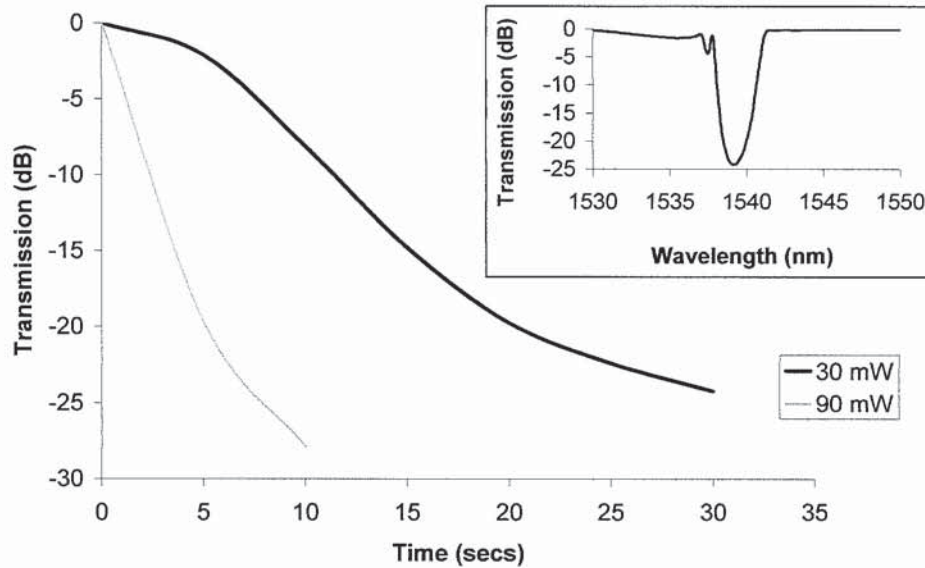


Figure 6-9: Comparison of the growth of FBGs fabricated using 244 nm UV at 30 mW and 90 mW laser powers. Inset: 30 mW grating profile.

The difference in strength and the time taken to reach saturation between the gratings inscribed with 325 nm radiation and those inscribed with 244 nm is mainly attributed to the different inscription mechanisms of the two different wavelengths (244 nm absorption leading to singlet-to-singlet transition and 325 nm absorption leading to a singlet-to-triplet transition). The diffraction efficiency of the phase mask also differs depending on the inscription wavelength (see chapter 2) which affects the fringe visibility of the gratings and consequently the resulting strength of the gratings.

6.3 Fibre Bragg Gratings in Polymer Optical Fibre

All the available polymer optical fibres were investigated for successful grating inscription using the vertical phase mask setup. Unfortunately, attempts at fabrication in the core of the Paradigm Optics Ltd polymer optical fibre were unsuccessful. This may be due to the fibre having no unreacted monomer left in the constituent material of the fibre (see section 5.6).

However, grating inscription was achieved in all other varieties of available polymer optical fibre and the results are detailed in the following sections.

6.3.1 Step Index Polymer Optical Fibre

The first successful fabrication was achieved in few-moded Peng POF (FMPengPOF). Due to the charring seen in the blind exposure tests completed in section 6.1.2.1, the laser power was attenuated using Neutral Density Filters to 3.8 mW, resulting in a power density on the fibre of ~ 200 mW/mm². This allowed longer exposure, providing more time for any photochemical reaction to take place without deformation of the fibre occurring through heat build up from the inscription beam. The fibre was exposed for an hour.

During the exposure the grating was monitored in transmission but no grating was observed. Weak gratings are easier to observe in reflection and so a 2×2 50:50 coupler was used and the reflection arm inputted into an OSA. Since the physical location of the grating was offset to the launch end of the fibre, observing the grating in reflection reduced the length of polymer the light had to travel through. Due to the high attenuation of polymer at 1550 nm (see chapter 5) reducing the amount of fibre the probing light experiences, reduces the experienced attenuation dramatically. A fibre Bragg grating reflection was observed and can be seen in Figure 6-10.

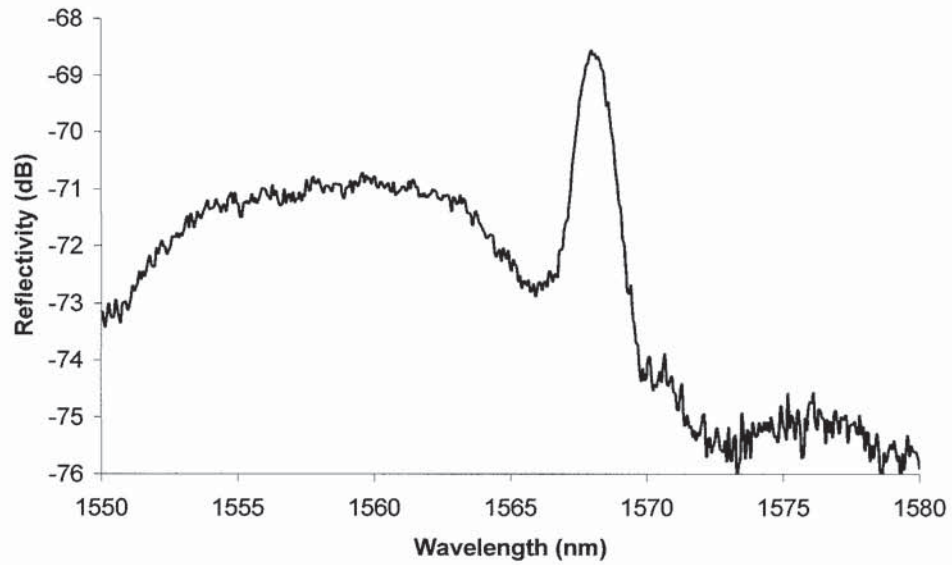


Figure 6-10: First FBG in POF fabricated in few-moded POF.

The resulting grating was located at 1568 nm, had a length associated with the beam diameter ($1/e^2$) of the laser beam of 1.2 mm, a FWHM of 2.0 nm and a reflected signal above the general background reflections of 4.7 dB. To ensure that the reflection peak observed was attributed to a Bragg grating and not to any artefacts or reflections at the launching silica end, a soldering iron with a temperature of 345 °C was held a distance of 1 cm above the grating to check for an induced wavelength shift. A blue wavelength shift was observed; see Figure 6-11.

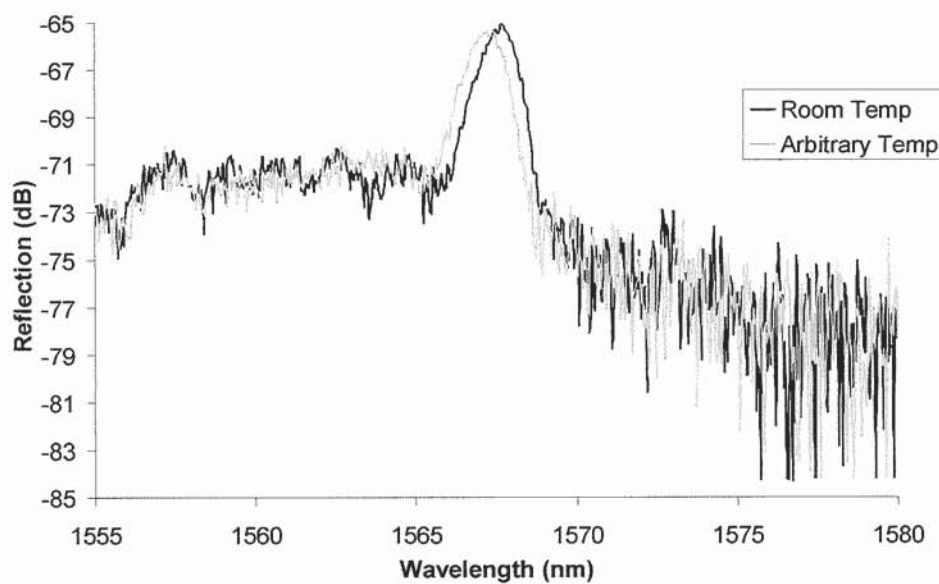


Figure 6-11: Temperature effect on FBG in POF. Black line: room temperature, grey line: arbitrary quantity of heat applied.

Liu *et al* [150] showed polymer fibre Bragg gratings to have a negative temperature coefficient resulting in blue wavelength shifts occurring as a result of increasing temperatures. Consequently, the observed blue shift with temperature verified that a fibre Bragg grating had been inscribed. No side-lobes were observed in the reflection profile of the grating. This is attributed to the Gaussian profile of the laser beam, combined with the static fabrication system, creating a self-apodised FBG.

Although successful inscription was achieved, the strength of the grating was weak compared to silica gratings. To increase the grating strength a second lens was incorporated into the fabrication set up to expand the static laser beam and hence inscribe a longer grating. The extra lens was placed a distance of 56.5 cm away from the fibre; just before the first periscope resulting in the length of any inscribed gratings changing from 1.2 mm to approximately 1 cm. The neutral density filters were also removed, exposing the 1 cm length of fibre to the full output power of the laser. Previously, the full laser power resulted in charring the surface of the polymer optical fibre provided by Paradigm Optics Ltd. However, expanding the laser beam distributed the laser power over a larger area resulting in a power density of $\sim 200 \text{ mW/mm}^2$, the same value as for the unexpanded laser beam with neutral density filters.

During inscription the FBG was monitored in reflection and the growth of the grating recorded. The resulting spectra of the gratings fabricated by this technique in FMPengPOF and SMPengPOF can be seen in Figure 6-12.

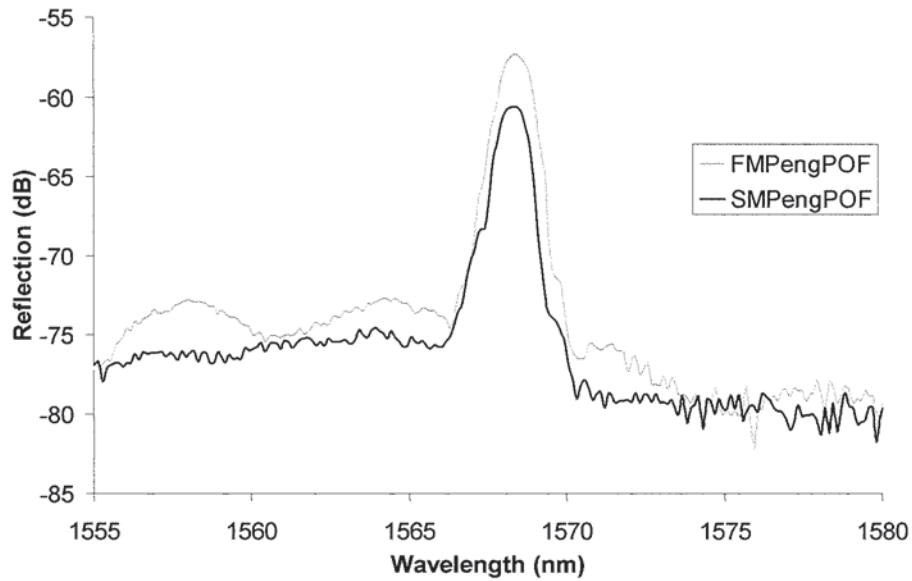


Figure 6-12: FBGs in few and single mode step index POF; OSA resolution 1 nm, grating length 10 mm.

Both gratings were centred at 1568.4 nm. The FMPengPOF grating had a signal above the noise floor of 18 dB and a FWHM of 1.2 nm. The SMPengPOF FBG had a signal of 15 dB and a FWHM of 1.1 nm. The attainable induced refractive index change for the grating has a saturation level related to the quantity of un-reacted monomer in the fibre. Consequently, increasing the exposure region increased the strength of the grating since more un-reacted monomer was accessible. Therefore expanding the laser beam and increasing the laser power had the desired effect of increasing the strength of the grating as well as reducing the bandwidth.

The growth characteristics of the FBG inscribed in FMPengPOF can be seen in Figure 6-13; data collected every minute. The graph shows that the growth rate of the grating is slowing down as it becomes close to the saturation point of the fibre.

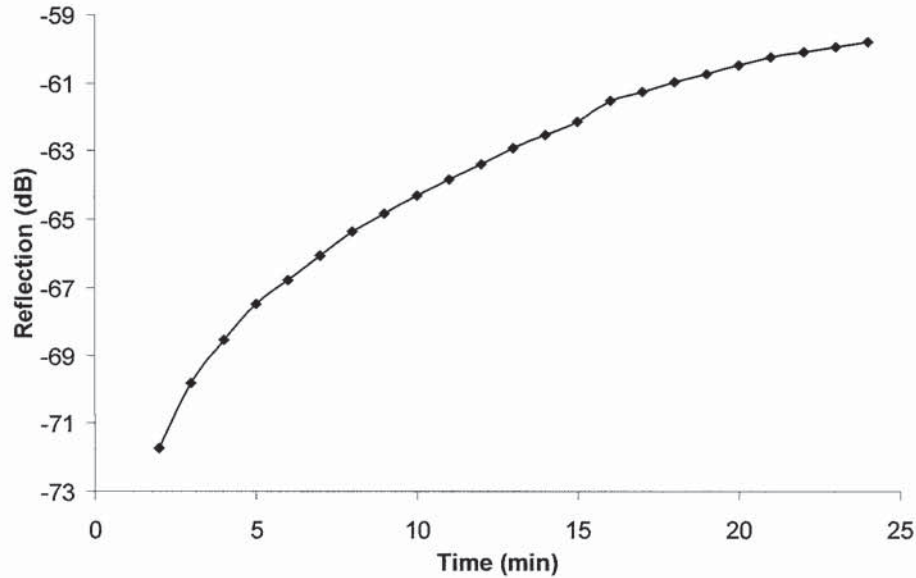


Figure 6-13: Growth characteristics of an FGB in FMPengPOF.

6.3.1.1 Interferometric Devices in POF

Amongst optical sensing techniques, interferometry incorporating silica-based optical fibres has demonstrated the highest measurement resolution. Some interferometric systems can be achieved by using directional couplers to implement amplitude division in Michelson [151] or Mach-Zehnder arrangements [152]. These techniques however, have the disadvantage of being difficult to incorporate into other systems. Interferometric devices fabricated into optical fibres by utilising fibre Bragg gratings overcome this problem whilst maintaining the high resolution of interferometric devices. Consequently, the viability of fabricating these devices into POF, where the sensitivity of the grating to external measurands is already enhanced over their silica counterparts, was investigated.

Phase shifted gratings

Phase shifted gratings are a uniform fibre Bragg grating which has a phase shift within the grating structure itself. The phase change creates two gratings out of phase with each other which act as a wavelength selective Fabry-Pèrot resonance allowing light at the resonance to penetrate the stop-band of the original grating; see Figure 6-14 for a grating transmission profile with a π phase shift [153].

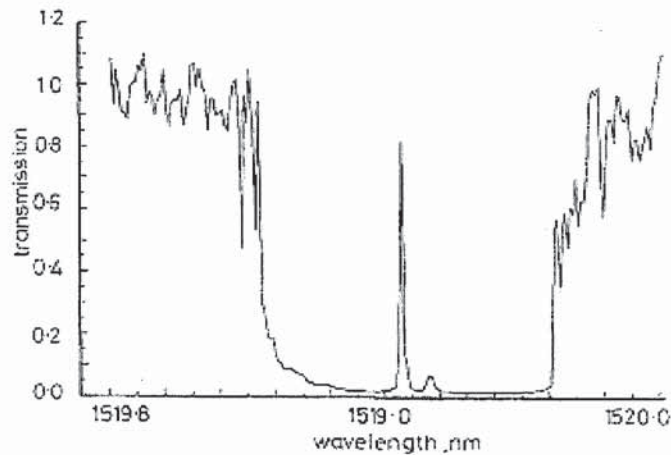


Figure 6-14: Grating profile with a π phase shift [153].

The phase shift can be introduced by several different methods:-

1. Using a phase mask with a shift incorporated into the design [154]
2. Post-processing of a grating by exposing a region of the grating to further UV radiation [153]
3. Post-fabrication processing using localised heat treatment [155]

The first method has been used to successfully fabricate a phase shifted FBG in a polymer waveguide [156]. However, phase shifted FBGs in POF have not been previously reported and is demonstrated in this section. To achieve the phase shift, the second method was utilised. A 1 cm standard uniform grating was fabricated to saturation and the unexpanded laser beam, approximately 1 mm, used to expose the centre of the grating. The resulting phase shifted grating can be seen in Figure 6-15.

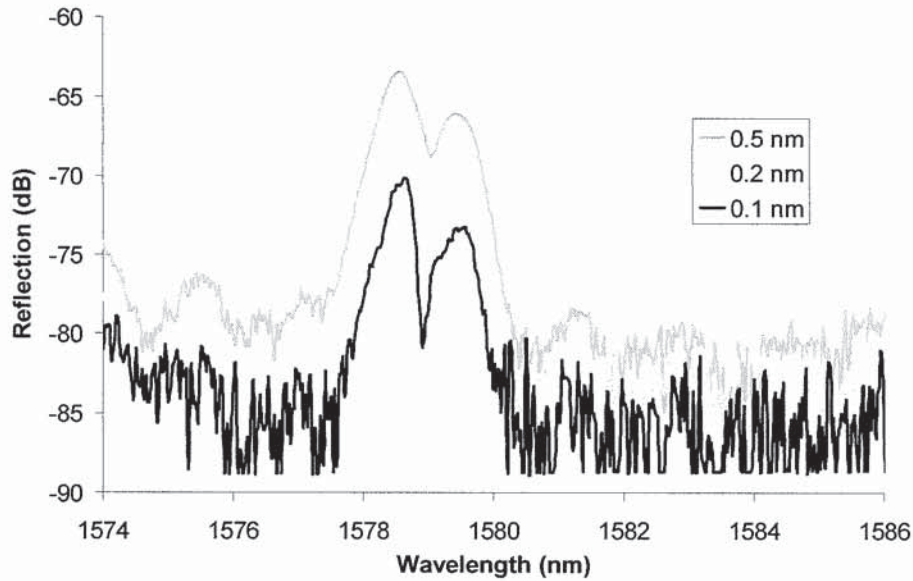


Figure 6-15: Phase shifted FBG in single mode POF for different OSA bandwidths.

The resulting stop band had a FWHM of 0.16 ± 0.02 nm which equates to a ~ 19 GHz passband. The width of the stopband is large compared to silica based devices which is likely to be attributed to the large attenuation of polymer at these wavelengths and the weak reflectivity of the grating. Shifting the gratings to lower wavelengths should result in a sharper feature which can be correspondingly monitored with higher precision.

Despite the weak grating and broad stop band, the feasibility of creating such devices in POF has been demonstrated for the first time.

6.3.2 Microstructured Polymer Optical Fibre

The air-hole geometry of microstructured polymer optical fibre presents a particular challenge for FBG inscription. The presence of several rings of holes surrounding the core scatters the incident side exposed laser beam, resulting in significantly reduced optical intensity in the core. FBGs have however been fabricated in silica microstructured optical fibres with a small germanium doped core by deuterium loading the fibre and then exposing it to 242 nm radiation from a frequency-doubled excimer-pumped dye laser for 1000 seconds [80]. The resulting FBG had a length of 4 cm, a length of 3 dB with a Δn of 10^{-3} . FBGs have also been fabricated in pure silica microstructured fibre using a ArF 193

nm laser with a pulse width of ~ 15 ns operating at a repetition rate of 40 Hz [157]. This resulted in an FBG which had a strength of ~ 14 dB, a length of 1 cm and a Δn of 2×10^{-4} after an exposure time of 3.8 hours. Inscription was also achieved in pure silica microstructured fibre using a 267 nm femtosecond laser (120 fs pulses) with a repetition rate of 1 kHz [158]. After an exposure time of 60 minutes, 10-12 dB strength FBGs were achieved with a length of 4 mm and a Δn of 4×10^{-4} .

All these examples demonstrate that grating inscription was achievable in these fibre geometries but that high energy pulses were deemed necessary to compensate for the attenuation due to the hole-induced scattering. Despite these potential restrictions fibre Bragg gratings have been inscribed in microstructured polymer optical fibre using the low power continuous wave helium cadmium laser using the following method.

It was found that the orientation of the fibre geometry with respect to the incident laser beam was critical for successful photoinscription. In step index fibres, the alignment of the inscription laser beam to the fibre affects the quality of the fabricated gratings, incorrect alignment when inscribing gratings in mPOF completely prevents inscription from occurring. Inspection of the back reflections of the HeCd beam from the mPOF revealed two different diffraction patterns as the fibre was rotated; one thin and bright and the other broad and dull. The thin bright pattern was found to be successful for grating inscription to occur. The two different patterns are shown in Figure 6-16. The successful bright diffraction pattern is likely to coincide with the laser beam being incident on the ΓM (flat side of the hexagon) axis of the photonic crystal structure due to this orientation causing less light scattering [159].

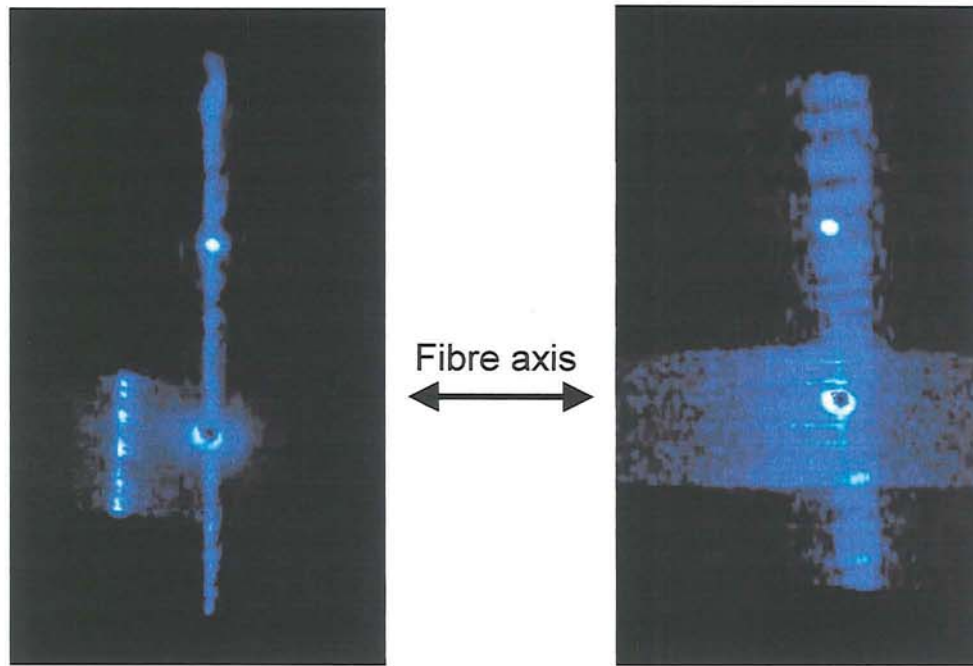


Figure 6-16: Backscattered diffraction patterns of the HeCd laser viewed by fluorescence; the pattern on the left was needed for successful inscription. Note that for clarity in the images, the fibre has been twisted slightly in order to shift the backscatter off the core region to the left of the main pattern; for correct alignment these would be superimposed. (photo: David Webb)

Inscription was initially attempted without expanding the laser beam so that the maximum energy could be focused down to the core region. Successful inscription was achieved in all three microstructured polymer optical fibre varieties: endlessly single mode microstructured POF (SMmPOF), few-moded microstructured POF (FMmPOF) and multimode microstructured POF (MMmPOF); see section 5.4 for geometries, see Figure 6-17 for grating spectra.

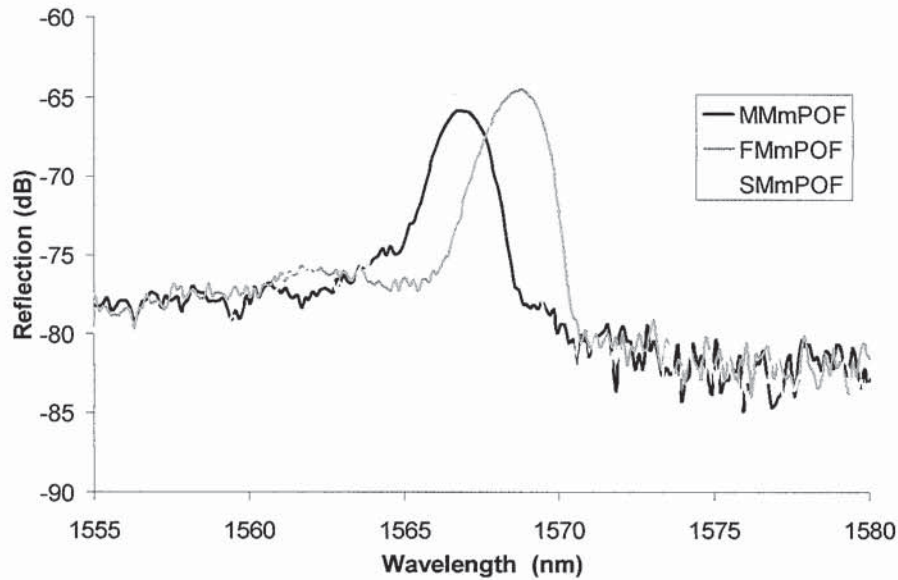


Figure 6-17: Grating profiles in the 3 different varieties of mPOF grating length 1 mm, OSA resolution 1 nm.

The spectral properties of the resultant gratings and the exposure times for the fabrication are shown in Table 6-1.

Table 6-1: Table containing the different fabrication conditions for the different fibre types.

POF Type	Exposure Time	Bragg Wavelength	Signal	FWHM
SMmPOF	16 mins	1566.8 nm	14 dB	2.6 nm
FMmPOF	15.5 mins	1568.8 nm	15 dB	2.0 nm
MMmPOF	20 mins	1566.8 nm	13 dB	1.9 nm

The different wavelength locations of the FBGs is either due to differing amounts of strain on the fibres during fabrication or thermal annealing during inscription.

Fibre Bragg gratings were also fabricated with the second lens incorporated into the inscription system producing narrower gratings. For this setup, the exposure time for the FMmPOF was 60 minutes at a room temperature of 29 °C before saturation of the grating

occurred. The resulting FBG had a Bragg wavelength of 1570 nm, a FWHM of 1 nm, a length of 1 cm and a reflective signal above the noise level of 7dB. Figure 6-18 shows the grating profile (OSA bandwidth = 0.2 nm) and the growth characteristics. Evidence for the few-moded structure of the reflectivity profile can be clearly seen.

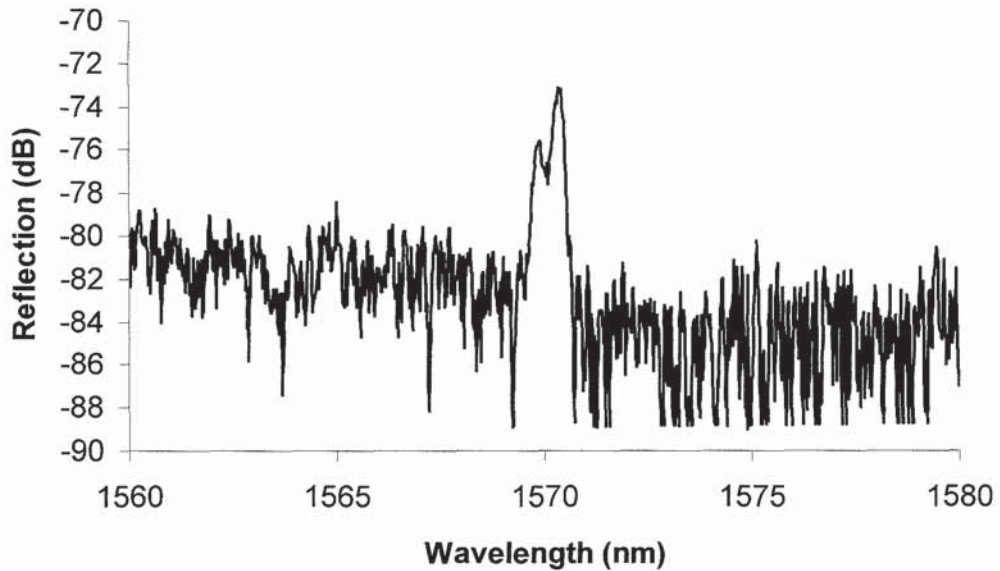


Figure 6-18: Reflection profile of FBG fabricated in few-moded mPOF.

The growth characteristics can be seen in Figure 6-19.

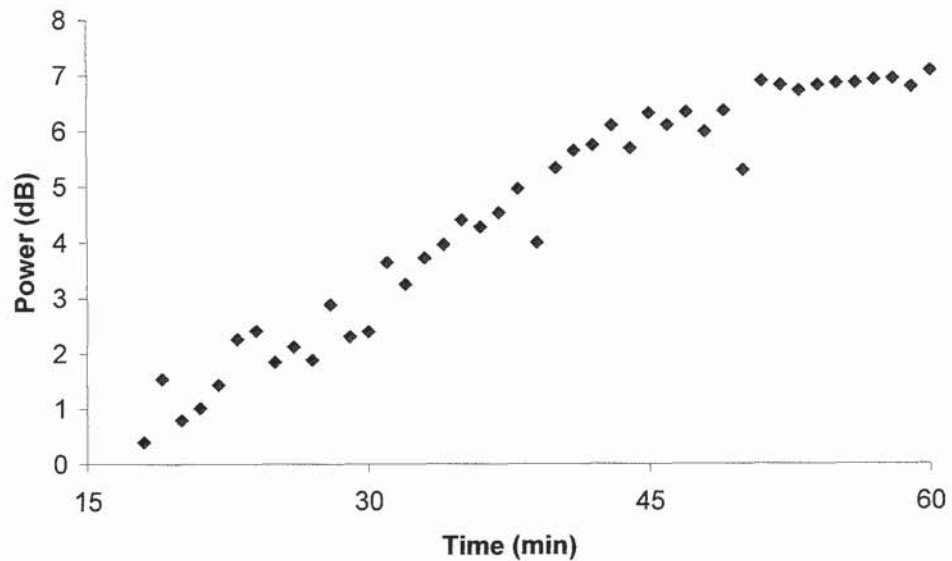


Figure 6-19: Growth characteristics of the FBG in FMmPOF.

The return signal was observed to be comparable to the Fresnel reflection from the end of the fibre launching light into the POF in the absence of index matching gel. The attenuation of the POF at the grating wavelength is around 72 dB/m [160]; consequently, the 3 cm distance to the grating from the input face of the POF implies that the reflectivity of the grating will be at least 10 %, which using the equation:

$$dB = 10 \log \left(\frac{1}{1 - \frac{\%}{100}} \right), \quad (6.3)$$

gives a transmission value of 0.46 dB. Possibly due to the high fibre attenuation at these wavelengths and weak grating, it was not possible to observe the grating in transmission.

The fibre Bragg grating inscribed in SMmPOF with the expanded laser beam had a Bragg wavelength of 1569 nm, a FWHM of 0.5 nm, a length of 1 cm and a reflective power above the noise level 2 dB less than that in the few-moded fibre. The grating profile (OSA bandwidth = 0.2 nm) and growth curve can be seen in Figure 6-20 and Figure 6-21 respectively.

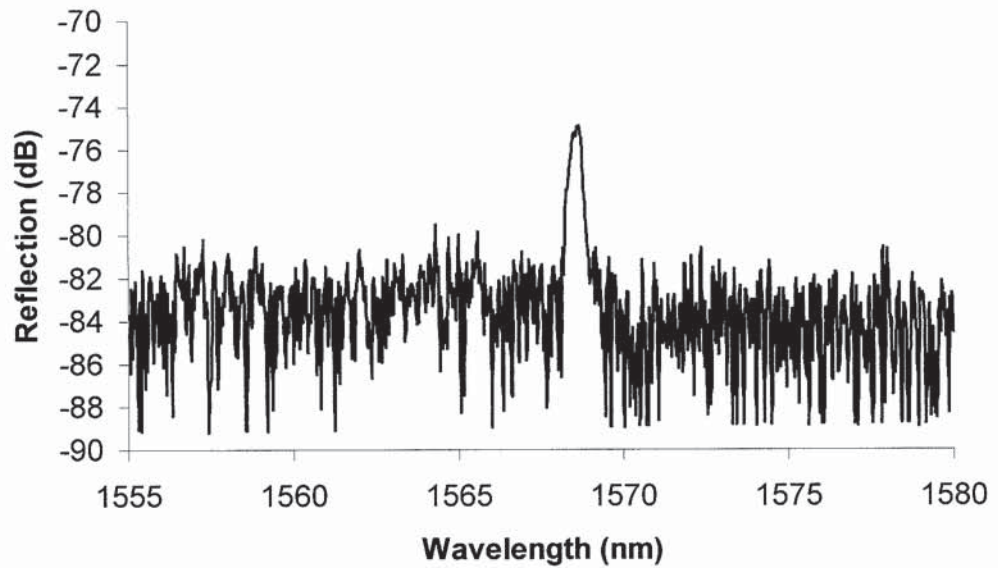


Figure 6-20: Reflection profile of FBG fabricated in SMmPOF.

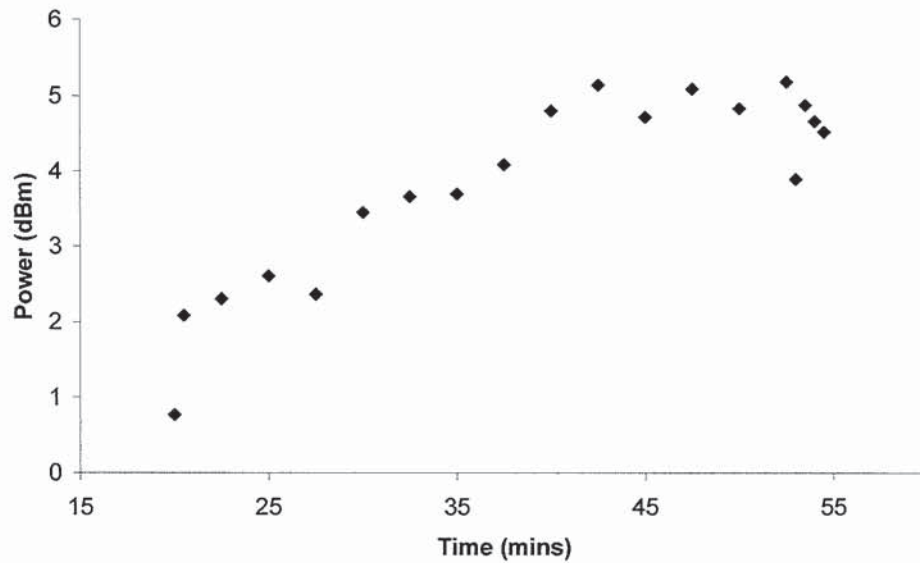


Figure 6-21: Growth characteristics of the FBG in SMmPOF.

6.3.2.1 Transmission Profile of FBG in Microstructured Polymer Optical Fibre

Although fibre Bragg gratings were fabricated in the investigated polymer optical fibres, attempts to observe the gratings in transmission were unsuccessful. The transmission spectra of the fibre consisted of a continuously moving set of fringes, thought to be accounted for by stimulated cladding modes; see section 5-8. Not being able to measure the transmission spectrum meant that the exact strength of the gratings was not known.

As part of the collaboration with the OFTC in Australia, some of the fabricated gratings were sent to the group. After several attempts, they were able to successfully observe one of the 1 cm long gratings in transmission; see Figure 6-22.

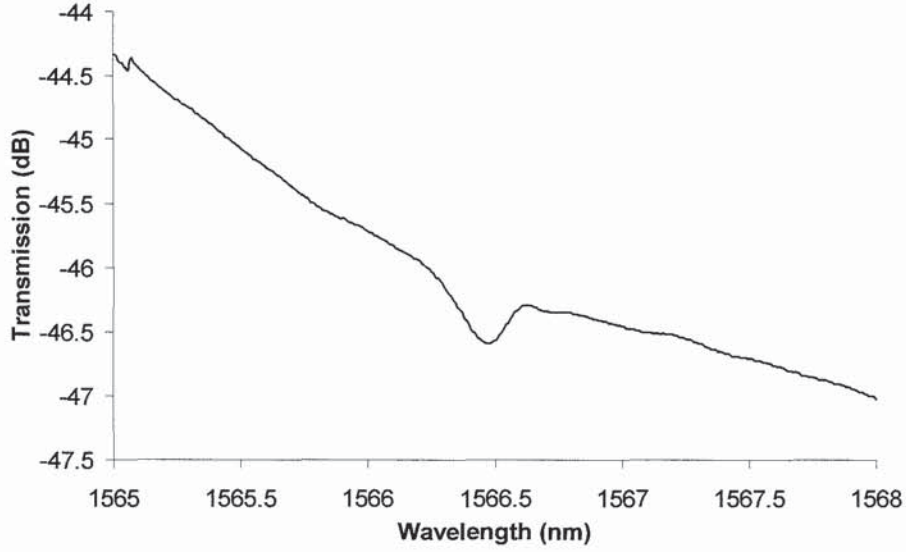


Figure 6-22: Transmission profile of FBG in mPOF [data provided by A. Argyros].

They achieved this result by butt coupling single mode silica fibres to the mPOF at both ends. The single mode silica fibre was spliced to a coupler, which was connected to an erbium ASE source. The grating strength of 0.42 dB is consistent with the value of 0.46 dB estimated from the reflected strength.

Although the grating was weak, the exponential growth characteristics of the gratings level off indicating saturation of the induced refractive index change in the gratings. If the inscription mechanism is photopolymerisation this would indicate that the resultant grating strength is determined by the quantity of monomer remaining within the polymer. The dc average spatial induced refractive index change, $\overline{\delta n_{eff}}$, was found to be $\sim 3 \times 10^{-5}$ by using the equation:

$$R_{max} = \tanh^2(\kappa L), \quad (6.4)$$

to calculate the coupling coefficient, κ , (0.0314 mm^{-1}) and then equation [11]:

$$\kappa = \frac{\pi}{\lambda} s \overline{\delta n_{eff}}, \quad (6.5)$$

to calculate $\overline{\delta n_{eff}}$, using $s=0.5$ for a weak grating.

Typical values for fibre Bragg gratings induced by UV radiation in silica-based optical fibres range from 1×10^{-3} to 1×10^{-5} depending on the exact fibre type and UV inscription wavelength [3]. This emphasizes the fact that the fibre Bragg gratings fabricated in the polymer optical fibre are extremely weak.

6.4 Discussion

The ability to inscribe fibre Bragg gratings into polymer optical fibres opens up a range of potential applications.

The group at the OFTC in Sydney Australia have demonstrated that a Rhodamine 6G (R6G) doped PMMA microstructured polymer optical fibre can lase at 568 nm if pumped with 532 nm radiation supplied from a frequency doubled Q-switched Nd:YAG laser [161]. The ability to lase was found to depend on the geometry of the microstructure and the length of the fibre used; long lengths of fibre with a small core resulted in stimulated Raman scattering dominating, which depletes the pump preventing lasing threshold being reached [162-163]. For successful lasing, a 5 m length of doped fibre was used which had a 50 μm radius core region. The laser cavity was created by having flat cleaves on the fibre ends. Fibre lasers typically operate by incorporating fibre Bragg gratings into the system, which define the laser cavity and lasing wavelength. The ability to fabricate fibre Bragg gratings in microstructured polymer optical fibre, especially the multimode mPOF which has a core region of 50 μm , is clearly important for this particular application. The fact that the multimode mPOF FBG still maintains the relatively narrow FWHM of 1.9 nm for a grating length of 1 mm results in it potentially being used in this application. Also the

tunability of fibre Bragg gratings in polymer optical fibre to strain [102] presents the possibility of fabricating a tunable laser cavity. Rhodamine 6G PMMA mPOF is likely to be provided by the OFTC in Australia for grating inscription attempts to be conducted with this application in mind.

Biomedical applications could also benefit from the development of grating devices in polymer optical fibre. Optical fibre sensors offer the huge advantage of electric isolation whilst the small size of optical probes enables minimally invasive procedures and accurate profiling of, for example, temperature. However, in the case of silica-based optical fibres, precautions must be taken to ensure no breakages occur inside the patient. The inherent biocompatibility of organic polymers could make this precaution redundant. When this is coupled with the fact that fibre Bragg gratings in polymer optical fibre are expected to have enhanced thermal sensitivity means they have huge potential in this field.

However, the fibre Bragg gratings presented here are extremely weak and this must first be improved for accurate interrogation of the devices. In order to achieve this, phase masks are being purchased which have improved diffraction efficiencies for 325 nm radiation increasing the fringe visibility and strength of the resulting gratings. The phase masks are also designed to produce fibre Bragg gratings at 800 nm where the attenuation of the polymer is significantly lower.

Improvements could also be implemented in the fabrication set up. Currently, the phase mask is placed on top of the optical fibre with layers of tape defining the separation distance between mask and fibre. A new phase mask holder could be designed to rigidly suspend the mask above the fibre without it resting on the optical fibre. This would not only allow for easier alignment of the phase mask to the optical fibre but also reduce any mechanical vibrations on the mask. A beam expander instead of a lens could be used in the system to expand the beam further making longer fibre Bragg gratings and increasing the resulting reflectivity.

As well as perfecting the inscription set up, different polymeric materials need to be investigated to see if stronger gratings can be fabricated in them. For example, trans-4-stilbenmethanol doped PMMA mPOF is being provided by the PFTC in Australia. This material has significantly higher UV absorption than pure PMMA [164] so has the potential to produce stronger gratings.

The OFTC are also hoping to provide a fibre with a flat side so that the orientation of the holes can be known, making the alignment of the fibre to the inscription laser beam easier.

6.5 Summary

Different techniques for fabricating fibre Bragg gratings have been presented. Explanations for the use of the phase mask technique over the Amplitude-Division Interferometry technique is given with experimental justification. It was found that for successful inscription in polymer optical fibre, the entire length of the fibre needs support to eliminate fractional movements of the fibre reducing the fringe visibility. Fibre Bragg gratings have been fabricated in several different varieties of PMMA based polymer optical fibres including standard step index fibre and microstructured fibre using a continuous wave helium cadmium laser. A table summarising the resulting fabricated FBGs is shown in Table 6-2.

Table 6-2: Table containing a summary of the different varieties of POF investigated for FBG inscription and the resulting spectral characteristics of the FBGs.

POF Type	Supplier	FBG Fabricated	Length of FBG	Wavelength (nm)	Reflection (dB)	FWHM (nm)
SMPOF	Paradigm Optics Ltd	No	-	-	-	-
MMPOF	Paradigm Optics Ltd	No	-	-	-	-
SPengPOF	G.D. Peng	Yes	1 cm	1568.4	15	1.1
FMPengPOF	G.D. Peng	Yes	1 mm	1568.0	4.7	2.0
			1 cm	1568.4	18	1.2
SMmPOF	M.J. Large	Yes	1 mm	1566.8	14	2.6
			1 cm	1569.0	5	0.5
FMmPOF	M.J. Large	Yes	1 mm	1568.8	15	2.0
			1 cm	1570.0	7	1.0
MMmPOF	M.J. Large	Yes	1 mm	1566.8	13	1.9

7

Thermal Tuning of Fibre Bragg Gratings in Plastic Optical Fibres

Described in this chapter are initial temperature characterisation experiments carried out on fibre Bragg gratings in two different geometries of polymer optical fibre. The emphasis of the characterisation is to establish the upper temperature working limit of such fibre Bragg gratings to verify their practical usability. The results demonstrate that polymer optical fibre Bragg gratings have enhanced temperature sensitivity over their silica-based counterparts by at least a factor of six. Different varieties of polymer optical fibre have been found to have different upper working temperature limits but both display hysteresis upon exceeding a specific temperature. Finally, the large thermal sensitivity of the POF FBGs is utilised to manufacture a device by coating a polymer optical fibre Bragg grating in a thin layer of copper and tuning it via joule heating.

7.1 Introduction

To enable fibre Bragg gratings in polymer optical fibre to be incorporated into commercial systems, the thermal response and long term stability of the gratings must be established. To date only a few investigations have been concerned with the temperature response of fibre Bragg gratings in step index polymer optical fibre [105,150]. The first reported temperature response showed a total wavelength shift of 18 nm between 20-70 °C [150].

Although the response was non-linear, no hysteresis was observed between heating and cooling the grating. Later work involved using a silica and polymer FBG together in the same sensing head to discriminate between strain and temperature effects [105]. The temperature response of the polymer optical fibre grating in this work was $-145 \text{ pm}/^\circ\text{C}$ with no reported hysteresis up to 65°C .

Whilst these results are of importance, the upper working limit of these gratings had not been established and at what point, if any, hysteresis starts affecting the results. Consequently, this chapter describes work aimed at investigating these potential limitations of the devices in step index and previously un-reported microstructured POF. Work then progresses to use the enhanced sensitivity to produce a grating based device in polymer optical fibre.

7.2 Temperature Characteristics of POF and mPOF gratings

The temperature sensitivity of gratings in both SMPengPOF and SMmPOF were investigated using the setup shown in Figure 7-1.

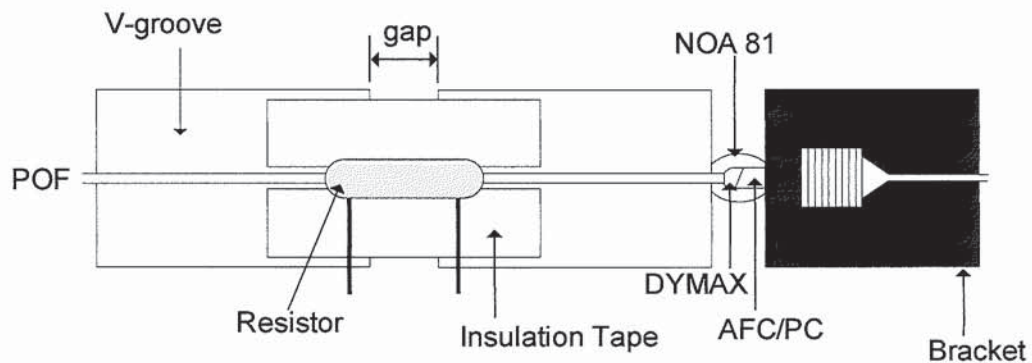


Figure 7-1: Setup of heating equipment for temperature calibration of POF FBG.

The POF resided in a series of v-groove blocks. To isolate the FBG from the thermally conductive properties of the metallic v-grooves, the FBG was located in an air gap between two v-grooves. To ensure the optical launch conditions remained constant during the investigations, the POF and AFC/PC connector were glued together. Connecting silica to polymer optical components together is notoriously difficult since the

epoxy needs to have good bonding to both materials whilst maintaining good optical transmission with a refractive index ideally between that of silica and polymer. All of these requirements were not found in a single epoxy resulting in two different epoxies being used; DYMAX OP 45 which had a refractive index of 1.47 but had weak tensile strength once cured (325 psi) and Norland Optical Adhesive 81 which had a refractive index of 1.5 but high tensile strength (4000 psi). In order to monitor the FBG in reflection, the Fresnel reflections from the end of the fibre need to be minimised which is achieved by having a material whose refractive index is closely matched to that of the fibre. The DYMAX epoxy had a refractive index between that of silica and polymer facilitating its effectiveness to aid coupling between the two fibres and reduce the Fresnel reflections. Its low tensile strength though was insufficient to hold the bond for the duration of the investigations. Subsequently, it was encapsulated in Norland Optical Adhesive to hold the joint together. Both epoxies were UV cured since temperature cured epoxies could damage the POF and FBG. Care was taken to ensure that only the epoxy was exposed to the UV curing lamp.

A high power resistor (150Ω , 2.2W) was then placed over the top of the FBG to achieve joule heating of the device. Finally, the FBG and resistor were enclosed by a polystyrene hood to ensure an equilibrium temperature surrounded the grating. Different amounts of current were passed through the resistor and the resulting temperature inside the hood measured using a thermocouple to provide a calibration curve.

7.2.1 Thermal Response of FBGs in Single Mode Step Index POF (SMPengPOF)

The fibre Bragg grating inscribed in the SMPengPOF had a length of 1 cm, a reflection signal of 8 dB above the noise floor, a FWHM of ~ 1 nm and a wavelength of 1579.4 nm. The reflection spectrum can be seen in Figure 7-2.

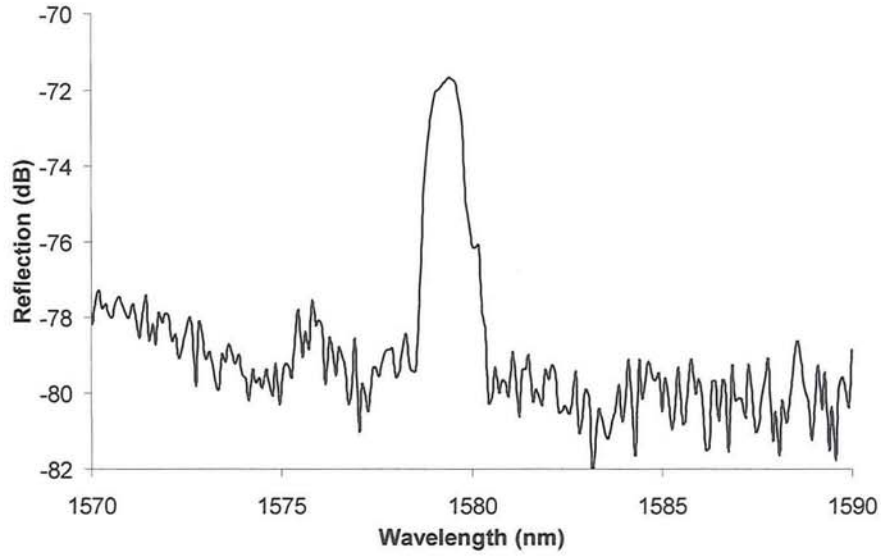


Figure 7-2: Spectral profile of the FBG in SMPengPOF.

To ensure thermal equilibrium, each resistor current setting was held for 15 minutes and then the resulting spectral shift of the grating recorded. Between each current setting, the power to the resistor was turned off for a further 15 minutes to record any hysteresis in the room temperature spectral location. The temperature sensitivity of the FBG in SMPengPOF is shown in Figure 7-3.

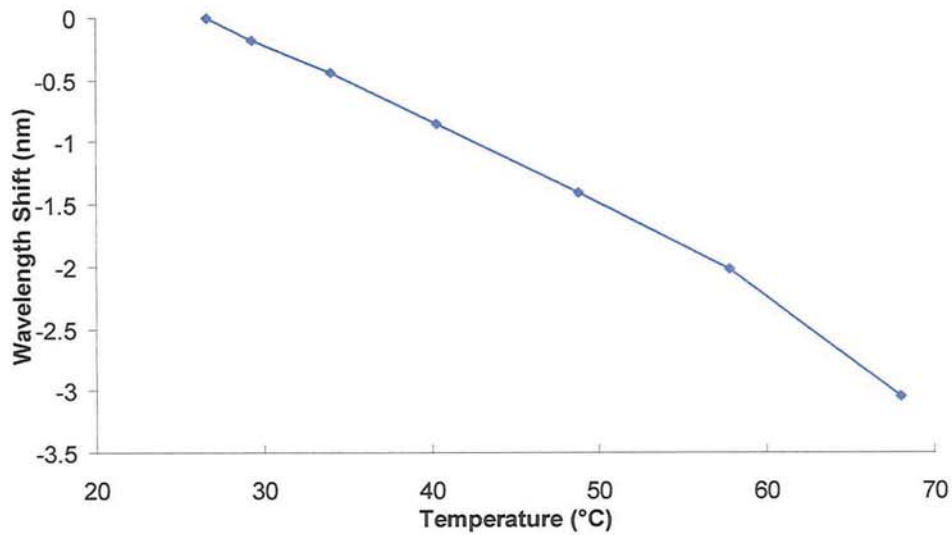


Figure 7-3: Temperature sensitivity of the FBG in SMPengPOF.

Figure 7-3 shows a total wavelength shift of 3 nm over the temperature range 26.6–68 °C with a linear temperature response of -64.4 pm/°C between 26.6–57.8 °C followed by an

increased sensitivity of $-101 \text{ pm}/^\circ\text{C}$ between $57.8\text{-}68.0^\circ\text{C}$. Both of these values are significantly higher in magnitude than the $\sim +10 \text{ pm}/^\circ\text{C}$ temperature sensitivity displayed by silica-based optical fibres [19]. The temperature sensitivity of FBGs, $\Delta\lambda_{BT}$, is defined by:

$$\Delta\lambda_{BT} = \lambda_B (\alpha_\Lambda + \alpha_n) \Delta T, \quad (7.1)$$

Consequently, the difference in thermal sensitivity between silica and polymer FBGs is attributed to differing values for the thermal expansion coefficient, α_Λ , and the thermo-optic coefficient, α_n , between the two materials; see Table 7.1. Both of these coefficients are higher in PMMA explaining the increased thermal sensitivity.

Table 7.1: Table showing the values for the thermal expansion coefficient, α_Λ , and the thermo-optic coefficient, α_n , of silica and PMMA [150].

	$\alpha_\Lambda \text{ (cm/cm}/^\circ\text{C)}$	$\alpha_n \text{ (}/^\circ\text{C)}$
Silica	0.55×10^{-6}	8.6×10^{-6}
PMMA	8.0×10^{-5}	-1×10^{-4}

Increasing the temperature further from 68.0 to 80.3°C resulted in the grating being permanently erased. The erasure of the grating between the temperatures of $68.0\text{-}80.3^\circ\text{C}$ is likely to be attributed to the core composition of the fibre; methyl-ethyl-benzyl methacrylate. Whilst the ratio of composition of these monomers is unknown, the glass transition temperature of methyl methacrylate is 105°C , ethyl methacrylate is 66°C and benzyl methacrylate is 54°C . The combination of these three glass transition temperatures could result in an overall glass transition temperature in the range $68.0\text{-}80.3^\circ\text{C}$. Below the glass transition temperature only local movements of segments of the polymer chains can occur. However, this particular fibre has a high degree of molecular alignment introduced during high tension drawing of the fibre, evidenced by the fraying observed during the cleaving experiments shown in section 5.7. Upon exceeding the glass transition temperature, movement of the entire polymer chain can occur allowing the molecules to

relax back to a more random arrangement. This consequently, shortens the fibre length and could erase the grating by significantly reducing the fringe visibility.

The hysteresis observed in the room temperature spectral location of the grating after each consecutive temperature setting is shown in Figure 7-4.

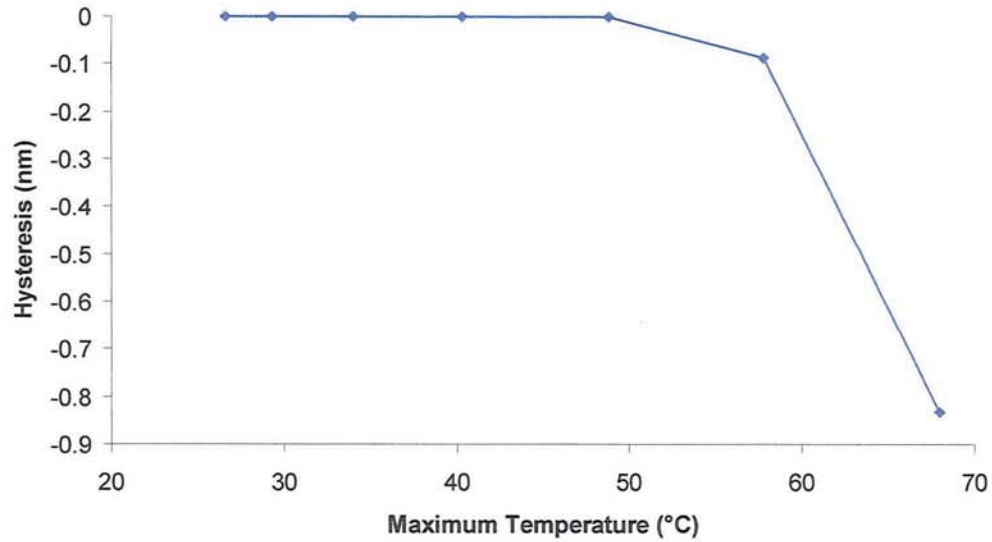


Figure 7-4: The shift in room temperature spectral location of the grating after each consecutive heating step. The x-axis depicts the temperature the grating was heated to before returning to room temperature.

It can be seen from Figure 7-4 that between the temperatures of 49°C and 58°C the grating no longer returned to its original spectral location demonstrating a permanent structural change. Increasing temperatures make this effect more prominent shifting the spectral location further away from its original position. A hysteresis of 0.83 nm was observed before the grating was erased.

7.2.1.1 Discussion

These results significantly differ from those reported by Liu *et al* [105] for a similar composition and structure polymer optical fibre. Their investigations yielded a -145 pm/°C sensitivity with no hysteresis up to 65 °C. The grating investigated by Liu *et al* had a wavelength of 1523.1 nm compared with 1579.4 nm reported here. Ishigure *et al* [127]

have investigated the wavelength dependence of the refractive indices of PMMA, PF and compared them to silica; see Figure 7-5. As well as demonstrating that the refractive index of PF has a lower dependence on wavelength than silica and PMMA, they showed that the response of silica and PMMA is extremely similar. Consequently, the thermo-optic coefficient, which equals:

$$\alpha_n = \frac{1}{n_{eff}} \left(\frac{\partial n_{eff}}{\partial T} \right), \quad (7.2)$$

would not be significantly different if the composition of the two different fibres was comparable.

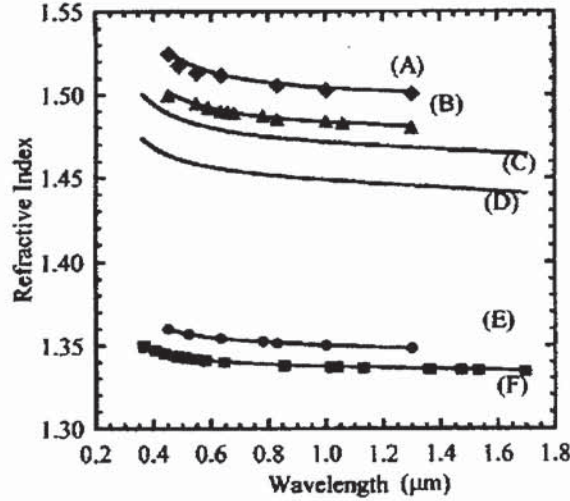


Figure 7-5: Wavelength dependence of the refractive indices of PMMA, PF polymer and silica. (A): 15 wt.% benzyl benzoate (BEN) added PMMA; (B) PMMA homopolymer; (C) 13.5 mol% GeO₂-doped SiO₂; (D) pure SiO₂; (E) 5.5 wt.% PF dopant added PF polymer; (F) PF homopolymer. Plots: experimental data. Solid line: approximated by Sellmeier equation [127].

However, the FBGs investigated by Liu *et al* had a reflectivity of 80% instead of the 10% investigated here. Since the photosensitivity mechanism of PMMA is possibly due to photo-polymerisation upon exposure to 325 nm radiation, the gratings used by Liu would have contained more fully polymerised polymer. The refractive index of a monomer differs from that of the polymerised monomer; methyl methacrylate (MMA) is between 1.4118 - 1.4125 [165] whereas PMMA is 1.49. Since the thermo-optic coefficient, α_n ,

depends on the effective refractive index of the grating region this could potentially result in different thermal responses. The difference however, is still unlikely to be the sole contributory factor to the observed discrepancy.

7.2.2 Thermal Response of FBGs in Single Mode Microstructured POF (SMmPOF)

The fibre Bragg grating inscribed in microstructured POF (mPOF) had a length of 1 mm, a reflected signal above the noise floor of 11.5 dB, a FWHM of ~5 nm and a wavelength of 1562.1 nm. Investigating the thermal response of gratings in this fibre showed them to survive temperatures up to at least 106.1 °C for 15 minutes. The spectral profile at room temperature and 106.1 °C is shown in Figure 7-6.

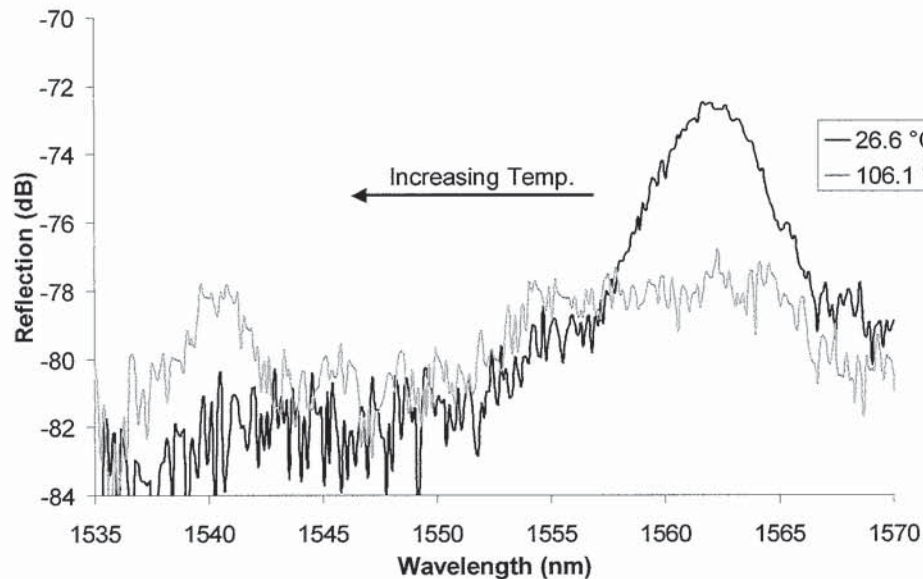


Figure 7-6: Spectral profile of the FBG in SMmPOF at 26.6 °C and at 106.1 °C.

A total wavelength shift of -21.5 nm was achieved over the 79.5 °C temperature range. After the initial results, the experiment was repeated to see if the same spectral shift could be achieved. The temperature sensitivity of the initial and secondary heating can be seen in Figure 7-7.

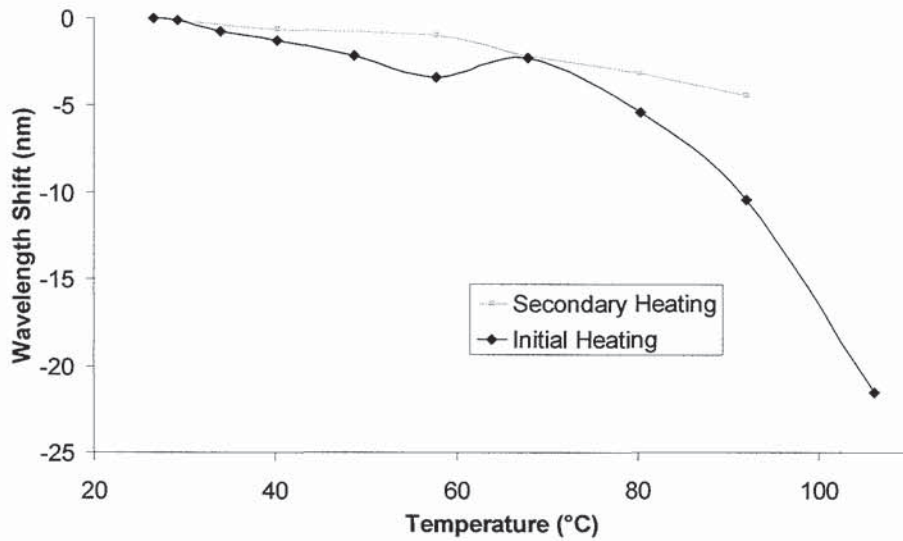


Figure 7-7: Temperature sensitivity of an FBG in SMmPOF. Black: Initial temperature cycling; Grey: second temperature cycle.

The temperature sensitivity of the secondary temperature cycling was measured to be $-63.3 \text{ pm}/^{\circ}\text{C}$ which is comparable with the temperature sensitivity of $-64.4 \text{ pm}/^{\circ}\text{C}$ recorded for the SMPengPOF.

The hysteresis of the room temperature spectral location of the grating was found to be 19.2 nm after the initial temperature cycling and no further hysteresis was observed during, or after, the second thermal cycle; see Figure 7-8. No hysteresis after the second cycle indicates that a permanent change in the material of the optical fibre occurred during the initial heating experiment with no changes occurring on subsequent heating.

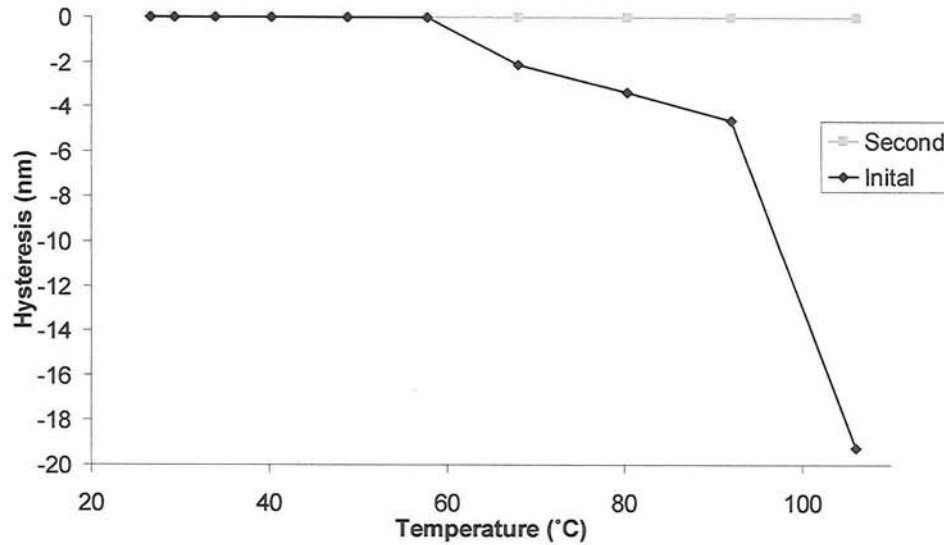


Figure 7-8: The shift in room temperature spectral location of the grating after each consecutive heating. The x-axis depicts the temperature the grating was heated to before returning to room temperature.

7.2.3 Explanation of Thermal Hysteresis

The observed hysteresis in the spectral location of the fibre Bragg grating at room temperature following heating can be explained by the mechanical changes which occur in PMMA at certain temperatures. The temperature sensitivity and hysteresis are intrinsically linked to the effect of temperature on the Young's Modulus, E , of PMMA; see Figure 7-9 [166].

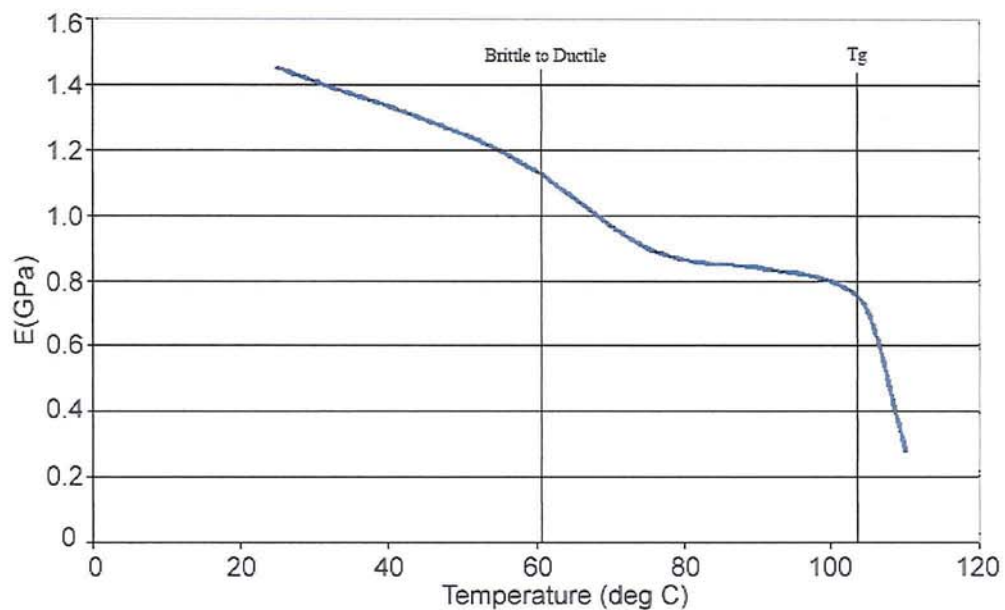


Figure 7-9: The effect of temperature on the young's modulus of PMMA. (graph obtained from [166]).

The distinctive shape of the graph in Figure 7-9 is very similar to that obtained for the temperature sensitivity and hysteresis of the FBG in mPOF (which is constructed of pure PMMA). Matsushige *et al* [146] in 1976 investigated the stress/strain characteristics of polystyrene and PMMA as a function of temperature and found a brittle-to-ductile transition to occur in PMMA at 50 °C. This is the yield point of the material after which the material no longer obeys Hooke's Law. In Figure 7-9 this transition occurs at 60 °C, the difference between this value and that reported by Matsushige *et al* (50 °C) is likely to be attributed to a difference in molecular weight [167]. The brittle-to-ductile transition is the point at which the material's fracture mechanism changes from being brittle (no plastic deformation) to ductile (extensive deformation due to the sliding of the polymer chains). Once this point is exceeded, the fibre and consequently the fibre Bragg grating experiences permanent deformation resulting in hysteresis. Figure 7-8 shows hysteresis occurred once temperatures over 58.8 °C had been reached. As well as this effect, the molecular rearrangement with temperature also contributes to the hysteresis with the consequent shortening of the fibre producing the permanent blue wavelength shift of the grating. Although this effect is less prolific in the microstructured POF, due to this fibre being drawn under less tension than the step index POF, it is still a contributory factor. The substantial decrease in the Young's Modulus shown in Figure 7-9 and Figure 7-8 is attributed to the polymer exceeding its glass transition temperature, T_g , which for PMMA is 105 °C.

7.2.4 Discussion

Fibre Bragg gratings inscribed into step index and microstructured POF have been shown to have enhanced temperature sensitivity over their silica counterparts. This enhanced sensitivity allows the potential use of lower resolution, simpler and therefore cheaper interrogation systems or alternatively enables accurate temperature monitoring over a small temperature range, for example for *in vivo* temperature profiling. The inherent biocompatibility of organic polymers makes them ideal for biomedical applications since

they eliminate the precautions needed to prevent silica fibre breakages, ultimately reducing the complexity of the device.

However, the grating in step-index POF was erased in the temperature range 68.0-80.3 °C. Consequently, an accurately defined operational temperature range needs to be identified before implementation into a commercial system can be achieved. Both gratings experienced hysteresis in the results upon exceeding a specific temperature limit; SMPengPOF in the range 48.8-57.8 °C and SMmPOF in the range 57.8-68.0 °C. Since different polymers have different stress/strain curves, FBGs inscribed into a variety of polymers will have different practical working limits. This presents an opportunity to choose polymers for specific applications. The two polymers presented here have upper limits higher than 48.8 °C which considering the maximum body temperature is approximately 40 °C makes them ideal for biomedical applications.

However, a lot of experiments still need to be conducted to help understand the mechanisms involved with these types of gratings and consequently evaluate their reliability and lifetime.

- Polymer is a very fluid material and so over time there is a possibility that any remaining monomer could diffuse into the grating region affecting the spectral profile.
- Accelerated aging experiments need to be conducted, for example, temperature cycling the gratings between 20-40 °C for extended periods of time to investigate if the grating deteriorates over continued use. Also standard annealing investigations need to be conducted to observe the evolution of a grating held at an elevated temperature for long periods of time.

- The investigations into the thermal response of the mPOF FBG showed that once 106.1 °C had been reached, subsequent temperature cycling experienced no hysteresis. Consequently, the thermal response of FBGs inscribed into pre-annealed fibre (105-110 °C for 2 days) needs to be investigated to see if the hysteresis can be eliminated.
- Thermal sensitivity experiments on fibre Bragg gratings inscribed in other types of polymer optical fibres to investigate if they have any beneficial characteristics.

7.3 Tuning Copper Coated Polymer Optical Fibre Bragg Gratings

Tunable fibre Bragg gratings which use thin film metallic layers deposited on the surface of the optical fibre as actuators have been shown to have applications in telecommunications [168-171]. Passing current through these metallic films causes joule heating to occur, the rate and magnitude of which depends on the electrical current and resistance of the coating. This process results in devices which are compact, have a fast response and good efficiency. Whilst these devices in silica-based optical fibres have been characterised [168-171], devices in polymer-based optical fibres are reported here. The different thermal conductivities and emissivities of glass and polymer result in differing responses.

7.3.1 Copper Coating Procedure

One centimetre long fibre Bragg gratings fabricated in single mode step-index POF (SM PengPOF) and single mode microstructured POF (SMmPOF) were sent to the Department of Electrical Engineering of University College London to be coated with a copper metallic layer. Unlike other metallic deposition techniques, their process operates at room temperature and at a low vacuum pressure of 10^{-2} mbar [172-173]. As shown by section 7.2, temperatures above 50 °C permanently change the spectral characteristics of the grating so the low temperature deposition was extremely important.

The metallic deposition was initiated by exposing the POF to a vacuum UV (VUV) light source operating at a wavelength of 172 nm. Section 5.6 demonstrated that the penetration depth of this wavelength in PMMA is in the order of a few microns and therefore causes no damage to the grating device. However, the UV light causes the surface of the POF to undergo a chemical roughing, since the radiation initiates bond scission. The resulting free radicals are consequently able to bond physically and chemically to the metallic particles. The VUV exposure times ranged from 1-10 minutes. The resulting deposited metallic thickness is determined by the concentration of a precursor and the UV irradiation time.

7.3.2 Wavelength Response of the Device

The metallic coating procedure was found to be successful for the step index POF with no deterioration of the spectral profile of the grating. However, the FBG in the microstructured POF did not survive the process. The transmission spectrum of the mPOF before and after the coating procedure is shown in Figure 7-10 and is synonymous with microstructured fibre which has experienced hole collapse along its structure. The hole collapse most likely occurred at the optical fibre mounting points in the vacuum chamber. The remaining experiments were consequently conducted using solely the step index POF.

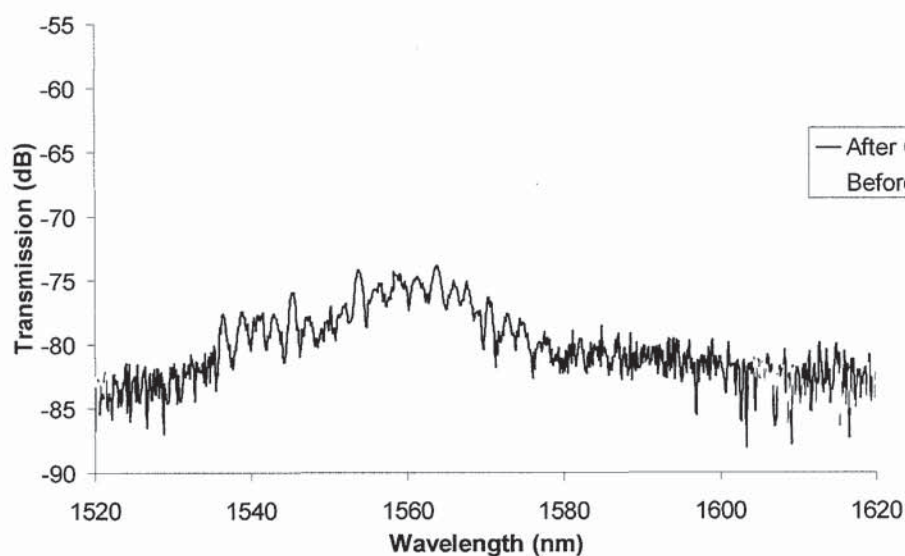


Figure 7-10: Transmission of ASE light source through SMmPOF before and after copper coating.

The copper coating on this particular fibre Bragg grating had a thickness of $\sim 8 \mu\text{m}$ around the whole of the fibre. Fine gauge copper wire was fixed to the thin metal film either side of the FBG using silver loaded paint. The separation of the electrodes was 12 mm encompassing the 10 mm FBG. The total resistance of the film surrounding the grating, and the connection via the copper wires and silver-loaded paint, was measured to be 3.2Ω . The induced wavelength shift caused by joule heating on passing a direct current through the metallic film is shown in Figure 7-11.

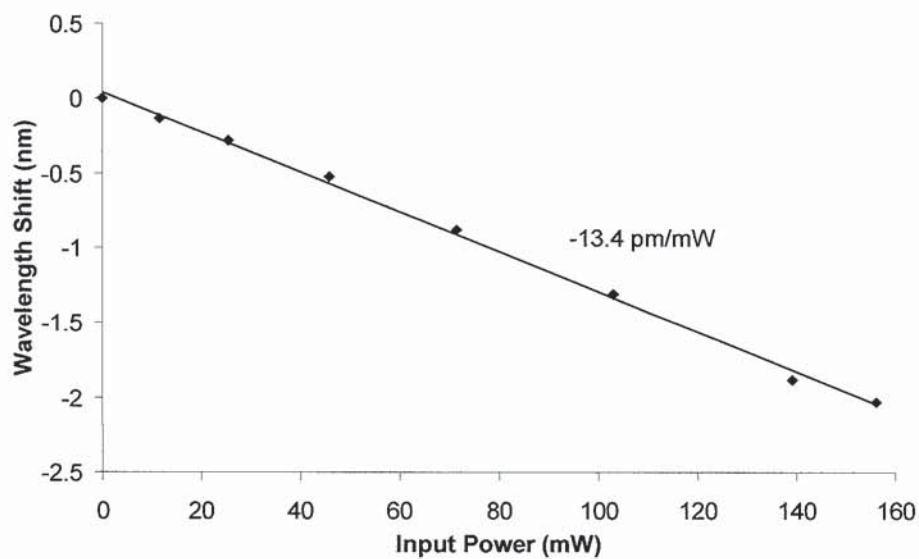


Figure 7-11: Wavelength Shift of the Bragg grating as a function of input power.

As the grating was tuned the grating spectrum remained unchanged indicating that heating was occurring uniformly across the grating. After each applied power setting, the electrical power was switched off to investigate any effects of hysteresis. None were observed. Figure 7-11 demonstrates a linear wavelength shift to applied power with a coefficient of -13.4 pm/mW . This coefficient demonstrates that this particular polymer device has a higher sensitivity compared with the results from Limberger *et al* [168] who measured a coefficient of 4.1 pm/mW for a silica FBG coated in 20 nm of titanium and 300 nm of platinum (Pt) and with the results from Rodgers *et al* [169] who measured a sensitivity of $\sim 3 \text{ pm/mW}$ for a silica FBG coated in 200 nm of Gold.

7.3.3 Tunable Filter Time Response

For switching applications it is important to know the response time of the filter for successful integration into an operational system. The response time was measured by recording the spectral location of the grating at set time intervals after a sudden application of power at $t=0$ s. The time response of the device can be seen in Figure 7-12 for three different electrical powers, 45.8, 71.5, and 103.2 mW.

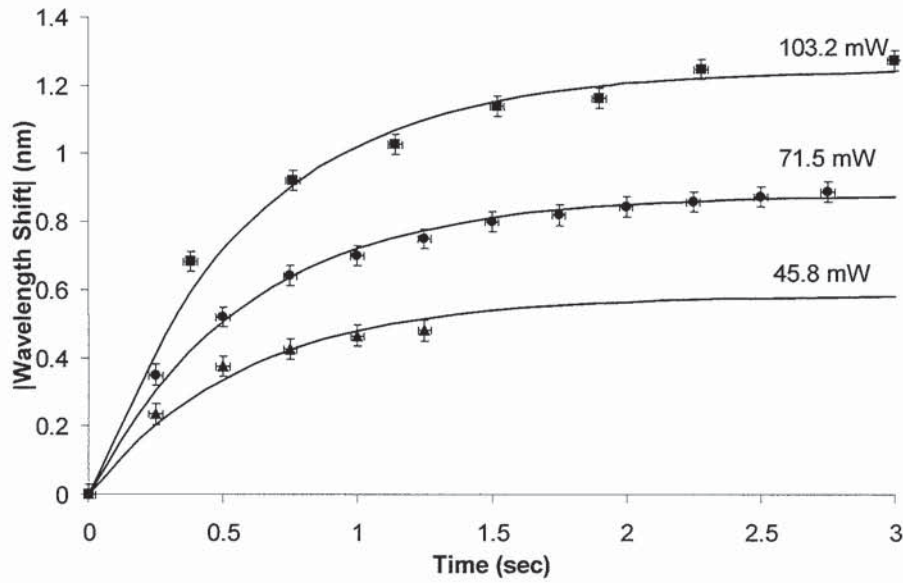


Figure 7-12: Rise time of thermally tuned fibre Bragg grating using a thin film copper coating as a resistive heater.

The filter response curves all fit a single exponential each with a time constant of $a=1.7\text{ s}^{-1}$ demonstrating that there is no dependence of the response time on the applied power. The time constant of the results presented by Rogers *et al* [169] was $\sim 2.5\text{ s}^{-1}$ demonstrating that the polymer tunable filter presented here not only has a higher coefficient but a quicker response time than reported silica optical fibre counterparts.

Rogers *et al* [169] demonstrated that a measurement of a provides information about the rate of heat flow out of the fibre and is related to the surface conductance of the fibre, h , by:

$$a = \frac{2h}{\rho c_p R_{fibre}}. \quad (7.3)$$

where ρ and c_p are the thermal density and constant pressure heat capacity of the polymer (or silica), respectively. R_{fibre} is the radius of the fibre which for the polymer optical fibre investigated here is 120 μm . A table comparing the typical values for these parameters in PMMA and silica is shown below [169,174].

Table 7.2: Table comparing parameters between the silica and polymer thin film heaters.

	ρ (kg/m ³)	c_p (J/kgK)	R_{fibre} (μm)
PMMA	1190	1450	120
Silica	2200	730	62.5

The surface conductance of the polymer optical fibre was calculated to be 110.0 W/m²K. This value is comparable to the surface conductance of the silica fibre used by Rogers *et al* [169] which was 125.5 W/m²K. Consequently, the main explanation for the difference in filter response time between the polymer and silica coated devices is the difference in constant pressure heat capacity between the two materials.

The heat flow through and along the surface of the fibre is characterised by the Biot number [169]:

$$Bi = \frac{hR_{fibre}}{\kappa}, \quad (7.4)$$

where κ is the thermal conductivity of the material; $\kappa_{PMMA}=0.17$ W/mK and $\kappa_{Silica}=1.38$ W/mK [170]. When the Biot number is less than 0.1, any thermal gradients that may exist radially across the grating become negligible since the thermal conductance over the length R_{fibre} is significantly greater than the surface conductance. The Biot number for the POF device was found to be 0.0485 compared with 0.0057 for the silica device used by Rogers *et al* [169]. Since the Biot number is less than 0.1, the POF device can be treated as a simple one-dimensional system, ignoring any radial thermal gradients and the effect of

the thin metal coating. Consequently, the temperature flow through the device is given by the equation [169]:

$$\frac{\partial T(x,t)}{\partial t} = \kappa \frac{\partial^2 T(x,t)}{\partial x^2} + \frac{P_{in}(x,t) - P_{out}(x,t)}{\rho c_p \pi R_{fibre}^2}, \quad (7.5)$$

where x is the distance along the fibre, $T(x,t)$ is the change in temperature, $P_{in}(x,t)$ is the heating generated by the thin film heater and $P_{out}(x,t)$ is the rate of heat loss from the fibre to the air. $P_{in}(x,t)$ is provided by:

$$P_{in}(x,t) = I^2(t)R(x), \quad (7.6)$$

where $I(t)$ is the electrical current and $R(x)$ is the resistance per unit length of the coating.

Making the assumption that the rate of flow is proportional to the change in temperature, $P_{out}(x,t)$ equals:

$$P_{out}(x,t) = a|T(x,t) - T_{air}|, \quad (7.7)$$

However, the heat loss from the metal to the air actually follows radiative heat transfer from two grey bodies in the form:

$$2\pi R_{fibre} \sigma (T(x,t)^4 - T_{air}^4) \quad (7.8)$$

where σ is the coefficient of thermal radiation dissipation, which given the low temperature range used here, can be approximated to:

$$(T(x,t) - T_{air}). \quad (7.9)$$

Consequently, since the rate of heat loss is linearly proportional to the change in temperature, $P_{out}(x, t)$ is provided by the equation:

$$P_{out}(x, t) = 2\pi R_{fibre} hT(x, t). \quad (7.10)$$

Rogers *et al* [169] state that when the input power is uniform the temperature variation as a function of time is defined by:

$$T(t) = \frac{P'_{in}}{a} [1 - \exp(-at)], \quad (7.10)$$

where P'_{in} is related to the input power, P_{in} , but depends on the thermal capacity of the PMMA and metal film by the equation:

$$P'_{in} = \frac{P_{in}}{\rho c_p V}, \quad (7.11)$$

where V is the volume of the fibre given by $V = \pi R_{fibre} L$ where L is the length of fibre heated, which for the polymer device was 12 mm.

Therefore the temperature reached by the fibre for the three different electrical power inputs was calculated and is shown in Table 7.3.

Table 7.3: Table showing the calculated temperatures of the three different electrical input power.

Input Power (P_{in})	Temperature ($^{\circ}\text{C}$)
45.8 mW	28.8
71.5 mW	44.9
103.2 mW	64.8

A graph of these temperatures with the corresponding fibre Bragg grating wavelength shift from room temperature is shown in Figure 7-13.

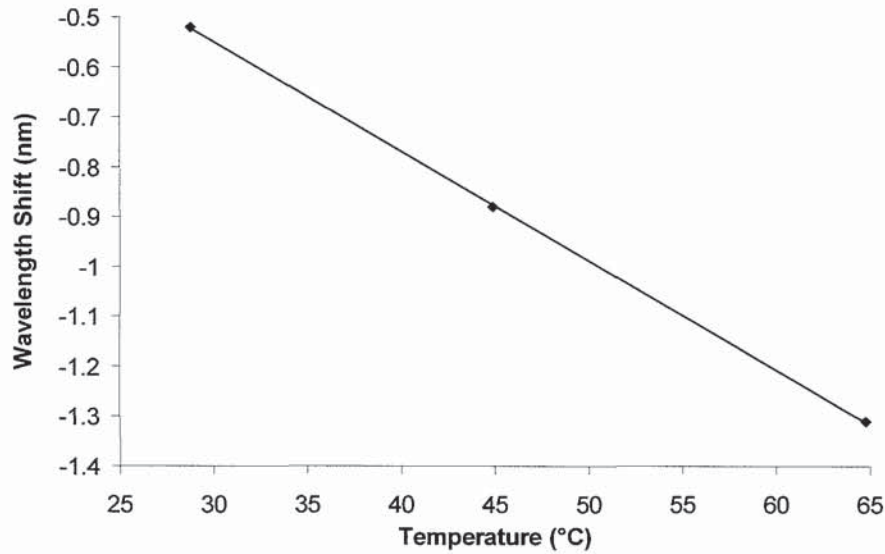


Figure 7-13: Temperature of the three input powers and the corresponding Bragg wavelength shift.

Figure 7-13 shows this device to have a temperature sensitivity of $-21.9 \text{ pm}/^{\circ}\text{C}$ which is approximately a third less sensitive than the $-64.4 \text{ pm}/^{\circ}\text{C}$ sensitivity shown in section 7.2.1.

The exact explanation for the difference in sensitivities is still under investigation. Mathematical investigations into whether any inaccuracies in the measurement of the fibre diameter and the length of copper being heated, could significantly affect the calculated temperature, revealed these to not account for the discrepancy. One potential explanation could arise from the constants, ρ (thermal density) and c_p (constant pressure heat capacity). The values of these constants used to calculate the temperatures were for pure PMMA. However, the core of the fibre investigated here consists of a mixture of methylmethacrylate, ethylmethacrylate and benzylmethacrylate. This could result in significantly different values for these constants which might help to account for the difference in thermal sensitivity.

No hysteresis was observed during the experiments. Since the temperature reached a calculated 64.8°C at an input power of 103.2 mW , hysteresis was expected. However, the expansion coefficient of copper is $1.7 \times 10^{-5} \text{ cm}/\text{cm}/^{\circ}\text{C}$ [175] which is less than the value of

8.0×10^{-5} cm/cm/°C for PMMA, the copper could restrict the expansion rate and molecular rearrangement of the polymer with temperature, resulting in the yield point of the stress/strain curves (i.e. the brittle to ductile transition) being shifted to a higher temperature.

7.3.4 Summary

An FBG in step index POF was successfully coated in a continuous layer of copper. The grating was thermally tuned via joule heating on passing an electric current through the metallic film. The grating device demonstrated a linear wavelength shift to applied electric power giving a coefficient of -13.4 pm/mW. The response time of the device was found to be 1.7 s⁻¹ which compared well against ~ 2.5 s⁻¹ reported for similar silica devices.

8

Thesis Conclusions

This thesis has been concerned with inscribing fibre gratings into alternative optical fibres with the aim of achieving enhanced or differing spectral sensitivity to various measurands. The results presented in this thesis have arisen from investigations using silica-based photonic crystal fibre and a variety of polymer optical fibres.

Long period gratings were fabricated into two different silica-based photonic crystal fibres using the electric-arc technique. Evaluation of the gratings revealed differing sensing characteristics between the two fibres attributed to the different air-hole geometries of the fibres. The spectral sensitivity of long period gratings depends on the dispersion properties of the optical fibres. Since the air-hole geometry dictates the dispersion characteristics of these fibres, different geometrical layouts result in different sensing characteristics. Consequently, these fibres have the potential to be designed specifically to have enhanced sensitivity to some measurands whilst removing any unwanted cross-sensitivity to other measurands.

Future research into using long period gratings in Photonic Crystal Fibre as sensing devices could include embedding the fibres into various substrates to investigate the mechanical robustness of these fibres for potential applications. Theoretical modelling on the sensing characteristics needs to be continued with the response to bending

investigated. Once full sensing performances are understood there is a potential to design these fibres for specific applications.

Fibre Bragg gratings have been successfully inscribed into step index and for the first time microstructured polymer optical fibre. A significant proportion of the PhD time was concerned with achieving a successful inscription set up in order to fabricate the gratings. It was found that for inscription to occur the fibre needed to be supported along its entire length, preventing fibre movement during fabrication. The orientation of the microstructured polymer optical fibre with respect to the incident inscription laser beam was also found to be critical for successful inscription. Thermal analysis of the gratings in both fibre types revealed a temperature sensitivity of ~ 64 pm/ $^{\circ}$ C up to a temperature of ~ 49 $^{\circ}$ C. Higher temperatures resulted in hysteresis in the room temperature location of the grating attributed to a physical change in the polymer. A fibre Bragg grating in standard step index polymer optical fibre was successfully coated in a thin layer of copper and tuned through joule-heating. Investigations into the response of this device demonstrated a higher coefficient of -13.4 pm/mW compared with a highest report coefficient of 4.1 pm/mW for a silica device.

Future work in this field is concerned with changing the properties of the metallic coating and investigating the resulting effect on the fibre Bragg gratings. For example, work is planned to coat a polymer fibre Bragg grating with a non-uniform thickness across the grating. When current is passed through a tapered coating, a temperature gradient is produced across the grating producing a chirp in the spectral profile of the grating. This can lead to applications in dispersion compensating systems. Further work is planned to change the coating material from copper to palladium. Optical fibres coated in a thin film of palladium have been shown to be good hydrogen sensors [176-177]. Upon exposure to hydrogen or a hydrogen containing gas, a hydride is formed in the palladium which has a lattice constant proportional to the hydride composition and consequently the concentration of hydrogen in the gas being sensed [176]. The coating expands with the

formation of the hydride which in turn stretches the optical fibre and shifts the Bragg wavelength of the fibre Bragg grating [177]. With the potentially high strain sensitivity of polymer fibre Bragg gratings [105] there is a possibility of an extremely sensitive hydrogen sensor. Detection of hydrogen leaks is extremely important for the prevention of explosions and is becoming essential with the development of hydrogen fuel cells for the automotive industry as an alternative fuel source.

There is still a significant amount of research to be conducted in the field of polymer optical fibre Bragg gratings. As stated in chapter 5, polymers containing hydrogen atoms absorb moisture. This presents the possibility of using fibre Bragg gratings inscribed in such polymers as humidity sensors. Also the strain response of these gratings needs to be investigated. Since polymers have a higher response to strain than silica, the strain response of fibre Bragg gratings is expected to be significantly higher leading to higher accuracy strain measurements. However, as shown in chapter 7, the Young's modulus is affected by relatively low temperatures and so not only does the effect of strain need investigating but also the effect of temperature on the strain response. Consequently, upper strain limits need to be established for different environmental conditions. Ultraviolet inscribed long period gratings have yet to be achieved in any polymer optical fibre. Since these gratings have enhanced sensitivity over fibre Bragg gratings in the same fibre, they are expected to have beneficial sensing qualities. Long period gratings inscribed into microstructured polymer optical fibre with asymmetric holey regions are also expected to have enhanced directional bend sensitivity over silica fibres making them ideal for shape sensing applications. Consequently, the ability to embed polymer optical fibre into composite materials for such applications also needs investigating. Polymer optical fibre is only in its infancy when compared to silica-based optical fibres so there is vast amounts of research to be conducted to fully unleash the potential of these fibres.

Apart from the work presented in this thesis, other alternative optical fibres types have been investigated in collaboration with Dr. Tom Allsop, also of the Photonics Group at

Aston. Long period gratings have been inscribed using 244 nm ultra-violet radiation in elliptical core three-layered D-shaped optical fibre. The gratings were polarisation sensitivity with a separation of around 15 nm between the two orthogonal polarisation states. Attenuation bands with overlapping orthogonal polarisation states were observed. Bending the grating devices resulted in sensitivities of -3.56 nm.m and $+6.51 \text{ nm.m}$ for convex and concave bending respectively demonstrating reasonable directional sensitivity with potential applications in shape sensing. The use of neighbouring attenuation bands to the overlapped orthogonally polarisation states enabled discrimination between temperature and bending effects.

Investigations have also been conducted on long period gratings fabricated into a concentric circularly symmetric progressive three-layered fibre. This long period grating had two attenuation bands associated with a single cladding mode which were located either side of a modal turning point (the point where the sign of the slope of a phase matching curve changes). On bending, one band experienced a blue wavelength shift and the other a red shift until the bands converged. This resulted in spectral sensitivities of $+22.3 \text{ nm.m}$ and -19.1 nm.m which are the highest values seen for this fibre.

All of these examples demonstrate the advantageous sensing characteristics that alternative optical fibres can provide and that it has been, and will be, worthwhile pursuing further research into this area. This has been reflected by the interest received from the worldwide research community with one invited paper being awarded on the long period gratings inscribed in photonic crystal fibre and three invited papers as a direct result of the work on polymer optical fibre gratings. Fibre gratings in polymer optical fibre have attracted special attention and as a result Aston University's Photonics Research Group has been approached by groups in Switzerland, France, Brazil, South Africa and Australia wanting to collaborate in this field as a direct result of the research presented in this thesis.

9

Publications

9.1 Publications on Work Reported in this Thesis

- [1] K. Kalli, H. Dobb, D.J. Webb, Q. Fang, I. Boyd and G.D. Peng. ‘Electrically tunable Bragg gratings in single mode polymer optical fibre.’ *Optics Letters*, 32 (3) (2007): 214-216
- [2] H. Dobb, K. Carroll, D.J. Webb, K. Kalli, M. Komodromos, C. Themistos, G.D. Peng, A. Argyros, M. Large, M. van Eijkelenborg, Q. Fang and I. Boyd. ‘Thermal response of Bragg gratings in POF.’ *The Joint International Conference on Plastic Optical Fibre and Microoptics 2006*, Seoul, Korea [B3-3] (2006)
- [3] J.S. Petrović, D.J. Webb, V. Mezentsev, H. Dobb, K. Kalli and I. Bennion. ‘Nondestructive index profiling of long period gratings in Photonic Crystal Fibres.’ Submitted to *Optical Quantum Electronics*
- [4] V. Mezentsev, J.S. Petrović, H. Dobb, D.J. Webb and I. Bennion. ‘Dynamics of the long period gratings in photonic crystal fibres as a tool for index profiling.’ *Proceedings of the XV International Workshop on Optical Waveguide Theory and Numerical Modelling*, (1) (2006): 59
- [5] J.S. Petrović, V. Mezentsev, H. Dobb, D.J. Webb, K. Kalli and I. Bennion. ‘Multiple-period resonances in long-period gratings in Photonic Crystal Fibre.’ *Optical and Quantum Electronics*, 38 (1-3) (2006): 209-216
- [6] H. Dobb, K. Kalli and D.J. Webb. ‘Measured sensitivity of long-period grating sensors in photonic crystal.’ *Optics Communications*, 260 (1) (2006): 184-191

- [7] T. Allsop, H. Dobb, A. Main, A. Martinez, M. Dubov, K. Kalli, D.J. Webb, I. Bennion. 'A comparison of the spectral properties of high temperature annealed long-period gratings inscribed by Femtosecond laser, UV and Fusion-Arc.' *Proceedings-SPIE The international Society For Optical Engineering-Photonics Europe '06*, Strasbourg, France [6193-14] (2006)
- [8] H. Dobb, K. Carroll, D.J. Webb, K. Kalli, M. Komodromos, C. Themistos, G.D. Peng, A. Argyros, M. Large, M. van Eijkelenborg, Q. Fang and I. Boyd. 'Reliability of fibre Bragg gratings in polymer optical fibre.' *Proceedings-SPIE The International Society For Optical Engineering-Photonics Europe '06*, Strasbourg, France [6193-16] (2006) Invited Paper
- [9] H. Dobb, K. Carroll, D.J. Webb, K. Kalli, M. Komodromos, C. Themistos, G.D. Peng, A. Argyros, M. Large, M. van Eijkelenborg, Q. Fang and I. Boyd. 'Grating based devices in polymer optical fibre.' *Proceedings-SPIE The International Society For Optical Engineering-Photonics Europe '06*, Strasbourg, France [6189-01] (2006) Invited Paper
- [10] D.J. Webb, M. Aressy, A. Argyros, J.S. Barton, H. Dobb, M.A. van Eijkelenborg, A. Fender, J.D.C. Jones, K. Kalli, S. Kukureka, M.C.J. Large, W. MacPherson, G.D. Peng and M. Silva-Lopez. 'Grating and Interferometric Devices in POF.' *Presented at the 14th International Conference for Polymer Optical Fibre*, Kowloon, HongHong (2005) pp 325 Invited Paper
- [11] H. Dobb, D.J. Webb, K. Kalli, A. Argyros, M.C.J. Large and M.A. van Eijkelenborg 'UV light induced fibre Bragg gratings microstructured polymer optical fibre.' *Presented at the 14th International Conference for Polymer Optical Fibre*, Kowloon, HongHong p341 (2005)
- [12] H. Dobb, D.J. Webb, K. Kalli, A. Argyros, M.C.J. Large and M.A. van Eijkelenborg. 'CW UV light induced fibre Bragg gratings in few- and single-moded microstructured polymer optical fibre.' *Optics Letters*, 30 (24) (2005): 3296-3298
- [13] M. Silva-Lopez, A. Fender, W.N. MacPherson, J.S. Barton, J.D.C. Jones, D. Zhao, H. Dobb, D.J. Webb, L. Zhang and I. Bennion. 'Strain and temperature sensitivity of a single-mode polymer optical fiber.' *Optics Letters*, 30 (23) (2005): 3129-3131
- [14] J.S. Petrović, V. Mezentssev, H. Dobb, D.J. Webb and I. Bennion. 'Multiple Period Resonances of Long Period Gratings in Photonic Crystal Fibre.' *Presented at the XIII International Workshop on Optical Waveguide Theory and Numerical Modelling*, Grenoble, France, [Sa3-6] (2005)

- [15] J.S. Petrović, V. Mezentsev, H. Dobb, D.J. Webb and I. Bennion. 'Multiple Period Resonances of Long Period Gratings in Photonic Crystal Fibre.' *Presented at the conference on Lasers and Electro-Optics*, Baltimore, USA [1:689] (2005)
- [16] H. Dobb, J.S. Petrović, V. Mezentsev, D.J. Webb and K. Kalli. 'Long-period grating sensors in photonic crystal fibre.' *Proceedings of the 17th International Conference on Optical Fibre Sensors (OFS 2005)*, Bruges, Belgium [23403] (2005)
- [17] H. Dobb, K. Kalli, D.J. Webb. 'Temperature insensitive long-period grating sensors in photonic crystal fibre.' *Proceedings-SPIE The International Society For Optical Engineering-Photonics North 04*, Ottawa, Canada [5579-09] (2004) Invited Paper
- [18] H. Dobb, K. Kalli, D.J. Webb. 'Temperature insensitive long-period grating sensors in photonic crystal fibre.' *Presented at Photon '04*, Glasgow, UK [OPD4.2] (2004)
- [19] H. Dobb, K. Kalli and D.J. Webb. 'Temperature insensitive long period grating sensors in photonic crystal fibre.' *Electronics Letters*, 40 (11) (2004): 657-658
- [20] D.J. Webb, T. Allsop, H. Dobb, K. Kalli, T. Earthrowl, V. Mezentsev, A. Gillooly, R. Neal, I. Bennion. 'Sensing applications of long-period gratings in various fibre types.' *Presented at the European Workshop for Optical Fibre Sensors (EWOFs '04)*, Santander, Spain, SPIE 4402 (2004): 104-107

9.2 Publications on Work Not Reported in this Thesis

- [1] K. Kalli, H. Dobb, G. Simpson, M. Komodromos, D. Webb and I. Bennion. 'Annealing and temperature coefficient study of Type IA fibre Bragg gratings inscribed under strain and no strain - implications to optical fibre component reliability.' *Proceedings-SPIE The International Society For Optical Engineering-Photonics Europe 06*, Strasbourg, France [6193-13] (2006)
- [2] T. Allsop, H. Dobb, V. Mezentsev, T. Earthgrowl, A. Gillooly, D.J. Webb and I. Bennion. 'The spectral sensitivity of Long Period Gratings fabricated in elliptical core D-Shaped Optical Fibre.' *Optics Communications*, 259 (2) (2006): 537-544
- [3] T. Allsop, H. Dobb, D.J. Webb, I. Bennion, R. Neal, D. Mapps and K Kalli. 'Enhanced spectral sensitivity of fibre long-period gratings to refractive index of aqueous solutions utilising copper patterned coatings.' *Proceedings-SPIE The International Society For Optical Engineering-Optics West '06*, San Jose, USA [6083-28] (2006)
- [4] A. Gillooly, H. Dobb, L. Zhang and I. Bennion. 'Distributed load sensor by use of a chirped moiré fiber Bragg grating.' *Applied Optics*, 43 (35) (2004): 6454-6457

- [5] T.D. Allsop, T. Earthrowl-Gould, H. Dobb, V. Mezentsev, D.J. Webb, A.M. Gillooly, I. Bennion. 'Spectral sensitivity of long-period gratings fabricated in elliptical core D-shaped optical fiber.' *Proceedings-SPIE The International Society For Optical Engineering-Optics East '04*, Philadelphia, USA [5589-36] (2004)
- [6] H. Dobb, T. Allsop, D.J. Webb, K. Kalli. 'Gratings in Novel Fibre Geometry for Applications in Shape Sensing.' *Proceedings-SPIE The International Society For Optical Engineering-Photonics Europe '04*, Strasbourg, France [5459-13] (2004)
- [7] H. Dobb, T. Allsop and D.J. Webb. 'Gratings in Novel Fibre Geometry for Applications in Shape Sensing.' *Presented at Photonex '03*, Coventry, UK (2003)

10

References

- [1] K.O. Hill, Y. Fujii, D.C. Johnson and B.S. Kawasaki. 'Photosensitivity in optical fiber waveguides: Application to reflection filter fabrication.' *Applied Physics Letters*, 32 (10) (1978): 647-649
- [2] F. Bilodeau, D.C. Johnson, S. Therault, B. Malo, J. Albert and K.O. Hill. 'An all-fiber dense-division multiplexer/demultiplexer using photo-imprinted Bragg gratings.' *IEEE Photonics Technology Letters*, 7 (4) (1995): 388-390
- [3] A. Othonos and K. Kalli. 'Fiber Bragg gratings: Fundamentals and applications in telecommunications and sensing.' *Artech House*, Boston, London (1999)
- [4] G.A. Ball and W.W. Morey. 'Continuously tunable single-mode erbium fiber laser.' *Optics Letters*, 17 (6) (1992): 420-422
- [5] www.spilasers.com
- [6] N.D. Dykes, M.J. O'Dwyer, S.W. James, R.P. Tatam, P.E. Irving, G.R. Tomlinson and W.A. Bullough, 'Mechanical and sensing performance of embedded in-fibre Bragg grating devices during impact testing of carbon fibre reinforced polymer composite.' *Workshop on Smart Systems Demonstrators: Concepts and Applications*, Harrogate, UK (1998): 168-175
- [7] G. Wang, K. Pran, G. Sagvolden, G.B. Havsgård, A.E. Jensen, G.A. Johnson and S.T. Vohra. 'Ship hull structure monitoring using fibre optic sensors.' *Smart Materials and Structures*, 10 (2002): 472-478
- [8] Y.J. Rao, D.A. Jackson, D.J. Webb, L. Zhang and I. Bennion. 'In-fibre Bragg grating flow-directed thermolulution catheter for cardiac monitoring.' *Proceedings of the Optical Fiber Sensors Conference (OFS 12)*, Williamsburg, USA (1997): 354-357
- [9] Y.J. Rao. 'In-fibre Bragg grating sensors.' *Measurement Science and Technology*, 8 (4) (1997): 355-375
- [10] H. Kogelnik. 'Theory of optical waveguides.' in *Guided Wave Optoelectronics*. T. Tamir Ed. New York: Springer Verlag, 1990.

- [11] T. Erdogan. 'Fiber Grating Spectra.' *Journal of Lightwave Technology*, 15 (8) (1997): 1277-1294
- [12] S.W. James and R.P. Tatam. 'Optical fibre long-period grating sensors: characteristics and application.' *Measurement Science and Technology*, 14 (2003): R49-R61
- [13] A.M. Vengsarkar, P.J. Lemaire, J.B. Judkins, V. Bhatia, T. Erdogan and J.E. Sipe. 'Long-period fibre gratings as band-rejection filters.' *Journal of Lightwave Technology*, 14 (1) (1996): 58-64
- [14] X. Shu, L. Zhang and I. Bennion. 'Sensitivity characteristics of long period fiber gratings.' *Journal of Lightwave Technology*, 20 (2) (2002): 255-266
- [15] T. Erdogan. 'Cladding-mode resonances in short and long period fiber gratings filters.' *Journal of the Optical Society of America, A*, 14 (8) (1997): 1760-1773
- [16] A. Yariv. 'Coupled-mode theory for guided wave optics.' *IEEE Journal of Quantum Electronics*, QE9 (1973): 919-933
- [17] P.St.J. Russell, J.L. Archambault and L. Reekie. 'Fibre gratings.' *Physics World*, October 1993: 41-46
- [18] G. Meltz and W.W. Morey. 'Bragg grating formation and germaosilicate fiber photosensitivity.' *International Workshop on Photoinduced Self-Organization Effects in Optical Fibre*, Quebec City, Quebec, May 10-11, Proceedings SPIE, 1516, (1991): 47-54
- [19] A.D.Kersey, M.A. Davies, H.J. Patrick, M. LeBlanc, K.P. Koo, C.G. Askins, M.A. Putman and E.J. Friebele. 'Fibre grating sensors.' *Journal of Lightwave Technology*, 15 (8) (1997): 1442-1463
- [20] V. Bhatia. 'Applications of long-period grating to single and multi-parameter sensing.' *Optics Express*, 4 (11) (1999): 457-466
- [21] M.P. DeLisa, Z. Zhang, M. Shiloach, S. Pilevar, C.C. Davis, J.S. Sirkis and W.E. Bentley. 'Evanescent wave long period fiber Bragg gratings as an immobilized antibody biosensor.' *Analytical Chemistry*, 72 (2000): 2895-900
- [22] D.M. Constantini, C.A.P. Muller, S.A. Vasiliev, H.G. Limberger and R.P. Salathe. 'Tunable loss filter based on metal coated long-period fibre grating.' *IEEE Photonics Technology Letters*, 11 (11) (1999): 1458-1460
- [23] S.W. James, N.D. Rees, G.J. Ashwell and R.P. Tatam. 'Optical fibre long period gratings with Langmuir Blodgett thin film overlays.' *Optics Letters*, 27 (9) (2002): 686-688
- [24] Y. Liu, L. Zhang, J.A.R. Williams and I. Bennion. 'Bend sensing by measuring the resonance splitting of long-period fibre gratings.' *Optics Communications*, 193 (2001): 69-72
- [25] G. Meltz, W. Morey and W. Glenn. 'Formation of Bragg gratings in optical fibres by a transverse holographic method.' *Optics Letters*, 14 (11) (1989): 823-825
- [26] R. Kashyap. 'Fiber Bragg Gratings.' Academic Press, 1999
- [27] K.O. Hill, B. Malo, F. Bilodeau, D.C. Johnson and J. Albert. 'Bragg gratings fabricated in monomode photosensitive optical fibre by UV exposure through a phase mask.' *Applied Physics Letters*, 62 (1993): 1035-1037
- [28] D.Z. Anderson, V. Mizrahi, T. Erdogan and A.E. White. 'Production of in-fibre gratings using a diffractive optical element.' *Electronics Letters*, 29 (6) (1993): 566-568

- [29] P.E. Dyer, R.J. Farley and R. Giedl. 'Analysis of grating formation with excimer laser irradiated phase masks.' *Optics Communications*, 115 (1995): 327-334
- [30] Z. Xiong, G.D. Peng, B. Wu and P.L.Chu. 'Effects of the Zeroth-order diffraction of a phase mask on Bragg gratings.' *Journal of Lightwave Technology*, 17 (11) (1999): 2361-2365
- [31] Q. Zhang, D.A. Brown, L. Reinhart, T.F. Morse, J.Q.Wang and G. Xiao. 'Tuning Bragg wavelength by writing gratings on restrained fibers.' *IEEE Photonics Technology Letters*, 6 (7) (1994): 839-841
- [32] B. Malo, K.O. Hill, F. Bilodeau, D.C. Johnson and J. Albert. 'Point-by-point fabrication of micro-Bragg gratings in photosensitive fibre using single excimer pulse refractive index modification techniques.' *Electronics Letters*, 29 (18) (1993): 1668-1669
- [33] A. Martinez, M. Dubov, I. Khrushchev and I. Bennion. 'Direct writing of fibre Bragg gratings by femtosecond laser.' *Electronics Letters*, 40 (19) (2004): 1170-1171
- [34] L. Zhang, Y. Liu, L. Everall, J. Williams and I. Bennion. 'Design and realization of long-period grating devices in conventional and high birefringence fibers and their novel applications as fiber-optic load sensors.' *IEEE Journal of Selected Topics in Quantum Electronics*, 5 (5) (1999): 1373-1378
- [35] M. Fujumaki, Y. Ohki, J.L. Brebner and S. Roorda. 'Fabrication of long-period optical fibre gratings by use of ion implantation.' *Optics Letters*, 25 (2) (2000): 88-90
- [36] Y. Kondo, K. Nouchi, T. Mitsuyu, M. Watanabe, P. Kazansky and K. Hirao. 'Fabrication of long-period fibre gratings by focused irradiation of infra-red femtosecond laser pulses.' *Optics Letters*, 24 (10) (1999): 646-648
- [37] A. Dragomir, D.N. Nikogosyan, A.A. Ruth, K.A. Zagorul'ko and P.G. Kryukov. 'Long-period fibre grating formation with 264nm femtosecond radiation.' *Electronics Letters*, 38 (6) (2002): 269-270
- [38] M. Dubov, I. Bennion, S.A. Slattery and D.N. Nikogosyan. 'Strong long-period fiber gratings recorded at 352 nm'. *Optics Letters*, 30 (19) (2005): 2533-2535
- [39] D.D. Davis, T.K. Gaylord, E.N. Glytsis, S.G. Kosinski, S.C. Mettler and A.M. Vensarkar. 'Long-period fibre grating fabrication with focused CO₂ laser beams.' *Electronics Letters*, 34 (3) (1998): 302-303
- [40] D.D. Davis, T.K. Gaylord, E.N. Glytsis and S.C. Mettler. 'Very-high-temperature stable CO₂-laser-induced long-period fibre gratings.' *Electronics Letters*, 35 (9) (1999): 740-742
- [41] S.G. Kosiniski and A.M. Vengsarkar. 'Splice-based long-period fiber gratings.' *In OFC'98 Tech. Dig, ThG3*: 278-279
- [42] G. Rego, O. Okhotnikov, E. Dianov and V. Sulimov. 'High-temperature stability of long-period fiber gratings produced using an electric arc.' *Journal of Lightwave Technology*, 19 (10) (2001): 1574-1579
- [43] G. Rego, P.V.S Marques and J.L. Santos. 'Arc-induced long-period gratings.' *Fiber and Integrated Optics*, 24 (3/4) (2005): 245-259
- [44] J.W. Berthold III. 'Historical Review of Microbend Fiber-Optic Sensors.' *Journal of Lightwave Technology*, 13 (7) (1995): 1193-1199

- [45] G.M. Rego, P.V.S. Marques, J.L. Santos and H.M. Salgado. 'Estimation of the fibre temperature during the inscription of arc-induced long-period gratings.' *Optics Communications*, 259 (2) (2006): 620-625
- [46] J.M Senior. 'Optical fiber communications, principles and practice.' (Prentice Hall, New York 1992)
- [47] A. Malki, G. Humbert, Y. Ouerdane, A. Boukhenter and A. Boudrioua. 'Investigation of the writing mechanism of electric-arc-induced long-period fiber gratings.' *Applied Optics*, 42 (19) (2003): 3776-3779
- [48] D.P. Hand and P.St.J. Russell. 'Photoinduced refractive-index changes in germanosilicate fibers.' *Optics Letters*, 15 (2) (1990): 102-104
- [49] H.G. Limberger, P.-Y. Fonjallaz, R.P. Salathé and F. Cochet. 'Compaction and photoelastic-induced index changes in fibre Bragg gratings.' *Applied Physics Letters*, 68 (22) (1996): 3069-3071
- [50] B. Pommellec, P. Niay, M. Douay, and J.F. Bayon. 'The UV-induced refractive index grating in Ge:SiO₂ preforms: Additional CW experiments and the microscopic origin of the change in index.' *Journal of Physics D: Applied Physics*, 29 (7) (1996): 1842-1856
- [51] E.J. Friebele, D.L. Griscom and G.H. Sigel, Jr. 'Defect centres in a germanium-doped silica-core optical fiber.' *Journal of Applied Physics*, 45 (8) (1974): 3424-3428
- [52] E.J. Friebele and D.L. Griscom. 'Color centers in glass optical fiber waveguides.' *Materials Research Society Symposium Proceedings*, 61 (1986): 319-331
- [53] P.St.J. Russell, D.P. Hand and L.J. Poyntz-Wright. 'Frequency doubling, absorption grating formation in glass fibres: Effective defects or defective effects?' *Fiber Laser Sources and Amplifiers II, Proceedings SPIE*, 1373 (1990): 126-139
- [54] P.St.J. Russell, D.P. Hand and Y.T. Chow. 'Optically-induced creation, transformation and organisation of defects and colour-centres in optical fibres.' *International Workshop on Photoinduced Self-Organization Effects in Optical Fiber*, Quebec City, Quebec, May 10-11, Proceedings SPIE, 1516 (1991): 47-54
- [55] P.J. Lemaire, R.M. Atkins, V. Mizrahi and W.A. Reed. 'High pressure H₂ loading as a technique for achieving ultra high UV photosensitivity and thermal sensitivity in GeO₂ doped optical fibres.' *Electronics Letters*, 29 (13) (1993): 1191-1193
- [56] R.M. Atkins, P.J. Lemaire, T. Erdogan and V. Mizrahi. 'Mechanisms of enhanced UV photosensitivity via hydrogen loading in germanosilicate glasses.' *Electronics Letters*, 29 (14) (1993): 1234-1235
- [57] P.J. Lemaire. 'Reliability of optical fibres exposed to hydrogenation: prediction of long-term loss increases.' *Optical Engineering*, 30 (6) (1991): 780-789
- [58] Y. Kato, S. Seikai and M. Tateda. 'Arc-fusion splicing of single-mode fibers. 1: Optimum splice conditions.' *Applied Optics*, 21 (7) (1982): 1332-1336
- [59] J.N. Jang, H.G. Kim, S.G. Shin, M.S. Kim, S.B. Lee and K.H. Kwack. 'Effects of hydrogen molecule diffusion on LP_{0m} mode coupling of long-period gratings.' *Journal of Non-Crystalline Solids*, 259 (1999): 156-164
- [60] K. Fujita, Y. Masuda, K. Nakayama, M. Ando, K. Sakamoto, J-P. Mohri, M. Yamauchi, M. Kimura, Y. Mizutani, S. Kimura, T. Yokouchi, Y. Suzaki and S. Ejima. 'Dynamic evolution of the spectrum of long-period fiber Bragg gratings fabricated from

- hydrogen-loaded optical fiber by ultraviolet laser irradiation.' *Applied Optics*, 44 (33) (2005): 7023-7038
- [61] S.H. Nam, C. Zhan, J. Lee, C. Hahn, K. Reichard, P. Ruffin, K-L. Deng and S. Yin. 'Bend-insensitive ultra short long-period gratings by the electric arc method and their applications to harsh environmental sensing and communication.' *Optics Express*, 13 (3) (2005): 731-737
- [62] www.cost270.com
- [63] T. Erdogan, V. Mizrahi, P.J. Lemaire and D. Monroe. 'Decay of ultraviolet induced fiber Bragg gratings.' *Journal of Applied Physics*, 76 (1) (1994): 73-80
- [64] S.R. Baker, H.N. Rourke, V. Baker and D. Goodchild. 'Thermal decay of fiber Bragg gratings written in boron and germanium codoped silica fiber.' *Journal of Lightwave Technology*, 15 (8) (1997): 1470-1477
- [65] T. Allsop, H. Dobb, A. Main, A. Martinez, M. Dubov, K. Kalli, D.J. Webb, I. Bennion. 'A comparison of the spectral properties of high temperature annealed long-period gratings inscribed by Femtosecond laser, UV and Fusion-Arc.' *Proceedings-SPIE The international Society For Optical Engineering-Photonics Europe 06*, Strasbourg, France 6-8th September [6193-14]
- [66] W.D. Kingery, H.K. Bowen and D.R. Uhlmann. 'Introduction to Ceramics.' New York: Wiley (1976): 595-603, 704-766
- [67] A. Fernandez Fernandez, B. Brichard, F. Berghmans and M. Decréton. 'Dose-rate dependencies in gamma-irradiated in-fiber Bragg gratings.' *IEEE Transactions on Nuclear Science*, 49 (2002): 2874-2878
- [68] G. Rego, A. Fernandez Fernandez, A. Gusarov, B. Brichard, F. Berghmans, J.L. Santos and H.M. Salgado. 'Effect of ionizing radiation on the properties of arc-induced long-period fiber gratings.' *Applied Optics*, 44 (29) (2005): 6258-6263
- [69] H. Patrick, G.M. Williams, A.D. Kersey, J.R. Pedrazzani and A.M. Vengsarkar. 'Hybrid fiber Bragg grating/long period fiber grating sensor for strain/temperature discrimination.' *IEEE Photonics Technology Letters*, 8 (9) (1996): 1223-1225
- [70] T. Allsop, L. Zhang, D.J. Webb and I. Bennion. 'Discrimination between strain and temperature effects using first and second-order diffraction from a long-period grating.' *Optics Communications*, 211 (2002): 103-108
- [71] V. Bhatia, D. Champbell, R.O. Claus and A.M. Vengsarkar. 'Simultaneous strain and temperature measurement with long-period gratings.' *Optics Letters*, 22 (9) (1997): 648-650
- [72] T. Allsop, D.J. Webb and I. Bennion. 'Bend and index insensitive long period grating in progressive three layered optical fibre.' *Electronics Letters*, 39 (6) (2003): 508-509
- [73] R.P. Espindola, R. Windler, A. Abramov, B. Eggleton, T. Strasser and D. DiGiovanni. 'External refractive index insensitive air-clad long period fibre grating.' *Electronic Letters*, 35 (4) (1999): 327-328
- [74] L. Dong, L. Reekie and J.L. Cruz. 'Long period gratings formed in depressed cladding fibres.' *Electronics Letters*, 33 (22) (1997): 1897-1898
- [75] V. Bhatia, D.K. Campbell, D. Sherr, T.G. D'Alberto, N.A. Zabaronick, G.A. Ten Eyck, K.A. Murphy and R.O. Claus. 'Temperature-insensitive and strain insensitive long-

- period grating sensors for smart structures.' *Optical Engineering*, 36 (7) (1997): 1872-1876
- [76] T.A. Birks, J.C. Knight and P. St. J. Russell. 'Endlessly single-mode photonic crystal fibre.' *Optics Letters*, 22 (13) (1997): 961-963
- [77] J.C. Knight, T.A. Birks, P.St.J. Russell and D.M. Atkin. 'All-silica single-mode optical fiber with photonic crystal cladding.' *Optics Letters*, 21 (19) (1996): 1547-1549
- [78] J. Broeng, D. Mogilevestev, S.E. Barkou and A. Bjarklev. 'Photonic Crystal Fibres: A new class of optical waveguides.' *Optical Fiber Technology*, 5 (3) (1999): 305-330
- [79] J.C. Knight, T.A. Birks, P.St.J. Russell and J.P. Sandro 'Properties of photonic crystal fiber and the effective index model.' *Journal of the Optical Society of America, Part A*, 15 (3) (1998): 748-752
- [80] B.J. Eggleton, P.S. Westbrook, R.S. Windeler, S. Spälter, and T.A. Strasser. 'Grating resonances in air-silica microstructured optical fibres.' *Optics Letters*, 24 (21) (1999): 1460-1462
- [81] G. Humbert, A. Malki, S. Février, P. Roy and D. Pagnoux. 'Electric arc-induced long-period grating in Ge-free air-silica microstructure fibres.' *Electronics Letters*, 39 (4) (2003): 349-340
- [82] J.H. Lim, K.S. Lee, J.C. Kim and B.H. Lee. 'Tunable fiber gratings fabricated in photonic crystal fiber by use of mechanical pressure.' *Optics Letters*, 29 (4) (2004): 331-333
- [83] www.crystal-fibre.com
- [84] PhD Thesis: Jovana Petrović. 'Modelling of Long Period Gratings in PCFs inscribed by an Electric Arc and Gratings in SMF Inscribed by Femtosecond Laser Pulses.' Aston University, November 2006.
- [85] G. Humbert and A. Malki. 'Electric-arc-induced gratings in non-hydrogenated fibres: fabrication and high-temperature characterizations.' *Journal of optics A: Pure and Applied Optics*, 4 (2) (2002): 194-198
- [86] T. Allsop, T. Earthrowl-Gould, D.J. Webb and I. Bennion. 'Embedded progressive-three-layered fiber long-period gratings for respiratory monitoring.' *Journal of Biomedical Optics*, 8 (3) (2003): 552-558
- [87] T. Allsop, A. Gillooly, V. Mezentsev, T. Earthgrowl-Gould, R. Neal, D.J. Webb and I. Bennion. 'Bending and orientational characteristics of long period gratings written in D-shaped optical fibre.' *IEEE Transactions on Instrumentation and Measurement*, 53 (1) (2004): 130-135
- [88] T. Allsop, H. Dobb, V. Mezentsev, T. Earthgrowl, A. Gillooly, D.J. Webb and I. Bennion. 'The spectral sensitivity of long period gratings fabricated in elliptical core D-shaped optical fibre.' *Optics Communications*, 259 (2) (2006): 537-544
- [89] H.J. Patrick. 'Self-aligning, bipolar bend transducer based on long period grating written in eccentric core fibre.' *Electronics Letters*, 36 (21) (2000): 1763-1764
- [90] T. Allsop, M. Dubov, A. Martinez, F. Floreani, I. Khrushchev, D.J. Webb and I. Bennion. 'Long period grating directional bend sensor based on asymmetric index modification of cladding.' *Electronics Letters*, 41 (2) (2005): 59-60

- [91] W. Du, H. Tam, M. Liu, and X. Tao. 'Long-period fiber grating bending sensors in laminated composite structure.' SPIE Conf. Proc. Smart structures and materials, SPIE, San Diego, 1998, Vol. 3330, pp 284-292
- [92] G. Rego, P.V.S. Marques, H.M. Salgado and J.L. Santos. 'Simultaneous measurement of temperature and strain based on arc-induced long-period fibre gratings.' *Electronics Letters*, 41 (2) (2005): 60-61
- [93] G.B. Hocker. 'Fibre-optic sensing of pressure and temperature.' *Applied Optics*, 18 (9) (1979): 1445-1448
- [94] D.J. Webb, T. Allsop, H. Dobb, K. Kalli, T. Earthrowl, V. Mezentsev, A. Gillooly, R. Neal, I. Bennion. 'Sensing applications of long-period gratings in various fibre types.' *Presented at the European Workshop for Optical Fibre Sensors (EWOFS '04)*, Santander, Spain, SPIE 4402 (2004): 104-107
- [95] T. Ishigure, E. Nihei, S. Yamazaki, K. Kobauahi and Y. Koike. '2.5 Gbit/s 100m data transmission using graded-index polymer optical fibre and high speed laser diode at 650nm wavelength.' *Electronics Letters*, 31 (6) (1995): 467-468
- [96] I.T. Monroy, H.P.A. vd Boom, A.M.J. Koonen, G.D. Khoe, Y. Watanabe, Y. Koike, and T. Ishigure. 'Data transmission over polymer optical fibers.' *Optical Fiber Technology*, 9 (3) (2000): 159-171
- [97] Y. Koike. 'Status of POF for Broadband Society.' Int. Conf. On Polymer Optical Fiber (POF 2005), Hong Kong, 20-22 Sept
- [98] Asahi Glass Company, Lucina: Graded Index-Cytop Optical Fiber. www.agc.co.jp/english
- [99] W. Daum, J.Krauser, P.E. Zamzow and O. Ziemann. 'Polymer Optical Fibers for Data Communication.' Springer (Verlag Berlin 2002)
- [100] G. Giaretta, W. White, M. Wegmuller and T. Onishi. 'High speed (11 Gbit/s) Data Transmission using perfluorinated graded-index polymer optical fibers for short interconnects (<100m).' *IEEE Photonics Technology Letters*, 12 (3) (2000): 347-349
- [101] A. Kondo, T. Ishigure and Y. Koike. 'Fabrication process and optical properties of perdeuterated graded-index polymer optical fiber.' *Journal of Lightwave Technology*, 23 (8) (2005): 2443-2448
- [102] Z. Xiong, G.D. Peng, B. Wu and P.L. Chu. 'Highly tunable Bragg gratings in single mode polymer optical fibers.' *IEEE Photonics Technology Letters*, 11 (3) (1999): 352-354
- [103] A.M. Gillooly, L. Zhang and I. Bennion. 'Implementation of a distributed temperature sensor utilising a chirped moiré fibre Bragg grating.' *Optics Communications*, 242 (2004): 511-515
- [104] S. Legoubin, M. Douay, P. Bernage, and P. Niay, S. Boj and E. Delevaque. 'Free spectral range variations of grating-based Fabry-Perot filters photowritten in optical fibres.' *Journal of the Optical Society of America, A*: 12 (8) (1995): 1687-1694
- [105] H.B. Liu, H.Y. Liu, G.D. Peng and P.L. Chu. 'Strain and temperature sensor using a combination of polymer and silica fibre Bragg gratings.' *Optics Communications*, 219 (2003): 139-142

- [106] D.J. Webb, M.W. Hathaway, D.A. Jackson, S. Jones, L. Zhang and I. Bennion. 'First in-vivo trials of a fiber Bragg grating based temperature profiling system.' *Journal of Biomedical Optics*, 5 (1) (2000): 45-50
- [107] Y.J. Rao, D.J. Webb, D.A. Jackson, L. Zhang and I. Bennion. 'In-situ temperature monitoring in NMR machines with a prototype in-fibre Bragg grating sensors system.' Proceeding of the Optical Fiber Sensors conference (OFS-12), Williamsburg, VA, USA (1997): 646-649
- [108] A. Argyros, I.M. Bassett, M.A. van Eijkelenborg, M.C.J. Large, J. Zagari, N.A.P. Nicorovici, R.C. McPhedran and C. Martijn de Sterke. 'Ring structures in microstructured polymer optical fibres.' *Optics Express*, 9 (13) (2001): 813-820
- [109] N.P. Bansal, R.H. Doremus. 'Handbook of Glass Properties.' New York Academic (1986)
- [110] H.M. Reeve, A.m. Mescher and A.F. Emery. 'Steady-state heat transfer and draw force for POF manufacture.' Int. Conf. On Polymer Optical Fiber (POF 2003), Seattle, USA, 15-17 Sept: 220
- [111] S. Wu. 'Surface and interfacial tensions of polymer melts. II Poly (methylmethacrylate), poly (*n*-butylmethacrylate), and polystyrene.' *Journal of Physical Chemistry*, 74 (3) (1970): 632-638
- [112] A.D. Fitt, K. Furusawa, T.M. Monro and C.P. Please. 'Modelling the fabrication of hollow fibers: capillary drawing.' *Journal of Lightwave Technology*, 19 (12) (2001): 1924-1932
- [113] M.A. van Eijkelenborg. 'Imaging with microstructured polymer fibre.' *Optics Express*, 12 (2) (2004): 342-346
- [114] <http://www.newscientist.com/article.ns?id=dn4589>
- [115] J. Ballato, S.H. Foulger and D.W. Smith Jr. 'Optical properties of perfluorocyclobutyl polymers. II. Theoretical and experimental attenuation.' *Journal of the Optical Society of America B*, 21 (5) (2004): 958-967
- [116] Polymer Handbook (John Wiley & Sons, New York, 4th edition, 1999)
- [117] H.Y. Liu, G.D. Peng and P.L. Chu. 'Thermal stability of gratings in PMMA and CYTOP polymer fibres.' *Optics Communications*, 204 (2002): 151-156
- [118] www.paradigmoptics.com
- [119] W.J. Tomlinson, I.P. Kaminow, E.A. Chandross, R.L. Fork and W.T. Silfvast. 'Photoinduced Refractive Index Increase in Poly(Methylmethacrylate) and its Applications.' *Applied Physics Letters*, 16 (12) (1970): 486-489
- [120] J.M. Moran and I.P. Kaminow. 'Properties of Holographic Gratings Photoinduced in Polymethyl Methacrylate.' *Applied Optics*, 12 (8) (1973): 1964-1970
- [121] M.J. Bowden, E.A. Chandross and I.P. Kaminow. 'Mechanism of the Photoinduced Refractive Index Increase in Polymethyl Methacrylate.' *Applied Optics*, 13 (1) (1974): 112-117
- [122] D.W. Garvey, K. Zimmerman, P. Young, J. Tostenrude, J.S. Townsend, Z. Zhou, M. Lobel, M. Dayton, R. Wittorf, M.G. Kuzyk, J. Sounick and C.W. Dirk. 'Single-mode nonlinear-optical polymer fibers.' *Journal of the Optical Society of America B*, 13 (9) (1996): 2017-2023

- [123] C. Jiang, M.G. Kuzyk, J.-L. Ding, W.E. Johns and D.J. Welker. 'Fabrication and mechanical behaviour of dye-doped polymer optical fiber.' *Journal of Applied Physics*, 92 (1) (2002): 4-12
- [124] G. Barton, M.A. van Eijkelenborg, G. Henry, M.C.J. Large and J. Zagari. 'Fabrication of microstructured polymer optical fibres.' *Optical Fiber Technology*, 10 (4) (2004): 325-335
- [125] M.A. van Eijkelenborg, A. Argyros, G. Barton, I.M. Bassett, M. Fellew, G. Henry, N.A. Issa, M.C.J. Large, S. Manos, W. Padden, L. Poladian and J. Zagari. 'Recent process in microstructured polymer optical fibre fabrication and characterisation.' *Optical Fiber Technology*, 9 (4) (2003): 199-209
- [126] T. Kaino. 'Polymer Optical Fibers,' in *Polymers for Lightwave and Integrated Optics: technology and applications*. (L. Hornak, ed., M. Dekker, New York, 1992)
- [127] T. Ishigure, Y. Koike and J.W. Fleming. 'Optimum index profile of the perfluorinated polymer-based GI polymer optical fiber and its dispersion properties.' *Journal of Lightwave Technology*, 18 (2) (2000): 178-184
- [128] H.P.A. van den Boom, W. Li, P.K. van Bennekorn, I. Tafur Monroy and G.-D. Khoe. 'High-capacity transmission over polymer optical fiber.' *IEEE Journal on Selected Topics in Quantum Electronics*, 7 (3) (2001): 461-470
- [129] T. Kaino. 'Influence of water absorption on plastic optical fibers.' *Applied Optics*, 24 (23) (1985): 4192-4195
- [130] J. Ballato, D.W. Smith Jr, S.H. Foulger and E. Wagener. 'Theoretical performance of polymer optical fibers, planar waveguides and amplifiers.' *Proceedings of the SPIE*, vol 4805 (2002): 1-8, "Design and fabrication of planar optical waveguide devices and material"
- [131] C.E. Barnes. 'Mechanism of Vinyl Polymerization.' 1. Role of Oxygen.' *Journal of the American Chemical Society*, 67 (2) (1945): 217-220
- [132] M.P. Hiscocks, M.A. van Eijkelenborg, A. Argyros and M.C.J. Large. 'Stable imprinting of long-period gratings in microstructured polymer optical fibre.' *Optics Express*, 14 (11) (2006): 4644-4649
- [133] C. Wochnowski, S. Metev, G. Sepold. 'UV-laser-assisted modification of the optical properties of polymethylmethacrylate.' *Applied Surface Science*, 154-155 (2000): 706-711
- [134] R. Srinivasan, B. Braren and K.G. Casey. 'Ultraviolet laser ablation and decomposition of organic materials.' *Pure and Applied Chemistry*, 62 (8) (1990): 1581-1584
- [135] A. Zoubir, C. Lopez, M. Richardson and K. Richardson. 'Femtosecond laser fabrication of tubular waveguides in poly(methyl methacrylate).' *Optics Letters*, 29 (16) (2004): 1840-1842
- [136] R.S. Taylor and C. Hnatovsky. 'Particle trapping in 3-D using a single fiber probe with an annular light distribution.' *Optics Express*, 11 (21) (2003): 2775-2782
- [137] E. N. Glezer, M. Milosavljevic, L. Huang, R.J. Finlay, T.H. Her, J.P. Callan and E. Mazur. 'Three-dimensional optical storage inside transparent materials.' *Optics Letters*, 21 (24) (1996): 2023-2025

- [138] J. Oiu, K. Kojima, K. Miura, T. Mitsuyu and K. Hirao. 'Infra-red femtosecond laser pulse induced permanent reduction of Eu^{3+} to Eu^{2+} in a fluorozirconate glass.' *Optics Letters*, 24 (11) (1999): 786-788
- [139] K. Miura, J. Oiu, S. Fujiwara, S. Sakaguchi and K. Hirao. 'Three-dimensional optical memory with rewritable and ultra high density using the valance-state change of samarium ions.' *Applied Physics Letters*, 80 (13) (2002): 2263-2265
- [140] H. Jiu, H. Tang, J. Zhou, J. Xu, Q. Zhang, H. Xing, W. Huang and A. Xia. 'Sm(DBM)3 Phen-doped polymethylmethacrylate for three-dimensional multilayered optical storage.' *Optics Letters*, 30 (7) (2005): 774-776
- [141] J. Si, J. Qiu, J. Zhai, Y. Shen and K. Hirao. 'Photoinduced permanent gratings inside bulk azodye-doped polymers by the coherent field of a femtosecond laser.' *Applied Physics letters*, 80 (3) (2002): 359-361
- [142] Y. Li, K. Yamada, T. Ishizuka, W. Watanabe, K. Itoh and Z. Zhou. 'Single femtosecond pulse holography using polymethyl methacrylate.' *Optics Express*, 10 (21) (2002): 1173-1178
- [143] P.J. Scully, D. Jones and D.A. Jaroszynshi. 'Femtosecond laser irradiation of polymethylmethacrylate for refractive index gratings.' *Journal of Optics A: Pure and Applied*, 5 (4) (2003): S92-S96
- [144] C. Wochowski, Y. Cheng, K. Meteva, K. Sugioka, K. Midorikawa and S. Metev. 'Femtosecond-laser induced formation of grating structures in planar polymer substrates.' *Journal of Optics A: Pure and Applied*, 7 (9) (2005): 493-501
- [145] S.H. Law, J.D. Harvey, R.J. Kruhlak, M. Song, E. Wu, G.W. Barton, M.A. van Eijkelenborg and M.C.J. Large. 'Cleaving of microstructured polymer optical fibres.' *Optics Communications*, 258 (2) (2006): 193-202
- [146] K. Matsushige, S.V. Radcliffe and E. Baer. Pressure and temperature effects on brittle-to-ductile transition in PS and PMMA.' *Journal of Applied Polymer Science*, 20 (7) (1976): 1853-1866
- [147] R.P. Kusy and D.T. Turner. Influence of molecular-weight of poly(methylmethacrylate) on fracture morphology in notched tension.' *Polymer* 18 (4) (1977): 391-402
- [148] J. Canning, M. Åslund and P-F. Hu. 'Ultraviolet-induced absorption losses in hydrogen-loaded optical fibers and in presensitized optical fibers.' *Optics Letters*, 25 (22) (2000): 1621-1623
- [149] H. Dobb, D.J. Webb, K. Kalli, A. Argyros, M.C.J. Large and M.A. van Eijkelenborg. 'CW UV light induced fibre Bragg gratings in few- and single-moded microstructured polymer optical fibre.' *Optics Letters*, 30 (24) (2005): 3296-3298
- [150] H.Y. Liu, G.D. Peng and P.L. Chu. 'Thermal Tuning of Polymer Optical Fiber Bragg Gratings.' *IEEE Photonics Technology Letters*, 13 (8) (2001): 824-826
- [151] R. Kashyap and B.K. Nayar. 'An all single-mode fibre Michelson interferometer sensor.' *IEEE Journal of Lightwave Technology*, LT-1 (3) (1983): 619-624
- [152] T. Mizuochi, T. Kitayama, K. Shimizu and K. Ito. 'Interferometric cross talk-free optical add/drop multiplexer using cascaded Mach-Zehnder fiber gratings.' *Journal of Lightwave Technology*, 16 (2) (1998): 265-276

- [153] J. Canning and M.G. Sceats. 'Pi-phase-shifted periodic disturbed structures in optical fibres by UV post-processing.' *Electronics Letters*, 30 (16) (1994): 1344-1345
- [154] R. Kashyap, P.F. McKee and D. Armes. 'UV written reflection grating structures in photosensitive optical fibres using phase-shifted phase masks.' *Electronics Letters*, 30 (23) (1994): 1977-1978
- [155] D. Uttamchandani and A. Othonos. 'Phase-shifted Bragg gratings formed in optical fibres by post-fabrication thermal processing.' *Optics Communications*, 127 (1996): 200-204
- [156] W.C. Wang, M. Fisher, A. Yacoubian and J. Menders. 'Phase-shifted Bragg grating filters in polymer waveguides.' *IEEE Photonics Technology Letters*, 15 (4) (2003): 548-550
- [157] N. Groothoff, J. Canning, E. Buckley, K. Lyttikainen and J. Zagari. 'Bragg grating in air-silica structured fibers.' *Optics Letters*, 28 (4) (2003): 233-235
- [158] L.B. Fu, G.D. Marshall, J.A. Bolger, P. Steinvurzel, E.C. Magi, M.J. Withford and B.J. Eggleton. 'Femtosecond laser writing Bragg gratings in pure silica photonic crystal fibres.' *Electronics Letters*, 41 (11) (2005): 638-639
- [159] P. Domachuk, H. C. Nguyen, and B. J. Eggleton, M. Straub and M. Gu. 'Microfluidic tunable photonic band-gap device.' *Applied Physics Letters*, 85 (11) (2004): 1838-1840
- [160] From private communication with the OFTC in Australia
- [161] A. Argyros, M.A. van Eijkelenborg, S.D. Jackson and R.P. Mildren. 'Microstructured polymer optical fibre laser.' *Optics Letters*, 29 (16) (2004): 1882-1884
- [162] U. Gibson and U. Österberg. 'Comment on "Microstructured polymer fibre laser".' *Optics Letters*, 30 (14): 1827-1828
- [163] A. Argyros, M.A. van Eijkelenborg, S.D. Jackson and R.P. Mildren. 'Reply to comment on "Microstructured polymer optical fibre laser".' *Optics Letters*, 30 (14) (2005): 1829-1830
- [164] J-M. Yu, X-M Tao and H-Y Tam. 'Trans4-stilbenemethanol-doped photosensitive polymer fibers and gratings.' *Optics Letters*, 29 (2) (2004): 156-158
- [165] <http://www.chemicaland21.com/industrialchem/functional%20Monomer/METHYL%20METHACRYLATE.htm> (Accessed May 2006)
- [166] http://biomems.uta.edu/Research/Poster%202-1_files/frame.htm (Accessed July 2005)
- [167] P.I. Vincent. *Polymer*, 1 (1960): 425
- [168] H.G. Limberger, N. H. Ky, D.M. Costantini, R.P. Salathé, C.A.P. Muller and G.R. Fox. 'Efficient miniature fiber-optic tunable filter based on intracore Bragg grating and electrically resistive coating.' *IEEE Photonics Technology Letters*, 10 (3) (1998): 361-363
- [169] J.A. Rodgers, P. Kuo, A. Ahuja, B.J. Eggleton and R.J. Jackman. 'Characteristics of heat flow in optical fiber devices that use integrated thin-film heaters.' *Applied Optics*, 39 (28) (2000): 5109-5116
- [170] A. Abramov, B.J. Eggleton, J.A. Rogers, R.P. Espindola, A. Hale, R.S. Windeler and T.A. Straaser. 'Electrically tunable efficient broadband long-period fiber grating filter.' *IEEE Photonics Technology Letters*, 11 (4) (1999): 445-447

- [171] J.A. Rogers, B.J. Eggleton, R.J. Jackman, G.R. Kowach and T.A. Strasser. 'Dual on-fiber thin-film heaters for fiber gratings with independently adjustable chirp and wavelength.' *Optics Letters*, 24 (19) (1999): 1328-1330
- [172] Q. Fang, D.G. Chetwynd and J.W. Gardner. 'Conducting polymer films by UV-photo processing.' *Sensors and Actuators, A*, 99 (2002): 74-77
- [173] Q. Fang, G. He, W.P. Cai, J-Y- Zhang and I.W. Boyd. 'Palladium nanoparticles on silicon by photo-reduction using 172 nm excimer UV lamps.' *Applied Surface Science*, 226 (2004): 7-11
- [174] H. Dobb, K. Carroll, D. J. Webb, K. Kalli, M. Komodromos, C. Themistos; G. D. Peng A. Argyros, M. C. J. Large, M. A. van Eijkelenborg, Q. Fang, I. W. Boyd. 'Grating based devices in polymer optical fibre.' *Proceedings-SPIE The International Society For Optical Engineering-Photonics Europe 06*, Strasbourg, France 6-8th September 2006 [6189-01]
- [175] http://en.wikipedia.org/wiki/Volumetric_thermal_expansion_coefficient (Accessed July 2006)
- [176] M.A. Butler and D.S. Ginley. 'Hydrogen sensing with palladium-coated optical fibers.' *Journal of Applied Physics*, 64 (7) (1988): 3706-3712
- [177] B. Sutapun, M. Tabib-Azar and A. Kazemi. 'Pd-coated elastooptic fiber optic Bragg grating sensors for multiplexed hydrogen sensing.' *Sensors and Actuators, B*, 60 (1) (1999): 27-34